Contribution to the Control of the Hybrid Excitation Synchronous Machine for Embedded Applications

Rita Mbayed

Année 2012

UNIVERSITE DE CERGY PONTOISE

THESE

Présentée pour obtenir le grade de

DOCTEUR DE L'UNIVERSITE DE CERGY PONTOISE

Ecole doctorale: Sciences et Ingénierie
Spécialité: Génie Electrique

Soutenance publique prévue le 12 Décembre 2012

Par

Rita MBAYED

Contribution to the Control of the Hybrid Excitation Synchronous Machine for Embedded Applications

---

JURY

Rapporteurs	:	Prof. Gérard CHAMPENOIS Prof. Eric SEMAIL	Université de Poitiers Ecole Nationale d'Arts et Métiers ParisTech
Examinateurs	:	Prof. Francis LABRIQUE Prof. Mohamed GABSI Dr. Vincent LANFRANCHI	Université Catholique de Louvain Ecole Normale Supérieure Cachan Université de Technologie de Compiègne
Directeur de thèse	:	Prof. Eric MONMASSON	Université de Cergy Pontoise
Co-directeurs	:	Prof. GeorgesSALLOUM Dr. Lionel VIDO	Université Libanaise Université de Cergy Pontoise

Laboratoire SATIE - UCP/UMR 8029, 1 rue d'Eragny, 95031 Neuville sur Oise France

The secret is comprised in three words: Work, finish, publish.

Michael Faraday

Ere many generations pass, our machinery will be driven by a power obtainable at any point of the universe. This idea is not novel. Men have been led to it long ago by instinct or reason; it has been expressed in many ways, and in many places, in the history of old and new. We find it in the delightful myth of Antheus, who derives power from the earth; we find it among the subtle speculations of one of your splendid mathematicians and in many hints and statements of thinkers of the present time. Throughout space there is energy. Is this energy static or kinetic? If static our hopes are in vain; if kinetic - and this we know it is, for certain - then it is a mere question of time when men will succeed in attaching their machinery to the very wheelwork of nature.

Nikola Tesla, "Experiments with alternate currents of high potential and high frequency", February 1892.

Abstract

This thesis is a contribution to the control of the Hybrid Excitation Synchronous Machine (HESM) in embedded applications. The HESM combines the advantages of the Permanent Magnets (PM) machine and the wound rotor machine. The excitation flux in this machine is produced by two different sources: the PMs and a DC field winding that is placed at the stator to preserve a brushless structure. The latter source is used to control the flux in the air gap. The machine model is based on a Park model and it takes into account the iron losses and the magnetic circuit saturation effect. The electric parameters of the laboratory prototype are identified. The machine is controlled in generator mode and motor mode. In power generation system, the study treats in particular the aircraft power supply in more electric aircrafts. Two distribution networks are studied: High voltage variable frequency network and high voltage DC network. In the latter case, the HESM is coupled to a diode bridge rectifier. In both cases, the control aims to maintain the output voltage magnitude equal to its reference via action on the field current only. The control is scalar. Simulation with Matlab/Simulink and experiments validate the approach. For the motor mode, the attention is paid to the electric propulsion in an electric vehicle. An optimal current control with minimal losses is elaborated. The copper losses are considered in a first place. Iron losses are added next. Finally, the optimization problem is extended and it includes the losses due to the inverter and the chopper. Analytical expressions of the reference armature and field currents are computed using extended Lagrange multiplier method (Kuhn-Tucker conditions). Simulation with Matlab/Simulink software proves that the analytical solution yields indeed to the current combination that guarantees the minimal losses over the New European Driving Cycle.

Keywords: Hybrid excitation synchronous machine; control; optimization; embedded application; aircraft; electric vehicle.

Résumé

Le travail présenté dans cette thèse est une contribution à la commande de la Machine Synchrone à Double Excitation (MSDE) pour des applications embarquées. La MSDE allie les avantages de la machine synchrone à aimants permanents et la machine synchrone à rotor bobiné. Le flux d'excitation dans cette machine est généré par deux sources : les aimants permanents et un enroulement qui est placé au stator afin d'éviter les contacts glissants. Cette dernière source permet de régler le flux dans l'entrefer. Le modèle de la machine est basé sur un modèle de Park et prend en considération les pertes fer et la saturation des circuits magnétiques. Les paramètres du prototype existant au laboratoire ont été identifiés. La commande de la MSDE est effectuée en deux modes : générateur et moteur. En génératrice, l'application visée est la génération électrique en avionique. Deux réseaux de distribution sont traités : Réseau à haute tension et à fréquence variable et réseau haute tension DC. Dans ce dernier cas, la MSDE est associée à un pont redresseur à diodes. Dans les deux cas, la commande est élaborée dans le but de maintenir l'amplitude de la tension constante via le control du courant d'excitation uniquement. Le control est scalaire. L'approche est validée par simulation avec Matlab/Simulink et par expérimentation. Pour le mode moteur, l'application visée est la propulsion dans un véhicule électrique. Une commande optimale des courants est étudiée en vue de minimiser les pertes. Les pertes joules sont considérées premièrement. Ensuite, les pertes fer sont ajoutées. Finalement, le problème de minimisation est étendu pour inclure les pertes dues à l'onduleur et au hacheur. L'optimisation par la méthode des multiplicateurs de Lagrange (Kuhn-Tucker conditions) est utilisée pour trouver des expressions analytiques des courants statoriques et inducteur optimaux. Des simulations avec Matlab/Simulink prouvent que la solution obtenue est celle qui assure les pertes minimales tout au long du nouveau cycle de conduite européen.

Mots-clés : Machine synchrone à double excitation ; commande ; optimisation ; applications embarquées ; avionique ; véhicule électrique.

Preface

The work presented in this thesis was accomplished at the SETE[1] team, SATIE[2] laboratory, Cergy Pontoise University. The experiments were performed at the SATIE laboratory, *Ecole Normale Supérieure* (*ENS*) Cachan. The research was carried out under the supervision of Prof. Eric Monmasson and Dr. Lionel Vido, both from SATIE, Cergy Pontoise University, and Prof. Georges Salloum from the Lebanese University.

Firstly, my sincere gratitude goes to my supervisor Prof. Monmasson for his confidence, foremost, and his guidance. Despite the fact that my stay in France was relatively short and temporary, he was always aware of my progress, available to review my work and to suggest new prospects. I am honored to work under the supervision of such an exceptional person.

Secondly, I would like to express my deepest recognition to my co-supervisor Prof. Salloum for his moral and professional support. I would not be here today without his devoted contribution. I would like to thank him as well for the effort he made to assure the best working conditions for me.

I am also thankful to my second co-supervisor Dr. Lionel Vido for his kindness and his help, especially during my stay in France. I appreciate particularly the attention he pays to little details.

I am grateful to Prof. Mohamed Gabsi, *SATIE, ENS Cachan*, for the interest he showed in my work and his helpful comments throughout the thesis stages.

I would like to thank the assessment committee chairman Prof. Francis Labrique, *SST/EPL, Université Catholique de Louvain (UCL)*, and all the committee members: Prof. Gerard Champenois, *LAII, Université de Poitiers*, Prof. Eric Semail, *L2EP, Ecole Nationale d'Arts et Métiers ParisTech*, Prof. Mohamed Gabsi, *SATIE, ENS Cachan*, and Dr. Vincent Lanfranchi, *LEC, Université de Technologie de Compiègne*, who accepted to evaluate my work. The effort extended by Prof. Champenois and Prof. Semail to review the manuscript is much appreciated.

Regards go to all the personnel of SATIE laboratory and my fellow PhD students for their help and friendly companionship.

I particularly appreciate the encouragement of my colleagues, especially at the Lebanese University, Faculty of Engineering II, as well as my students along the past five years.

Special thanks go to my friends, in Lebanon and in France, who were always there for me. I know that things would have been much harder without their continuous support.

Finally, I want to thank my family: my father, my mother and my sister. They have patiently supported this endeavor. This achievement is theirs. I just want them to be proud of me.

---

[1] **S**ystèmes d'**E**nergies pour les **T**ransports et l'**E**nvironnement : Energy systems for transport and environment.

[2] **S**ystèmes et **A**pplications des **T**echnologies de l'**I**nformation et de l'**E**nergie : Systems and Applications in Information and Energy Technologies

Table of contents

Nomenclature

Acronyms

DC	Direct Current
DCM	Direct Current Machine
DTC	Direct Torque Control
EMF	ElectroMotive Force
ELMM	Extended Lagrange Multiplier Method
EV	Electric Vehicle
FEA	Finite Element Analysis
ICEV	Internal Combustion Engine Vehicle
MEA	More Electric Aircraft
HESM	Hybrid Excitation Synchronous Machine
HVAC	High Voltage Alternating Current (source, network)
HVDC	High Voltage Direct Current (source, network)
MTPA	Maximum Torque Per Ampere (motor control technique)
NEDC	New European Driving Cycle
PF	Power Factor
PI	Proportional Integral (controller)
PM	Permanent Magnet
POR	Point Of Regulation
RMS	Root Mean Square
SOC	State Of Charge (of the battery)

Symbols

$\boldsymbol{x}$, $\boldsymbol{X}$	Vector , matrix
$\boldsymbol{I}_a$	Identity matrix of size a
$\nabla f(\boldsymbol{x})$	Gradient of the function $f(\boldsymbol{x})$

$\nabla^2 f(\boldsymbol{x})$	Hessian of the function $f(\boldsymbol{x})$
$\lVert X \rVert$	Magnitude of the quantity X
$\lvert X \rvert$	Absolute value of the quantity X
s	Laplace transform variable
ω	Frequency (rad/s)
f	Frequency (Hz)
λ	Lagrange multiplier
μ	Kuhn-Tucker multiplier
$\boldsymbol{R}$	Rotation matrix
$\boldsymbol{P}$	Park transformation
$\boldsymbol{C}_{23}$, $\boldsymbol{C}_{32}$	Forward Clarke transformation, inverse Clarke transformation
$G(s)$	Open-loop transfer function
$H(s)$	Closed-loop transfer function
$C(s)$	Controller

Indexes and Exponents

X_n	Nominal quantity
X_{ref}	Reference quantity
X^*	Optimal reference quantity
$\hat{X}$	Estimated quantity
X_s	Quantity related to the stator
X_f	Quantity related to the field winding
X_{exc}	Quantity related to the excitation flux
X_{DC}	Quantity related to DC side of the diode bridge rectifier / inverter
X_{batt}	Quantity related to the battery
X_l	Quantity related to the load

X_0	Quantity at no load
X_3	Three-phase quantity
X_a, X_b, X_c	three-phase quantities
C_α , C_β	Components of a three-phase quantity in Clarke (or Concordia) reference frame
C_d , C_q	Components of a three-phase quantity in Park reference frame
$\boldsymbol{x}^t$, $\boldsymbol{X}^t$	Transpose of $\boldsymbol{x}$, transpose of $\boldsymbol{X}$

Physical quantities

θ	Rotor mechanical position (rad)
Ω	Rotor speed (rad/s)
T	Torque (N.m)
V_{DC}	Constant DC voltage across the inverter terminal / Constant DC bus voltage (V)
v	Voltage instantaneous value (V)
i	Current instantaneous value (A)
e	EMF / back EMF instantaneous value (V)
V	Voltage RMS value (V)
I	Current RMS value (A)
E	EMF / back EMF RMS value (V)
ϕ	Magnetic Flux (Wb)
φ	Phase shift angle between the armature voltage and the armature current (rad)
ψ	Phase shift angle between the EMF / back EMF and the armature current (rad)
δ	Phase shift angle between the armature voltage and the EMF / back EMF (rad)
P	Active Power (W)
P_{ir}	Iron losses (W)
E_{onT}, E_{offT}	IGBT turn-on energy, IGBT turn-off energy (J)
E_{offD}	Diode turn-off energy (J)

t_s	Settling time at 95% of the final value (s)
τ_{sd}	Direct axis time constant (s)
τ_{sq}	Quadrature axis time constant (s)
τ_f	Field circuit time constant (s)
τ_m	Mechanical time constant (s)

HESM Parameters

R_s	Stator winding resistance per phase (Ω)
R_f	Field winding resistance (Ω)
L_{sd} , L_{sq}	Stator direct and quadrature axis inductances (H)
L_f	Field winding inductance (H)
M_{sf}	Maximum value of the armature-to-field mutual inductance (H)
Φ_M	Maximum magnetic flux produced by the permanent magnets in an armature winding (fundamental) (Wb)
$\Phi_{M\ f}$	Maximum magnetic flux produced by the PMs in the field winding (Wb)
Φ_{exc}	Maximum magnetic flux produced by the PMs and the DC excitation current in an armature winding (fundamental) (Wb)
V_{smax}	Maximum value of the RMS armature voltage (voltage limit) (V)
I_{smax}	Maximum value of the RMS armature current (current limit) (A)
ω_s	Armature voltage and current radian frequency (rad/s)
Ω_b	Rotor base speed (rad/s)
T_{em}	Electromagnetic torque produced by the machine (N.m)
T_b	Braking torque (N.m)
T_{f0}	Dry friction torque (N.m)
f_v	Viscous friction coefficient (kg.m^2/s)
J	Moment of inertia (kg.m^2)
p	Number of poles pairs
n_s	Number of turns in a stator winding per phase

f_{sw}	Inverter switching frequency (Hz)
f_{chop}	Chopper chopping frequency (Hz)

Introduction

HESM in brief

Permanent Magnet (PM) synchronous machines offer high efficiency and reliability, low inertia and brushless structure. Nevertheless, their limitation is the lack of the field control. The excitation flux produced by the PMs is hard to regulate once the machine is designed. On the other hand, rotor wound synchronous machines present good magnetic field regulation but their structure includes slip rings and brushes. In addition, they suffer from a low efficiency due to the losses in the excitation winding.

The Hybrid Excitation Synchronous Machine (HESM) combines the advantages of the PM machine and the wound rotor machine. As its name reveals, the excitation flux in this machine is produced by two different sources: the PMs and a DC field winding that is usually placed at the stator to preserve a brushless structure. The latter source is used to control the flux in the air gap with a minimum of conduction losses [43]. In motor mode, weakening the field in the air gap leads to a constant power operation over a wide speed range. In generator mode, the electrical excitation allows the regulation of the output voltage without the need of a controllable converter on the stator side.

The HESM structure design has been widely treated in the literature. Several topologies have been reported: HESM with series excitation [37], HESM with juxtaposed structure [122], HESM with imbricate structure [6] [71] [132], consequent pole HESM [11] [21] [67] [86] [124]. Conversely, only few papers studied the control of this machine [95] [96] (generator mode) [116] [117] (motor mode).

Context outline

In response to concerns about energy cost, energy dependence and environmental damage, the automotive industry and the aerospace industry are facing challenges in terms of improving carbon dioxide emissions, fuel economy, and cost. They are moving toward more electric architectures. The mechanical and pneumatic systems are replaced with electrical systems [30] [141]. To meet these challenges in the automotive industry, significant work has been done in the areas of electric and hybrid vehicles. As for the airplanes, More Electric Aircraft (MEA) is the emerging trend.

A number of recent technologies have rekindled the concept of a MEA for optimizing the performance and the life cycle cost of the aircraft (Airbus A350, Boeing B787 and Lockheed Martin F-35…) [136]. The MEA emphasizes the use of electrical power as opposed to hydraulic and pneumatic power. The trend is to use the electrical power to supply the non-propulsive systems of the aircraft. This concept offers significant overall system benefits in reliability, less maintenance, lower weight, reduction of fuel consumption per passenger, efficiency on energy conversion and sustainability payoff [97] [101]. On the other hand, it imposes increasing demands on the on-board electrical power system, not only in terms of increasing the kilowatt power requirements but also in terms of higher fault-tolerance and reliability which mandates an innovative power generation, distribution and management [9][65][87]. New voltage levels are applied: wide frequency High Voltage Alternating Current (HVAC) distribution network (360-720 Hz, 230 V) [59] and/or High Voltage Direct Current (HVDC) distribution network (±270 V) [48] [104]. Novel connectivity topologies are studied too [31]. The evolution of the aircraft electric

power system results in more challenging requirements on the electric components, especially the electric generators.

Presently, aircraft embedded generators are based on a structure composed of three separated brushless generators mounted on the same shaft [20] [103]. This structure is standalone, it avoids slip rings and brushes and allows the control of the main generator excitation. However, the price to pay is its complexity.

Concerning Electric Vehicles (EVs), it is known that historically electric cars have not been widely adopted because of their limited driving distance, long recharging time and battery cost and weight especially when compared to Internal Combustion Engine Vehicle (ICEV). However, as battery technology improves, simultaneously increasing energy storage and reducing cost, a kindling of interest in EVs has taken an accelerated pace. In the last few years, major automakers began introducing to the market new generations of electric cars: BMW i3, BYD e6, Chevy Volt, Ford Focus Electric, Mercedes-Benz BlueZERO, Tesla Roadster, Mitsubishi i-MiEV, Renault Fluence Z.E., Honda Fit EV, Toyota FT-EV II, Smart ED, Mini E…

EV has several benefits compared to conventional ICEV including a significant reduction of local air pollution, reduced greenhouse gas emissions (depending on the electricity generation source) and less vulnerability to oil price. As power plants improve efficiency and turn to cleaner fuels such as natural gas and zero-emission renewable sources, EV will be the best solution towards attaining clean air. In addition, EV is mechanically much simpler than ICEV, has one moving part and requires less maintenance with no filters, no spark plug, since the EV is propelled by one or more electric motors [22].

The PM motors are the most used machines in electric propulsion [28]. However, their drawback is the difficulty of the field control. The flux control is typically accomplished by acting on the d-axis armature current component. This approach generates significant increase in copper losses and involves the risk of irreversible demagnetization of the PMs and consequently a reduction in the machine efficiency since the torque capability of the machine is permanently diminished.

This thesis is a contribution to the control of the HESM. With its brushless structure, high power density and DC field winding, this machine is suitable for embedded applications; in particular, aircraft power generation system and EV propulsion system. It shall be pointed that for the embedded systems of MEA and EV, the high power density of the electrical machine (generator or motor) is a common requirement [141].

In generator mode, the HESM can replace the three-stage synchronous machine presently in use in most of the aircraft power systems. The electrical excitation allows the output voltage control.

In motor mode, thanks to the DC field winding, it is possible to perform the air gap flux weakening and eliminate the effect of the d-axis current injection.

Document organization

This document is divided into three parts.

Part I is dedicated to model the HESM. The machine model is built in Chapter 1. The considered HESM has salient poles and an imbricate structure with no dampers. The PMs are placed at the rotor. The DC excitation coil is placed at the stator to avoid sliding contacts. The derived mathematical model is based on a classic Park model of the synchronous machine. The model is

then enhanced by introducing the magnetic circuit saturation effect and the iron losses. In Chapter 2, the laboratory scale HESM main parameters are identified.

Part II of this thesis investigates the HESM operating as a standalone generator for aircraft power supply system. Two distribution networks are considered: Chapter 3 deals with the variable frequency HVAC network and Chapter 4 treat the HVDC network. For the HVDC network, the HESM is cascaded with a diode bridge rectifier. In both cases, the output voltage, phase voltage magnitude or DC bus voltage, is driven by the field current. The main contribution to the approach is that the control is scalar. The armature current components are not part of the compensation scheme. The control strategy is validated by simulation and experiments.

Part III studies the HESM control when operating in motor mode for EV application. The vector control aims in a first place to meet torque and speed requirements. With an extra degree of freedom, that is the field current, an additional condition can be satisfied. Since the drive is powered by a battery source, loss reduction is an important objective in order to guarantee the best autonomy distance range. In Chapter 5, copper loss minimization is considered at first. Iron losses are then included in the optimization problem. In Chapter 6, the battery, inverter and chopper are modeled and incorporated to the simulation model. The overall losses of the electric propulsion set are minimized. The main innovating contribution of the approach is that it presents analytical expressions for the optimal reference armature currents i_{sd} and i_{sq} as well as for the field current i_f with respect to armature current and voltage constraints. In both chapters, Extended Lagrange Multiplier Method (ELMM) (Kuhn-Tucker conditions) is used to compute these optimal reference currents. Calculations with Matlab software prove that the proposed solution is the one presenting minimal losses. In addition, simulation results over the New European Driving Cycle (NEDC) are compared to those obtained with commonly used synchronous motor control strategies. This driving cycle is supposed to represent the typical usage of a car in Europe.

This manuscript comprises two appendixes. Appendix A explains in brief the ELMM used to solve an optimization problem. Appendix B lists the laboratory prototype main characteristics.

Part I. Hybrid Excitation Synchronous Machine

Introduction of Part I

HESM - State of art

PM machines are widely used in many applications due to their high power density and efficiency, high reliability, low inertia and brushless structure. Depending on the PM arrangement, the PM motors can be classified as surface mounted magnet or buried magnet. The surface mounted designs use less magnets while the buried magnet designs achieve higher air gap flux density. However, the limitation of the PM machines is the lack of the field control. The excitation flux produced by the PMs is hard to regulate once the machine is designed. Thus, the voltage regulation in generator mode and the speed increase in motor mode are difficult to be realized.

In order to control the excitation flux, new PM machine topologies were studied. Two concepts are reported in the literature:

- In the first approach, the flux weakening is performed by an external mechanical action.
- The second approach proposes the addition of an auxiliary source that can strength or weaken the PM flux. This new type of machines is called Hybrid Excitation Synchronous Machine (HESM).

PM machine with flux weakening by a mechanical action

Different structures with flux weakening by a mechanical action have been presented. Yet, the concept is almost the same: part of the PM flux is reduced by a mechanical action on external magnetic circuits. The most illustrious structures are listed hereby.

A doubly salient variable reluctance machine having PMs mounted on the stator is proposed. The flux weakening is accomplished by controlled movement of steel insets toward and away from the sides of the stator proximate the PMs to provide a controllable bypass flux path thereabout as shown in Figure I.1 [69] [112]. Alternatively, the field weakening might be accomplished by flux bypass collar that may be angularly positioned around the stator to bridge the PMs of the motor with discrete magnetic sections, thereby providing an alternate bypass flux path around the PMs in addition to the main air gap flux path [112]. A third alternative is accomplished by controlled axial sliding of the PMs themselves into and out from the stator [112]. In this structure, relatively large forces must be overcome to position the magnet accurately. The flux weakening capability of the machine is tested experimentally [112].

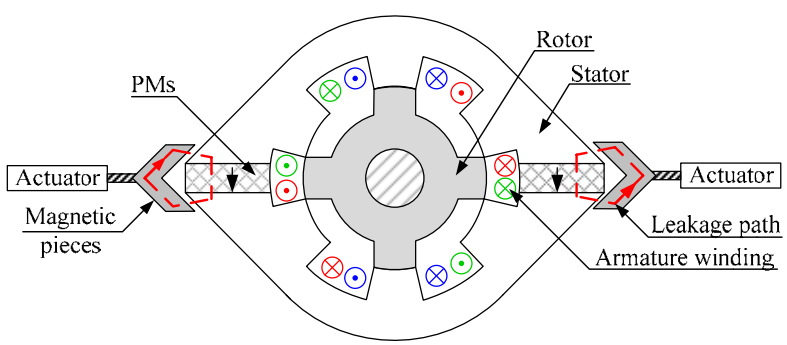

Figure I.1. Field Weakening of the machine derived by a movable magnetic shorting piece

An automatic flux weakening with the rotor speed is presented in [13]. The structure of the rotor is shown in Figure I.2. The centrifugal force that acts on the magnetic conductor material increases following the rising speed of the rotor. The magnetic conductor material moves toward outside of the circle, the magnetic reluctance reduces, the flux through the air gap decreases, and the flux weakening is implemented (Figure I.3). The flux weakening is proven by Finite Element Analysis (FEA).

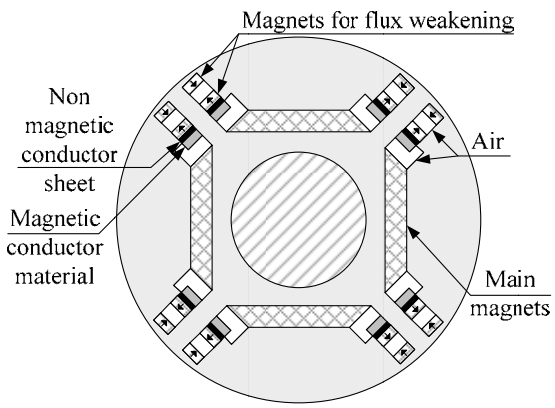

Figure I.2. PM motor with flux weakening based on centrifugal force: rotor section

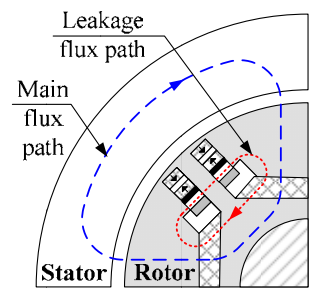

Figure I.3. Flux paths during flux weakening based on centrifugal force

An interior PM synchronous machine with adjustable PM armature flux linkage by means of adapting flux shortening iron plates at the both sides of rotor is introduced in [73]. The PM armature flux linkage can be adjusted by controlling the gap length between iron plates and rotor. The principle of the proposed machine is illustrated in Figure I.4. The position of the movable iron plates is adjusted using two actuators installed on each side of the stator.

In another structure, the rotor comprises two PM fields (Figure I.5). The secondary field is capable of relative rotation with respect to the first one [55] [56] [57] [80]. At low speed, the poles having the same polarity are aligned. Their fluxes are added. At high speed, a simple shifting between the rotor parts allows the flux weakening in the air gap. The excessive use of PMs increases the machine cost.

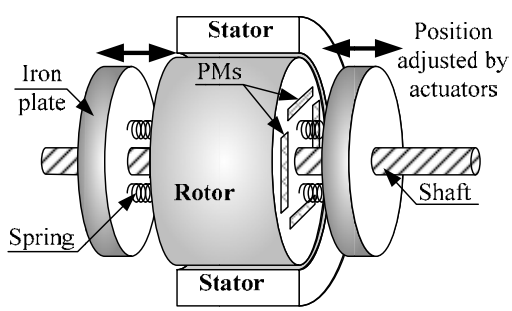

Figure I.4. Interior PM with movable iron plates

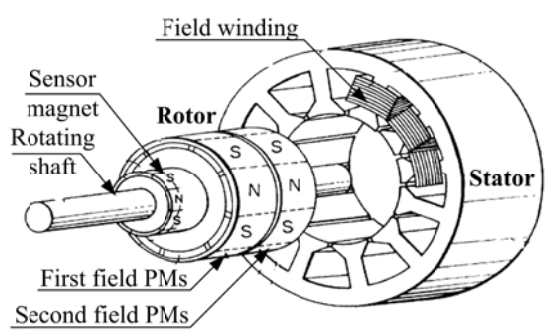

Figure I.5. PM motor with rotating rotor parts: view where the magnetic poles are not shifted [80]

Synchronous machine with hybrid excitation

The excitation flux in the HESM is produced by two different sources: the PMs and a DC field winding (or PMs too) [43] [111]. The latter source is used to control the excitation level of the machine. Depending on the field current direction, the flux is weakened or strengthened [2] [3] [7] [32] [66] [70] [72] [102]. The HESM are classified in two categories: series hybrid excitation and parallel hybrid excitation.

HESM with series excitation structure

In series structures [37], the flux produced by the PMs and the flux produced by the DC field winding pass through the same magnetic circuit, as shown in Figure I.6. Depending on the field current direction, the total excitation flux can be reduced or reinforced. The flux weakening occurs along the entire magnetic circuit, thus it induces a reduction in the machine iron losses. The main drawback of the series structure is that the magnetic path crossed by the field winding flux presents high reluctance since it comprises the PMs. Thus, high field current is needed in order to perform the flux weakening. This implies high copper losses and the risk of PM demagnetization.

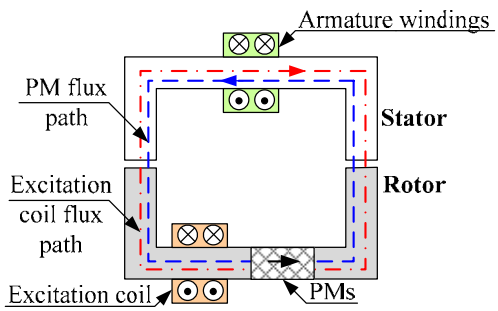

Figure I.6. Principle of series hybrid excitation during flux weakening

HESM with parallel structure

In parallel structure the flux produced by the PMs and the one produced by the DC field winding are superimposed in the air gap and the armature windings only. In this type of machines, the flux weakening does not usually yield to iron losses reduction. Several parallel topologies are proposed in the literature [68]. Only the common structures are presented herein.

The juxtaposed structure [122] [123] consists of stator winding surrounding a rotor with a wound field portion and a PM portion acting in combination as shown in Figure I.7. The rotor winding may be excited with a forward or reverse polarity current to increase or decrease the magnetomotive force. This structure suffers from high iron losses especially during flux weakening. In addition, the wound part of the rotor has to be long enough to ensure efficient flux weakening operation.

Consequent pole PM machine consists of a rotor divided into two sections. One section has surface mounted PMs and the other has a laminated iron poles (Figure I.8). The stator is composed of a conventional three-phase windings and a circumferential field winding [41] [42]. Injecting DC current into the field winding generates a flux that flows from one iron pole to the next pole through the stator and rotor yoke. This flux combines with the PM flux in the air gap. The winding generated flux goes to add/subtract to/from PM flux according to the field current direction. The same principle can be used for either radial gap PM machines [86] [124] or axial gap PM machines

[10] [11] [21] [67] [99]. The principle for an axial gap PM is illustrated in Figure I.9. Three-dimensional flux distribution in consequent pole PM machine increases material requirement and introduces some manufacturing difficulties [12] [124]. Several prototypes are evaluated by FEA [10] and/or experimentally [21] [42] [99] [124].

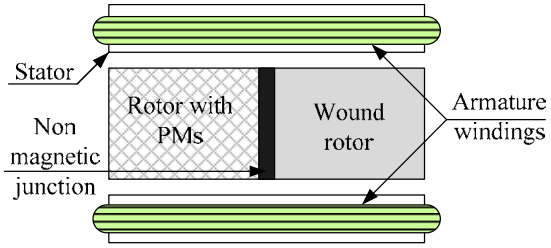

Figure I.7. HESM with juxtaposed structure

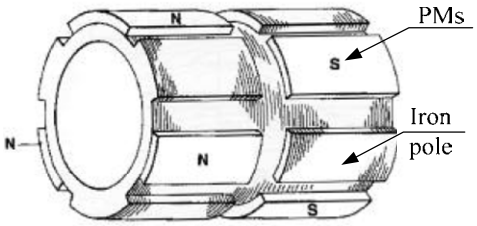

Figure I.8. Rotor of a consequent pole PM machine with radial gap [86]

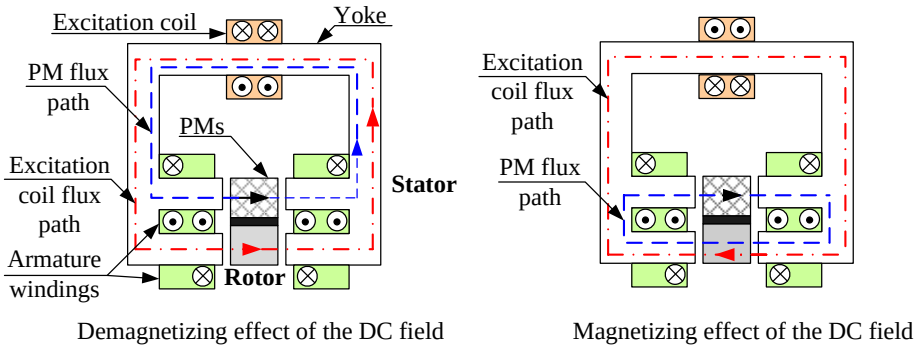

Figure I.9. Consequent pole PM machine with axial gap

In flux switching HESM [40], all the active parts are located on the stator. The salient rotor is passive. The hybrid excitation is an association of PMs and a wound exciter. According to the position of the mobile part, the magnetic flux linkage in the armature winding can be positive or negative and thus it is alternating. An elementary magnetic cell (shown in Figure I.10) helps to explain the operating principle of this structure. Due to its passive rotor, the machine presents high robustness. In addition, the flux weakening yields to iron losses reduction. The machine performances are evaluated by FEA and experiments.

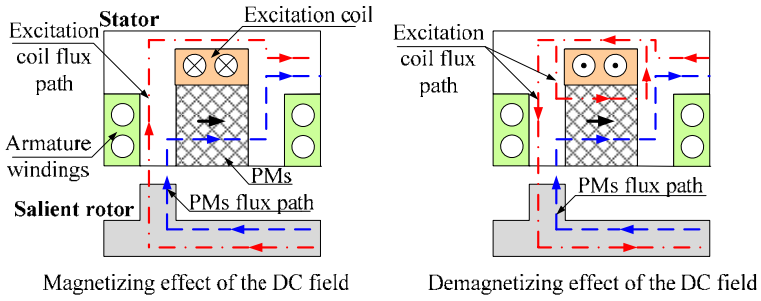

Figure I.10. Elementary cell of the flux switching HESM

In imbricate HESM [6] [71] [132], the rotor is composed of two parts: one contains the PMs and the other is used to direct the excitation flux. The stator consists of a laminated part where armature windings and DC field winding are placed. In addition, the stator contains external yoke and end shields that are used to channel the flux generated by the field winding. Thanks to the machine particular configuration, the field winding flux does not pass through the PMs. Thus, the control of the air gap flux is performed without any risk of magnet demagnetization. Figure I.11 explains schematically the principle of operation of imbricate HESM. The rotor can be assembled to have a homopolar or a bipolar configuration. In homopolar configuration, the DC field acts on one magnetic pole only. In bipolar configuration, both north and south magnetic poles are affected by the field winding flux. Hence, bipolar configuration allows better control of the excitation flux [131]. Different prototypes were tested by FEA [16] and experiments [38] [131] [132]. The HESM used for simulation and experiments in this thesis is based on this structure. Its configuration is detailed in section 1.1.

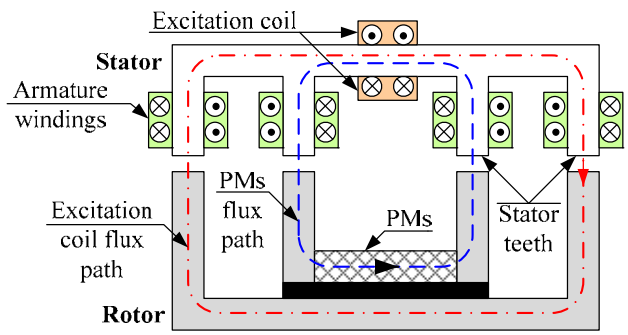

Figure I.11. Schematic showing the flux paths in an imbricate HESM

Part I organization

Part I is dedicated to model the HESM.

In Chapter 1, the machine structure is outlined in a first place. The mathematical model of the HESM is elaborated next. At first, a classic Park model is developed. It is then improved by taking into account the iron losses and the magnetic circuit saturation effect. As it is done in PM synchronous machine modeling, the iron losses are introduced by an equivalent shunting resistor. The resistance varies according to speed, field current and armature voltage values. In order to take into consideration the magnetic circuit saturation in the simulation model, the inductances and excitation flux are expressed in terms of the armature and field currents. The inductance-current relationships are found based on curves obtained by FEA.

One challenge when developing a mathematical model of a machine is the determination of the parameters that have to be used in the model. Thus, the laboratory scale HESM parameters are identified in Chapter 2. The estimation of the machine armature winding and field winding resistances is simple and straightforward. The field inductance is computed based on field current step response. In order to determine the permanent magnet flux and the armature-to-field mutual inductance, the excitation flux is computed in terms of the field current by means of ElectroMotive Force (EMF) measurements. The armature direct and quadrature axes inductances are evaluated using particular combinations of armature reference currents with hysteresis controllers while the machine rotor is locked. The extracted parameters are used to simulate the machine under Matlab/Simulink and to design the machine controllers in Part II and Part III.

Chapter 1. HESM Modeling

Introduction

The considered HESM presents salient poles with no dampers. The machine imbricate structure is described briefly in section 1.1. In section 1.2, the HESM mathematical model is presented. It is based on the Park first harmonic model of the synchronous machine. It is then improved by taking into account the iron losses (section 1.3) and the magnetic circuit saturation effect (section 1.4). The sign conventions are those of the motor operation. Yet, by multiplying the armature voltage expressions by −1, the model represents a hybrid excitation synchronous generator. The established model is used in simulation and helps to elaborate the machine control in generator mode and in motor mode, as it will be detailed in Part II and Part III respectively.

1.1. HESM with imbricate structure

The considered machine is a HESM with imbricate structure. Its rotor core consists of independent laminated parts and ferrite PMs. In order to obtain the highest air gap flux density, the PMs are set according to the flux focusing principle [144]. The stator consists of a laminated part where the armature windings are located. In order to control the excitation flux in the air gap, two annular excitation coils are placed at the stator avoiding brushes and sliding contacts. External yoke, end shields and rotor flux collector are added to channel the field winding flux through the active air gap. Depending on the direction of the DC field current, the air gap flux can be reinforced or reduced. Thanks to the machine particular configuration, the air gap flux is compensated without any risk of magnets demagnetization since the path of the flux produced by the excitation coils and the PM flux path overlap only in the active air gap and the armature windings. The rotor is modular and can be assembled in a homopolar (Figure 1.1) or bipolar (Figure 1.2) configuration.

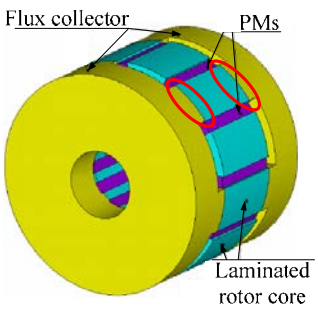

Figure 1.1. Rotor in homopolar configuration [132]

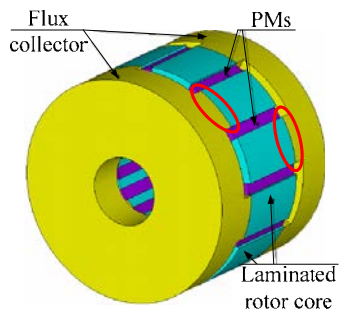

Figure 1.2. Rotor in bipolar configuration [132]

In order to understand the principle of each configuration, flux paths of the magnetic flux sources (PMs, field winding) are to be observed. Two types of flux path exist: homopolar flux path and bipolar flux path. A homopolar flux path passes through the active air gap only once and returns via the end shields and the rotor flux collector. A bipolar flux path passes through the active air gap twice creating north and south poles [38].

In homopolar configuration, the field winding excitation flux acts on one magnetic pole only (north or south). DC currents of opposite direction flow in the excitation coils. PM flux follows a bipolar path (Figure 1.3) and a homopolar path (Figure 1.4). Whereas, DC coils excitation flux follows only a homopolar path (Figure 1.5).

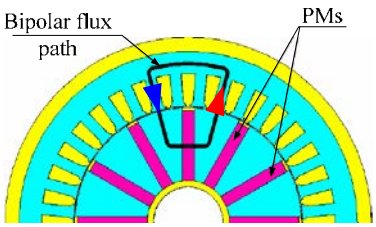

Figure 1.3. PM bipolar flux path [132]

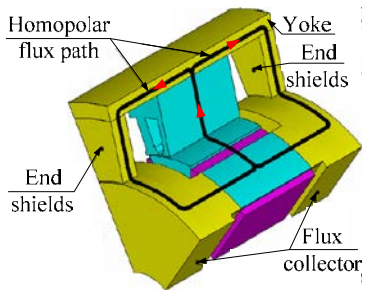

Figure 1.4. PM homopolar flux path in homopolar configuration [132]

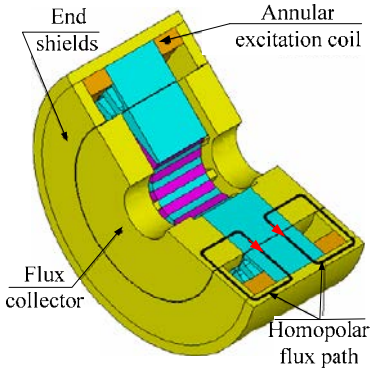

Figure 1.5. Excitation coils homopolar flux path in homopolar configuration [132]

In bipolar configuration, the flux produced by the excitation coils acts on both PM poles. The currents flowing in these coils have same direction. Each coil acts on one type of poles. Figure 1.6 and Figure 1.7 depict the homopolar PM flux path and the homopolar DC coils flux path in bipolar configuration. The bipolar PM flux path remains the same as in homopolar configuration (Figure 1.3).

It is proven that bipolar configuration allow a wider flux variation [131] [132]. In addition, HESM with homopolar configuration is more affected by the magnetic circuit saturation than HESM with bipolar configuration [131]. Thus, the rotor of the prototype used for experiments is assembled in a bipolar configuration.

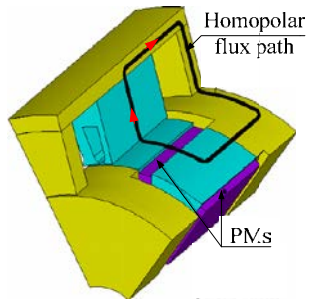

Figure 1.6. PM homopolar flux path in bipolar configuration [132]

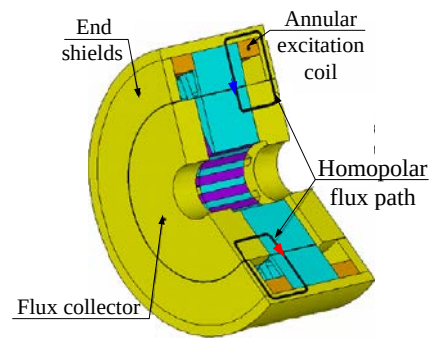

Figure 1.7. Excitation coils homopolar flux path in bipolar configuration [132]

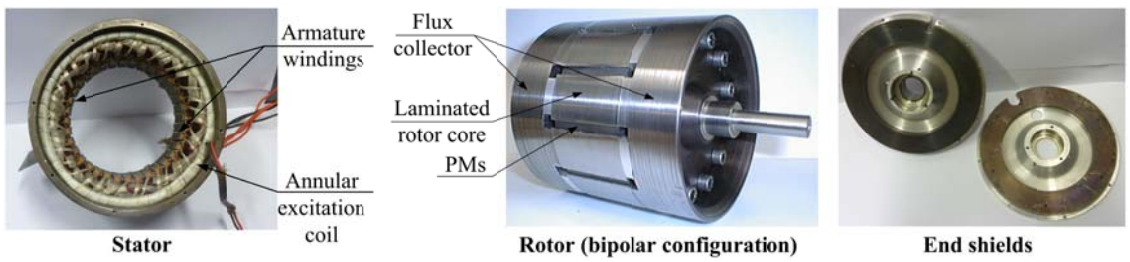

Figure 1.8. HESM prototype

1.2. Mathematical model

1.2.1. Voltage, flux and current relationships

Though the excitation winding is located at the stator, it creates a rotating field in the air gap that is equivalent to the one produced by a rotor excitation coil in classical wound synchronous machine. Under the hypothesis of linearity, symmetry and sinusoidal waveforms, the relationships between currents and fluxes are given by (1.1) for the armature windings and (1.2) for the field winding.

$$\boldsymbol{\phi}_{s3} = \boldsymbol{L}_s(p\theta)\boldsymbol{i}_{s3} + \boldsymbol{M}_{sf}(p\theta)i_f + \boldsymbol{\phi}_{Ms}(p\theta) \tag{1.1}$$

$$\phi_f = L_f i_f + \boldsymbol{M}_{sf}{}^t(p\theta)\boldsymbol{i}_{s3} + \Phi_{Mf} \tag{1.2}$$

Matrices are defined by (1.3), (1.4) and (1.5).

$$\boldsymbol{L}_s(p\theta) = \begin{bmatrix} L_{s1} & M_s & M_s \\ M_s & L_{s1} & M_s \\ M_s & M_s & L_{s1} \end{bmatrix} + L_{s2}\begin{bmatrix} cos(2p\theta) & cos\left(2p\theta - 2\pi/3\right) & cos\left(2p\theta - 4\pi/3\right) \\ cos\left(2p\theta - 2\pi/3\right) & cos\left(2p\theta - 4\pi/3\right) & cos(2p\theta) \\ cos\left(2p\theta - 4\pi/3\right) & cos(2p\theta) & cos\left(2p\theta - 2\pi/3\right) \end{bmatrix} \tag{1.3}$$

$$\boldsymbol{M}_{sf}(p\theta) = M_{sf}\left[cos(2p\theta) \quad cos\left(2p\theta - 2\pi/3\right) \quad cos\left(2p\theta - 4\pi/3\right)\right]^t \tag{1.4}$$

$$\boldsymbol{\phi}_{Ms}(p\theta) = \Phi_M \left[\cos(2p\theta) \quad \cos\left(2p\theta - 2\pi/3\right) \quad \cos\left(2p\theta - 4\pi/3\right) \right]^t \tag{1.5}$$

The armature voltage is given by (1.6).

$$\boldsymbol{v}_{s3} = R_s \boldsymbol{i}_{s3} + \frac{d\boldsymbol{\phi}_{s3}}{dt} \tag{1.6}$$

The voltage across the field winding is expressed by (1.7).

$$v_f = R_f i_f + \frac{d\phi_f}{dt} \tag{1.7}$$

A Park transformation is applied using successively a Clarke transformation (1.9) and a rotation of the coordinate system through a counterclockwise angle ξ (1.10).

$$\boldsymbol{x}_{\alpha\beta} = \boldsymbol{C}_{23}\boldsymbol{x}_{abc} \qquad \boldsymbol{x}_{dq} = \boldsymbol{R}(\xi)\boldsymbol{x}_{\alpha\beta} \tag{1.8}$$

$$\boldsymbol{C}_{23} = \frac{2}{3}\begin{bmatrix} 1 & -1/2 & -1/2 \\ 0 & \sqrt{3}/2 & -\sqrt{3}/2 \end{bmatrix} \tag{1.9}$$

$$\boldsymbol{R}(\xi) = \begin{bmatrix} cos(\xi) & sin(\xi) \\ -sin(\xi) & cos(\xi) \end{bmatrix} \tag{1.10}$$

ξ denotes the angle between the d-q frame and the reference frame. The d-axis of the synchronously rotating d-q frame coincides with the North pole of the rotor. Thus, $\xi = p\theta$.

In the d-q coordinate system, the HESM is described by (1.11) to (1.13).

$$v_{sd} = R_s i_{sd} + L_{sd}\frac{di_{sd}}{dt} + M_{sf}\frac{di_f}{dt} \underbrace{- p\Omega L_{sq} i_{sq}}_{e_{sd}} \tag{1.11}$$

$$v_{sq} = R_s i_{sq} + L_{sq}\frac{di_{sq}}{dt} + \underbrace{p\Omega\left(L_{sd} i_{sd} + \Phi_M + M_{sf} i_f\right)}_{e_{sq}} \tag{1.12}$$

$$v_f = R_f i_f + L_f \frac{di_f}{dt} + \frac{3}{2} M_{sf}\frac{di_{sd}}{dt} \tag{1.13}$$

With $L_{sd} = \frac{3}{2}\left(L_{s1} + L_{s2}\right)$ and $L_{sq} = \frac{3}{2}\left(L_{s1} - L_{s2}\right)$.

e_{sd} and e_{sq} are the d-q axis components of the back EMF.

1.2.2. Electro-mechanical conversion

The machine instantaneous power expression is given by (1.14).

$$p(t) = \boldsymbol{v}_{s3}{}^t \boldsymbol{i}_{s3} + v_f i_f = \boldsymbol{v}_{sdq}{}^t \boldsymbol{R}(p\theta)\boldsymbol{C}_{23}\boldsymbol{C}_{32}\boldsymbol{R}(-p\theta)\boldsymbol{i}_{sdq} + v_f i_f = \frac{3}{2}\boldsymbol{v}_{sdq}{}^t \boldsymbol{i}_{sdq} + v_f i_f \tag{1.14}$$

The machine energy transfer is then computed by (1.15).

$$p(t)\,dt = \underbrace{\left(\frac{3}{2}R_s\left(i_{sd}{}^2 + i_{sq}{}^2\right) + R_f i_f{}^2\right)}_{A} dt + \underbrace{\frac{3}{2}\left(d\phi_{sd} i_{sd} + d\phi_{sq} i_{sq}\right) + d\phi_f i_f}_{B} + \underbrace{\frac{3}{2}p\Omega\left(\phi_{sd} i_{sq} - \phi_{sq} i_{sd}\right)}_{C} dt \tag{1.15}$$

The term A represents the copper losses in the machine. B stands for the energy variation in the machine magnetic circuit. C is the mechanical energy. Accordingly, the electromagnetic torque is given by (1.16). It is the sum of a hybrid torque and a reluctance torque.

$$T_{em} = \frac{3}{2}p\left(\left(L_{sd} - L_{sq}\right)i_{sd} + M_{sf} i_f + \Phi_M\right)i_{sq} \tag{1.16}$$

The mechanical speed variation equals the sum of the torques applied on shaft as formulated by (1.17). T_l is the load torque; T_{f0} is the dry friction torque. $f_v\Omega$ is due to the viscous friction losses. The windage losses (proportional to the square of the rotor speed) are usually very small compared to the other losses and thus are neglected.

$$J\frac{d\Omega}{dt} = T_{em} - T_l - T_{f0} - f_v\Omega = T_{em} - T_b - f_v\Omega \tag{1.17}$$

1.2.3. HESM bloc diagram

The HESM model is represented by Figure 1.9. This bloc diagram is built based on (1.11) to (1.13), (1.16) and (1.17).

1.3. HESM model taking into consideration the iron losses

Thanks to its flux weakening capability, the HESM can operate at high speeds where the iron losses cannot be neglected. Thus, taking into account the iron losses in the HESM modeling is important. The iron losses in a HESM are evaluated in a first place. The modifications that shall be applied to the model built in section 1.2 are detailed next.

1.3.1. Iron losses computation

1.3.1.a. <u>Iron losses evaluation in PM machine</u>

The iron losses include the hysteresis losses and the eddy current losses. Different methods are proposed in order to evaluate these losses [83] [106] [129]. One empiric equation used to estimate the core losses in PM machine at no load is given by (1.18) [39] [83] [84] [90]. In addition, based on a widely adopted assumption, the iron losses are not depending of the load. Thus, (1.18) remains valid when the armature currents are not nil.

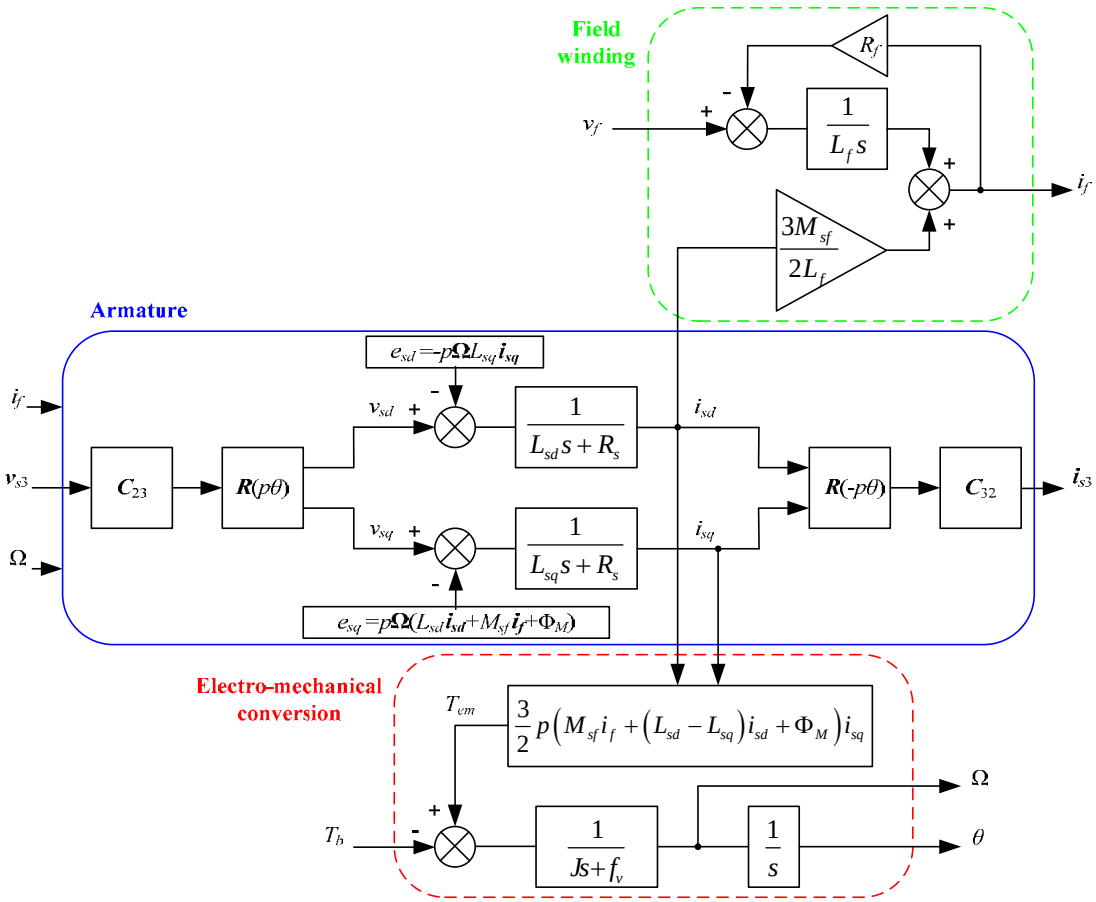

Figure 1.9. HESM bloc diagram

$$P_{ir} = 2q\left(\frac{f_s}{f_{ref}}\right)^{1.3}\left(M_y\left(\frac{B_y}{B_{ref}}\right)^2 + M_{st}\left(\frac{B_{st}}{B_{ref}}\right)^2\right) \tag{1.18}$$

With

q	Coefficient related to iron sheet quality, equal to 3.3 W/kg
f_{ref}	Reference frequency, equal to 50 Hz
B_{ref}	Reference induction, equal to 1.5 T
B_y	Induction in the yoke
B_{st}	Induction in the stator teeth
M_y	Yoke mass
M_{st}	Stator teeth mass

The induction in the stator teeth is given by (1.19).

$$B_{st} = \frac{\Phi_M}{n_s p l_a l_{st}} \tag{1.19}$$

n_s is the number of stator turns, l_a is the machine active length, l_{st} is the width of one stator tooth.

Under the hypothesis of flux conservation, the induction in the yoke is evaluated by (1.20).

$$B_y = \frac{3l_{st}}{2e_y} B_{st} \tag{1.20}$$

e_y is the yoke thickness.

Equation (1.18) is then reformulated.

$$P_{ir} = 2q \frac{1}{\left(2\pi f_{ref}\right)^{1.3} \left(pn_s B_{ref} l_a\right)^2} \left(\frac{9M_y}{\left(2e_y\right)^2} + \frac{M_{st}}{\left(l_{st}\right)^2} \right) \omega_s^{1.3} \Phi_M{}^2 \tag{1.21}$$

1.3.1.b. Iron losses evaluation in a HESM

The HESM is seen, from a general point of view, as a PM machine with an extra excitation coil. Therefore, the iron losses in a HESM can be estimated using in (1.21) under the condition of replacing the PM flux by the sum of the PM flux and the excitation coil flux.

$$P_{ir} = 2q \frac{1}{\left(2\pi f_{ref}\right)^{1.3} \left(pn_s B_{ref} l_a\right)^2} \left(\frac{3M_y}{\left(2e_y\right)^2} + \frac{M_{st}}{\left(l_{st}\right)^2} \right) \omega_s^{1.3} \left(M_{sf} i_f + \Phi_M\right)^2 \tag{1.22}$$

Iron losses were determined experimentally by means of torque measurement at no load for a given speed and excitation current [4]. The measurement results are superimposed by the losses computed by (1.22). The iron losses approximation is validated as shown in Figure 1.10. The dimensions of the laboratory scale machine used for the measurements and simulation are listed in Appendix B.

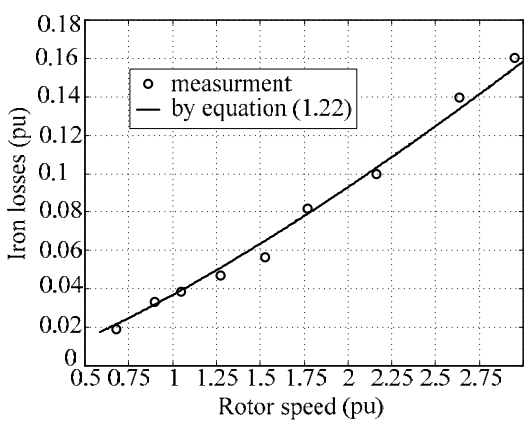

Figure 1.10. Iron losses for different rotor speeds and no field current

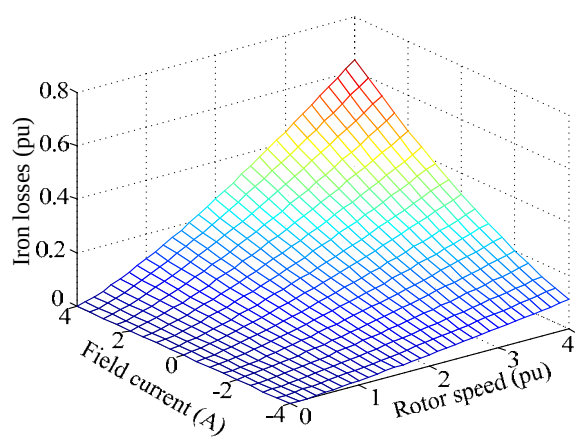

Figure 1.11. Iron losses versus rotor speed and field current

As it can be deduced from (1.22), once the machine is designed, the iron losses will depend on two quantities: the rotor speed and the excitation flux. Figure 1.11 shows the iron loss evolution versus speed and excitation current variation.

As noted in Figure 1.11, the iron losses decrease when the field current is negative. This is not correct for all HESM machine structures. In fact, the direct flux sum operated in (1.22) is true in the air gap. In HESM with series structures, the sum remains valid over the entire magnetic circuit since the excitation coil flux and the PM flux follow the same path. However, for parallel structures, the flux reduction occurs mainly in the air gap and the armature windings. A more accurate evaluation of the iron losses has to take into account the flux over the several magnetic field lines. Yet, the price to pay in this case is the difficulty to elaborate a generic analytical expression estimating these losses. Therefore (1.22) is used to model the iron losses in both HESM structures (series and parallel).

1.3.2. Direct and quadrature axis equivalent circuits

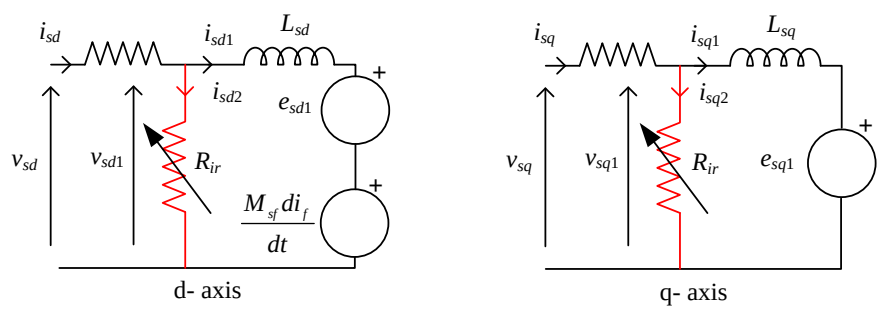

Figure 1.12. HESM dynamic equivalent circuits

Figure 1.12 represents the d-q axis equivalent circuits, drawn based on (1.11) and (1.12) respectively. A variable resistor R_{ir} is added in order to include the iron losses in the machine simulation model [90] [115]. Part of the armature current is lost in this parallel resistor. R_{ir} is computed during the simulation by (1.23). It exhibits different values with speed, field current and/or armature voltage variation.

$$R_{ir} = \frac{3V_{s1}^{\ 2}}{P_{ir}} = \frac{3\left(v_{sd1} + v_{sq1}\right)^2}{2P_{ir}} \tag{1.23}$$

Back to the equivalent circuits, the Kirchhoff voltage and current laws yield to (1.24) and (1.25).

$$\boldsymbol{v}_{sdq} = R_s \boldsymbol{i}_{sdq} + \boldsymbol{v}_{sdq1} \tag{1.24}$$

$$\boldsymbol{i}_{sdq} = \boldsymbol{i}_{sdq1} + \frac{\boldsymbol{v}_{sdq1}}{R_{ir}} \tag{1.25}$$

From (1.24) and (1.25), the d-q axis current components are computed.

$$\boldsymbol{i}_{sdq} = \frac{R_{ir}\boldsymbol{i}_{sdq1} + \boldsymbol{v}_{sdq}}{R_{ir} + R_s} \tag{1.26}$$

Replacing $\boldsymbol{i}_{sdq}$ by (1.26) in (1.24) gives the voltage expressions in terms of the machine internal currents when iron losses are taken into consideration.

$$v_{sd} = \left(\frac{R_s + R_{ir}}{R_{ir}}\right)\left(\frac{R_s R_{ir}}{R_s + R_{ir}} i_{sd1} + L_{sd}\frac{di_{sd1}}{dt} + M_{sf}\frac{di_f}{dt} \underbrace{- p\Omega L_{sq} i_{sq1}}_{e_{sd1}}\right) \tag{1.27}$$

$$v_{sq} = \left(\frac{R_s + R_{ir}}{R_{ir}}\right)\left(\frac{R_s R_{ir}}{R_s + R_{ir}} i_{sq1} + L_{sq}\frac{di_{sq1}}{dt} + \underbrace{p\Omega\left(L_{sd} i_{sd1} + \Phi_M + M_{sf} i_f\right)}_{e_{sq1}}\right) \tag{1.28}$$

$$v_f = R_f i_f + L_f \frac{di_f}{dt} + \frac{3}{2} M_{sf}\frac{di_{sd1}}{dt} \tag{1.29}$$

Practically, even at high speeds where R_{ir} is the lowest, $\frac{R_{ir}}{R_s} > 10$, therefore $\left(\frac{R_s + R_{ir}}{R_{ir}}\right)$ tends to one and $\frac{R_s R_{ir}}{R_s + R_{ir}} \cong R_s$.

The electromagnetic torque is produced by the machine internal currents.

$$T_{em} = \frac{3}{2} p\left(\left(L_{sd} - L_{sq}\right) i_{sd1} + M_{sf} i_f + \Phi_M\right) i_{sq1} \tag{1.30}$$

When taking into account the iron losses, the HESM is modeled by (1.26) to (1.30).

1.4. Magnetic circuit saturation

In the HESM model established in section 1.2, the inductances and PM flux are assumed constant. However, practically it is not the case. Their values decrease due to the magnetic circuit saturation [133].

In order to take into account the saturation effect in the simulation model, the inductances and the excitation flux are computed in terms of the armature current and the field current based on curves obtained by FEA of the machine [4]. L_{sd}, L_{sq}, M_{sf} and Φ_{exc} are evaluated during the simulation given the instantaneous current values. Thus, in the machine simulation model, they are not constant anymore and vary with the current variation.

1.4.1. Variation of the direct and quadrature axis inductance versus current variation

FEA of the machine helps to depict the evolution of the permeances versus the armature current density [4] as shown in Figure 1.13. The permeances decrease by almost 45%.

The magnetic circuit saturation effect occurs starting 10 A/mm^2. This current density is equivalent to 10 A since the wires section equals 1 mm^2.

It is noted that the q-axis permeance is more affected by the saturation. The field lines of the d-axis armature reaction pass through the PMs that create a bigger equivalent air gap if compared with the air gap seen by the field lines of the q-axis armature reaction. This explains the reduced saturation impact on the d-axis permeance.

Analytical functions computing the permeances in terms of the armature current are found by fitting the curves obtained by FEA.

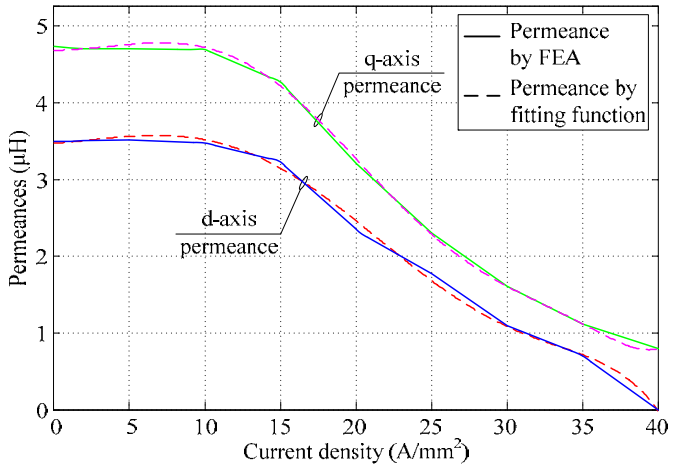

Figure 1.13. Permeances evolution versus armature current density

Equation (1.31) recalls the relationship between the permeance and the inductance.

$$permeance = \frac{inductance}{n_s^{\,2}} \tag{1.31}$$

n_s being the number of turns in a stator winding per phase.

Given (1.31), the stator direct and quadrature axes inductances are then evaluated in terms of the armature current magnitude (1.32) (1.33). The polynomials f_1 and f_2 are found by least mean square identification. I_s is the armature current Root Mean Square (RMS) value as given by (1.34). If I_s is limited to 15 A, that corresponds to 150% of the machine rated armature current, f_1 and f_2 can be reduced to third order polynomials.

$$\begin{aligned} L_{sd}(I_s) = &-1.6\times10^{-11} I_s^{\,6} + 1.2\times10^{-9} I_s^{\,5} - 2.2\times10^{-8} I_s^{\,4} \\ &- 2.3\times10^{-7} I_s^{\,3} + 2.6\times10^{-6} I_s^{\,2} + 1.3\times10^{-5} I_s + 0.0038 = f_1(I_s) \end{aligned} \tag{1.32}$$

$$\begin{aligned} L_{sq}(I_s) = &-1.4\times10^{-11} I_s^{\,6} + 1.1\times10^{-9} I_s^{\,5} - 5.2\times10^{-8} I_s^{\,4} \\ &+ 3\times10^{-6} I_s^{\,3} + 1.8\times10^{-5} I_s^{\,2} + 1.6\times10^{-4} I_s + 0.0051 = f_2(I_s) \end{aligned} \tag{1.33}$$

$$I_s = \sqrt{\frac{i_{sd}^2 + i_{sq}^2}{2}} \tag{1.34}$$

The effect of the field current is considered as well. The field current produces the same demagnetizing effect on the d-axis armature inductance as on the armature-to-field mutual inductance. On the other hand, its effect on the q-axis inductance is neglected. Under these two hypotheses, the stator inductances are then computed by (1.33) and (1.35).

$$L_{sd}(I_s, i_f) = f_1(I_s) - 0.2\times10^{-3}\,|i_f| \tag{1.35}$$

1.4.2. Armature-to-field mutual inductance variation versus current variation

Figure 1.14 represents the flux produced by the field winding versus the field current. This curve is generated by FEA [4]. It is superimposed by the one obtained by least mean square identification. The saturation effect occurs starting $i_f = 6$ A. M_{sf} decreases by 70%. Based on Figure 1.14, the evolution of the mutual inductance is computed in terms of the field current (Figure 1.15, (1.36)).

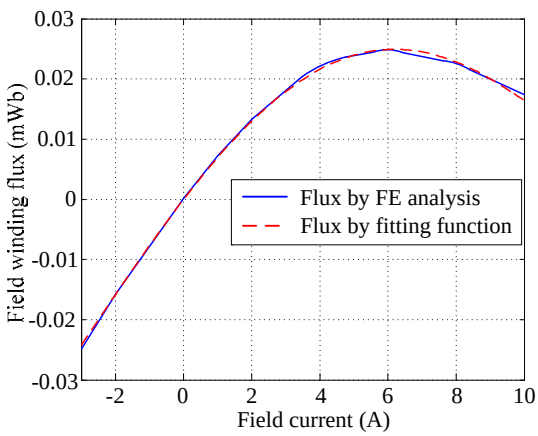

Figure 1.14. Field winding flux versus field current

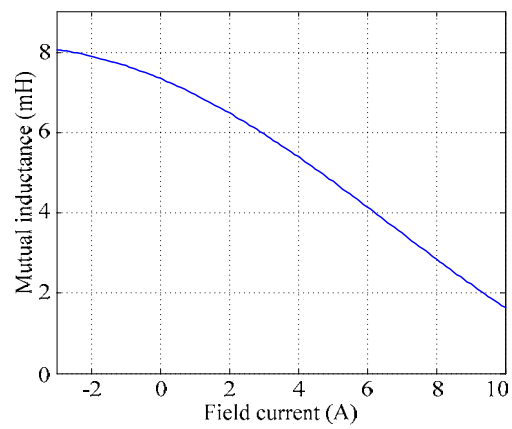

Figure 1.15. Armature-to-field mutual inductance versus field current

$$M_{sf}\left(i_f\right) = 9.1\times10^{-7} i_f^{\,3} - 3.1\times10^{-5} i_f^{\,2} - 3.6\times10^{-4} i_f + 0.0073 = f_3\left(i_f\right) \tag{1.36}$$

Another term is added to (1.36) in order to take into account the effect of the armature current on the armature-to-field inductance. The effect of I_s on M_{sf} is added as shown in (1.37).

$$M_{sf}\left(i_f, I_s\right) = f_3\left(i_f\right) - 0.025\times10^{-3} I_s \tag{1.37}$$

1.4.3. Excitation flux variation versus current variation

The excitation flux (produced by the PMs and the field winding) variation versus the field current variation is shown in Figure 1.16. The curve is drawn point by point based on EMF measurements as detailed in section 2.2. The excitation flux and field current dependence is approached by a forth order polynomial (1.38).

$$\Phi_{exc}\left(i_f\right) = -4\times10^{-5} i_f^{\,3} - 3\times10^{-4} i_f^{\,2} + 0.0076 i_f + 0.0992 = f_4\left(i_f\right) \tag{1.38}$$

The effect of the armature current is to be considered too. It is mainly the i_{sq} that affects the excitation flux. The impact is evaluated based on measurments done with a PMSM, it is quantified as shown in (1.39).

$$\Phi_{exc}\left(i_f, i_{sq}\right) = f_4\left(i_f\right) - 0.66\times10^{-3}\left|i_{sq}\right| \tag{1.39}$$

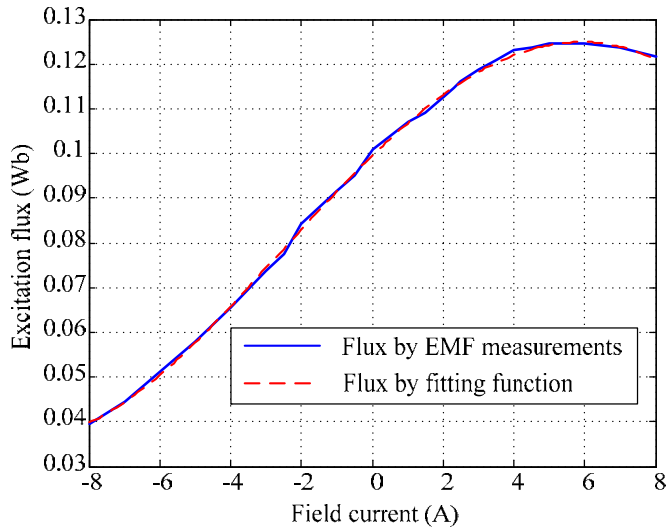

Figure 1.16. Excitation flux versus field current

Conclusion

A HESM with imbricate structure is used for simulation and experiments. In this chapter, a mathematical model describing the machine functioning is developed under the first harmonic hypothesis. The model is then improved by including the iron losses, represented by a variable shunting resistor. The magnetic circuit saturation is taken into account too. The inductances and the excitation flux are found in terms of the armature and field currents. They are computed while the simulation is running, given the current instantaneous values.

The fidelity of the HESM mathematical representation depends, among other factors, on the accurate knowledge of the machine parameters. Thus, the HESM parameter identification follows in Chapter 2.

Chapter 2. HESM Parameter Identification

Introduction

The identification of the machine parameters is needed for modeling, performance analysis and control design. The main parameters to be estimated are the resistances, the different model inductances and the PM flux. The estimation of the armature winding and the field winding resistances is done in section 2.1. The PM flux estimation and the armature-to-field mutual inductance estimation are performed next in section 2.2 based on EMF measurements. Though determining the field inductance is simple, as seen in section 2.3, the estimation of the d-q axis stator inductances is not a trivial task as it is noted in section 2.4. Finally, in section 2.5, the mechanical time constant of the HESM coupled to a DC Machine (DCM) is measured. This data is needed especially when synthesizing speed compensator in motor control.

2.1. Armature winding and field winding resistances

The stator resistance estimation is simple and can be done by a DC measurement of phase voltage and current. The stator resistance per phase is the mean value of three measurements for each couple of phases: $R_s = 0.75\ \Omega$.

The field winding resistance is measured in a similar manner. The machine has two excitation coils. The resistance of the first one is 1.45 Ω. The resistance of the second equals 1.37 Ω. Since, the coils are connected in series, the field winding resistance is $R_f = 2.82\ \Omega$.

2.2. Excitation flux versus field current

In order to determine the PM flux and the armature-to-field mutual inductance, the excitation flux is computed using the EMF measurements for different field current values. The HESM is operating in generator mode. It is driven by a DC motor at no load. Hence, the voltage measured at the machine terminals is the internal induced voltage (EMF). Applying Clarke transformation yields to (2.1).

$$\sqrt{2}E_0 = \omega_s \Phi_{exc} \tag{2.1}$$

The EMF is measured for different excitation currents. Figure 2.1 shows the EMF for $i_f = 0$ A, $i_f = 8$ A and $i_f = -8$ A. As noted, the EMF is not sinusoidal. A Fourier transform is applied. The first harmonic is extracted. Its magnitude is used to compute the excitation flux in terms of the field current. The EMF spectrums are shown in Figure 2.2. The machine rotates at 2000 rpm. The EMF fundamental frequency is at 200 Hz. It is noted that the harmonics of odd order are higher than the harmonics of even order. The excitation flux in terms of the field current is given in Figure 2.3.

The PM flux is equal to the flux obtained when $i_f = 0$ A: $\Phi_M = 0.1$ Wb. The mutual inductance M_{sf} is equal to the slope at the linear portion of the curve (around $i_f = 0$ A): $M_{sf} = 0.007$ H.

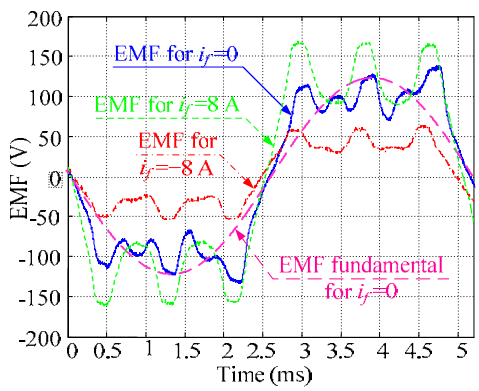

Figure 2.1. EMF for different field currents

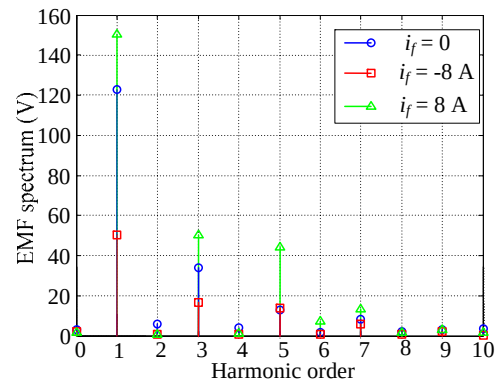

Figure 2.2. EMF spectrum for different field currents

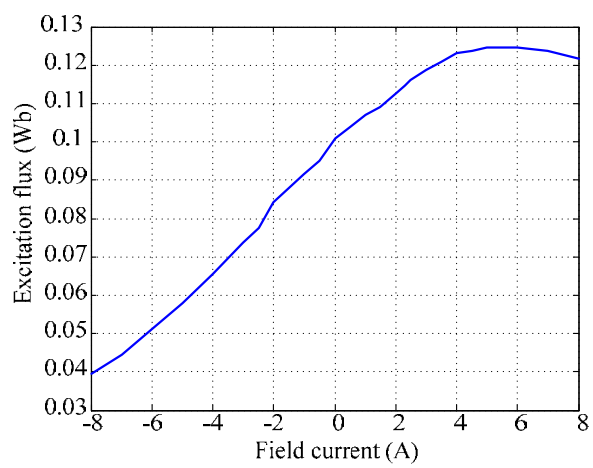

Figure 2.3. Excitation flux versus field current

2.3. Field winding inductance

When the armature windings carry no current and the machine is standstill, the excitation circuit is equivalent to a first order system. Its inductance can be computed once its time constant is known. Figure 2.4 shows the current step response with $\tau_f = 0.0042$ s. A 10 Ω resistor is added in series with the excitation circuit. Given R_f (section 2.1), then $L_f = 0.0538$ H.

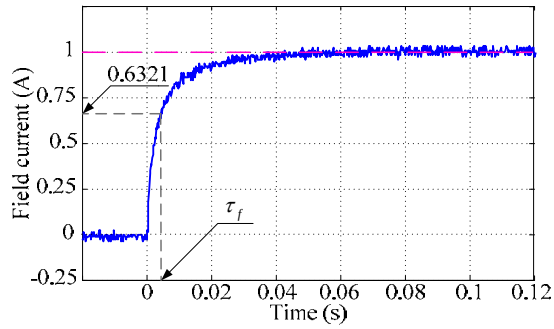

Figure 2.4. Field current step response

2.4. Stator direct and quadrature axis inductances

The HESM model, as developed in Chapter 1, is based on a two-axis theory. Thus, determining the armature direct and quadrature axis inductances is needed.

2.4.1.a. State of art

A common method of determining parameters for direct and quadrature axis models of synchronous machines is the standstill frequency response test [25]. The procedure is outlined in detail in IEEE Standard 115A [46]. The test is carried out by applying very low currents with frequencies varying typically from 0.001 Hz to 200 Hz. The machine parameters are extracted by looking at the frequency response data. In order to obtain the data related to d-axis, phases *a* and *b* are connected in series and supplied by sinusoidal voltage and the rotor is aligned to the axis of phase *a*. As for the data associated to q-axis, the connection remains the same, but the rotor is placed in an orthogonal axis to phase *a* [46]. In both cases, the magnitude of the sinusoidal voltage should not saturate the magnetic circuit of the machine.

A major drawback of the standstill frequency response test is its time-consuming nature due to the large number of measurements and long measurement time, particularly when the machine parameters are to be identified at low frequencies. In order to achieve satisfactory results, the standard recommends taking measurements with at least ten frequencies per decade. Thus, for the 200 Hz HESM used for the experiments, the total number of measurements exceeds hundred [130].

Therefore, another method is to be used in order to determine the stator direct and quadrature axis inductances. The proposed method is based on the one detailed in [89]. It is performed via a hysteresis current control of the d-q axis components of the armature current with a locked rotor. It consists of applying a step reference to one armature current component while the other component is maintained nil. The d-q axis stator inductances are then deduced from the current responses. It shall be pointed that with the proposed identification method the magnetic circuit saturation is neglected.

2.4.1.b. Hysteresis based current controller method

The machine operates in motor mode. In the d-q coordinate system, the armature currents are given by (2.2).

$$i_{sd} = \frac{1}{R_s + L_{sd}s}\left(v_{sd} + \omega_s \Phi_{sq}\right)$$
$$i_{sq} = \frac{1}{R_s + L_{sq}s}\left(v_{sq} - \omega_s \Phi_{sd}\right) \tag{2.2}$$

If the rotor is locked at a fixed position θ_0, then $p\Omega = 0$ rad/s and (2.2) becomes (2.3).

$$i_{sd} = \frac{v_{sd}}{R_s + L_{sd}s}$$
$$i_{sq} = \frac{v_{sq}}{R_s + L_{sq}s} \tag{2.3}$$

No interaction remains between the direct and quadrature axis currents. The armature is now equivalent to two first order independent systems.

On the other hand, i_{sd} and i_{sq} can be expressed in terms of the line currents (2.4) and vice-versa (2.5) via Park transformation. The armature windings are arranged in Y configuration.

$$i_{sd} = \frac{2}{3}\left(i_{sa}\, cos\left(p\theta_0\right) + i_{sb}\, cos\left(p\theta_0 - \frac{2\pi}{3}\right) + i_{sc}\, cos\left(p\theta_0 - \frac{4\pi}{3}\right)\right)$$
$$i_{sq} = -\frac{2}{3}\left(i_{sa}\, sin\left(p\theta_0\right) + i_{sb}\, sin\left(p\theta_0 - \frac{2\pi}{3}\right) + i_{sc}\, sin\left(p\theta_0 - \frac{4\pi}{3}\right)\right) \tag{2.4}$$

$$i_{sa} = i_{sd}\, cos\left(p\theta_0\right) + i_{sq}\, sin\left(p\theta_0\right)$$
$$i_{sb} = i_{sd}\, cos\left(p\theta_0 - \frac{2\pi}{3}\right) + i_{sq}\, sin\left(p\theta_0 - \frac{2\pi}{3}\right)$$
$$i_{sc} = i_{sd}\, cos\left(p\theta_0 - \frac{4\pi}{3}\right) + i_{sq}\, sin\left(p\theta_0 - \frac{4\pi}{3}\right) \tag{2.5}$$

In addition, if the rotor is locked at the specific position $\theta_0 = 0$ rad, (2.4) and (2.5) are simplified as shown in (2.6) and (2.7) respectively.

$$i_{sd} = \frac{2}{3}\left(i_{sa} - \frac{i_{sb}}{2} - \frac{i_{sc}}{2}\right)$$
$$i_{sq} = \frac{2}{3}\left(\frac{\sqrt{3}}{2} i_{sb} - \frac{\sqrt{3}}{2} i_{sc}\right) \tag{2.6}$$

$$i_{sa} = i_{sd}$$
$$i_{sb} = -\frac{i_{sd}}{2} - \frac{\sqrt{3}}{2} i_{sq}$$
$$i_{sc} = -\frac{i_{sd}}{2} + \frac{\sqrt{3}}{2} i_{sq} \tag{2.7}$$

The machine line currents are controlled by three independent hysteresis controllers.

In order to determine the direct axis inductance L_{sd}, the reference currents are set as in (2.8).

$$\begin{cases} i_{sa,ref} = I_s \\ i_{sb,ref} = -0.5 I_s \\ i_{sc,ref} = -0.5 I_s \end{cases} \tag{2.8}$$

Replacing the currents in (2.6) by their values as given in (2.8) yields to (2.9).

$$\begin{aligned} i_{sd} &= i_{sa} = I_s \\ i_{sq} &= 0 \end{aligned} \tag{2.9}$$

The control strategy is then equivalent to impose a step reference current for the direct axis current while setting a nil quadrature current.

Since R_s is known from section 2.1, L_{sd} is computed from the time constant of i_{sa} step response (refer to (2.3)).

Using similar procedure, the quadrature axis inductance L_{sq} is calculated with new line reference current combination (2.10).

$$\begin{cases} i_{sa,ref} = 0 \\ i_{sb,ref} = \dfrac{\sqrt{3} I_s}{2} \\ i_{sc,ref} = -\dfrac{\sqrt{3} I_s}{2} \end{cases} \tag{2.10}$$

The d-q axis armature current components are then given by (2.11).

$$\begin{aligned} i_{sd} &= 0 \\ i_{sq} &= I_s = \frac{2}{\sqrt{3}} i_{sb} \end{aligned} \tag{2.11}$$

The control strategy is equivalent to setting a step reference current for the quadrature axis current while imposing a nil direct current.

The time constant of i_{sb} step response gives L_{sq} (refer to (2.3))

The method exposed here is detailed and validated for a wound rotor synchronous machine in [89]. Since, it consists of measuring the current response when the rotor is locked, hence the PMs and the exciter current have no impact on the measurement and there is no apparent objection on adopting this method to determine the HESM stator direct and quadrature axis inductances.

2.4.1.c. <u>Measurements</u>

Figure 2.5 shows the device designed at the laboratory in order to block the rotor (shaft) at a given position.

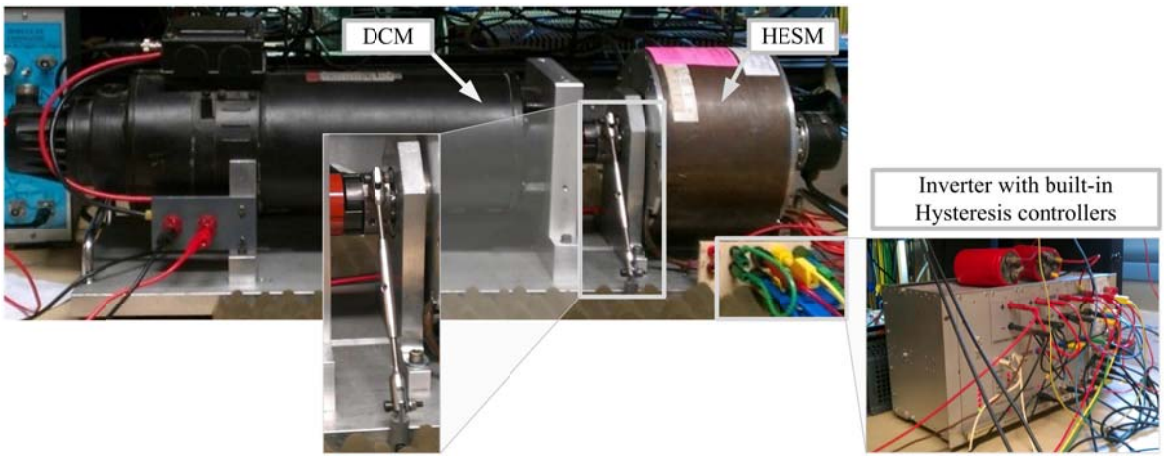

Figure 2.5. Device locking the rotor needed for L_{sd} and L_{sq} identification

The currents response $i_{sa}(t)$ and $i_{sb}(t)$ obtained with the reference currents $i_{sa,ref} = 1$ A, $i_{sb,ref} = -0.5$ A, $i_{sc,ref} = -0.5$ A are depicted in Figure 2.6. Measuring the time constant τ_{sd} of $i_{sa}(t)$ response, which is an image of $i_{sd}(t)$ step response allows the identification of the d-axis inductance: $L_{sd} = R_s\tau_{sd}$. R_s being identified in section 2.1. The same procedure is repeated with several reference currents (Figure 2.7). An average value for τ_{sd} is considered. The d-axis inductance is then found to be $L_{sd} = 3.6$ mH.

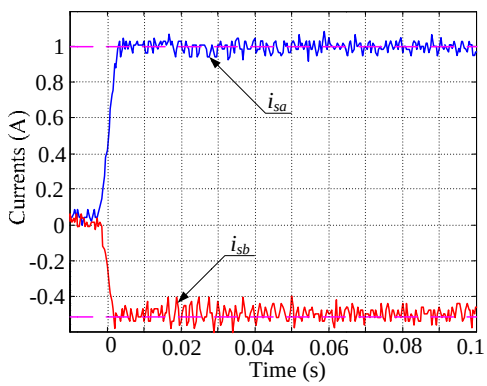

Figure 2.6. $i_{sa}(t)$ and $i_{sb}(t)$ with the reference currents $i_{sa,ref} = 1$ A, $i_{sb,ref} = -0.5$ A, $i_{sc,ref} = -0.5$ A

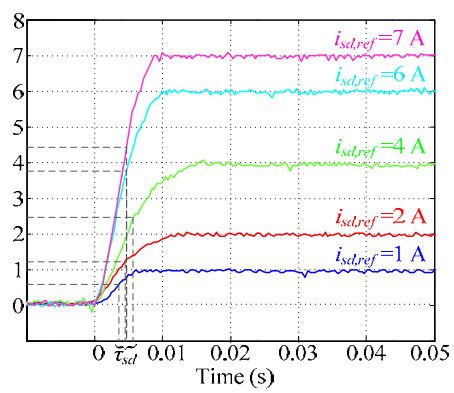

Figure 2.7. Time constant τ_{sd} for several $i_{sd,ref}$

Figure 2.8 shows the current response $i_{sa}(t)$ and $i_{sb}(t)$ obtained when the reference currents are $i_{sa,ref} = 0$ A, $i_{sb,ref} = \frac{\sqrt{3}}{2}$ A, $i_{sc,ref} = -\frac{\sqrt{3}}{2}$ A. For accurate results, the time constant is found for five reference currents (Figure 2.9). Its mean value is used to compute the quadrature axis inductance: $L_{sq} = R_s\tau_{sq} = 5.07$ mH.

2.5. Mechanical time constant

The HESM is coupled to the DCM. Among the mechanical losses, only the friction losses are retained. The speed is governed by (2.12).

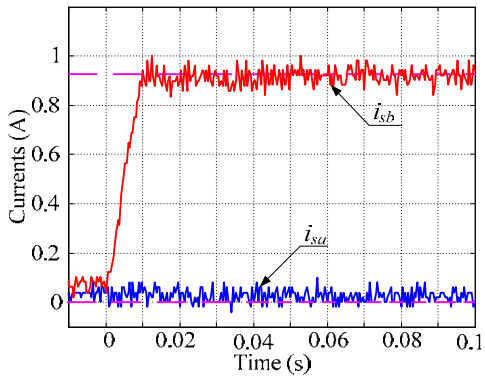

Figure 2.8. $i_{sa}(t)$ and $i_{sb}(t)$ with the reference currents $i_{sa,ref}$ =0 A, $i_{sb,ref} = \sqrt{3}/2$ A, $i_{sc,ref} = -\sqrt{3}/2$ A

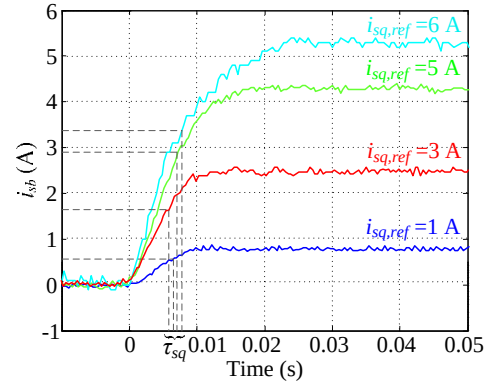

Figure 2.9. Time constant τ_{sq} for several $i_{sq,ref}$

$$J\frac{d\Omega}{dt} = T_{em} - T_b = T_{em} - \left(f_v\Omega + T_{f0}\right) - T_l \tag{2.12}$$

The HESM is driven at no load by the DC motor. No voltage is applied across the excitation coil inputs in a first place. When the DC motor supply is turned off, T_{em} becomes nil instantaneously. At no load, the rotor speed is then expressed by (2.13).

$$\Omega(t) = \left(\Omega_0 + \frac{T_{f0}}{f_v}\right)e^{\frac{-t}{\tau_m}} - \frac{T_{f0}}{f_v} \tag{2.13}$$

$\tau_m = \dfrac{J}{f_v}$ denotes the mechanical time constant.

The speed decay curve is depicted in Figure 2.10. The curve breakpoint evinces the presence of the dry friction torque. Otherwise, the speed would tend smoothly to zero. τ_m is given by (2.14).

$$\tau_m = \frac{t_1}{ln\left(\dfrac{\Omega(t_1) - \Omega_0}{\Omega(t_2) - \Omega(t_1)}\right)} \tag{2.14}$$

(t_1, $\Omega(t_1)$) and (t_2, $\Omega(t_2)$) are two distinct points of the curve with $t_2 = 2t_1$. The mechanical time constant equals τ_m = 8.08 s.

The estimation method does not take into account the core loss effect while evaluating the mechanical time constant. In order to figure out the impact of the iron losses on the speed decay, the test is repeated with positive and negative field current. Figure 2.11 proves that the core losses have an impact on the deceleration. As the friction losses, they tend to stop the machine. Indeed, when the excitation flux increases the iron losses increase and thus the deceleration is faster and vice versa when the field current decreases, the excitation flux is reduced (part of the PM flux is countered) and the machine rotates longer. However, the time constant variation does not exceed 9%.

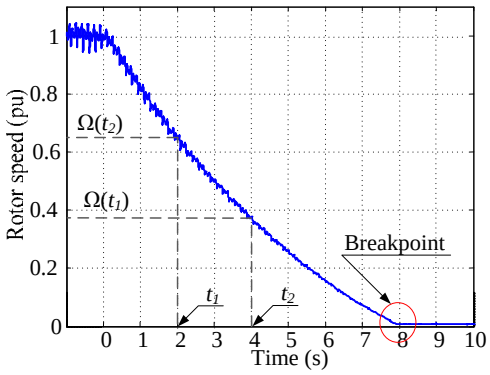

Figure 2.10. Speed decay curve for i_f =0 A

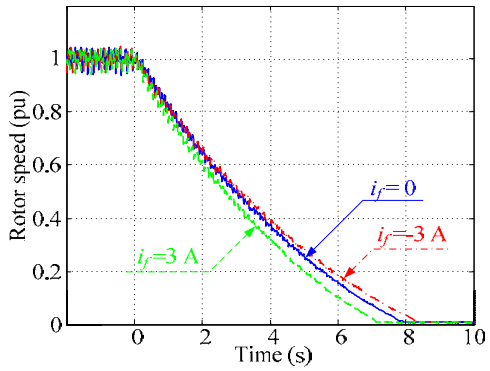

Figure 2.11. Impact of the iron losses on deceleration

Conclusion

In this chapter, the electrical parameters of the laboratory prototype HESM are identified. The Ohm's law is used to determine the winding resistances. The armature-to-field mutual inductance and the PM flux are identified based on the EMF measurements. The field winding inductance is computed given the time constant of the first order system when only the excitation circuit is supplied. The stator direct and quadrature axes inductances are evaluated by hysteresis based current control method. Finally, a range for the mechanical time constant of the HESM coupled to a DCM is determined based on the speed decay curve.

Even though the proposed methods may not be the most accurate ones, the obtained results are satisfactory for the intended applications. The extracted parameters are used in the machine simulation model and in the control design in the next chapters.

Part II. Hybrid Excitation Synchronous Machine in Generator Mode for More Electric Aircraft Application

Introduction of Part II

More Electric Aircrafts (MEA) – State of art

In conventional aircraft architecture, fuel is converted into power by the engines. Most of this power is used as propulsive power. The remainder is converted into four different secondary power distribution systems.

Pneumatic power derives pressure from a gas turbine off-take and provides heat and pressure for anti-ice protection engine start and cabin environmental control. Its drawbacks are its low efficiency and the difficulty in leak detection.

Mechanical system provides power for engine-mounted accessories such as oil, fuel and hydraulic pumps and electric generator.

Hydraulic system primarily provides actuation of flight surfaces, landing gear and doors. Its drawbacks are a heavy and inflexible infrastructure and the potential leakage of dangerous and corrosive fluids.

Electrical power, obtained from the main generator, supplies the avionics, cabin and aircraft lighting, galleys and other commercial and entertainment loads.

Advancements in aircraft electrical power system, electric drives and component technologies have resulted in renewed interest in the MEA concept [136]. Many non-propulsive functions that used to be operated by hydraulic, pneumatic and mechanical power are being replaced by electric power improving the performance and life cycle cost of the aircraft and reducing fuel consumption per passenger per mile [30] [101]. Compared with the conventional power distribution network, the MEA architecture demonstrates significant weight gains, flexibility, reduced maintenance requirements, increased reliability [97], increased efficiency on energy conversion and increased passenger comfort. In addition, it shall be pointed that among all other power forms, only electric power can handle the demands of all loads on an airplane.

The concept of an electric aircraft is not new. It has been considered by military aircraft designers since World War II, although the lack of electrical power generation capability, together with the volume of the power conditioning equipment especially in power electronic components and control devices, rendered the approach unfeasible back then especially for commercial and civil transport applications. Since the eighties, research into the technologies of aircraft power system has moved forward [54] [105]. Several programs have been started by different research groups of the European Union and the United States.

The National Aeronautics and Space Administration (NASA) has conducted a number of activities to foster the development of an all-electric airplane since the eighties [120]. In 1991, Air Force has awarded to Northrop/Grumman Military Aircraft Division the development of a five-phase power management and distribution system for a MEA (MADMEL) [135].

The first important integration initiative in Europe was the POA (Power Optimized Aircraft) project launched in 2002. The program studied the electrical loads management, which permits to introduce new technologies and architectures in on-board systems. In 2006, the MOET (More Open Electrical Technologies) project derives and aims to analyze the electric distribution architectures defined in POA program and to establish the new industrial standard for commercial aircraft design. Today the MEA topics have a relevant role in the research projects managed by the

CleanSky Joint Technology Initiative that is equally shared by the European Commission and the aeronautical industry, over the period 2008-2014 [20]. Its mission is to develop breakthrough technologies to significantly increase the environmental performances of airplanes and air transport, resulting in less noisy and more fuel-efficient aircraft.

MEA brings severe challenges to the on-board electrical power distribution system. To cope with this growing demand for electric power, new voltage levels and architectures are being applied [9] [31] [65] [87]. The first generation of electrical network was equipped with fixed frequency (115 V AC–400 Hz) integrated drive generators [59] as on the Airbus A320, A330, and A340. The A380 is the first generation MEA to remove the constant speed mechanical gearbox, permitting the fundamental electric frequency to vary over the range of engine speeds between 360-720 Hz. Distribution voltage is doubled to 230 V AC on next generation MEA (e.g. Boeing B787 and Airbus A350) giving the way to High Voltage Alternating Current (HVAC) distribution. Yet, research predicts that future all-electric aircraft will have a primarily High Voltage Direct Current (HVDC) electric distribution system ±270 V [9] [48] [104]. As for the military aircraft, the traditional voltage levels of 28 V DC and 115 V AC have evolved to 270 V DC in platforms like Lockheed Martin F-22 and F-35.

With HVDC distribution network, the overall cable cross section is reduced which results in reduction of material, cost and weight. In addition, only one rectifier per generator is needed. All the rectification blocks, integrated in most of the electric equipment, are eliminated. The drawback of this architecture is the risk of voltage and current oscillations due to the interactions between the different components [15] [142].

Studies have been conducted to identify the most suitable machine technologies for aircraft embedded generation [31] [103]. Due to the inaccessibility of the location, reliability is paramount and it is clear that a brushless machine format is required, ideally with a capability of operation without a rotor position sensor. Another important driver is the efficiency of the machine and its power density. The weight and volume constraints are also key parameters that affect the choice of machine type [141]. Presently, the current generator technology used on most commercial and military aircraft is the three-stage synchronous generator [20] [103]. It consists of three brushless generators mounted on the same shaft. The first machine is a PM generator that supplies a rectifier / chopper unit. The second machine is a synchronous machine with a stationary exciter and rotating three-phase windings. These windings are connected to a rotating rectifier coupled on the same shaft of the whole set. The rectifier supplies the rotor winding of the third machine that is the main generator [59]. This high performance brushless machine is inherently safe. However, the price to pay is its obvious complexity.

Switched reluctance and brushless PM machines are contenders for future high power embedded generation systems [103]. Induction motors are relatively rugged, but they have lower power density with respect to switched reluctance and PM machines.

Switched reluctance machine is characterized by an intrinsic high fault tolerance, temperature tolerance, robustness and construction simplicity. Its main disadvantages are its lower power and torque density with respect to the PM machine, high ventilation losses, small air gap, and the necessity of a complicated power converter.

The PM synchronous machine is widely used because of its high efficiency, high torque, and high power density. In addition, it offers the greatest potential for sensorless control [9] [81] [85]. However, the presence of the PMs is a major disadvantage due to their unavoidable sensitivity to the high temperatures and the impossibility to shut down their magnetic flux in case of stator

winding short-circuit fault. Another limitation in the PM machine is its low range of speed due to its poor field weakening capability. Nevertheless, this drawback is overcome in hybrid structures.

Therefore, the HESM that is a compact brushless PM machine with flux control capability is a potential candidate to be used for embedded generation applications such as aircraft power supply system [95] [96]. Moreover, a parametrical study shows that it is possible to maximize the efficiency of this alternator at a given speed by choosing an adequate hybridization ratio [5].

Part II organization

Part II investigates the use of HESM in embedded power generation systems; in particular, aircraft power supply. Two distribution networks are studied: HVAC and HVDC. In both cases, the voltage transient characteristics are chosen in accordance with the corresponding norm specifications (BS EN 2282[3] and MIL-STD-704F[4] respectively). The main contribution of the work is that the output voltage is controlled by action on the field current only. The armature currents are just monitored.

Chapter 3 studies the HESM operating as a variable frequency generator supplying an HVAC isolated network. The aim of the control is to maintain the RMS voltage equal to its reference under load and speed variation via the field current compensation. This approach is validated by simulation and experiments.

In Chapter 4, the HESM is cascaded by a diode bridge rectifier. The set operates as an HVDC generator. The bridge rectifier is modeled at first. The generator control is presented subsequently. The DC bus voltage is compensated through the action on the field current only. Simulation results as well as experiments validate the control.

[3] BS EN 2282: Characteristics of aircraft electrical supplies

[4] Military Standard, Department of Defense, USA: Aircraft electric power characteristics

Chapter 3. HESM Operating as Variable Frequency Generator Connected to an HVAC Isolated Network

Introduction

This chapter deals with the control of the HESM operating as a variable frequency generator that supplies an isolated three-phase load in embedded applications such as aircraft electrical power generation. The aim of the control is to maintain the output magnitude voltage (RMS value) constant when the load and/or the speed of the rotor vary via the unique action on the field current.

In section 3.1, the machine model, already developed in section 1.2, is revised and extended in order to be adapted to generator mode. The state space representation of the machine is computed and a proper point of regulation is defined. In section 3.2, the generator control is detailed. It consists of just two loops. No particular assumption is made on the armature currents. The control is validated by simulation with Matlab/Simulink software in section 3.4. The effect of the magnetic circuit saturation and the iron losses is investigated. An experimental validation of the proposed control strategy follows in section 3.5.

3.1. HESM modeled as a generator supplying an isolated three-phase load

3.1.1. State space representation

Equations (1.11) to (1.13) developed in Chapter 1 are written as in (3.1) to (3.3) with generator mode sign convention. Equations (3.1), (3.2) and (3.3) describe the hybrid excitation synchronous generator functioning. The iron loss consideration is neglected in a first place.

$$v_{sd} = -R_s i_{sd} - L_{sd}\frac{di_{sd}}{dt} - M_{sf}\frac{di_f}{dt} + p\Omega L_{sq} i_{sq} \tag{3.1}$$

$$v_{sq} = -R_s i_{sq} - L_{sq}\frac{di_{sq}}{dt} - p\Omega\left(L_{sd} i_{sd} + \Phi_M + M_{sf} i_f\right) \tag{3.2}$$

$$v_f = R_f i_f + L_f \frac{di_f}{dt} + \frac{3}{2} M_{sf} \frac{di_{sd}}{dt} \tag{3.3}$$

In generator mode, the speed is usually seen as a parameter. In aircraft applications particularly, the speed is imposed by the turbine. Thus, (3.1) to (3.3) denote a state space representation of the machine (3.4). [v_f, Φ_M, v_{sd}, v_{sq}] is the input vector. [i_{sd}, i_{sq}, i_f] is the state vector that is equal to the output vector.

$$\begin{cases} \dot{\boldsymbol{x}} = \boldsymbol{A}(\Omega)\,\boldsymbol{x} + \boldsymbol{B}(\Omega)\,\boldsymbol{u} \\ \boldsymbol{y} = \boldsymbol{C}\boldsymbol{x} \end{cases} \tag{3.4}$$

A is the state matrix, ***B*** is the input matrix and ***C*** is the output matrix. These matrices are given by (3.5), (3.6) and (3.7) respectively.

$$\boldsymbol{A} = \begin{bmatrix} \frac{-R_s L_f}{A_{fd}} & \frac{p\Omega L_f L_{sq}}{A_{fd}} & \frac{R_f M_{sf}}{A_{fd}} \\ \frac{-p\Omega L_{sd}}{L_{sq}} & \frac{-R_s}{L_{sq}} & \frac{-p\Omega M_{sf}}{L_{sq}} \\ \frac{3M_{sf} R_s}{2A_{fd}} & \frac{-3p\Omega L_{sq} M_{sf}}{2A_{fd}} & \frac{-R_f L_{sd}}{A_{fd}} \end{bmatrix} \tag{3.5}$$

$$\boldsymbol{B} = \begin{bmatrix} \frac{-M_{sf}}{A_{fd}} & 0 & \frac{-L_f}{A_{fd}} & 0 \\ 0 & \frac{-p\Omega}{L_{sq}} & 0 & \frac{-1}{L_{sq}} \\ \frac{L_{sd}}{A_{fd}} & 0 & \frac{3M_{sf}}{2A_{fd}} & 0 \end{bmatrix} \tag{3.6}$$

$$\boldsymbol{C} = \boldsymbol{I}_3 \tag{3.7}$$

With $A_{fd} = L_f L_{sd} - \frac{3}{2} M_{sf}{}^2$. $\boldsymbol{I}_3$ is the identity matrix of size 3.

3.1.2. Point of regulation

The machine, described by (3.4), is equivalent to a three-phase source of alternating current; the load is seen as a current source as well. Therefore, in order to define a proper Point Of Regulation (POR), the HESM is cascaded with fictitious capacitors and/or resistors as shown in Figure 3.1.

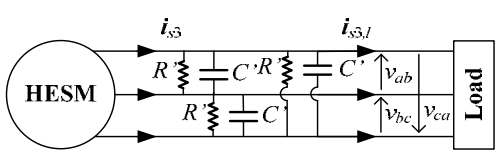

Figure 3.1. HESM cascaded with capacitors and resistors

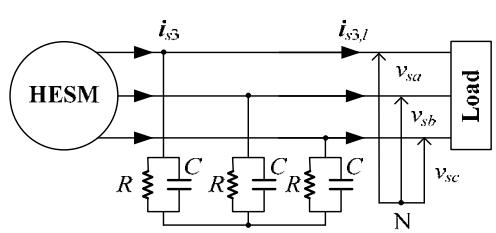

Figure 3.2. POR equivalent circuit

When the three-phase system is balanced, the circuit in Figure 3.1 is equivalent to the one in Figure 3.2 with $C = 3C'$ and $R = R'/3$.

Kirchhoff current law yields to (3.8).

$$\frac{d\boldsymbol{v}_{s3}}{dt} = \frac{1}{C}\left(\boldsymbol{i}_{s3} - \boldsymbol{i}_{s3,l} - \frac{\boldsymbol{v}_{s3}}{R}\right) \tag{3.8}$$

$\boldsymbol{i}_{s3,l}$ is the load current vector.

Park transformation maps (3.8) onto (3.9) in the d-q frame.

$$\frac{d\boldsymbol{v}_{sdq}}{dt} = \frac{1}{C}\left(\boldsymbol{i}_{sdq} - \boldsymbol{i}_{sdq,l} - \frac{\boldsymbol{v}_{sdq}}{R}\right) - p\Omega\begin{bmatrix} 0 & -1 \\ 1 & 0 \end{bmatrix}\boldsymbol{v}_{sdq} \tag{3.9}$$

The introduction of this new equation leads to an extended state space representation. The d-q axis armature voltage components are now part of the state vector and form the output vector.

$$\begin{cases} \dot{\boldsymbol{x}}' = \boldsymbol{A}'(\Omega)\,\boldsymbol{x}' + \boldsymbol{B}'(\Omega)\,\boldsymbol{u}' \\ \boldsymbol{y}' = \boldsymbol{C}'\boldsymbol{x}' \end{cases} \tag{3.10}$$

$\boldsymbol{x}' = \begin{bmatrix} i_{sd} & i_{sq} & i_f & v_{sd} & v_{sq} \end{bmatrix}^t$ is the state vector, $\boldsymbol{u}' = \begin{bmatrix} v_f & \Phi_M & i_{sd,l} & i_{sq,l} \end{bmatrix}^t$ is the input vector and $\boldsymbol{y}' = \begin{bmatrix} v_{sd} & v_{sq} & i_f \end{bmatrix}^t$ is the output vector.

$\boldsymbol{A}'(\Omega)$, $\boldsymbol{B}'(\Omega)$ and $\boldsymbol{C}'$ are easily derived from (3.5), (3.6), (3.7) and (3.10).

$$\boldsymbol{A}' = \begin{bmatrix} \frac{-R_s L_f}{A_{fd}} & \frac{p\Omega L_f L_{sq}}{A_{fd}} & \frac{R_f M_{sf}}{A_{fd}} & \frac{-L_f}{A_{fd}} & 0 \\ \frac{-p\Omega L_{sd}}{L_{sq}} & \frac{-R_s}{L_{sq}} & \frac{-p\Omega M_{sf}}{L_{sq}} & 0 & \frac{-1}{L_{sq}} \\ \frac{3M_{sf}R_s}{2A_{fd}} & \frac{-3p\Omega L_{sq}M_{sf}}{2A_{fd}} & \frac{-R_f L_{sd}}{A_{fd}} & \frac{3M_{sf}}{2A_{fd}} & 0 \\ \frac{1}{C} & 0 & 0 & \frac{-1}{CR} & p\Omega \\ 0 & \frac{1}{C} & 0 & -p\Omega & \frac{-1}{CR} \end{bmatrix} \tag{3.11}$$

$$\boldsymbol{B}' = \begin{bmatrix} \frac{-M_{sf}}{A_{fd}} & 0 & 0 & 0 \\ 0 & \frac{-p\Omega}{L_{sq}} & 0 & 0 \\ \frac{L_{sd}}{A_{fd}} & 0 & 0 & 0 \\ 0 & 0 & \frac{-1}{C} & 0 \\ 0 & 0 & 0 & \frac{-1}{C} \end{bmatrix} \tag{3.12}$$

$$\boldsymbol{C}' = \begin{bmatrix} 0 & 0 & 0 & 1 & 0 \\ 0 & 0 & 0 & 0 & 1 \\ 0 & 0 & 1 & 0 & 0 \end{bmatrix} \tag{3.13}$$

The machine defined by (3.10) is then equivalent to a three-phase source of AC voltage.

3.1.3. Capacitor and resistor values

The fictitious capacitances and resistances must be chosen carefully since the introduction of C and R in the model should not influence the behavior of the machine.

At no load, each phase is equivalent to the RLC circuit given in Figure 3.3. L varies between $\left(L_{sd}+L_{sq}\right)/2$ and $\left(L_{sd}-L_{sq}\right)/2$ which are the two bounds of the armature cyclic inductance taking into consideration the machine saliency.

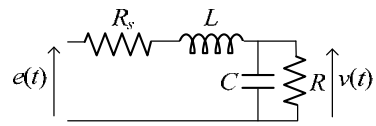

Figure 3.3. Stator phase equivalent circuit

This equivalent circuit corresponds to a second order system.

$$v(s) = \frac{1}{LCs^2 + \left(R_s C + L/R\right)s + 1 + R_s/R} e(s) \tag{3.14}$$

The damping ratio of the system is $m = \dfrac{R_s C + L/R}{2\sqrt{LC(1+R_s/R)}}$. The resonant frequency is given by $\omega_r = \sqrt{\dfrac{1+R_s/R}{LC}}\sqrt{1-2m^2}$.

C and R are chosen in order to satisfy the following criterion:

- The resonant frequency ω_r is at least ten times greater than $p\Omega_b$.
- The voltage gain at $\omega = p\Omega_b$ is less than 0.1 dB.
- The peak resonance is less than 30 dB.
- The power dissipated in the damping resistor R does not exceed 1% of the machine rated power.

It shall be noted that the addition of capacitors only with capacitance smaller than 1 μF satisfies the first two criterions but presents a high peak resonance which might cause an instability problem. Therefore, the use of a damping resistor is needed. A solution that verifies the four above-mentioned conditions is C = 0.1 μF and R = 10 kΩ. These values are retained in the remainder of this chapter.

3.2. Control strategy

The HESM operates as a variable frequency generator supplying an isolated load. Hence, only the armature voltage magnitude is to be regulated. The control aims to assure that the voltage magnitude tracks its reference under load and/or speed variation.

The generation system has only one degree of freedom: the voltage applied to the exciter. Therefore, the voltage magnitude compensation at the POR is performed through hierarchical loops: an inner loop where the field current is driven by the voltage applied to the field winding and an outer loop that compensates the armature voltage RMS value at the POR by action on the field current as shown in Figure 3.4. The control is scalar. No particular assumption is made regarding the armature currents.

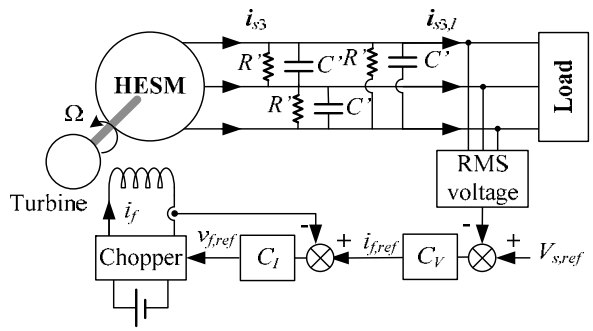

Figure 3.4. Control strategy of the HESM operating as a variable frequency generator

3.2.1. Field current control loop

Equation (3.15) is the Laplace transform of (3.3). The d-axis current component $i_{sd}(s)$ is considered as a disturbance. The plant to be controlled has a first order transfer function $G_I(s)$ (3.16). The field current control loop is represented in Figure 3.5. Since the chopper dynamic is very fast compared to the rest of the system, it is not taken into account in the transfer function.

$$i_f(s) = \frac{1}{L_f s + R_f} v_f(s) + \frac{3}{2} \frac{M_{sf} s}{L_f s + R_f} i_{sd}(s) \tag{3.15}$$

$$G_I(s) = \frac{i_f(s)}{v_f(s)} = \frac{1}{L_f s + R_f} \tag{3.16}$$

A Proportional Integral (PI) controller is designed in order to meet the following specifications:

- Zero steady state error;
- The settling time of the closed-loop is five times smaller than the open-loop settling time. Numerically, the closed-loop settling time is equal to 0.01 s and the inner closed-loop cutoff frequency is ω_I = 300 rad/s.

$H_I(s)$ represents the first order inner loop dynamic.

$$H_I(s) = \frac{\omega_I}{s + \omega_I} = \frac{300}{s + 300} \tag{3.17}$$

3.2.2. Voltage control loop

3.2.2.a. Transfer function

The output voltage magnitude is computed by (3.18).

$$\|v_s\| = \left(v_{sd}(t)^2 + v_{sq}(t)^2\right)^{1/2} \tag{3.18}$$

Equation (3.18) is approximated by its first order Taylor polynomial (3.19) near the operating point (v_{sd0}, v_{sq0}).

$$\begin{aligned}\|v_s\| &= \|v_{s0}\| + \left[\frac{2v_{sd0}}{2\left(v_{sd0}{}^2 + v_{sq0}{}^2\right)^{1/2}}\left(v_{sd} - v_{sd0}\right) + \frac{2v_{sq0}}{2\left(v_{sd0}{}^2 + v_{sq0}{}^2\right)^{1/2}}\left(v_{sq} - v_{sq0}\right)\right] \\ &= \left[\frac{v_{sd0}v_{sd} + v_{sq0}v_{sq}}{\left(v_{sd0}{}^2 + v_{sq0}{}^2\right)^{1/2}}\right]\end{aligned} \tag{3.19}$$

Let $k_{q0} = \frac{v_{sq0}}{\|v_{s0}\|}$. The ratio $\frac{v_{sd0}}{\|v_{s0}\|}$ can be computed in terms of k_{q0}: $\frac{v_{sd0}}{\|v_{s0}\|} = -\sqrt{1 - k_{q0}{}^2}$.

Each operating point is characterized by its own k_{q0}. However, for a load variation that goes from 0% to 150%, k_{q0} variation is limited to 12%. Thus, for the voltage compensator design, the value obtained with the full load is assigned to k_{q0} regardless the operating point, i.e. $k_{q0} = -0.864$

Equation (3.19) becomes (3.20).

$$\|v_s\|(t) = \left(-\sqrt{1 - k_{q0}{}^2}\, v_{sd}(t) + k_{q0} v_{sq}(t)\right) \tag{3.20}$$

Recalling the state space representation (3.10), transfer functions between the d-q axis voltage components and the field current are computed.

$$\frac{v_{sd}(s)}{i_f(s)} = \frac{-M_{sf}\, s}{L_{sd}Cs^2 + \left(R_s C + \frac{L_{sd}}{R}\right)s + \frac{R_s}{R} + 1} \tag{3.21}$$

$$\frac{v_{sq}(s)}{i_f(s)} = \frac{-p\Omega M_{sf}}{L_{sq}Cs^2 + \left(R_s C + \frac{L_{sq}}{R}\right)s + \frac{R_s}{R} + 1} \tag{3.22}$$

Equations (3.20), (3.21) and (3.22) yield to (3.23).

$$F_V(s) = \frac{\|v_s\|(s)}{i_f(s)} = M_{sf}\left(\frac{\sqrt{1-k_{q0}{}^2}\,s}{L_{sd}Cs^2 + \left(R_sC + L_{sd}/R\right)s + \frac{R_s}{R} + 1} + \frac{-k_{q0}\,p\Omega}{L_{sq}Cs^2 + \left(R_sC + L_{sq}/R\right)s + \frac{R_s}{R} + 1}\right) \tag{3.23}$$

The outer loop is illustrated by the block diagram in Figure 3.5. The control is done based on the RMS voltage measurement. The field current dynamic is taken into consideration.

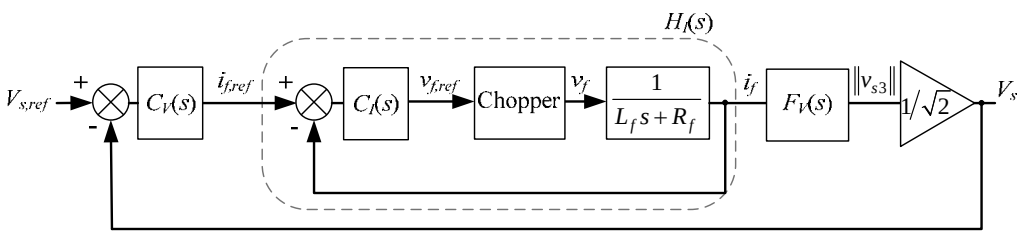

Figure 3.5. RMS voltage control: Outer loop block diagram

The transfer function is given by (3.24). Figure 3.6 depicts the poles and zeros map of $G_V(s)$.

$$G_V(s) = \frac{V_s(s)}{i_{f.ref}(s)} = \frac{1}{\sqrt{2}} F_V(s) H_I(s) \tag{3.24}$$

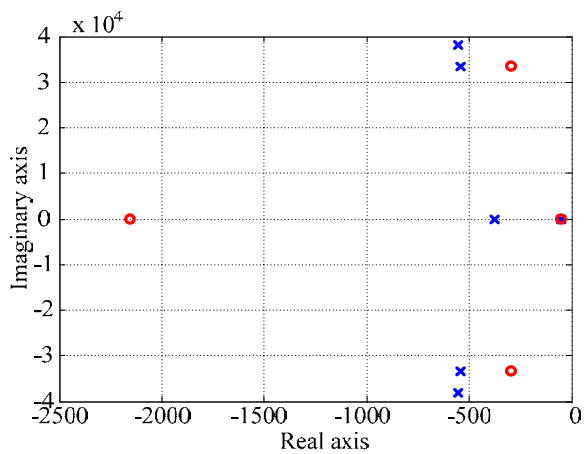

Figure 3.6. Pole and zero map of $G_V(s)$

The load impact is not explicitly shown in $G_V(s)$. However, the load variation affects the transfer function. In fact, the load has an effect on the armature current values that affects the flux. Moreover, the inductances vary with these currents, due to the magnetic circuit saturation. Consequently, it is expected to find for each load a slightly different $G_V(s)$.

Figure 3.7 shows Bode plots of $G_V(s)$ and the compensated open-loop transfer function for different loads. In these plots, $\Omega = \Omega_b$. Figure 3.8 shows Bode plots of $G_V(s)$ and the compensated open-loop transfer function for different rotor speeds at full load.

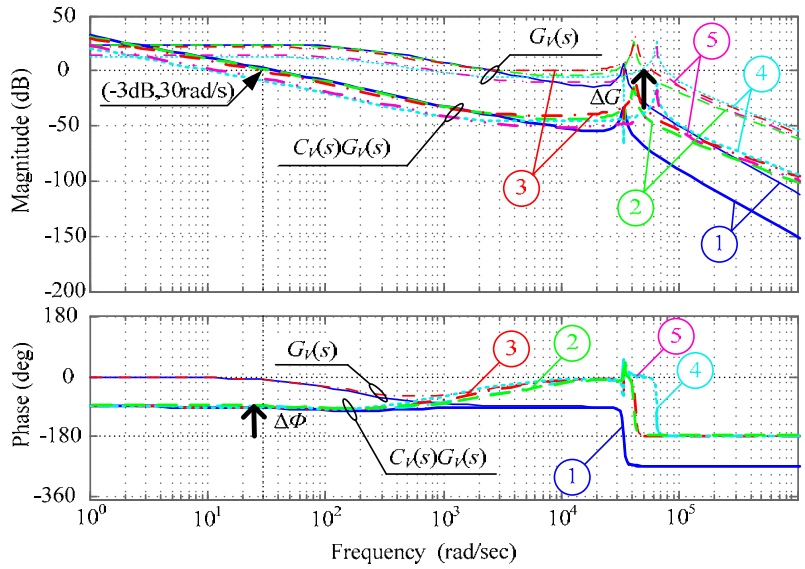

Figure 3.7. Bode plots of $G_V(s)$ and $G_V(s)C_V(s)$ at no load (1), 50% (2), 100% (3),150% (4) of the full load (resistive) and at 75% of the full load with a lagging power factor equal to 0.8 (5)

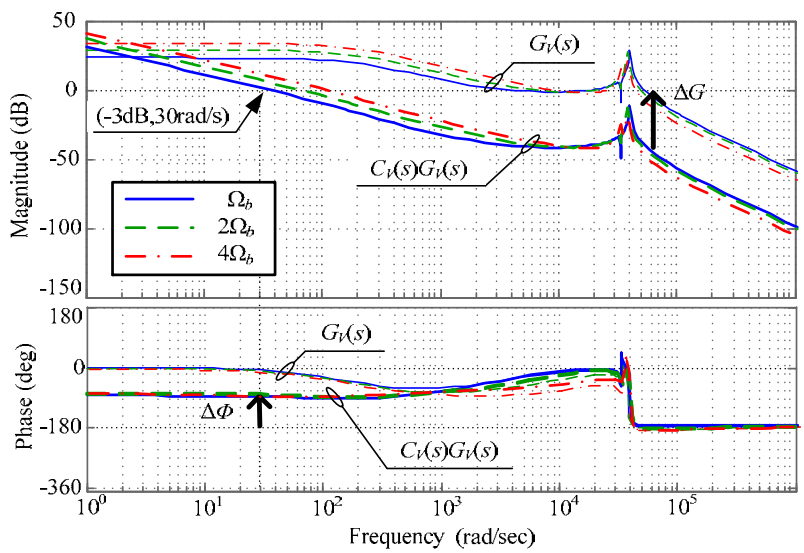

Figure 3.8. Bode plots of $G_V(s)$ and $G_V(s)C_V(s)$ for different rotor speeds

3.2.2.b. Specifications and outer loop compensator design

Figure 3.9 represents the transient envelopes of the voltage at the POR as specified by the BS EN 2282[1]. The limits in normal operation determine the required transient characteristics of the output voltage. A PI controller, $C_V(s)$, is synthesized based on the plots given in Figure 3.7 and Figure 3.8. The compensated system is stable. The stability margins are drawn in Figure 3.7 and Figure 3.8 for the full load and the base speed: $\Delta G = 46\ dB$, $\Delta\Phi = 87°$. These margins do not significantly vary over the considered load and speed range. Conversely, the cutoff frequency varies between 10 rad/s and 110 rad/s, which will be reflected by a settling time variation.

[1] BS EN 2282: Characteristics of aircraft electrical supplies

Figure 3.10 represents the step response plot of the voltage feedback loop at full load and base speed. The settling time equals 0.094 s, this value complies with the BS EN 2282 requirements.

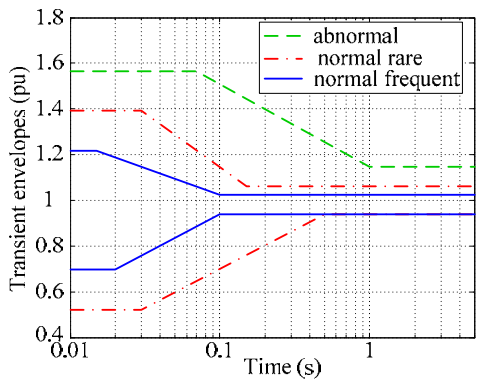

Figure 3.9. Transient envelops for the voltage at the POR as per BS EN 2282

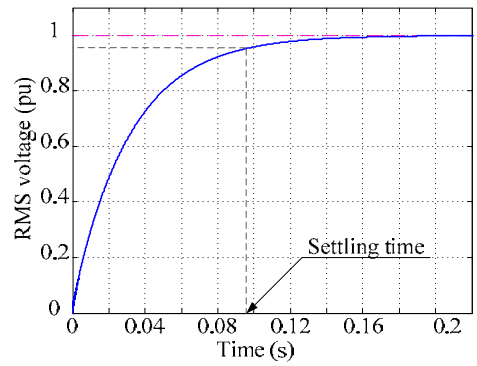

Figure 3.10. Closed-loop step response

3.3. Control with iron loss consideration

Iron losses introduce a shifting angle between the induced currents and the actual currents in the armature windings as shown by the equivalent d-q axis dynamic circuits (Figure 1.12). Nevertheless, taking into account the iron losses does not induce major modifications to the generator control. This is explained by the fact that, in generator mode, the control is scalar: the armature voltage magnitude is regulated via a unique action on the field current.

With the sign conventions of generator mode, (1.26) to (1.29) become (3.25) to (3.28).

$$v_{sd} = k\left(-R_s' i_{sd1} - L_{sd}\frac{di_{sd1}}{dt} - M_{sf}\frac{di_f}{dt} + p\Omega L_{sq} i_{sq1}\right) \tag{3.25}$$

$$v_{sq} = k\left(-R_s' i_{sq1} - L_{sq}\frac{di_{sq1}}{dt} - p\Omega\left(L_{sd} i_{sd1} + \Phi_M + M_{sf} i_f\right)\right) \tag{3.26}$$

$$v_f = R_f i_f + L_f\frac{di_f}{dt} + \frac{3}{2}M_{sf}\frac{di_{sd1}}{dt} \tag{3.27}$$

$$\boldsymbol{i}_{sdq} = \frac{R_{ir}\boldsymbol{i}_{sdq1} - \boldsymbol{v}_{sdq}}{R_{ir} + Rs} \tag{3.28}$$

With $k = \dfrac{R_s + R_{ir}}{R_{ir}}$ and $R_s' = \dfrac{R_s R_{ir}}{R_s + R_{ir}}$.

The generator extended state space representation (3.10) is modified accordingly.

$$\begin{cases} \dot{\boldsymbol{x}}'' = \boldsymbol{A}''(\Omega)\boldsymbol{x}'' + \boldsymbol{B}''(\Omega)\boldsymbol{u}'' \\ \boldsymbol{y}'' = \boldsymbol{C}''\boldsymbol{x}'' \end{cases} \tag{3.29}$$

The input vector remains the same $\boldsymbol{u}'' = \begin{bmatrix} v_f & \Phi_M & i_{sd,l} & i_{sq,l} \end{bmatrix}^t$. $\boldsymbol{x}'' = \begin{bmatrix} i_{sd1} & i_{sq1} & i_f & v_{sd} & v_{sq} \end{bmatrix}^t$ is the new state vector and $\boldsymbol{y}' = \begin{bmatrix} v_{sd} & v_{sq} & i_f & i_{sd} & i_{sq} \end{bmatrix}^t$ is the new output vector. $\boldsymbol{A}''(\Omega)$, $\boldsymbol{B}''(\Omega)$ and $\boldsymbol{C}''$ are given by (3.30), (3.31) and (3.32) respectively. It is recalled that R_{ir} varies with rotor speed and/or excitation flux.

$$\boldsymbol{A}'' = \begin{bmatrix} \frac{-R_s' L_f}{A_{fd}} & \frac{p\Omega L_f L_{sq}}{A_{fd}} & \frac{R_f M_{sf}}{A_{fd}} & \frac{-L_f k}{A_{fd}} & 0 \\ \frac{-p\Omega L_{sd}}{L_{sq}} & \frac{-R_s'}{L_{sq}} & \frac{-p\Omega M_{sf}}{L_{sq}} & 0 & \frac{-k}{L_{sq}} \\ \frac{3M_{sf} R_s'}{2A_{fd}} & \frac{-3p\Omega L_{sq} M_{sf}}{2A_{fd}} & \frac{-R_f L_{sd}}{A_{fd}} & \frac{3M_{sf} k}{2A_{fd}} & 0 \\ \frac{k}{C} & 0 & 0 & \frac{-(R + R_{ir} + R_s)}{CR(R_{ir} + R_s)} & p\Omega \\ 0 & \frac{k}{C} & 0 & -p\Omega & \frac{-(R + R_{ir} + R_s)}{CR(R_{ir} + R_s)} \end{bmatrix} \tag{3.30}$$

$$\boldsymbol{B}'' = \begin{bmatrix} \frac{-M_{sf}}{A_{fd}} & 0 & 0 & 0 \\ 0 & \frac{-p\Omega}{L_{sq}} & 0 & 0 \\ \frac{L_{sd}}{A_{fd}} & 0 & 0 & 0 \\ 0 & 0 & \frac{-1}{C} & 0 \\ 0 & 0 & 0 & \frac{-1}{C} \end{bmatrix} \tag{3.31}$$

$$\boldsymbol{C}'' = \begin{bmatrix} 0 & 0 & 0 & 1 & 0 \\ 0 & 0 & 0 & 0 & 1 \\ 0 & 0 & 1 & 0 & 0 \\ k & 0 & 0 & \frac{-1}{(R_{ir} + R_s)} & 0 \\ 0 & k & 0 & 0 & \frac{-1}{(R_{ir} + R_s)} \end{bmatrix} \tag{3.32}$$

Based on (3.29), the transfer function to the reference input is given by (3.33).

It is verified that when R_{ir} tends to infinity, (3.33) is the same as (3.24).

$$G_V(s)=\frac{V_s(s)}{i_{f.ref}(s)}=\frac{kM_{sf}}{\sqrt{2}}\left(\frac{\sqrt{1-k_{q0}{}^2}\,s}{L_{sd}Cs^2+\left(R_s{}'C+L_{sd}\frac{(R+R_{ir}+R_s)}{R(R_{ir}+R_s)}\right)s+k\left(\frac{R_s}{R}+1\right)}+\frac{-k_{q0}p\Omega}{L_{sq}Cs^2+\left(R_s{}'C+L_{sq}\frac{(R+R_{ir}+R_s)}{R(R_{ir}+R_s)}\right)s+k\left(\frac{R_s}{R}+1\right)}\right)H_I(s) \quad (3.33)$$

Practically $R_{ir} >> R_s$. As a result, $k \cong 1$ and $R_s{}' \cong R_s$. Consequently, the compensator synthesized in paragraph 3.2.2 remains adequate even when iron losses are taken into consideration and included in the transfer function.

3.4. Simulation results

Two simulation scenarios are undertaken in this chapter in order to test the control performance. The first simulation is done at constant speed Ω_b and different loads. The second simulation is carried out at variable speed. In all these simulations, the machine model includes iron losses and magnetic circuit saturation effect. At last, a comparison is done between the results obtained with the classic machine model and those obtained with the advanced model in order to evaluate the impact of the magnetic circuit saturation and the iron losses on the control.

In order to be able to test the control performance over a wide speed and load range, the reference voltage at the operating point is set equal to the voltage value obtained by the PM flux alone at 80% of the full resistive load and $\Omega = \Omega_b$.

3.4.1. Simulation with load variation

3.4.1.a. Machine startup with different load values

The simulation is done at constant speed Ω_b. Five cases are compared: startup at 25%, 50%, 75% and 100% of the full load with a Power Factor (PF) equal to one (resistive load) and startup at 90% of the full load with a lagging PF of 0.7. Figure 3.11 depicts the settling of the armature voltage magnitude for the different startup conditions. For loads below 80% of the full load, the voltage generated by the PM flux is greater than the set reference. Thus, the field current goes negative in order to reduce the voltage magnitude. At full resistive load, the time needed for the magnitude to settle at 95% of its final value is equal to 0.04 against 0.094 s found when simulating the outer control loop alone (paragraph 3.2.2.b). The settling time increases, 0.055 s, as the load PF decreases. In order to explain this increase, the field current evolution is to be observed.

The field current acts on the EMF in order to maintain the armature voltage equal to its reference. As the connected load increases, the needed field current increases too. However, a particular attention is paid for the case when the load introduces a lagging phase angle between the armature current and the armature voltage. When comparing plots 4 and 5 in Figure 3.11, it is observed that the field current needed to compensate the armature voltage with an inductive load is greater than the one needed with a resistive load. Referring to Blondel diagrams (Figure 3.12), it can be noted that for the same armature voltage and current RMS values, the EMF E_0 is greater with inductive load. The same is true even if the loads have the same active power. This explains the field current value generated by the outer loop compensator.

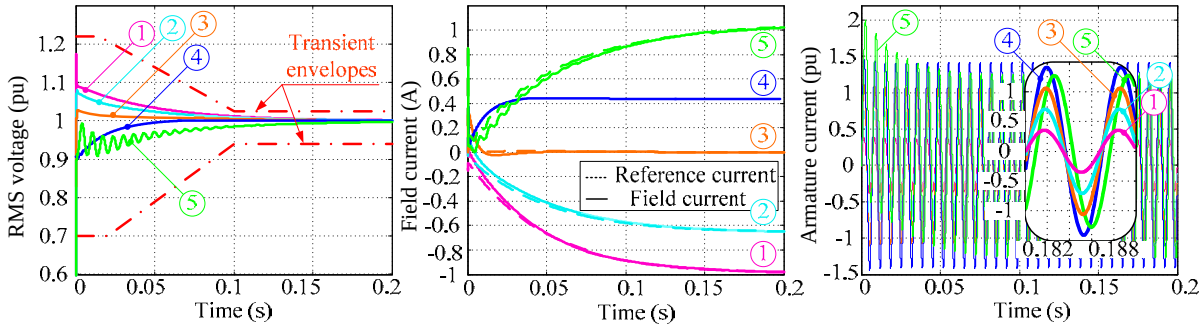

Figure 3.11. RMS voltage, field current and armature current for startup with PF =1 at 25% (1), 50% (2), 75% (3), 100% (4) of the full load and with PF =0.7 at 90% of the full load (5)

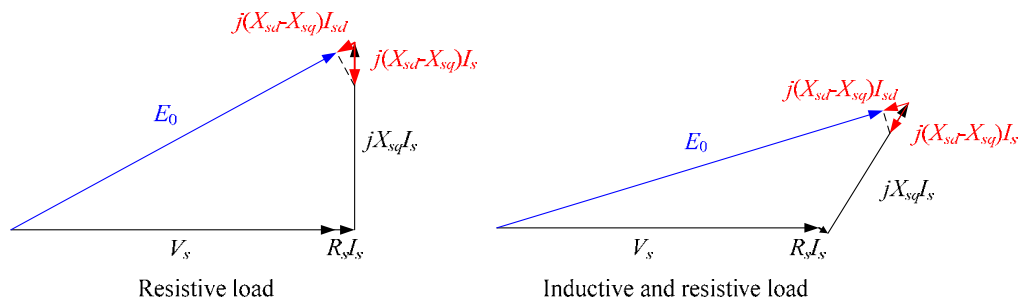

Figure 3.12. Blondel diagrams for resistive load and resistive - inductive load

3.4.1.b. Simulation with load variation

The simulation is done at base speed. The load varies gradually from 25% up to 100%. Two types of load are considered: resistive (PF = 1) and inductive (PF = 0.7). The simulation results are compared in Figure 3.13. As explained in 3.4.1.a, when the load presents a lagging PF, the field current generated by the outer loop compensator is greater than the one obtained with a resistive load. In both cases, the voltage magnitude remains within the norm transient envelopes.

3.4.2. Simulation with speed variation

The simulation is performed at 80% of the full load. The speed varies from Ω_b to $0.8\Omega_b$ then up to $2\Omega_b$ and $4\Omega_b$. Figure 3.14 shows the precise tracking of the excitation current to its reference. For speeds exceeding Ω_b, the field current is negative in order to assure the flux weakening. The voltage at the POR remains within the limits imposed by the BS EN 2282 in spite of the large speed variation.

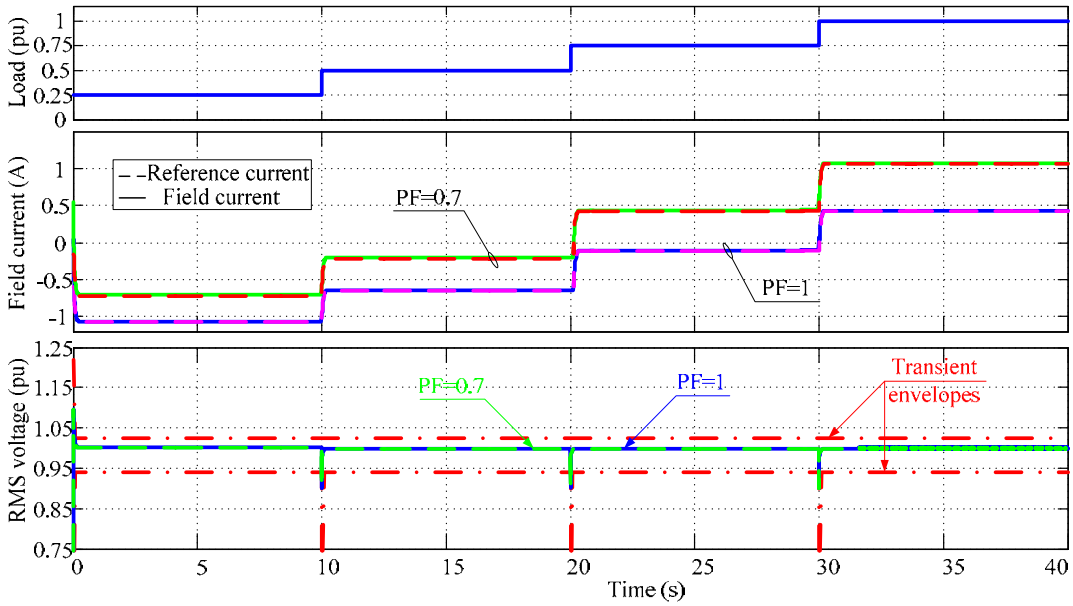

Figure 3.13. RMS voltage control: Simulation results under load variation

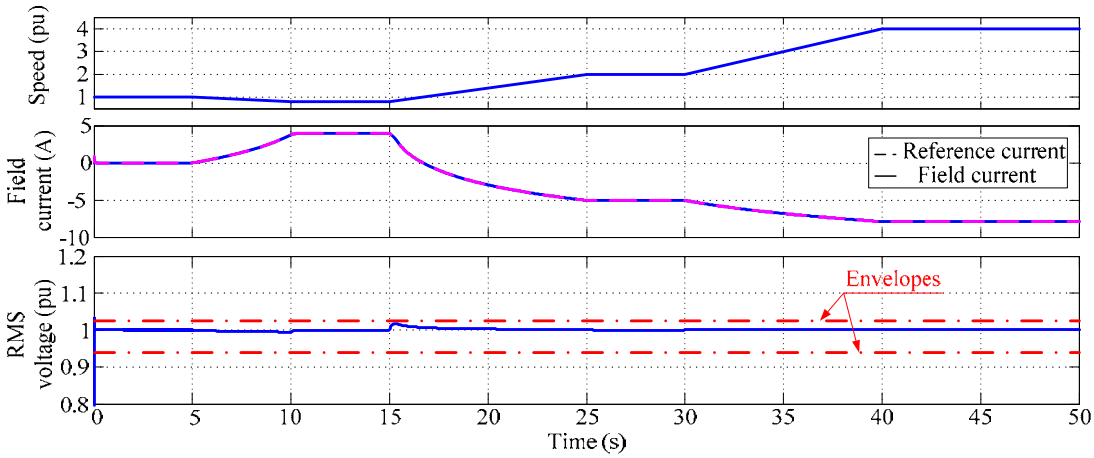

Figure 3.14. RMS voltage control: Simulation results under speed variation

3.4.3. Impact of the magnetic circuit saturation on the control performance

The machine starts at base speed and 25% of the full load. At t = 0.2 s, an additional resistor is connected and the generator supplies now its full load. Simulation is performed with a machine model where the inductances and the PM flux are kept constant; their values do not vary with the currents. The simulation results are compared to those obtained when the machine model takes into account the magnetic circuit saturation (Figure 3.15). For the model with linear magnetic conditions, the excitation flux is the direct sum of the PM flux and the field current multiplied by the mutual inductance M_{sf}. In the model with saturation, this linear relationship is not valid as shown in Figure 1.16. Thus, a greater field current is needed in order to compensate the armature voltage magnitude.

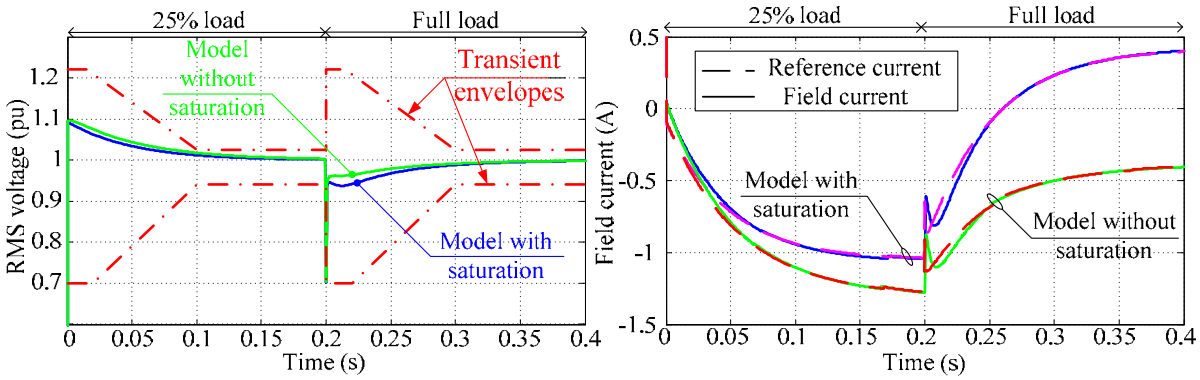

Figure 3.15. RMS voltage control: Simulation results with and without magnetic circuit saturation consideration

3.4.4. Impact of the iron losses on the control performance

Figure 3.16 shows the simulation results with and without iron loss consideration. In generator mode with a scalar control, the effect of the iron losses is compared to an additional load. A greater excitation current is needed in order to maintain the RMS voltage equal to its reference as shown in the zoom. The iron losses affect the efficiency but do not affect the control strategy. However, as noted in Figure 3.16 and stated in section 3.3, the impact of the iron loss consideration on the generator control is not significant.

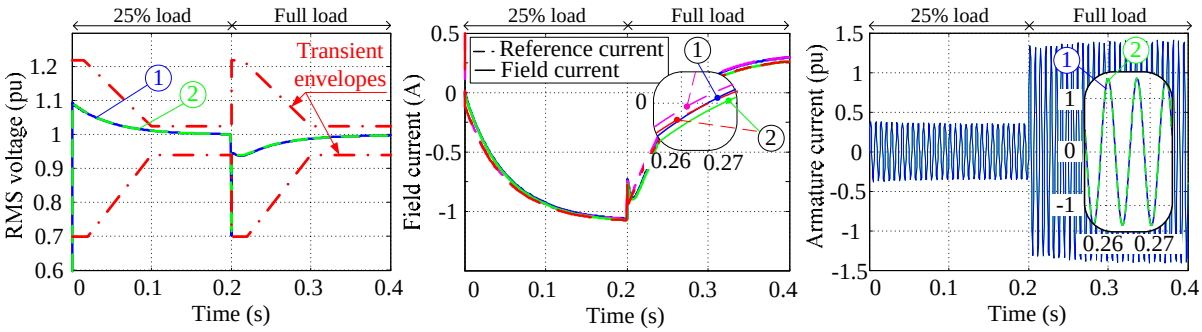

Figure 3.16. RMS voltage control: Simulation results when the machine model includes iron losses (1), and without losses (2)

3.5. Experiments

3.5.1. Experimental bench

The experimental bench is shown in Figure 3.17. The HESM is driven by a 2 kW DC motor. A voltage transducer is used to measure the armature voltage RMS value. Two-quadrant chopper (15 kHz) supplies the DC motor. The exciter is fed via a four-quadrant chopper (20 kHz). A DSpace card (DS1104) is used to control the generator (inputs: RMS voltage and field current, output: voltage to be applied to the excitation winding). The DSpace system is directly programmed from a block diagram representation of the compensators in Matlab/Simulink interface.

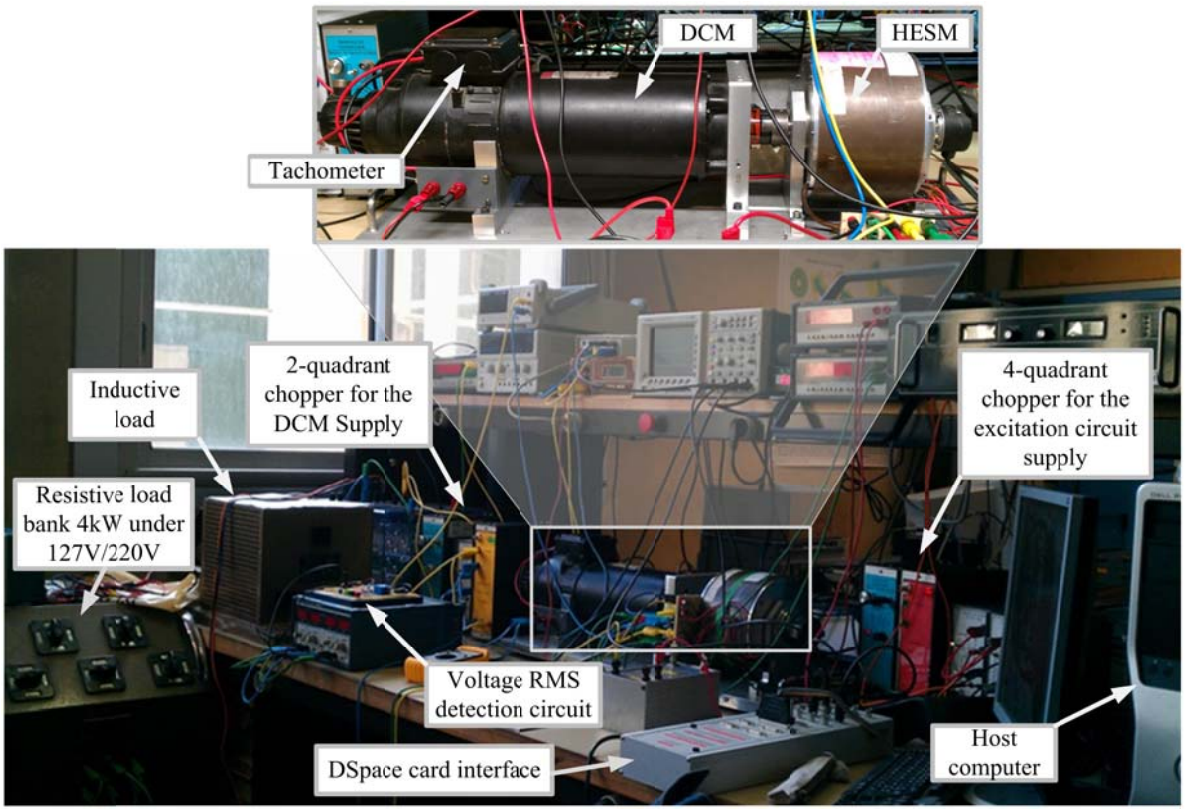

Figure 3.17. HVAC generator: experimental bench

3.5.2. Experimental results

The inner loop control is validated in a first place. Afterward, the control of the HESM is tested under load variation (resistive and inductive), reference voltage variation and rotor speed variation. It shall be noted that since the DCM speed is not compensated, the load and/or reference voltage variation causes speed variation too. The experimental results are compared to those obtained by simulation with Matlab/Simulink software under the same conditions.

3.5.2.a. Field current control validation

Prior to the test of the generation set control, it is mandatory to validate the inner loop compensator. The inner closed-loop step response is shown in Figure 3.18. The settling time is 0.01 s, which complies with the specifications.

3.5.2.b. Experimental results under load and speed variation

The first test is done with a purely resistive load. The load varies from 27% up to 93%. For the first 6 s, the voltage is not compensated and the generated voltage is greater than the set reference. At t = 6 s, the control is initiated. The DCM speed is not controlled during the test and it decreases when the power drawn from the HESM increases, i.e. the load increases. The motor speed drops to 73% of Ω_b at 93% of the full load. The experimental results are shown in Figure 3.19. They are superimposed to the simulation results obtained under the same conditions. The RMS voltage remains equal to its reference when the load and speed vary. The transient limits imposed by the BS EN 2282 are fully respected. In addition, the transient field current and the steady state current value comply with those obtained by simulation. The same is noted for the RMS voltage.

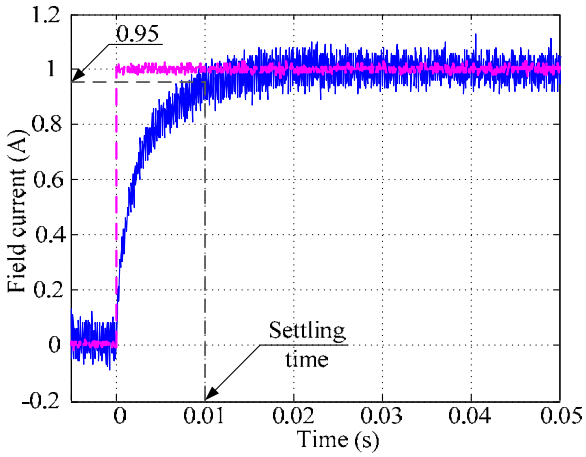

Figure 3.18. Inner closed-loop step response: Experimental result

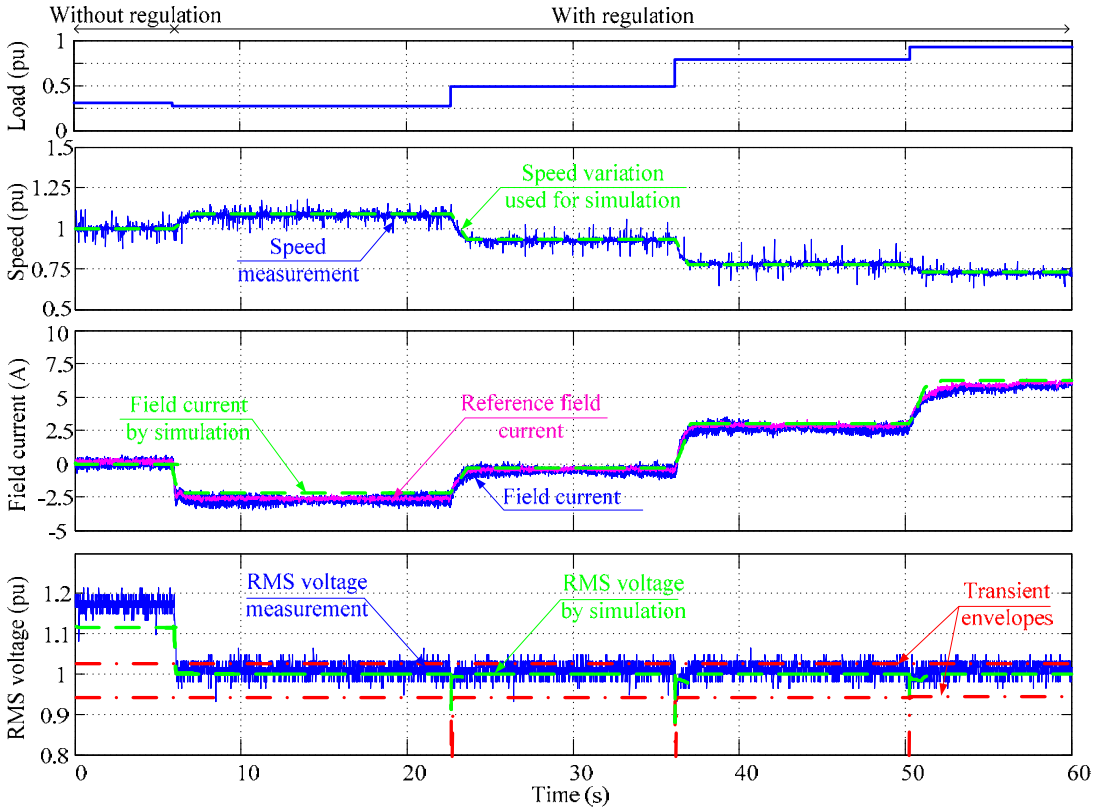

Figure 3.19. RMS voltage control: Experimental results under resistive load variation

Figure 3.20 shows the results obtained when the generator supplies an inductive load. The load varies from 28% to 80%. At the test startup, the PF is set to 0.5. However, since only the resistive part of the load is varied during the test, the PF varies. It is computed afterwards and added to the figure. The experimental results match those obtained by simulation. The RMS voltage remains equal to its reference and the transient envelopes are respected.

When comparing Figure 3.19 to Figure 3.20, two remarks are raised: as expected, with no compensation, the voltage generated with an inductive load is smaller than the one obtained with a

resistive load. On the other hand, the field current controlling the RMS voltage is greater when the load is inductive.

However, it is noted in Figure 3.19 and Figure 3.20 that the voltage generated without compensation in simulation is smaller than the one measured experimentally. Conversely, the field current obtained by simulation is slightly greater than the experimental one. In order to explain this deviation, a closer look to the phase voltage waveform over one period is needed. As shown in Figure 3.21, the real voltage waveform is not sinusoidal and it is affected by the armature current reaction. Therefore, the measured RMS voltage includes the contribution of higher order voltage harmonics. This contribution is not taken into consideration in the simulation since the machine simulation model considers the first harmonic only. As a result, a greater field current is obtained in simulation as shown in Figure 3.21. Yet, the difference does not exceed 10%.

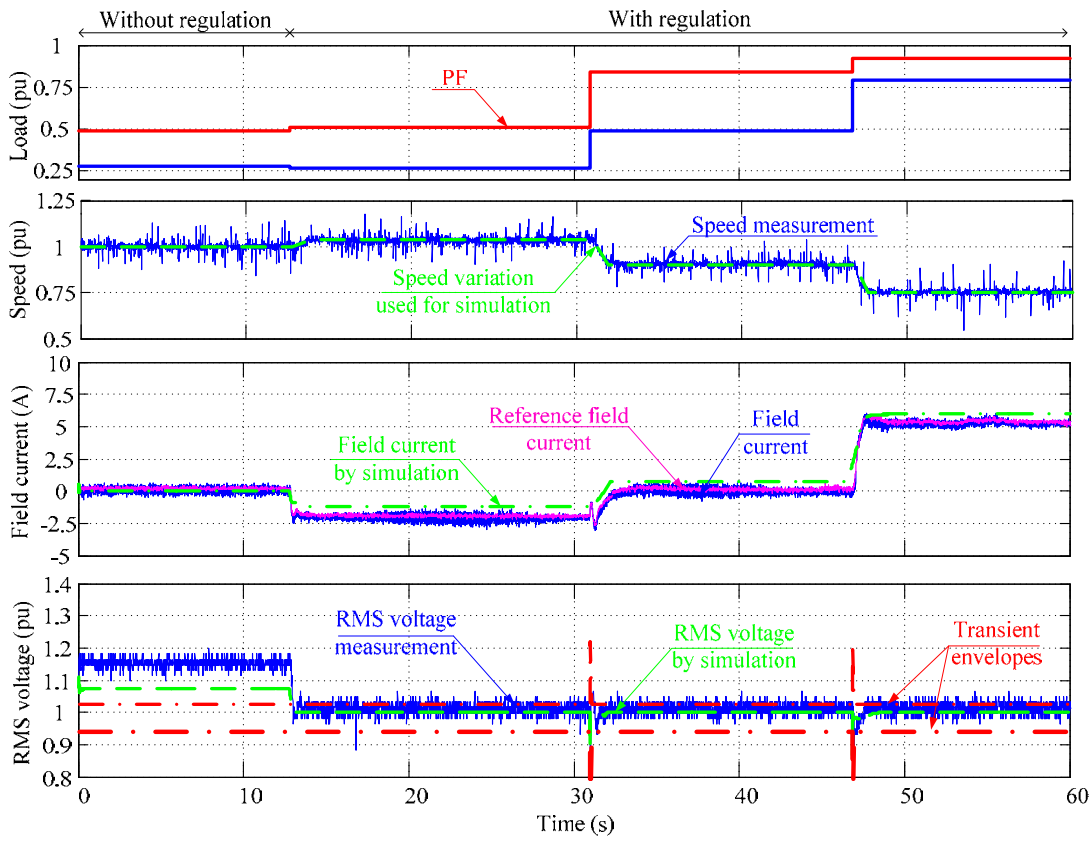

Figure 3.20. RMS voltage control: Experimental results with inductive load variation

3.5.2.c. Experimental results under reference voltage and speed variation

The test is done at 80% of the full load with PF = 1. The reference voltage varies by ± 15% and consequently the speed varies by ±12.5%. The experimental results are shown in Figure 3.22. The field current responds correctly to the reference voltage and speed change. The increase of the reference voltage results in an increase of the EMF and thus an increase of field current reference generated by the outer loop compensator. On the other hand, when the reference is set to 85%, the field current goes negative in order to reduce the excitation flux in the air gap and armature windings. Figure 3.22 bears out the voltage precise tracking to its reference. In addition, the transient limits are fully respected and the field current obtained by simulation is very close to the one measured experimentally. Less than 7% difference is recorded.

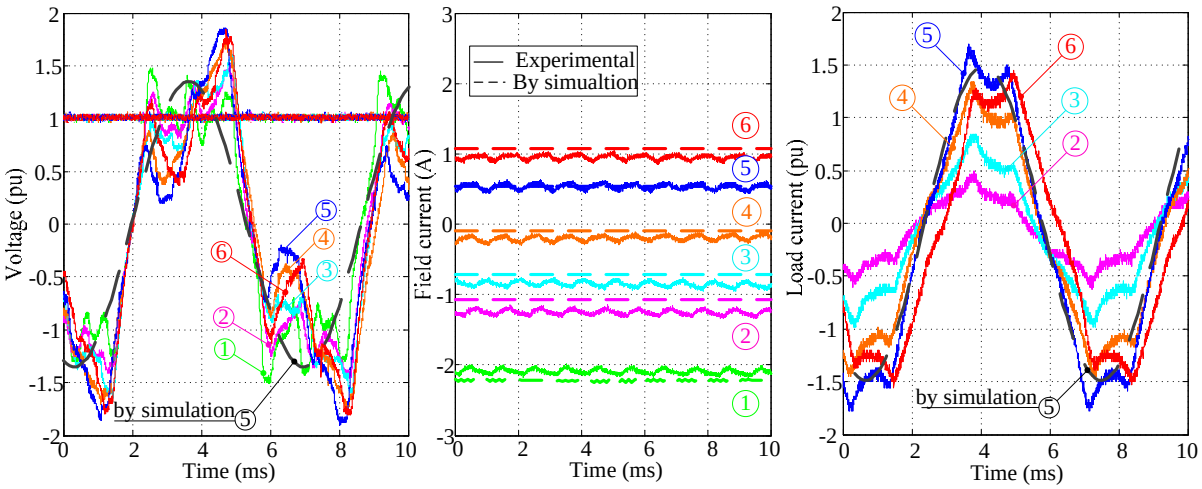

Figure 3.21. RMS voltage control: Experimental phase voltage, field current and load current waveforms for $\Omega = \Omega_b$ at no load (1), 25% (2), 50% (3), 75% (4), 100% (5) of the full load with PF =1 and at 90% of the full load with PF =0.7 (6)

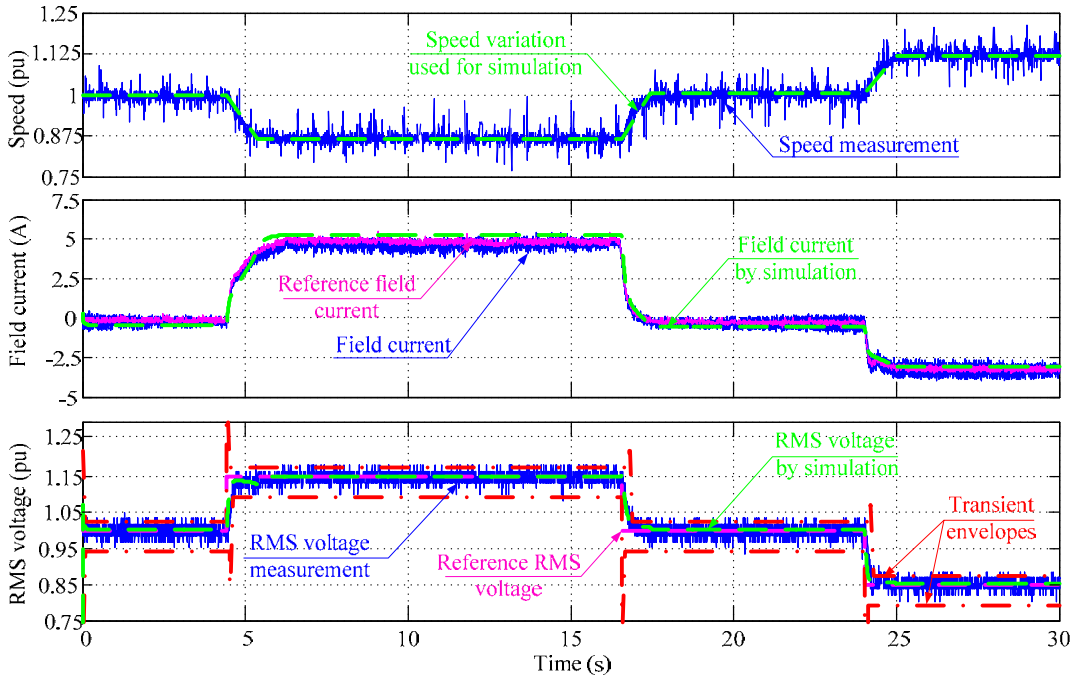

Figure 3.22. RMS voltage control: Experimental result under reference voltage variation

3.5.2.d. Experimental results under speed variation

The test is done at 80% of the full load with PF = 1. The speed goes from Ω_b down to $0.75\Omega_b$ and then increases to $1.5\Omega_b$. Due to the machine prototype field current limitation, it is not possible to reach the $4\Omega_b$ as in the simulation cycle in paragraph 3.4.2. Figure 3.23 proves the flux weakening capability of the HESM at high speed: The excitation current goes negative in order to maintain the voltage equal to its reference. On the other hand, the excitation current increases, as expected, when the speed decreases. The simulation results are reflected in Figure 3.23 too. The experimental RMS voltage and the field current transients match those obtained by simulation. The

field current steady state value generated by simulation is greater by maximum 8% than the measured current. This difference is justified in paragraph 3.5.2.b.

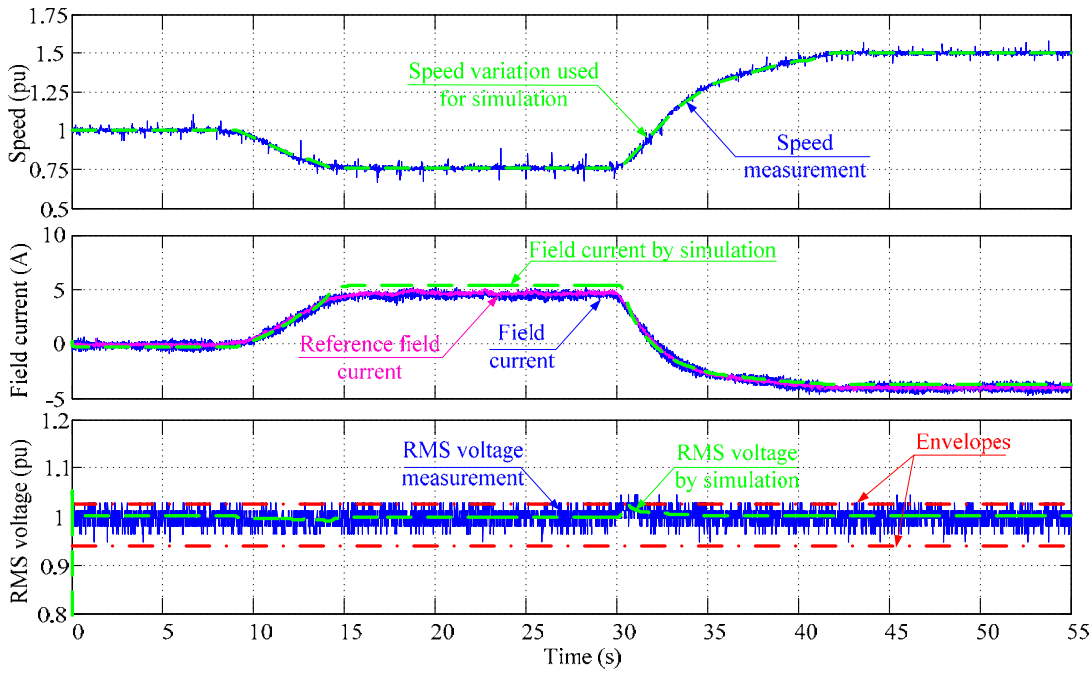

Figure 3.23. RMS voltage control: Experimental results under speed variation

Conclusion

The control of the HESM operating as an HVAC variable frequency generator supplying an isolated load is detailed and tested by simulation and experiments in this chapter.

The model of the machine is adapted to the generator mode in a first place. The control of the output voltage magnitude is studied. Simulation results prove the capability of the generator to operate correctly under load, reference voltage or speed variation.

Experiments are performed on a laboratory prototype HESM as well. The experimental results attest the control performance. These results match those obtained by simulation under the same condition. The RMS voltage remains equal to its reference despite the fact that the voltage waveform is not sinusoidal.

Chapter 4. HESM Operating as a Generator Connected to an HVDC Isolated Network

Introduction

Although preferred architecture for MEA power system for the commercial airplanes has not been established yet, the modern power optimized architecture tends to use HVDC network [9] [15] [142]. Previous work proved that the HESM could be successfully used in brushless electrical generation systems such as aircraft power supply. The grid supply is a DC bus. The machine is connected to a diode bridge rectifier [96] or a PWM rectifier [95]. In both cases, the DC voltage is maintained constant through actions on the field current and the armature currents. With the PWM rectifier, vector control is adopted [95]. When connected to the diode bridge rectifier, the armature current magnitude is controlled [96].

In this chapter, a simple control of the HESM supplying the load through a diode rectifier bridge is proposed. A diode rectifier is preferred to active rectifiers due to its simple configuration, high efficiency and high reliability suitable for an embedded application. In addition, it provides a low cost solution in rectifying the AC voltage. The main contribution of the approach is that the DC bus voltage is directly compensated via the action on the field current. The control is scalar and consists of just two loops. In section 4.1, the diode bridge rectifier is modeled and the DC generator bloc diagram is build. The generator control is detailed in section 4.2. The transient characteristics of the output voltage are specified by the MIL-STD-704F [1]. The iron losses are neglected in a first place. Their impact on the control is then studied in section 4.3. The DC generator control is validated by simulation with Matlab/Simulink software in section 4.4. Experimental validation follows in section 4.5.

[1] Military Standard, Department of Defense, USA: Aircraft electric power characteristics

4.1. HVDC generator modeling

The HESM is cascaded with a diode bridge rectifier and a filtering capacitive cell. The set operates as HVDC generator.

The hybrid excitation synchronous generator is described by (3.1), (3.2) and (3.3). These equations yield to the state space representation of the machine that is given by (3.4). [v_f, Φ_M, v_{sd}, v_{sq},] is the input vector. [i_{sd}, i_{sq}, i_f] is the state vector that is equal to the output vector.

4.1.1. Diode bridge rectifier mathematical model

The diode bridge is the simplest rectifier regarding the structure. Yet, it is a nonlinear system and it is difficult to model since the switching conditions are not controllable and depend on the three-phase currents. Figure 4.1 represents a generic model of the diode rectifier. e_{sa}, e_{sb}, e_{sc} are the EMF.

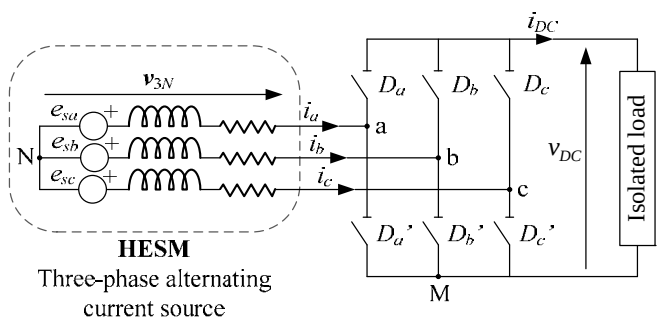

Figure 4.1. Diode bridge rectifier generic model

The diode bridge modeling is carried out under the assumptions of ideal switches, no losses and continuous conduction mode, which means that each diode conducts for 180° (instead of 120°) [79]. This assumption is practically verified given the machine inductive nature. The model is used to simulate the converter and to find a transfer function useful for the control design. It shall be pointed that this model does not describe accurately the system behavior for small timescale; it cannot be used when the control dynamic is of the same order of the alternating voltage period.

In order to describe the full operation of the diode bridge rectifier, two relationships shall be established: the first one gives the three-phase voltages in terms of the DC voltage; the second one computes the DC current given the three-phase currents.

Switching functions associated with the bridge legs are introduced. f_j is the switching function associated with the leg j ($j = a, b, c$). f_j is a Heaviside function [79].

- $f_j = 1$ if D_j is conducting and D_j' is in blocking state ($i_j(t) > 0$).
- $f_j = 0$ if D_j is in blocking state and D_j' is conducting ($i_j(t) < 0$).

The three-phase voltages are then computed by (4.1).

$$\boldsymbol{v}_{3M} = \boldsymbol{f}_3 v_{DC} \tag{4.1}$$

With $\boldsymbol{v}_{3M} = \begin{pmatrix} v_{aM} & v_{bM} & v_{cM} \end{pmatrix}^t$ and $\boldsymbol{f}_3 = \begin{pmatrix} f_a & f_b & f_c \end{pmatrix}^t$.

Equation (4.2) is verified no matter what the neutral system is.

$$\begin{pmatrix} v_{aN}-v_{bN} \\ v_{bN}-v_{cN} \\ v_{cN}-v_{aN} \end{pmatrix} = \begin{pmatrix} v_{aM}-v_{bM} \\ v_{bM}-v_{cM} \\ v_{cM}-v_{aM} \end{pmatrix} = \begin{pmatrix} f_a-f_b \\ f_b-f_c \\ f_c-f_a \end{pmatrix} v_{DC} \tag{4.2}$$

This system does not yield to a unique solution. A new constraint is added by assuming zero-sequence voltages. The three-phase voltages are then given by (4.3).

$$\boldsymbol{v}_{s3} = \boldsymbol{v}_{3N} = \frac{1}{3}\begin{bmatrix} 2 & -1 & -1 \\ -1 & 2 & -1 \\ -1 & -1 & 2 \end{bmatrix} \boldsymbol{f}_3 v_{DC} = \boldsymbol{Q}\boldsymbol{f}_3 v_{DC} \tag{4.3}$$

The current in each bridge leg is computed by (4.4). The Kirchhoff law yields to(4.5).

$$i_{Dj}(t) = i_j(t)\, f_j \tag{4.4}$$

$$i_{DC} = i_{Da} + i_{Db} + i_{Dc} = \boldsymbol{i}_{s3}{}^t \boldsymbol{f}_3 \tag{4.5}$$

Thus, the diode bridge rectifier is modeled by (4.3) and (4.5).

Since $\boldsymbol{Q} = \boldsymbol{C}_{32}\boldsymbol{C}_{23}$, (4.3) and (4.5) yield to (4.6) and (4.8) respectively. Consequently, the diode bridge is modeled by (4.7) and (4.9) in the d-q coordinate system.

$$\boldsymbol{v}_{s3} = \boldsymbol{C}_{32}\boldsymbol{v}_{s\alpha\beta} = \boldsymbol{C}_{32}\boldsymbol{C}_{23}\boldsymbol{f}_3 v_{DC} \Rightarrow \boldsymbol{v}_{s\alpha\beta} = \underbrace{\boldsymbol{C}_{23}\boldsymbol{f}_3}_{\boldsymbol{f}_{\alpha\beta}} v_{DC} \tag{4.6}$$

$$\boldsymbol{v}_{sdq} = \boldsymbol{R}(p\theta)\boldsymbol{v}_{s\alpha\beta} = \underbrace{\boldsymbol{R}(p\theta)\boldsymbol{C}_{23}\boldsymbol{f}_3}_{\boldsymbol{f}_{dq}} v_{DC} = \boldsymbol{f}_{dq} v_{DC} \tag{4.7}$$

$$i_{DC} = \left(\boldsymbol{C}_{32}\boldsymbol{i}_{s\alpha\beta}\right)^t \boldsymbol{f}_3 = \boldsymbol{i}_{s\alpha\beta}{}^t \boldsymbol{C}_{32}{}^t \boldsymbol{f}_3 = \boldsymbol{i}_{s\alpha\beta}{}^t \frac{3}{2}\boldsymbol{C}_{23}\boldsymbol{f}_3 = \frac{3}{2}\boldsymbol{i}_{s\alpha\beta}{}^t \boldsymbol{f}_{\alpha\beta} \tag{4.8}$$

$$i_{DC} = \frac{3}{2}\left(\boldsymbol{R}(-p\theta)\boldsymbol{i}_{sdq}\right)^t \boldsymbol{f}_{\alpha\beta} = \frac{3}{2}\boldsymbol{i}_{sdq}{}^t \boldsymbol{f}_{dq} \tag{4.9}$$

4.1.2. Capacitive filter

In order to reduce the DC voltage ripples, a capacitor is added at the DC side. A capacitance of C = 470 µF is chosen so that the ripple factor remains less than 1% at the nominal operating point.

Hence, the HESM, the diode bridge rectifier and the capacitor form a DC voltage source as shown in Figure 4.2. $i_{DC,l}$ is the DC load current.

The Kirchhoff current law yields to (4.10).

$$i_{DC} - i_{DC,l} = C\frac{dv_{DC}}{dt} \tag{4.10}$$

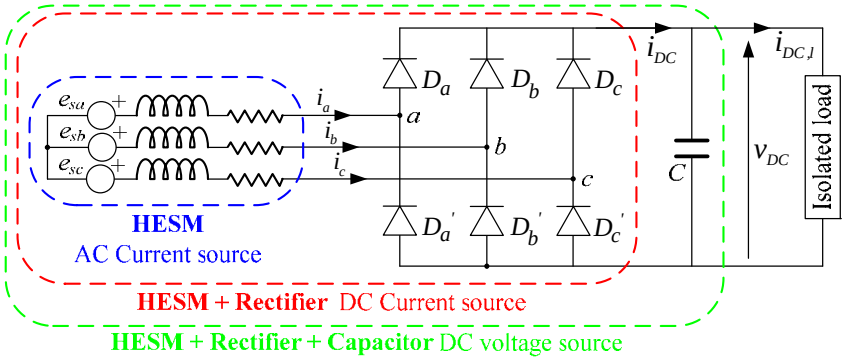

Figure 4.2. DC voltage source

4.1.3. HVDC generator bloc diagram

Based on (3.1), (3.2), (3.3), (4.7), (4.9) and (4.10), the DC generator bloc diagram is built (Figure 4.3). This bloc diagram helps to compute the transfer function and therefore to design the voltage compensator.

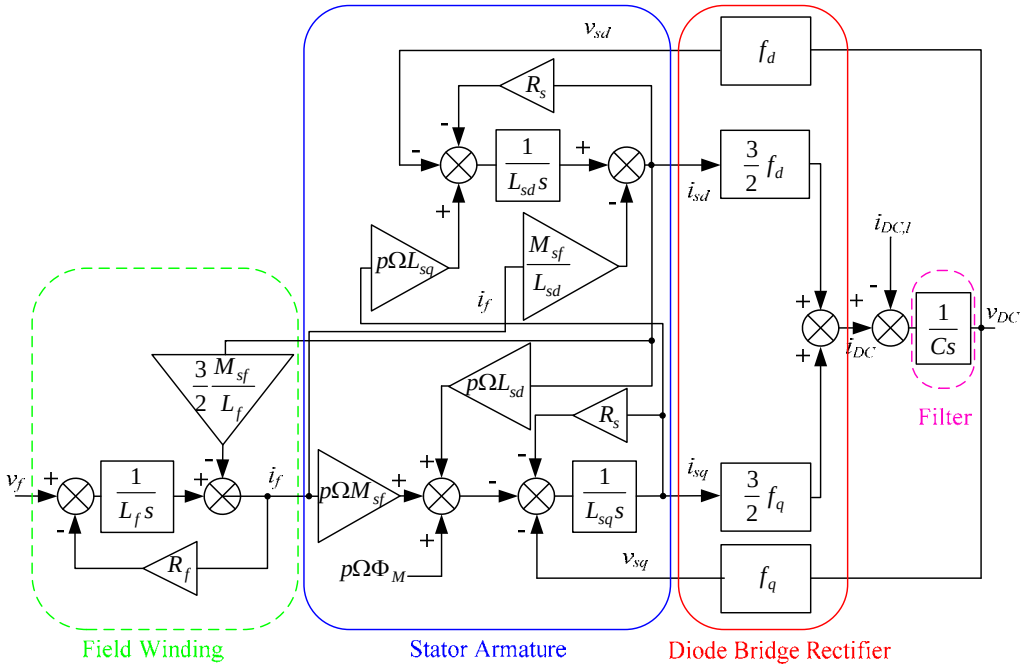

Figure 4.3. DC generator bloc diagram

4.2. Control strategy

The DC generator voltage is to be controlled. Since the converter considered is a diode rectifier, the generating system has only one degree of freedom: the voltage applied to the field winding terminals. The control of the DC bus voltage is performed through hierarchical loops: an inner field current control loop and an outer loop that compensates the DC voltage by action on the field current as shown in Figure 4.4. The main contribution of the approach is that the control is scalar. The field current regulates directly the DC bus voltage.

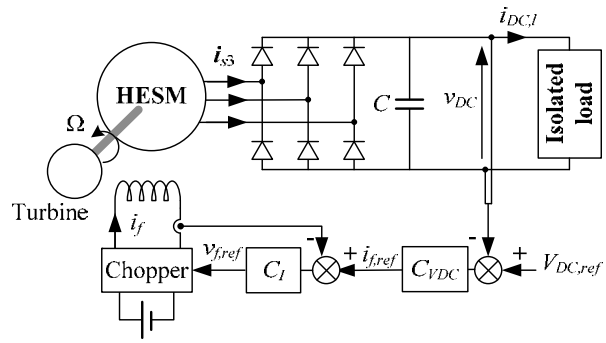

Figure 4.4. Control strategy of the DC generator

The field current loop is detailed in paragraph 3.2.1. The inner closed-loop bandwidth is equal to ω_I = 300 rad/s.

4.2.1. DC voltage control loop

4.2.1.a. Transfer function

The transfer function (4.11) is derived based on the block diagram given in Figure 4.3.

$$G_{VDC}(s) = \frac{v_{DC}(s)}{i_{f,ref}(s)} = F_{VDC}(s) H_I(s) \tag{4.11}$$

$H_I(s)$ represents the field current closed-loop dynamic as given by (3.17). $F_{VDC}(s)$ is given by (4.12).

$$F_{VDC}(s) = \frac{v_{DC}(s)}{i_f(s)} = \frac{\frac{-3}{2} M_{sf}\left(f_d\left(L_{sq}s + R_s\right)s + f_q p\Omega\left(L_{sd}s + R_s\right)\right)}{Cs\left(L_{sd}s + R_s\right)\left(L_{sq}s + R_s\right) + \frac{3}{2}\left(f_d^{\,2}\left(L_{sq}s + R_s\right) + f_q^{\,2}\left(L_{sd}s + R_s\right)\right)} \tag{4.12}$$

The outer loop bloc diagram is illustrated in Figure 4.5.

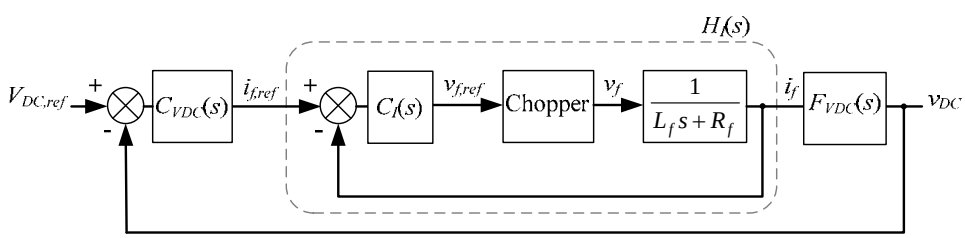

Figure 4.5. DC bus voltage control: outer loop bloc diagram

The quantities f_d and f_q are not constant. Figure 4.6 shows the waveforms of $f_d(t)$ and $f_q(t)$ over a period of the armature current. Figure 4.7 represents the poles and zeros map of the function $G_{VDC}(s)$ for six different values of ($f_d(t)$, $f_q(t)$). The dominant poles and zeros are almost the same for all these functions. Hence, in order to synthesize a compensator, any value of (($f_d(t_0)$, $f_q(t_0)$)) can be chosen from the waveform in Figure 4.6. Let $f_d = 0$ and $f_q = -0.6667$. This choice gives the simplest transfer function $G_{VDC}(s)$.

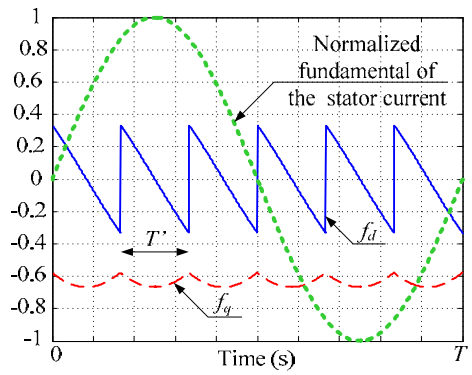

Figure 4.6. $f_d(t)$ and $f_q(t)$ waveforms over a period of the armature current

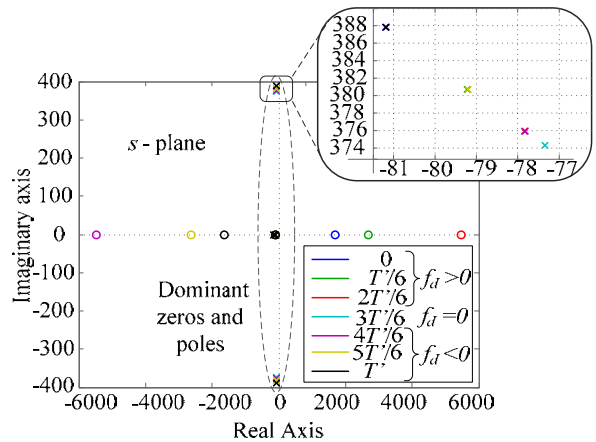

Figure 4.7. Pole and zero map of $G_{VDC}(s)$ for different values of (f_d, f_q)

The transfer function $G_{VDC}(s)$ depends on the rotor speed and the inductances and excitation flux values. However, these values vary with the load currents, due to the magnetic circuit saturation. Thus, in order to offer better performance over wide load and speed range, the compensator design is not limited to the nominal operating point. Figure 4.8 shows Bode plots of $G_{VDC}(s)$ and the compensated open-loop transfer function for different loads. In these plots, $\Omega = \Omega_b$. Figure 4.9 shows Bode plots of $G_{VDC}(s)$ and the compensated open-loop transfer function for different rotor speeds at full load. The stability margins of the uncompensated system are negative and the system is unstable.

4.2.1.b. Specifications and outer loop compensator design

The HVDC is currently used in military aircraft platforms like F-22 or F-35 [48]. Hence, the output DC voltage should comply with the MIL-STD-704F guidelines (Figure 4.10). This standard establishes the requirements and characteristics of electric power provided at the input terminals of electric utilization equipment in military aircrafts. Given the transient envelopes of the DC bus voltage as specified by this standard, the required transient characteristics of the output voltage are determined and a PI controller, $C_{VDC}(s)$, is synthesized based on the Bode plots given in Figure 4.8 and Figure 4.9. The compensated system is stable for the considered speed and load range. The phase and gain margins for the full load and base speed are shown in Figure 4.8 and Figure 4.9. The gain margin varies between 25dB and 15dB (when $\Omega = 4\Omega_b$), the phase margin is almost constant and is equal to 84º. The cutoff frequency varies between 13 rad/s and 45 rad/s, this variation translates into settling time variation.

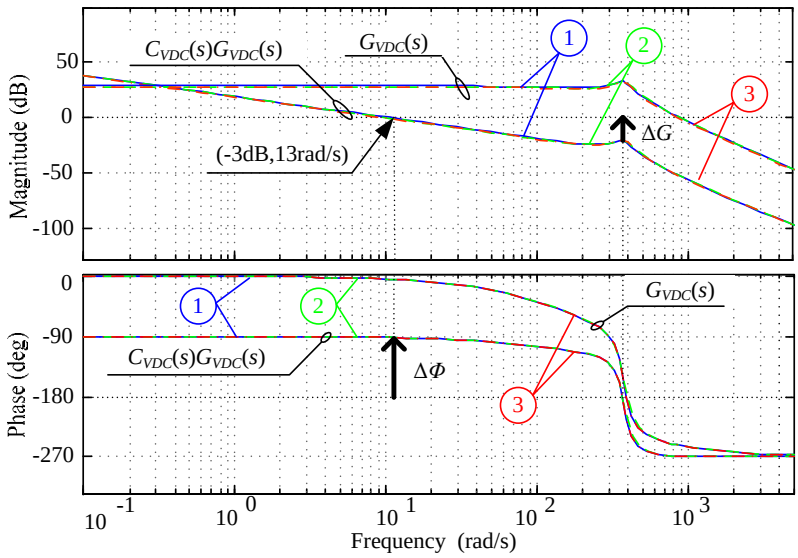

Figure 4.8. Bode plots of $G_{VDC}(s)$ and $C_{VDC}(s)G_{VDC}(s)$ at no load(1), half load (2), Full load (3)

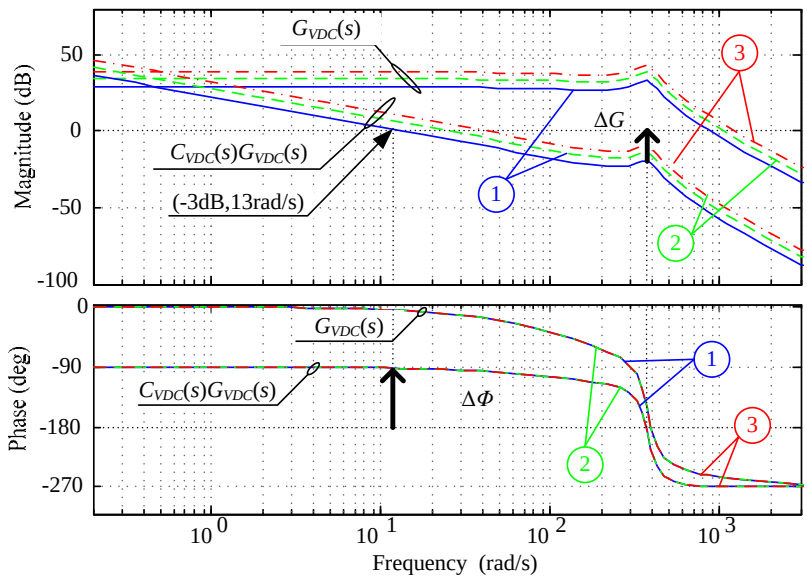

Figure 4.9. Bode plots of $G_{VDC}(s)$ and $G_{VDC}(s)C_{VDC}(s)$ for $\Omega = \Omega_b$ (1), $\Omega = 2\Omega_b$, (2), $\Omega = 4\Omega_b$ (3)

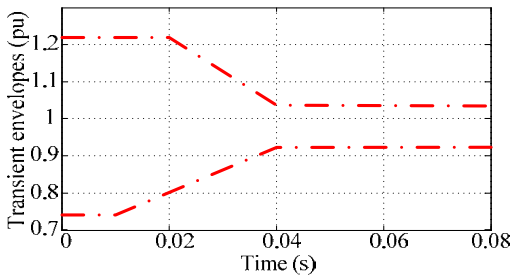

Figure 4.10. Transient envelops for the DC voltage as specified by MIL-STD-704F

4.3. Control with iron loss consideration

The generator control is scalar. Thus, it is not significantly affected by the shifting angle between the machine currents and the induced currents due to iron loss consideration. Based on (3.25) to (3.28), the DC generator bloc diagram of Figure 4.3 is modified as shown in Figure 4.11 in order to include the iron losses.

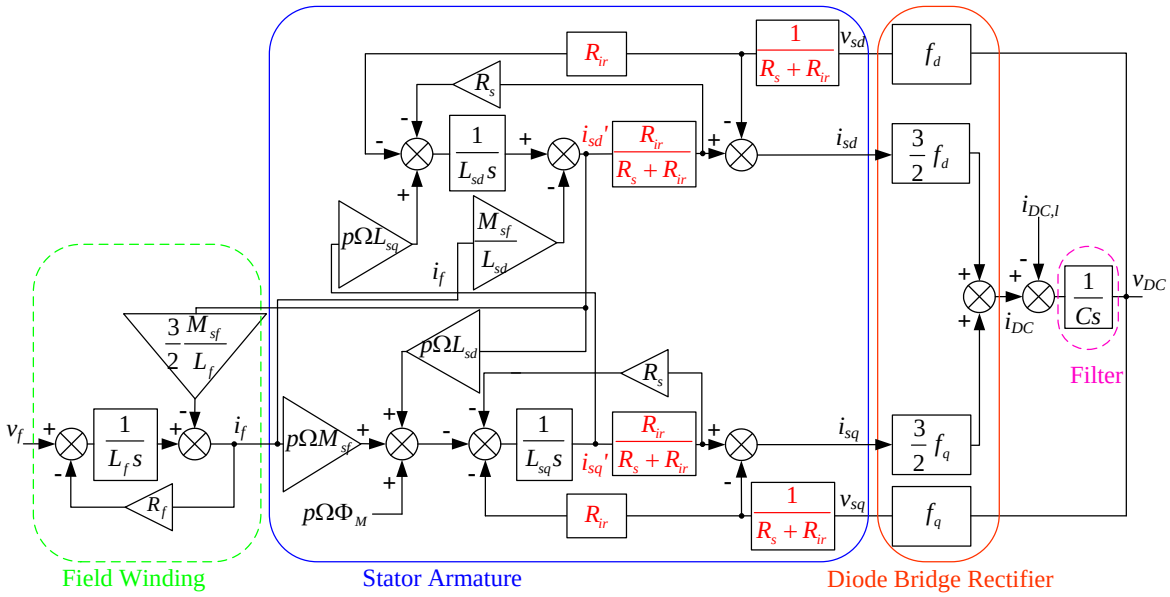

Figure 4.11. DC generator bloc diagram including iron losses

The transfer function is modified accordingly and is given by (4.13).

$$G_{VDC}(s)=\frac{v_{DC}(s)}{i_f(s)}=\frac{-3/2\,M_{sf}\left(f_d\left(L_{sq}s+R_s'\right)s+f_q p\Omega\left(L_{sd}s+R_s'\right)\right)}{\left(kCs+\frac{3}{2}\frac{\left(f_d^{\,2}+f_q^{\,2}\right)}{R_{ir}}\right)\left(L_{sd}s+R_s'\right)\left(L_{sq}s+R_s'\right)+A}H_I(s) \tag{4.13}$$

$$A=\frac{3}{2}k\left(f_d^{\,2}\left(L_{sq}s+R_s'\right)+f_q^{\,2}\left(L_{sd}s+R_s'\right)\right)$$

With $k=\dfrac{R_s+R_{ir}}{R_{ir}}$ and $R_s'=\dfrac{R_sR_{ir}}{R_s+R_{ir}}$.

4.4. Simulation results

Simulation is done using Matlab/Simulink software. The control performances are tested for different loads in a first place then for large speed variation. Lastly, simulations are undertaken in order to evaluate the impact of the iron losses and the magnetic circuit saturation on the control. The operating point is chosen in a way that the reference DC voltage can be generated by the PM flux with no need to the field current contribution for 80% of the full load at $\Omega = \Omega_b$.

4.4.1. Simulation with different loads

4.4.1.a. Machine startup with different loads

The simulation is done at constant speed Ω_b. Three cases are presented: startup at 25%, 50% and 100% of the full load. In all cases, the load is resistive. As noted in Figure 4.12, the voltage overshoot is smaller as the load increases. In fact, when the load current increases, the current shared by the parallel capacitor decreases and thus the voltage variation is damped. When the load increases, the field current increases too in order to counter the voltage drop due to the armature reaction and maintain the voltage equal to its reference (Figure 4.13). As mentioned above, for the considered operating point, the voltage generated by the PM flux is greater than the set reference when the load is below 75% of the full load; this justifies the negative values of the field current. Figure 4.14 shows the armature current. Figure 4.15 shows the DC load current.

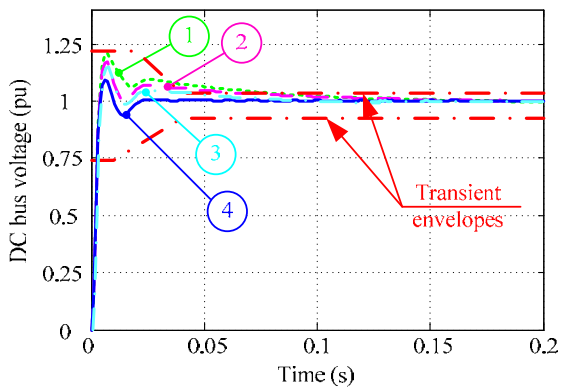

Figure 4.12. DC voltage settling for startup at 25% (1), 50%(2), 75% (3) and 100% (4) of the full load

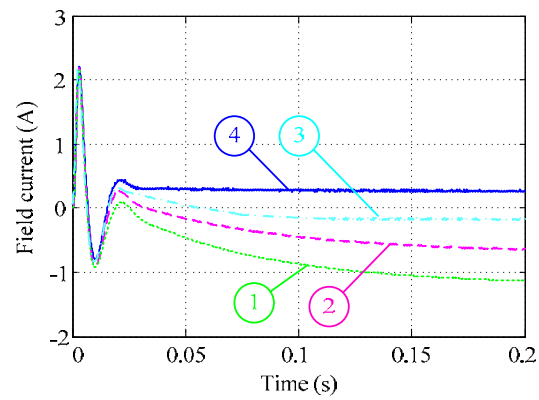

Figure 4.13. Field current for startup at 25% (1), 50%(2), 75% (3) and 100% (4) of the full load

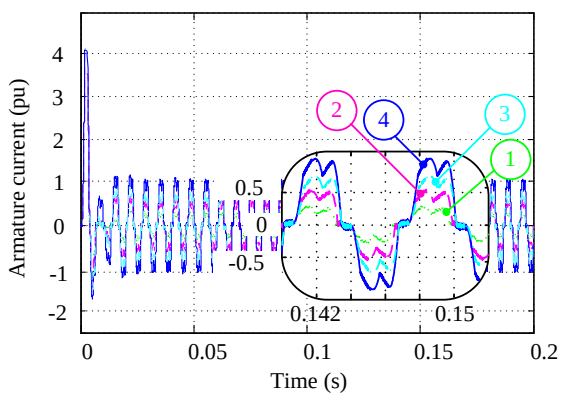

Figure 4.14. Armature current for startup at 25% (1), 50%(2), 75% (3) and 100% (4) of the full load

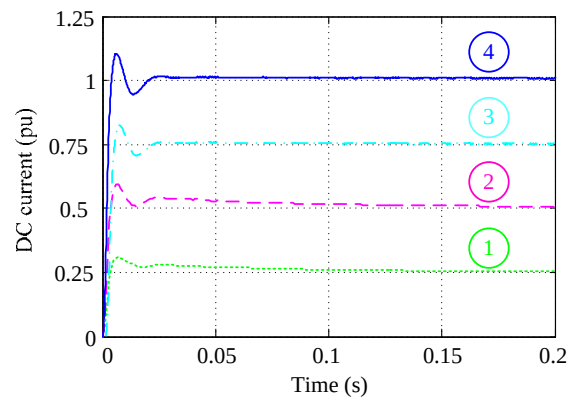

Figure 4.15. DC current for startup at 25% (1), 50%(2), 75% (3) and 100% (4) of the full load

It shall be pointed that the results remain unchanged when an inductive load is connected.

4.4.1.b. Simulation with load variation

The simulation is done at constant speed $\Omega = \Omega_b$. The load varies from 25% up to 100%. The simulation results are shown in Figure 4.16. The bounds specified by the standard envelopes are fully respected.

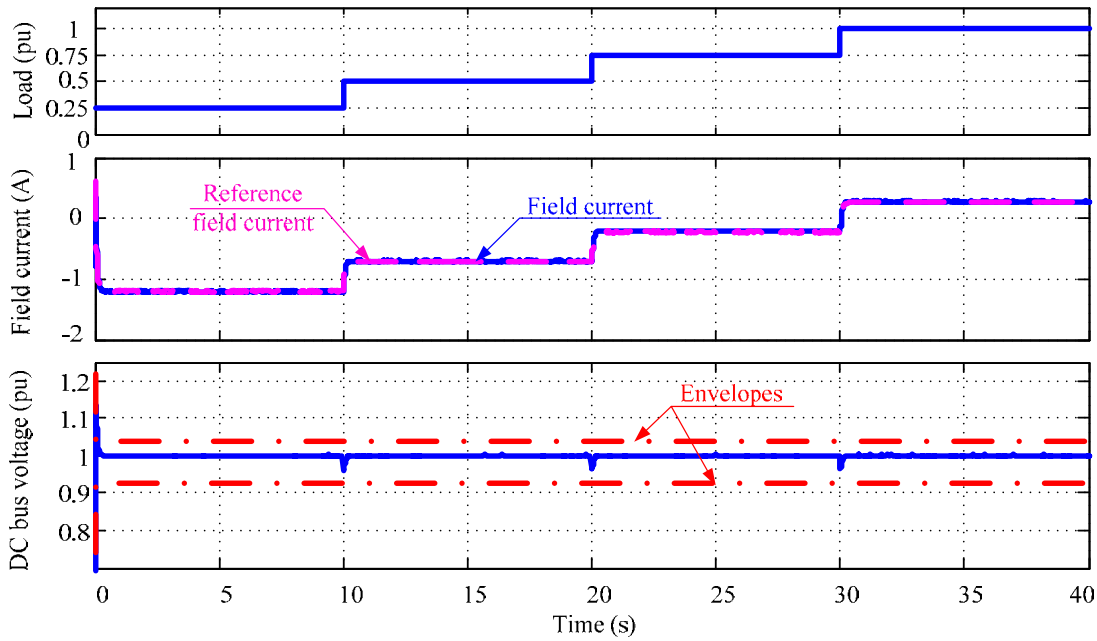

Figure 4.16. DC voltage control: Simulation result under load variation

4.4.2. Simulation with speed variation

Another simulation is performed at 75% of the full load with speed variation from Ω_b down to $0.8\Omega_b$ then up to $2\Omega_b$ and $4\Omega_b$. Figure 4.17 shows the precise tracking of the field current to its reference generated by the outer loop compensator. For speeds exceeding Ω_b, the excitation current is negative in order to assure the flux weakening. The DC bus voltage remains within the limits imposed by the MIL-STD-704F in spite of the large speed variation.

4.4.3. Impact of the magnetic circuit saturation on the control performance

In order to evaluate the impact of the magnetic circuit saturation, the results obtained with the machine model including this phenomenon are superimposed to those obtained with a model with linear magnetic conditions. The simulation results are depicted in Figure 4.18. The same conclusion made in 3.4.3 comes out for the HVDC case. For the model with saturation, a greater field current is needed in order to maintain the DC voltage equal to its reference since the excitation flux is not the direct sum of the PM flux and the wound exciter flux.

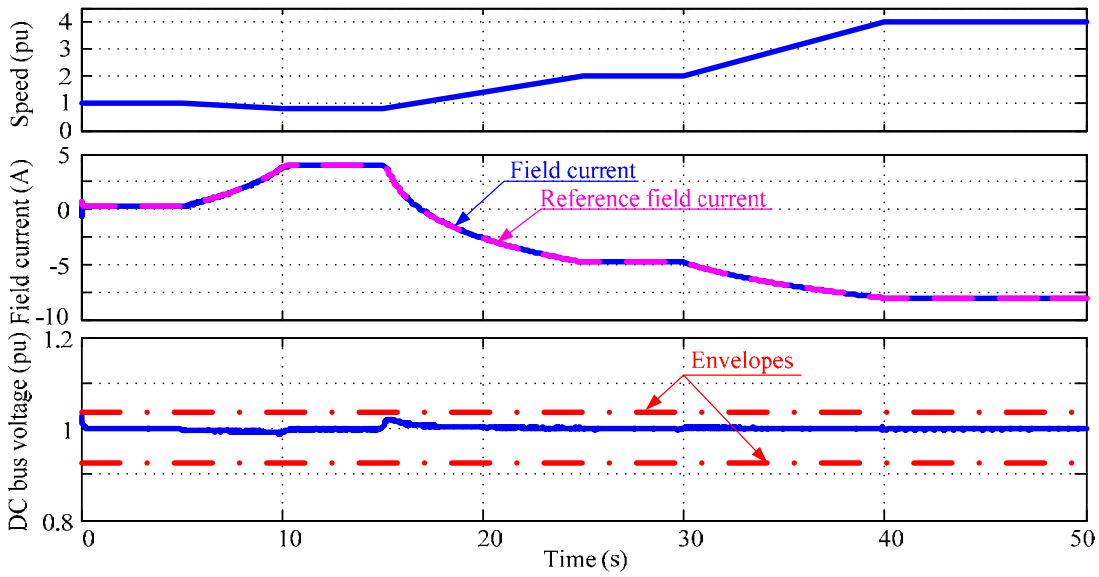

Figure 4.17. DC voltage control: Simulation results under speed variation

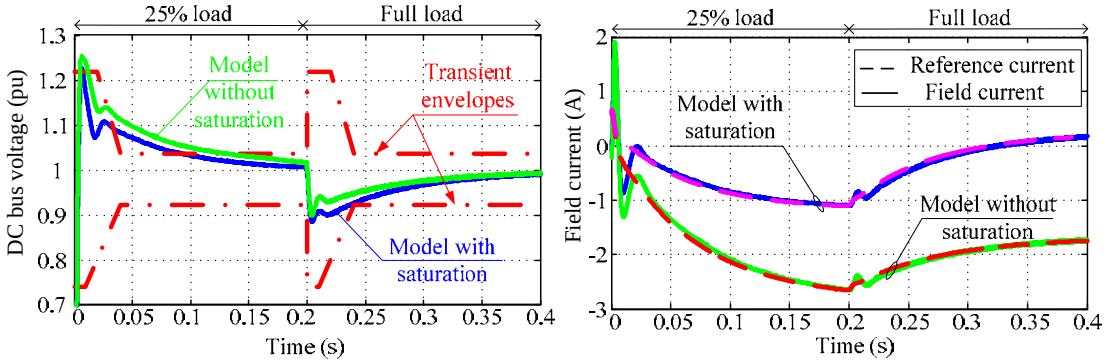

Figure 4.18. DC voltage control: Simulation results with and without magnetic circuit saturation consideration

4.4.4. Impact of the iron losses on the control performance

As it was discussed in 3.4.4, the iron loss consideration does not affect the control performance. In fact, for the scalar control in generator mode, the iron losses have the effect of an additional load. A greater field current is needed as shown in the detail of Figure 4.19.

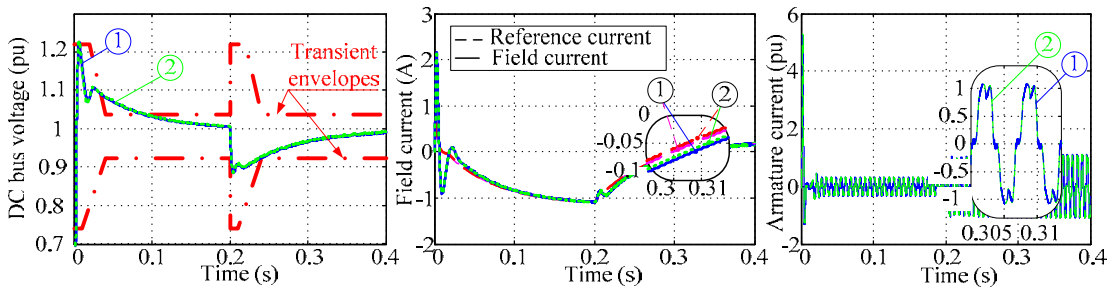

Figure 4.19. DC voltage control: Simulation results when the machine model includes iron losses (1), and without iron losses (2)

4.5. Experiments

4.5.1. Experimental bench

The experimental bench is shown in Figure 4.20. The HESM is coupled to a 2 kW DC motor. Two-quadrant chopper (15 kHz) supplies the DC motor. Four-quadrant chopper (20 kHz) supplies the exciter. A diode bridge rectifier with a 470 µF filtering capacitor is connected to the HESM terminals. The set operates as a DC voltage source and supplies an isolated resistive load. The measurements needed for the control (DC voltage and field current) and the control signal (voltage to be applied to the excitation winding) are driven by the DSpace card (DS1104) to/from the host PC. The DSpace system is directly programmed from a block diagram representation in Matlab/Simulink interface.

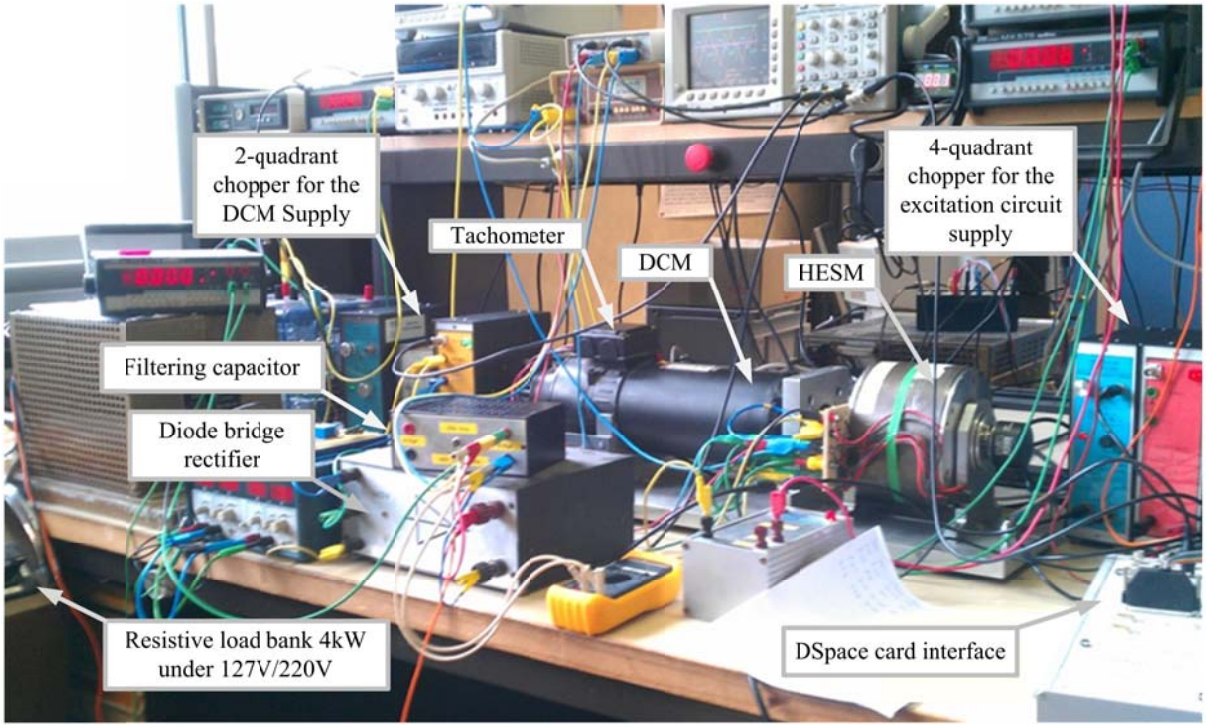

Figure 4.20. HVDC generator: experimental bench

4.5.2. Experimental results

Three experimental tests are carried out: control with load variation, with reference voltage variation and with speed variation. It is to be noted that in the first two tests, the speed varies too since the DCM speed is not regulated. The results are compared to those obtained by simulation under the same conditions.

4.5.2.a. <u>Experimental results under load and speed variation</u>

The test validates the control under load and speed variation. The load goes from 25% up to 83%. The DC motor speed is not controlled during the test and the load variation causes the speed variation too. The experimental results are shown in Figure 4.21. At the test startup, the generator is not controlled and the DC voltage is greater than the reference value. Once the control is activated, the field current goes negative in order to reduce the DC voltage and bring it back to its reference.

The DC voltage remains equal to its reference during the remainder of the test in spite of the load and speed variation. The field current increases in order to counter the speed decrease and the voltage drop due to the increasing load. Finally, Figure 4.21 attests the precise tracking of the field current to its reference generated by the voltage control loop. In addition, it is clearly verified that the measured field current matches the one obtained by simulation.

Figure 4.22 shows the phase voltage waveforms and the corresponding RMS voltage measurements for different load when the generator rotates at Ω_b. Figure 4.23 represents the line current waveform for different loads when the speed is set to Ω_b. The continuous conduction hypothesis made prior to the converter modeling is validated.

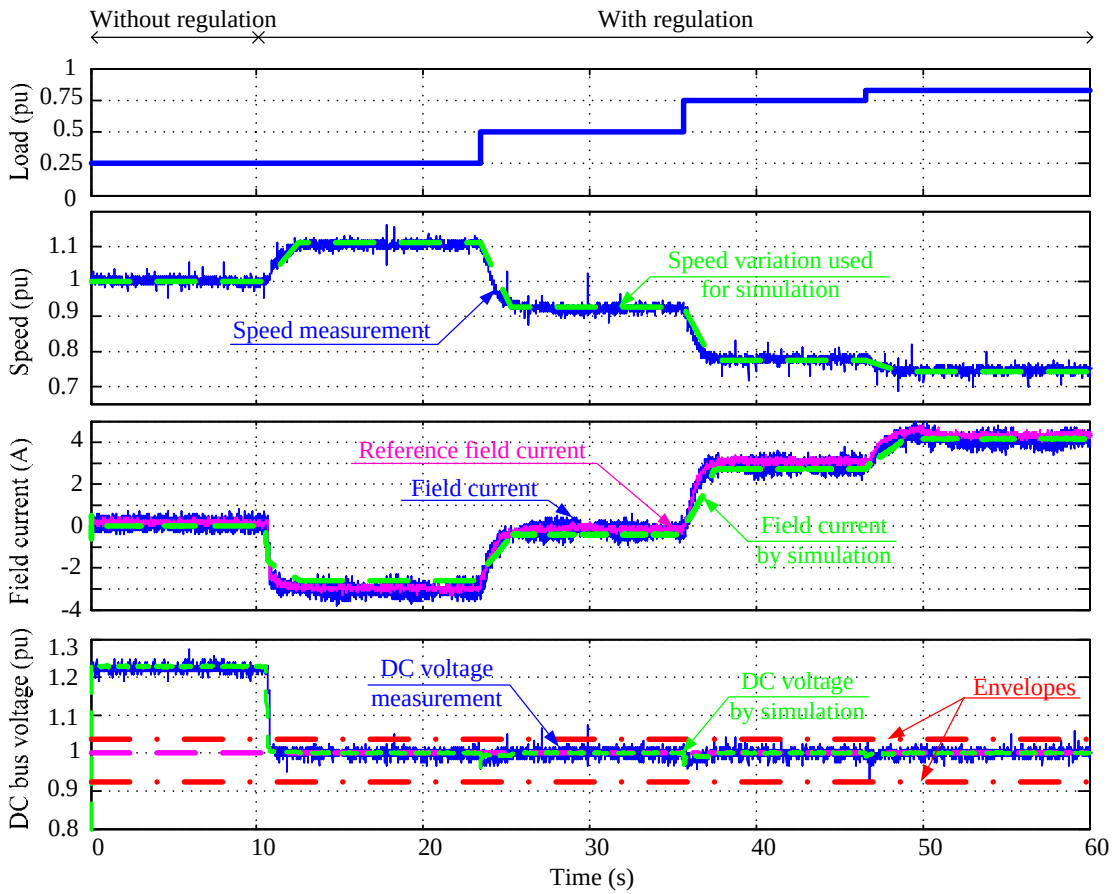

Figure 4.21. DC voltage control: Experimental results under load variation

4.5.2.b. Experimental results under reference voltage and speed variation

The test is done at 75% of the full load. The reference DC voltage is varied by ±15%. The reference voltage variation causes the DCM speed variation. The speed measurements and the experimental results are shown in Figure 4.24. The control is validated: the DC bus voltage tracks its reference and remains within the transient envelopes specified by the MIL-STD-704F. In addition, the experimental results match those obtained by simulation under the same conditions. The field current reacts correctly when the reference is set to 115% causing the speed decrease (by 11%). When the reference is reduced by 15%, the field current decreases in order to reduce the generated DC voltage and counter the speed increase (by 12%).

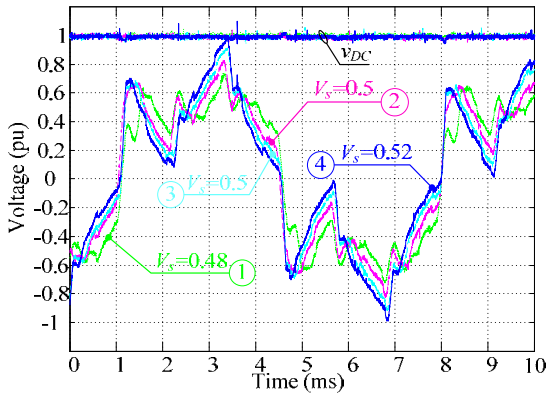

Figure 4.22. Experimental phase voltage for $\Omega = \Omega_b$ at 25% (1), 50% (2), 75% (3), 100% (4) of the full load

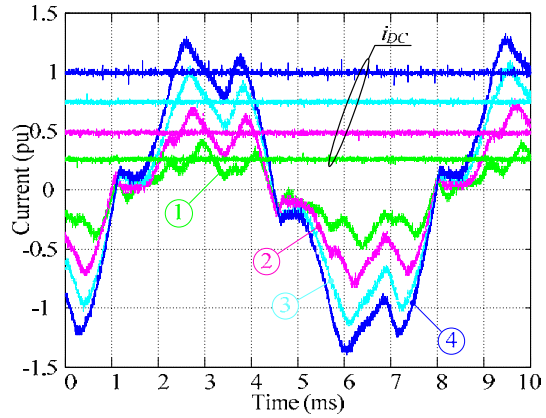

Figure 4.23. Experimental armature current for $\Omega = \Omega_b$ at 25% (1), 50% (2), 75% (3), 100% (4) of the full load

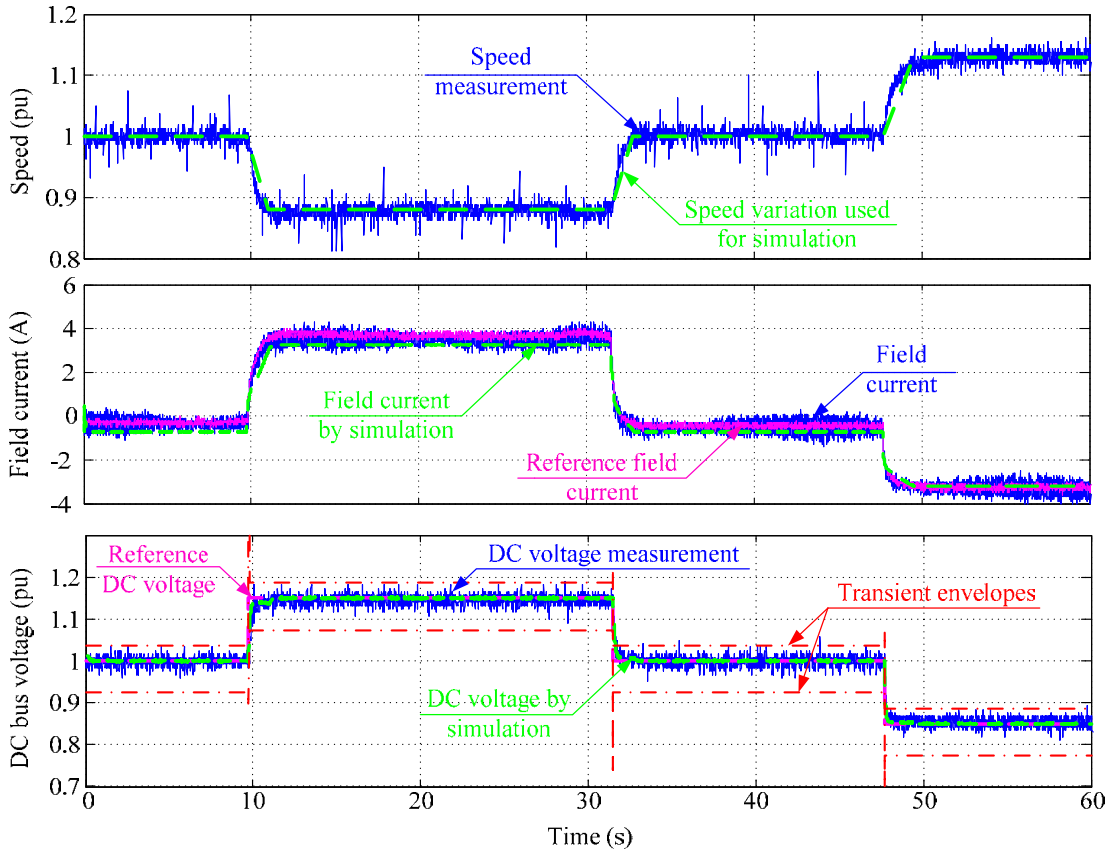

Figure 4.24. DC voltage control: Experimental results under DC bus reference voltage variation

4.5.2.c. Experimental results under speed variation

The test is done at 75% of the full load. It validates the control under speed variation by −20% then +50%. Due to HESM field current limitation, it is not possible to reach the $4\Omega_b$ as in the simulation cycle in 4.4.2. The experimental results are shown in Figure 4.25. The flux weakening capability of the machine is seen clearly at high speed: The field current goes negative in order to maintain the voltage equal to its reference. Conversely, the excitation current increases, as expected, when the speed decreases. The field current measured values comply perfectly with those obtained by simulation and the DC voltage remains within the limits imposed by the MIL-STD-704F.

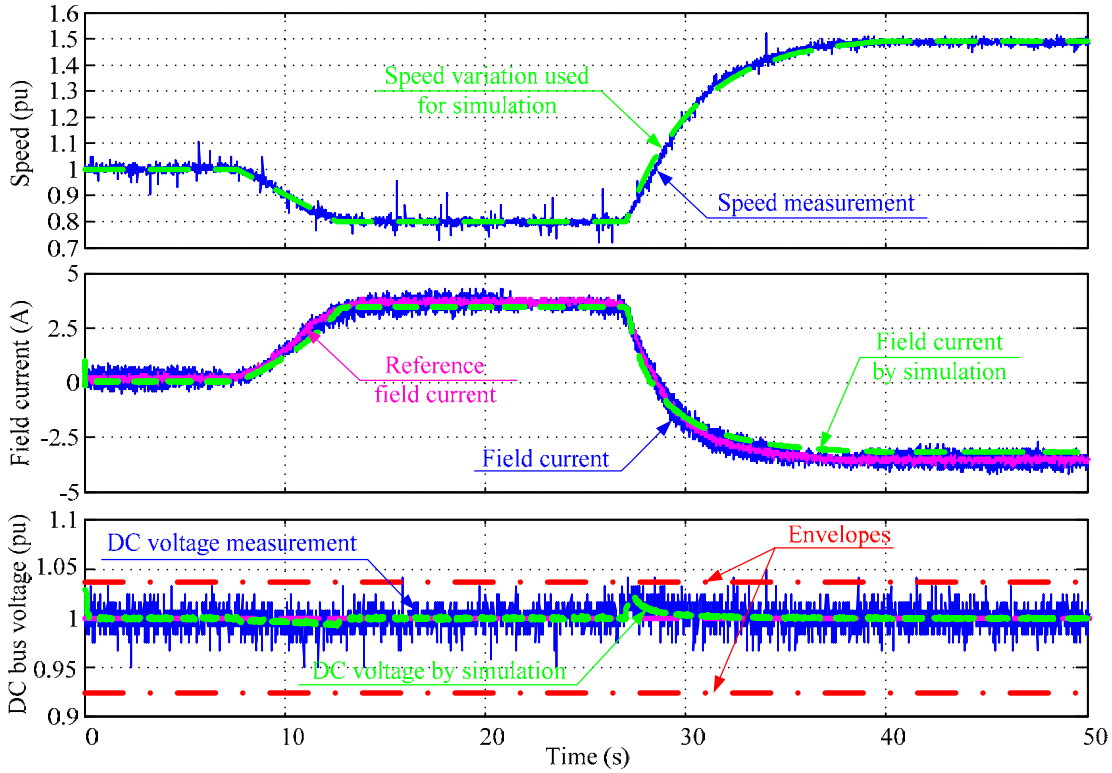

Figure 4.25. DC voltage control: Experimental results under speed variation:

Conclusion

This chapter presents the HESM associated to a diode bridge rectifier to be used as an HVDC generator supplying an isolated load.

The converter is modeled first. The DC bus voltage control is studied next. With one degree of freedom, it consists of only two loops: field current compensation (inner loop) and DC voltage compensation (outer loop). Simulation results prove the capability of the generator to operate correctly under a wide range of load or speed variation (up to 4 times the base speed). The DC bus voltage stays, in both cases equals to its reference.

Experiments are performed on a laboratory prototype HESM as well. The proposed control is validated under load, reference voltage and/or speed variation. The experimental results comply

with those obtained by simulation in spite of the first harmonic machine model and the idealized converter model.

Part III. Hybrid Excitation Synchronous Machine in Motor Mode for Electric Vehicle Application

Introduction of Part III

Electric Vehicle (EV) - State of art

The EV was invented in 1834. However due to the limitations associated with the batteries and the rapid advancement of ICEV, EVs have almost vanished from the scene since 1930. In the early 1970s, environmental impact of the petroleum-based transportation, along with the peak oil price, has led to renewed interest in EVs. After years of development, many advanced technologies are used to extend the driving range and reduce the cost of EV. Still, EV cannot compete yet with the ICEV.

EV is a road vehicle that evolves with electric propulsion. Compared to the ICEV, the configuration of EV is rather flexible since the energy flows in electrical wires instead of rigid mechanical links. In addition, the control of the electric motor can assure operation at different speeds, which means that the gearbox in ICEV can be replaced by a fixed gearing and the clutch can be removed. The weight and size of the mechanical transmission is then reduced [22]. In addition, EV produces no tailpipe emissions, reduces the energy dependency since the electricity is a domestic energy source and is more energy efficient than ICEV in converting its stored energy into power at the wheels. In addition, EV allows regenerative braking. Moreover, electric motors provide quiet, smooth operation and stronger acceleration and require less maintenance than ICEs.

EV includes Battery Electric Vehicle (BEV), Hybrid Electric Vehicle (HEV) and Fuel Cell Electric Vehicle (FCEV). Now and in the near future, batteries have been agreed to be the major energy source for EVs. The main drawback of the BEV is their limited driving range. The HEV has an ICE and an electric motor. The HEV represents a short-term solution since it depends on fossil fuels. The major challenge of HEV is the management of the multiple energy sources. The FCEV is an electrochemical device that converts the free-energy change of an electrochemical reaction. The ideal nonpolluting fuel for the fuel cell is the hydrogen that has the highest energy content per unit of weight. The result of the reaction with oxygen is plain water. FCEVs have the greatest potential to deliver the same range and performance of ICEV [22]. Unlike the BEV, the FCEV generates the electrical energy on-board rather than stores it. The main difficulty consists on producing the hydrogen. Different solutions are presented. The storage of hydrogen under liquid or gas state offers lightweight and fast refueling advantages but suffers from bulky size and safety concerns. The other solution consists of extracting hydrogen from gasoline or methanol using an on-board reformer. Thus, FCEVs are still in development phase.

Today, BEVs, HEVs and FCEVs are in different stage of development regarding mainly their energy sources. However, the improvement of these vehicles relays on a common key subsystem, which is the electrical propulsion. The electric propulsion includes the electric motor, the power converter and electronic controller.

Based on various driving cycles and other considerations, the major requirements of EV motor drive are listed [22]:

- High instant power and high power density;
- High torque at low speed for starting and climbing and high power at high speed for cruising;
- Very wide speed range including constant torque and constant power region;
- Fast torque response;

- High efficiency over wide speed and torque ranges;
- High efficiency for regenerative braking;
- High reliability and robustness for various vehicle operating conditions;
- Reasonable cost.

Figure III.1 represents a sketch of the speed-torque characteristic for EV application.

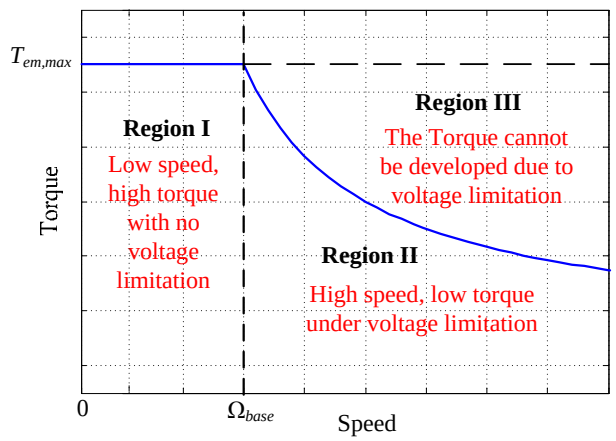

Figure III.1. Speed-torque characteristic

Different machines satisfy most of these requirements and thus can be proposed for EV application [17].

DC motors were first to be used in electric propulsion. Their speed-torque characteristic and their simple control suit well the application. Their drawback is the use of brushes and sliding contacts.

Induction motors are a solution adopted by many manufacturers due to their high reliability and simple construction and control. However, this machine suffers from a low efficiency especially at high speeds.

Switched reluctance motors have the definite advantages of simple construction, low manufacturing cost and suitable torque-speed characteristic [76]. However, their design and control are difficult.

The PM motors are the most used machines in electric propulsion due to their high power density and efficiency, high reliability, low inertia and brushless structure [28]. The limitation of the PM machines is the lack of the field control. Thus, the speed increase in the motor mode is difficult to be realized. To overcome this problem, new machine topologies were investigated. One alternative solution is the HESM [35].

Previous work has proven that HESM provides an efficient energy solution for vehicles propulsion [8]. With its compact size, brushless structure and excitation coil, the HESM is presented as an attractive choice for EV application. The attention is paid to BEV. However, the results might be useful for the other two structures.

Part III organization

Since the drive is powered by a battery source, improvement of the motor efficiency is a most important priority. Part III is divided into two chapters: Chapter 5 consists on elaborating a motor control strategy that minimizes the losses in the HESM (copper losses and iron losses). In Chapter 6, the optimization problem is extended and it includes the electric losses in the complete electric powertrain.

Chapter 5 presents an optimal control of the HESM. The control aims to meet the torque and speed requirements while insuring minimal losses. The main innovating contribution of the work is that it computes analytical expressions for the optimal reference armature currents (i_{sd} and i_{sq}) as well as for the field current i_f with respect to armature current and voltage constraints. ELMM, explained briefly in Appendix A, is used to find the optimal three reference current expressions that minimize the losses in the machine for a given operating point (defined by its torque and speed), without violating current and voltage constraints. Simulation with Matlab and Matlab/Simulink software proves that the analytical solution yields indeed to the current combination that guarantees the minimal losses over the NEDC.

To assure a good autonomy distance range in pure electric (zero emission) operating mode, the losses in the entire electric propulsion system have to be minimized. In Chapter 6, the optimization problem is extended and it includes the inverter and chopper losses as well. The battery, inverter and chopper are modeled at first. The converters model includes their respective losses. In this chapter too, the ELMM is used to solve the minimization problem. The analytical expressions of the optimal currents are found. Simulation with Matlab software proves that the currents obtained by these expressions are indeed the optimal currents for every operating point.

Chapter 5. Hybrid Excitation Synchronous Motor Optimal Control

Introduction

For HESM, the same torque can be produced by a variety of currents due to nonlinear relationship between torque and currents. Consequently, appropriate determination of a set of stator currents and field current plays a key role to achieve energy efficient and wide speed range operation. This chapter presents an optimal current control for the hybrid excitation synchronous motor using ELMM in order to minimize the machine losses.

In the early nineties, the ELMM was combined to other techniques, such as gradient method, Vector Optimization Problem (VOP) and FE calculations, in order to find the most appropriate design for a machine, in particular PM machines [107] [108] [134]. Iterative search was used to find the best multiplier values. With the advent of computational tools, the machine design problem becomes more challenging and involves huge number of parameters and criteria. Therefore, stochastic methods, like Genetic Algorithm (GA), Simulated Annealing (SA), combined with FEA are preferred and used to find the optimal machine design based on the multi-objective criteria. Nevertheless, ELMM remains the most adequate tool when dealing with constrained optimization problems. It is applied in different domains [24] [27] [33][36] [113] [128]. It is often associated to other techniques, such as Particle Swarm Optimization (PSO) [121], neural network [45] [98] or FEA [60].

Concerning the machine control, few attempts used ELMM to find optimal references when controlling the plant [14] [52]. Mathematical methods, such as Newton method [51], are commonly applied to obtain the numerical solutions. No analytical solution is usually formulated.

In this chapter, the ELMM is used to elaborate analytical expressions for the optimal reference armature currents as well as for the field current with respect to armature current and voltage constraints. In addition, Lagrange multipliers are part of the optimization problem. They are not found by iterative search process. The chapter is organized as follows. The common PM motor control techniques are recalled briefly in the state of art in section 5.1. The adopted control strategy

is detailed next (section 5.2). The control aims in a first place to meet the torque and speed requirements. The field-oriented control is used. The approach takes into account the machine's saliency, i.e. $i_{sd} = 0$ A is not a solution anymore. Classic current and speed compensators are used with optimal reference currents. The optimization criterion is the minimization of the electric losses in the machine. The copper loss minimization is considered at first in section 5.3. Secondly, the iron losses are added to the optimization problem in section 5.4. Regenerating braking is taken into account. By using Matlab software, it is proven that the proposed optimal control leads to the lowest losses compared to the results obtained by other synchronous motor control strategies over the NEDC. The proposed optimization method is validated by simulation in section 5.6.

5.1. Synchronous machine control - State of art

Two major PM motor control techniques are proposed in the literature: the current vector control, also called field-oriented control, and the Direct Torque Control (DTC). In a DTC structure, the torque and the flux are controlled directly via the armature voltage vector applied to the voltage source inverter [100]. DTC does not require mechanical sensors or current compensators in a rotating coordinate system [82] [143]. However, DTC suffers from high electromagnetic torque and current ripples, its steady state performance is poor and the inverter has variable switching frequency [53] [58].

Therefore, the field-oriented control is preferred and commonly used for PM motor in EV applications [26]. In vector control strategy, when the motor speed is below the base speed, Maximum Torque Per Ampere (MTPA) technique is often used. Under this condition, copper losses are minimized [44] [50] [64] [93] [137]. In a surface PM motor, MTPA is accomplished by keeping the d-axis armature current component equal to zero. In an interior PM motor, both d and q-axis components of armature current contribute to the developed torque. These currents are controlled according to torque-current nonlinear relationships obtained by solving (5.1) and recalled in (5.2) and (5.3) [52] [118] [119] [137] (point A in Figure 5.1).

$$\begin{cases} \dfrac{\partial\left(T_{em}/i_s\right)}{\partial i_{sd}} = 0 \\ \dfrac{\partial\left(T_{em}/i_s\right)}{\partial i_{sq}} = 0 \end{cases} \tag{5.1}$$

$$T_{em} = \frac{3}{2} p \sqrt{i_{sd}^{\ 2} - \frac{\phi_{exc} i_{sd}}{\left(L_{sq} - L_{sd}\right)}} \left(\phi_{exc} + i_{sd}\left(L_{sd} - L_{sq}\right)\right) \tag{5.2}$$

$$i_{sd} = \frac{\phi_{exc}}{2\left(L_{sq} - L_{sd}\right)} - \sqrt{\frac{\phi_{exc}^{\ 2}}{4\left(L_{sq} - L_{sd}\right)^2} + i_{sq}^{\ 2}} \tag{5.3}$$

When the speed exceeds the base speed, MTPA method cannot always satisfy the torque and speed requirements [94]. Thus, flux weakening control is proposed [1] [49]. The flux control is typically accomplished by acting on the d-axis armature current component as given in (5.4) and (5.5) [26] [118].

$$T_{em} = \frac{3}{2} p \left(\phi_{exc} \frac{L_{sq}}{L_{sd}} + \left(L_{sd} - L_{sq}\right) \sqrt{2\left(\frac{V_s}{L_{sd}\, p\Omega}\right)^2 - \left(\frac{L_{sq}}{L_{sd}}\right)^2 i_{sq}^{\ 2}} \right) i_{sq} \tag{5.4}$$

$$i_{sd} = \frac{-\phi_{exc}}{L_{sd}} + \sqrt{2\left(\frac{V_s}{L_{sd}\, p\Omega}\right)^2 - \left(\frac{L_{sq}}{L_{sd}}\right)^2 i_{sq}^{\ 2}} \tag{5.5}$$

Flux weakening control generates significant increase in copper losses, it involves also the risk of irreversible demagnetization of the PMs, and consequently a reduction in the machine efficiency since the torque capability of the machine is permanently diminished.

Thus, the common optimal synchronous motor control consists of developing a method that switches between the MTPA and the flux weakening conditions depending on the speed and torque status [19] [145]. This strategy is illustrated in Figure 5.1 [114] [137]. When the rotor electrical speed increases from ω_b to ω_c at constant torque, T_{em2} cannot be produced using the MTPA laws. The operating point slides from B to C along the constant torque curve. On the other hand, when the voltage limit is reached for a given speed (point B), a greater torque cannot be produced using the MTPA current equations. Operating point D can be attained by sliding from B along the voltage limit ellipse when ω_s equals ω_c. T_{em4} is the highest torque that can be reached for speeds equal or below ω_a (point E).

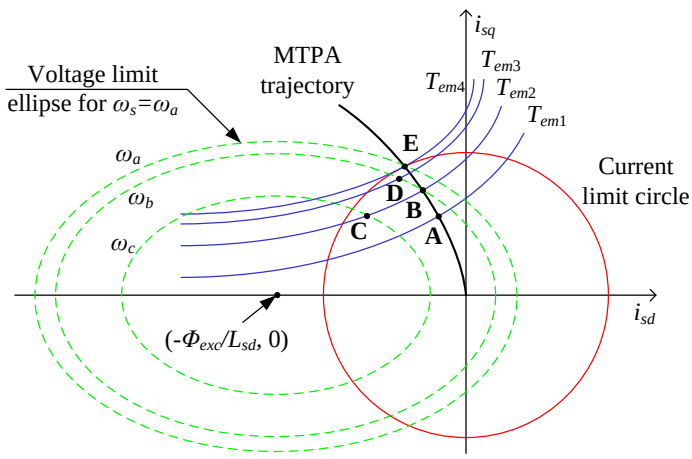

Figure 5.1. Interior PM motor control under voltage and current limits: $T_{em1} < T_{em2} < T_{em3} < T_{em4}$ and $\omega_a < \omega_b < \omega_c$

Compared to the PM motor, the HESM presents an additional control variable [35]: the field current. Hence, the optimal control of the HESM involves three current compensators.

The control of the HESM minimizing the motor copper losses for EV application has been treated [116] [117]. However, no saliency was considered. In addition, the reference currents, i_{sq} and i_f in this case, which lead to minimal copper losses were found using software recursive algorithm.

5.2. HESM vector control

The control aims in a first place to track a reference speed (generated by the driving cycle for example) in spite of the load torque variation. With three currents to be regulated, it is possible to achieve an additional objective. In the present study, loss minimization is considered. The control is performed through hierarchical loops. The outer loop is a speed control loop that generates the torque control reference. The inner loops compensate the armature and field currents.

5.2.1. Current control loops

The armature currents are controlled in a synchronous rotating reference frame. The q-axis armature current compensator is detailed. The d-axis armature current component compensator is synthesized in a similar manner. Equation (1.12) is recalled.

$$v_{sq} = R_s i_{sq} + L_{sq}\frac{di_{sq}}{dt} + p\Omega\left(L_{sd} i_{sd} + \Phi_M + M_{sf} i_f\right) = R_s i_{sq} + L_{sq}\frac{di_{sq}}{dt} + e_{sq} \tag{5.6}$$

The current control loop is depicted in Figure 5.2. The q-axis current is driven by the q-axis voltage component. Since the current dynamic is much faster than the mechanical dynamic, the speed is regarded as constant when designing current controllers. $\hat{e}_{sq}$ is a decoupling voltage that can be estimated. τ_{sq} is the time constant of the q-axis equivalent circuit. The current compensator is synthesis in order to satisfy the following specifications:

- Zero steady state error;
- The settling time of the closed-loop is less than the half of the open-loop settling time. Numerically, the closed-loop settling time is equal to 0.005 s.

A PI controller is enough to meet these requirements.

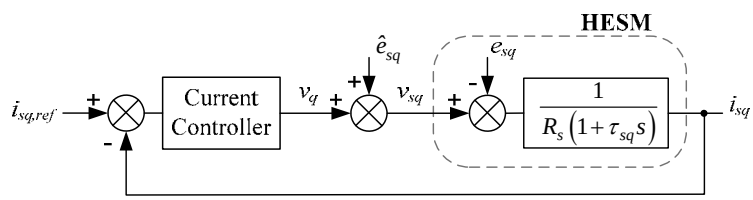

Figure 5.2. q-axis current control loop

The field current is controlled by a feedback current independent loop as detailed in paragraph 3.2.1.

5.2.2. Speed control loop

Equation (1.17) is used to model the mechanical part of the motor; it is recalled in (5.7). The load torque is regarded as a disturbance to the plant. The speed is driven by the electromagnetic torque as shown in the transfer function (5.8). τ_m is the mechanical time constant.

$$J\frac{d\Omega}{dt} = T_{em} - f_v\Omega - T_{f0} - T_l \tag{5.7}$$

$$\Omega = \frac{1}{f_v\left(1+\tau_m s\right)}T_{em} \tag{5.8}$$

On the other hand, referring to the phasor diagram in Figure 5.3, the direct and quadrature axis armature current components are expressed in terms of the angle ψ and the stator current magnitude (5.9). The electromagnetic torque expression is then reformulated (5.10).

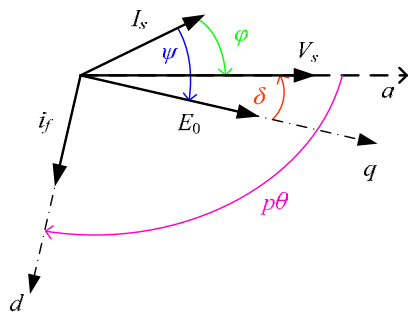

Figure 5.3. Phasor diagram

$$i_{sd} = \sqrt{2} I_s \sin\psi \qquad i_{sq} = \sqrt{2} I_s \cos\psi \tag{5.9}$$

$$T_{em} = \frac{3}{2} p \left(\phi_{exc} \sqrt{2} I_s \cos\psi + \left(L_{sd} - L_{sq} \right) I_s^{\,2} \sin 2\psi \right) \tag{5.10}$$

The maximum hybrid torque is obtained when $\psi_h = 0$ rad, this is equivalent to $i_{sd} = 0$ A control law used in non-salient PM motor. The reluctance torque reaches its maximum for $\psi_r = -\pi/4$. Computing $\frac{\partial T_{em}}{\partial \psi} = 0$ yields to the current phase angle that gives maximum torque for a constant excitation flux (given by (5.11)) [88]. This angle varies between ψ_r and ψ_h.

$$\psi = -\sin^{-1}\left(\frac{-\phi_{exc} + \sqrt{\phi_{exc}^{\,2} + 16\left(L_{sd} - L_{sq}\right)^2 I_s^{\,2}}}{4\sqrt{2}\left(L_{sd} - L_{sq}\right) I_s} \right) \tag{5.11}$$

A schematic speed control bloc diagram is shown in Figure 5.4. The speed controller, Proportional Integral Derivative (PID), is designed in order to meet the following specifications:

- Zero steady state error;
- Settling time at least ten times greater than the currents settling time in order to assure the separation between the electrical and mechanical modes;
- Limited torque control reference.

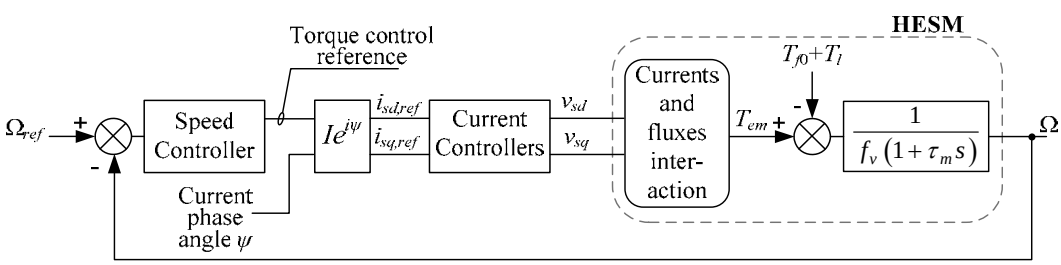

Figure 5.4. Speed control bloc diagram

5.2.3. Hierarchical loop control

5.2.3.a. Vector control bloc diagram

Figure 5.5 shows the system configuration for controlling the HESM in motor mode. The reference currents can be generated by any control strategy or optimization algorithm. In this study, ELMM is adopted. The optimal d-q axis current references define the optimal current phase angle ψ^*. The current compensators drive the inverter and chopper in order to regulate the machine armature voltage and excitation voltage respectively.

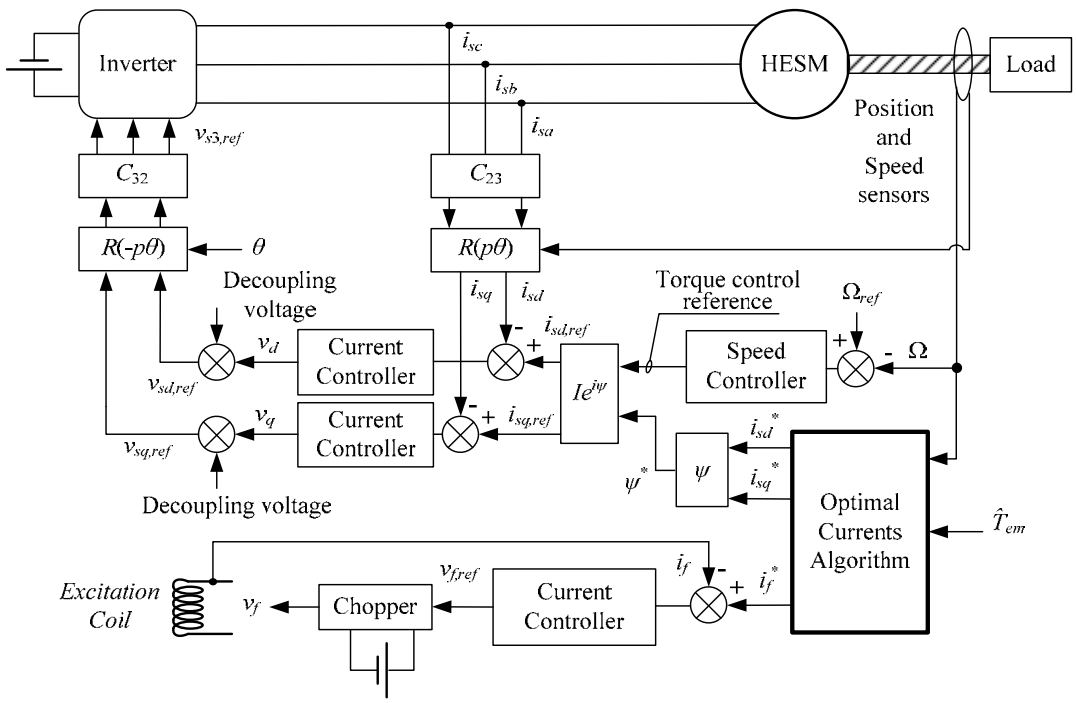

Figure 5.5. Vector control bloc diagram of the hybrid excitation synchronous motor

5.2.3.b. Impact of the iron loss on the control strategy

Iron losses have a significant effect on the synchronous machine vector control. They introduce an additional coupling mechanism to the *d* and *q* circuits. A shifting angle is generated between the induced currents and the actual currents in the armature windings. The shunting resistor R_{ir} will share the input armature current. Hence, the physical stator currents are no longer the currents that directly govern the electromagnetic torque [110] [138] [139]. On other hand, the optimization algorithm generates ideally the reference air gap current components, i.e. $i_{sd1,ref}$ and $i_{sq1,ref}$. These currents cannot be directly measured. To overcome this problem, a vector control with decoupling terms is proposed.

The effect of the iron loss introduction on the q-axis current control loop is studied below. The same approach is implemented on the d-axis current control. Figure 5.6 represents the q-axis equivalent circuit. In presence of iron losses, the q-axis armature voltage component is given by (5.12). Comparing to the current control loop without iron loss consideration, an additional coupling term $\left(R_s/R_{ir}\right)v_{sq1}$ has to be considered.

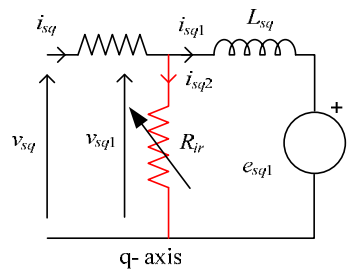

Figure 5.6. HESM dynamic q-axis equivalent circuit

$$v_{sq} = R_s\left(i_{sq1} + \frac{v_{sq1}}{R_{ir}}\right) + L_{sq}\frac{di_{sq1}}{dt} + \underbrace{p\Omega\left(L_{sd}i_{sd1} + \Phi_M + M_{sf}i_f\right)}_{e_{sq1}} \tag{5.12}$$

v_{sq1} and i_{sq1} are estimated in terms of the armature voltage and the armature current given the iron losses equivalent variable resistance as shown in (5.13) and (5.14). It is recalled that R_{ir} varies according to speed, field current and/or armature voltage variation.

$$\hat{v}_{sq1} = v_{sq} - R_s i_{sq} \tag{5.13}$$

$$\hat{i}_{sq1} = \frac{\left(i_{sq}\left(R_s + R_{ir}\right) - v_{sq}\right)}{R_{ir}} \tag{5.14}$$

The modified current loop control is shown in Figure 5.7.

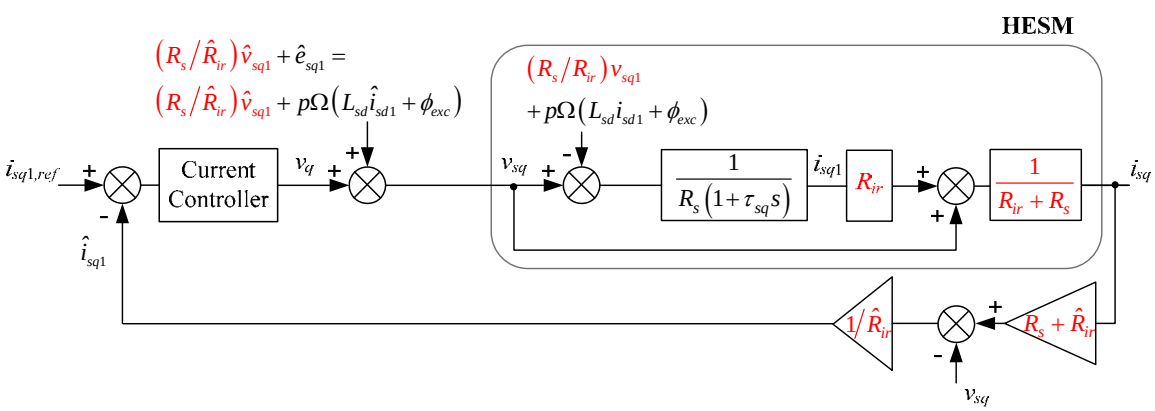

Figure 5.7. q-axis current control loop with decoupling terms

Taking into account the iron loss impact on the vector control scheme improves theoretically the control efficiency. However, it is pointed that the control becomes more complex. In addition, for a real optimal compensation, an accurate estimation of the iron losses equivalent resistance and the d-q axis air gap current components is required, which may be a problem in itself.

The simulation results obtained with and without decoupling terms are compared in paragraph 5.6.2. As it will be shown, in spite of the presence of the shunting resistor, the machine internal currents are practically directly driven by the armature voltages.

5.3. Hybrid excitation synchronous motor control with minimum copper losses

Most of the optimal motor control methods presented in the literature consider copper loss minimization. Copper losses are the major source of losses in a PM machine. With a proper current control, these losses can be significantly reduced. However, in the commonly used methods, in particular MTPA, copper loss minimization is performed below the base speed only. In this study, ELMM is used in an attempt to minimize the copper losses over the entire speed range.

5.3.1. Optimal reference currents with minimum copper losses

The ELMM, explained in Appendix A, is adopted in order to compute the optimal reference currents.

5.3.1.a. Problem Formulation

The function to minimize is the copper loss expression in terms of the machine currents.

$$f(\boldsymbol{x}) = P_{Copper} = \frac{3}{2} R_s \left(i_{sd}^{\ 2} + i_{sq}^{\ 2} \right) + R_f i_f^{\ 2} \tag{5.15}$$

One equality constraint exists; it is given by the electromagnetic torque equation.

$$h(\boldsymbol{x}) = \left(\left(L_{sd} - L_{sq} \right) i_{sd} + M_{sf} i_f + \Phi_M \right) i_{sq} - K_{em} = 0 \tag{5.16}$$

With $K_{em} = \dfrac{2}{3p} T_{em}$.

The feasible operation range is constrained by the following inequalities. The first one, $g_I(\boldsymbol{x})$, is set by the armature phase current limit and the second one $g_V(\boldsymbol{x})$ is the limit of the inverter output voltage.

$$g_I(\boldsymbol{x}) = \left(i_{sd}^{\ 2} + i_{sq}^{\ 2} \right) - 2 I_{s\max}^{\ 2} \le 0 \tag{5.17}$$

$$g_V(\boldsymbol{x}) = \left(v_{sd}^{\ 2} + v_{sq}^{\ 2} \right) - 2 V_{s\max}^{\ 2} \le 0 \tag{5.18}$$

The armature voltages at steady state are given by (5.19) and (5.20)

$$v_{sd} = R_s i_{sd} - p\Omega L_{sq} i_{sq} \tag{5.19}$$

$$v_{sq} = R_s i_{sq} + p\Omega \left(L_{sd} i_{sd} + M_{sf} i_f + \Phi_M \right) \tag{5.20}$$

However, the resistance voltage drop is negligible compared to the back EMF at high speed i.e. when the voltage constraint is active. Equation (5.18) is then simplified.

$$g_V(\boldsymbol{x}) = \left(\left(L_{sq} i_{sq} \right)^2 + \left(L_{sd} i_{sd} + M_{sf} i_f + \Phi_M \right)^2 \right) - 2 \left(\frac{V_{s\max}}{p\Omega} \right)^2 \le 0 \tag{5.21}$$

g_I and g_V define the voltage and current limits represented in Figure 5.1. If the motor presents no saliency, the voltage ellipse limit turns into a circle.

The variable vector is $\boldsymbol{x} = \begin{bmatrix} i_{sd} & i_{sq} & i_f \end{bmatrix}$. The reference current vector solution of the optimization problem is noted $\boldsymbol{x}^* = \begin{bmatrix} i_{sd}^* & i_{sq}^* & i_f^* \end{bmatrix}$.

As explained in Appendix A, four cases are to be considered: voltage constraint and/or current constraint are active and none of the constraints is active. Each case is a standalone problem and leads to different three analytical reference current expressions. The optimization algorithm generates optimal reference currents. The current transients are imposed by the controllers.

5.3.1.b. <u>Optimal reference currents with active voltage and current constraints</u>

The optimization problem is formulated as in (5.22).

μ_V is the voltage constraint multiplier. μ_I is the current constraint multiplier.

$$\begin{aligned}
&1.\ \mu_{V2} > 0 \text{ and } \mu_{I2} > 0 \\
&2.\ \nabla l(\boldsymbol{x},\lambda,\boldsymbol{\mu}) = \nabla f(\boldsymbol{x}) + \lambda \nabla h(\boldsymbol{x}) + \mu_{V2} \nabla g_V(\boldsymbol{x}) + \mu_{I2} \nabla g_I(\boldsymbol{x}) = 0 \\
&\quad h(\boldsymbol{x}) = 0 \\
&3.\ g_V(\boldsymbol{x}) = 0 \text{ and } g_I(\boldsymbol{x}) = 0 \\
&4.\ \boldsymbol{y}^T \nabla^2 l(\boldsymbol{x},\lambda,\boldsymbol{\mu}) \boldsymbol{y} > 0 \quad \forall \boldsymbol{y} \neq 0 \ \Big| \ \begin{cases} \nabla h(\boldsymbol{x}) \boldsymbol{y} = 0 \\ \nabla g_V(\boldsymbol{x}) \boldsymbol{y} = 0 \\ \nabla g_I(\boldsymbol{x}) \boldsymbol{y} = 0 \end{cases}
\end{aligned} \tag{5.22}$$

The gradient of Lagrange function is given by (5.23).

$$\begin{aligned}
\nabla l(\boldsymbol{x},\lambda,\boldsymbol{\mu}) = &\begin{bmatrix} 3R_s i_{sd} \\ 3R_s i_{sq} \\ 2R_f i_f \end{bmatrix} + \lambda \begin{bmatrix} L_{sdq} i_{sq} \\ L_{sdq} i_{sd} + M_{sf} i_f + \Phi_M \\ M_{sf} i_{sq} \end{bmatrix} + \mu_{I2} \begin{bmatrix} 2i_{sd} \\ 2i_{sq} \\ 0 \end{bmatrix} \\
&+ \mu_{V2} \begin{bmatrix} 2L_{sd}\left(L_{sd} i_{sd} + M_{sf} i_f + \Phi_M\right) \\ 2L_{sq}{}^2 i_{sq} \\ 2M_{sf}\left(L_{sd} i_{sd} + M_{sf} i_f + \Phi_M\right) \end{bmatrix}
\end{aligned} \tag{5.23}$$

With $L_{sdq} = L_{sd} - L_{sq}$.

Setting $\nabla l(\boldsymbol{x},\lambda,\boldsymbol{\mu}) = 0$ and given $h(\boldsymbol{x}) = 0$, $g_V(\boldsymbol{x}) = 0$, $g_I(\boldsymbol{x}) = 0$ yields to equations (5.24) to (5.29) with six variables.

$$3R_s i_{sd} + \lambda L_{sdq} i_{sq} + 2\mu_{V2} L_{sd}\left(L_{sd} i_{sd} + M_{sf} i_f + \Phi_M\right) + 2\mu_{I2} i_{sd} = 0 \tag{5.24}$$

$$3R_s i_{sq} + \lambda\left(L_{sdq} i_{sd} + M_{sf} i_f + \Phi_M\right) + 2\mu_{V2} L_{sq}{}^2 i_{sq} + 2\mu_{I2} i_{sq} = 0 \tag{5.25}$$

$$2R_f i_f + \lambda M_{sf} i_{sq} + 2\mu_{V2} M_{sf}\left(L_{sd} i_{sd} + M_{sf} i_f + \Phi_M\right) = 0 \tag{5.26}$$

$$\left(L_{sdq} i_{sd} + M_{sf} i_f + \Phi_M\right) i_{sq} - K_{em} = 0 \tag{5.27}$$

$$\left(\left(L_{sq}i_{sq}\right)^2+\left(L_{sd}i_{sd}+M_{sf}i_f+\Phi_M\right)^2\right)-2\left(\frac{V_{s\max}}{p\Omega}\right)^2=0 \tag{5.28}$$

$$\left(i_{sd}{}^2+i_{sq}{}^2\right)-2I_{s\max}{}^2=0 \tag{5.29}$$

Equations (5.27), (5.28) and (5.29) yield to (5.30).

$$2\left(L_{sq}{}^2I_{s\,max}{}^2-\left(\frac{V_{s\,max}}{p\Omega}\right)^2\right)i_{sq}{}^2-2K_{em}L_{sq}i_{sq}\sqrt{2I_{s\,max}{}^2-i_{sq}{}^2}+K_{em}{}^2=0 \tag{5.30}$$

Equation (5.30) has four roots given in (5.31).

$$i_{sq}=\pm\frac{K_{em}}{\sqrt{2}}\frac{\left(\left(\frac{V_{s\,max}}{p\Omega}\right)^2+L_{sq}{}^2I_{s\,max}{}^2\pm L_{sq}\sqrt{4I_{s\,max}{}^2\left(\frac{V_{s\,max}}{p\Omega}\right)^2-K_{em}{}^2}\right)^{1/2}}{\left(L_{sq}{}^2K_{em}{}^2+\left(L_{sq}{}^2I_{s\,max}{}^2-\left(\frac{V_{s\,max}}{p\Omega}\right)^2\right)^2\right)^{1/2}} \tag{5.31}$$

The quantity $\left(4I_{s\,max}{}^2\left(\frac{V_{s\,max}}{p\Omega}\right)^2-K_{em}{}^2\right)$ is proven positive using the electric and mechanical power expressions.

In addition, by rising to the power two (5.32), the inequality is verified.

$$\left(\frac{V_{s\,max}}{\omega_s}\right)^2+L_{sq}{}^2I_{s\,max}{}^2>L_{sq}\sqrt{4I_{s\,max}{}^2\left(\frac{V_{s\,max}}{p\Omega}\right)^2-K_{em}{}^2}\qquad\forall K_{em} \tag{5.32}$$

Thus, the four roots given by (5.31) are real. Two solutions are positive. The one corresponding to the smallest current is retained. The reference q-axis armature current, noted $i_{sq}{}^*$, is given in (5.33). It is positive when the electromagnetic torque is positive and turns negative in regenerative braking case. The two other reference currents, Lagrange multiplier and Kuhn-Tucker multipliers are computed given (5.24) to (5.29) and $i_{sq}{}^*$. It is pointed that since the relative magnetic permeability of the PMs is close to one, the magnetic reluctance in d-axis is considerably small compared to the magnetic reluctance in q-axis. Consequently, the motor presents inverse saliency ($L_{sdq}=L_{sd}-L_{sq}<0$) and the reference direct axis armature current, noted $i_{sd}{}^*$, is necessarily negative.

$$i_{sq}{}^*=\frac{K_{em}}{L_{sq}\sqrt{\frac{2}{L^2}\left(\frac{V_{s\,max}}{Lp\Omega}\right)^2+2I_{s\,max}{}^2+2\sqrt{\frac{4I_{s\,max}{}^2}{L^2}\left(\frac{V_{s\,max}}{p\Omega}\right)^2-\frac{K_{em}{}^2}{L_{sq}{}^2}}}} \tag{5.33}$$

$$i_{sd}{}^*=-\sqrt{2I_{s\,max}{}^2-i_{sq}{}^{*2}} \tag{5.34}$$

$$i_f^* = \frac{\left(K_{em} - L_{sdq} i_{sd}^* i_{sq}^* - \Phi_M i_{sq}^*\right)}{M_{sf} i_{sq}^*} \tag{5.35}$$

$$\mu_{V2}^* = \frac{R_f \left(K_{em} - L_{sdq} i_{sd}^* i_{sq}^* - \Phi_M i_{sq}^*\right)\left(L_{sdq} i_{sq}^{*3} - K_{em} i_{sd}^*\right)}{M_{sf}^2 K_{em}\left(L_{sq} i_{sq}^{*3} + L_{sq} i_{sd}^{*2} i_{sq}^* + K_{em} i_{sd}^*\right)} \tag{5.36}$$

$$\lambda^* = \frac{-2\mu_{V2}^* i_{sq}^* \left(L_{sd} K_{em} + L_{sq} L_{sdq} i_{sd}^* i_{sq}^*\right)}{\left(L_{sdq} i_{sq}^{*3} - K_{em} i_{sd}^*\right)} \tag{5.37}$$

$$\mu_{I2}^* = \frac{\left(-3R_s + 2\mu_{V2}^* L_{sq}^2\right) i_{sq}^{*2} - \lambda^* K_{em}}{2 i_{sq}^{*2}} \tag{5.38}$$

The final step is to verify the second order necessary and sufficient condition of Theorem A.3. This condition is verified as shown in (5.39).

$$\begin{aligned} \boldsymbol{y}^T \nabla^2 l\left(\boldsymbol{x}^*, \lambda^*, \boldsymbol{\mu}^*\right) \boldsymbol{y} \quad &= \left(3R_s + 2\mu_{I2}^*\right) y_1^2 + 2R_f y_3^2 + 2\mu_{V2}^* \left(y_1 L_{sd} + M_{sf} y_3\right)^2 \\ &+ 3y_2^2 \left(3R_s + 2\mu_{I2}^* + 2\mu_{V2}^* L_{sq}^2\right) > 0 \end{aligned} \quad \Big| \ \forall \boldsymbol{y} \neq 0 \tag{5.39}$$

5.3.1.c. <u>Optimal reference currents with active current constraint</u>

When the voltage constraint is inactive, μ_V is set to zero. $\nabla l\left(\boldsymbol{x}, \lambda, \boldsymbol{\mu}\right) = 0$, $h(\boldsymbol{x}) = 0$ and $g_I(\boldsymbol{x}) = 0$ yields to equations (5.40) to (5.44).

$$3R_s i_{sd} + \lambda L_{sdq} i_{sq} + 2\mu_{I1} i_{sd} = 0 \tag{5.40}$$

$$3R_s i_{sq} + \lambda\left(L_{sdq} i_{sd} + M_{sf} i_f + \Phi_M\right) + 2\mu_{I1} i_{sq} = 0 \tag{5.41}$$

$$2R_f i_f + \lambda M_{sf} i_{sq} = 0 \tag{5.42}$$

$$\left(L_{sdq} i_{sd} + M_{sf} i_f + \Phi_M\right) i_{sq} - K_{em} = 0 \tag{5.43}$$

$$\left(i_{sd}^2 + i_{sq}^2\right) - 2I_{s\max}^2 = 0 \tag{5.44}$$

This system yields to (5.45).

$$\frac{L_{sdq}^2}{K_{em}^2} i_{sq}^6 + i_{sq}^2 - 2I_{s\,max}^2 = 0 \tag{5.45}$$

Let $u = i_{sq}^2$. Equation (5.45) becomes a third order polynomial of *u*. Calculations prove that this polynomial has only one real root and it is positive. i_{sq}^*, given by (5.46), is its square root. It is noted that i_{sq}^* has the same sign as the electromagnetic torque.

$$i_{sq}{}^{*}=\left(\frac{K_{em}I_{s\,max}}{L_{sdq}}\right)^{1/3}\sqrt{\left(1+\sqrt{1+\frac{K_{em}{}^{2}}{27L_{sdq}{}^{2}I_{s\,max}{}^{4}}}\right)^{1/3}+\left(1-\sqrt{1+\frac{K_{em}{}^{2}}{27L_{sdq}{}^{2}I_{s\,max}{}^{4}}}\right)^{1/3}} \tag{5.46}$$

The expressions of the other currents and the multipliers are derived from (5.40) to (5.44) given (5.46).

$$i_{sd}{}^{*}=\frac{L_{sdq}}{K_{em}}i_{sq}{}^{*3} \tag{5.47}$$

$$i_{f}{}^{*}=\frac{\left(K_{em}-L_{sdq}i_{sd}{}^{*}i_{sq}{}^{*}-\Phi_{M}i_{sq}{}^{*}\right)}{M_{sf}i_{sq}{}^{*}} \tag{5.48}$$

$$\lambda^{*}=\frac{-2R_{f}i_{f}{}^{*}}{M_{sf}i_{sq}{}^{*}} \tag{5.49}$$

$$\mu_{I1}{}^{*}=-\frac{\lambda^{*}L_{sdq}}{2i_{sq}{}^{*2}}-\frac{3R_{s}}{2} \tag{5.50}$$

The second order necessary and sufficient condition is verified in (5.51).

$$\boldsymbol{y}^{T}\nabla^{2}l\left(\boldsymbol{x}^{*},\lambda^{*},\mu_{I1}{}^{*}\right)\boldsymbol{y}=\left(3R_{s}+2\mu_{I1}{}^{*}\right)y_{1}{}^{2}+2R_{f}y_{3}{}^{2}+y_{2}{}^{2}\left(9R_{s}+6\mu_{I1}{}^{*}\right)>0\ \mid\ \forall\boldsymbol{y}\neq 0 \tag{5.51}$$

5.3.1.d. <u>Optimal reference currents with active voltage constraint</u>

When the current constraint is inactive, μ_I is set to zero. $\nabla l\left(\boldsymbol{x},\lambda,\boldsymbol{\mu}\right)=0$, $h(\boldsymbol{x})=0$ and $g_V(\boldsymbol{x})=0$ yields to equations (5.52) to (5.56).

$$3R_{s}i_{sd}+\lambda L_{sdq}i_{sq}+2\mu_{V1}L_{sd}\left(L_{sd}i_{sd}+M_{sf}i_{f}+\Phi_{M}\right)=0 \tag{5.52}$$

$$3R_{s}i_{sq}+\lambda\left(L_{sdq}i_{sd}+M_{sf}i_{f}+\Phi_{M}\right)+2\mu_{V1}L_{sq}{}^{2}i_{sq}=0 \tag{5.53}$$

$$2R_{f}i_{f}+\lambda M_{sf}i_{sq}+2\mu_{V1}M_{sf}\left(L_{sd}i_{sd}+M_{sf}i_{f}+\Phi_{M}\right)=0 \tag{5.54}$$

$$\left(L_{sdq}i_{sd}+M_{sf}i_{f}+\Phi_{M}\right)i_{sq}-K_{em}=0 \tag{5.55}$$

$$\left(\left(L_{sq}i_{sq}\right)^{2}+\left(L_{sd}i_{sd}+M_{sf}i_{f}+\Phi_{M}\right)^{2}\right)-2\left(\frac{V_{s\,\max}}{p\Omega}\right)^{2}=0 \tag{5.56}$$

The system resolution yields to (5.57).

$$
\begin{aligned}
&-2R_f L_{sdq}\left(\underbrace{L_{sq}\Phi_M}_{A}+\underbrace{L_{sdq}\sqrt{2\left(\frac{V_{s\,max}}{p\Omega}\right)^2-L_{sq}{}^2 i_{sq}{}^2}}_{B}\right)i_{sq}{}^4\\
&+2\left(3R_s M_{sf}{}^2+2R_f L_{sd}L_{sdq}\right)\frac{K_{em}}{L_{sq}{}^2}\left(\frac{V_{s\,max}}{p\Omega}\right)^2 i_{sq}\\
&-\left(3R_s M_{sf}{}^2+2R_f L_{sd}{}^2\right)\frac{K_{em}{}^2}{L_{sq}{}^2}\sqrt{2\left(\frac{V_{s\,max}}{p\Omega}\right)^2-L_{sq}{}^2 i_{sq}{}^2}\\
&+2R_f\Phi_M\frac{L_{sd}}{L_{sq}}K_{em}i_{sq}\sqrt{2\left(\frac{V_{s\,max}}{p\Omega}\right)^2-L_{sq}{}^2 i_{sq}{}^2}=0
\end{aligned}
\tag{5.57}
$$

Equation (5.57) does not have an analytical solution. However, it is noted that the quantities A and B have opposite signs and the same order that is ten times smaller than the other equation coefficients. Thus, this sum can be neglected. The error induced by this simplification is less than 0.1% over the considered operating points range. Equation (5.57) becomes (5.58).

$$
\begin{aligned}
&2\left(\frac{3R_s}{2R_f}M_{sf}{}^2+L_{sd}L_{sdq}\right)\left(\frac{V_{s\,max}}{L_{sq}p\Omega}\right)^2 i_{sq}\\
&-\left(\frac{3R_s}{2R_f}M_{sf}{}^2+L_{sd}{}^2\right)\frac{K_{em}}{L_{sq}}\sqrt{2\left(\frac{V_{s\,max}}{L_{sq}p\Omega}\right)^2-i_{sq}{}^2}\\
&+\Phi_M L_{sd}i_{sq}\sqrt{2\left(\frac{V_{s\,max}}{L_{sq}p\Omega}\right)^2-i_{sq}{}^2}=0
\end{aligned}
\tag{5.58}
$$

Equation (5.58) has no apparent solution. The equality (5.59) is derived from (5.58). By rising (5.59) to the power two, a forth order polynomial arises (5.60). Thus, (5.58) is equivalent to (5.60) and an analytical solution can be found. Calculations prove that (5.60) has two real roots. The retained solution depends on electromagnetic torque sign as given by (5.61).

$$
\frac{\underbrace{-2\left(\frac{3R_s}{2R_f}M_{sf}{}^2+L_{sd}L_{sdq}\right)\left(\frac{V_{s\,max}}{L_{sq}p\Omega}\right)^2 i_{sq}}_{a}}{\underbrace{-\left(\frac{3R_s}{2R_f}M_{sf}{}^2+L_{sd}{}^2\right)\frac{K_{em}}{L_{sq}}}_{b}+\underbrace{\Phi_M L_{sd}}_{c}i_{sq}}=\sqrt{\underbrace{2\left(\frac{V_{s\,max}}{L_{sq}p\Omega}\right)^2}_{d}-i_{sq}{}^2}
\tag{5.59}
$$

$$
a^2 i_{sq}{}^4+2bci_{sq}{}^3+\left(a^2+b^2-c^2d\right)i_{sq}{}^2-2bcdi_{sq}-b^2d=0
\tag{5.60}
$$

$$
i_{sq}{}^*=0.5\left(sign\left(T_{em}\right)\left(-\sqrt{U-\frac{2A}{3}}+\sqrt{-U-\frac{4A}{3}+4S}\right)-\frac{b}{2c}\right)
\tag{5.61}
$$

With

$$A = \frac{a^2}{c^2} - \frac{b^2}{2c^2} - d$$

$$S = \sqrt{\frac{1}{4}\left(\frac{A}{3} + U\right)^2 - \frac{b^2}{4c^2}\left(\frac{a^2}{c^2} + \frac{b^2}{4c^2} - d\right)}$$

$$U = W + \frac{\left(\frac{a^2}{c^2} + \frac{b^2}{c^2} - d\right)^2}{9W}$$

$$W = \left(\frac{1}{27}\left(\frac{a^2}{c^2} + \frac{b^2}{4c^2} - d\right)^3 + \frac{2a^2b^2d}{c^4} + D\right)^{1/3}$$

$$D = \sqrt{\frac{4a^2b^2d}{c^4}\left(\frac{a^2b^2d}{c^4} + \frac{1}{27}\left(\frac{a^2}{c^2} + \frac{b^2}{c^2} - d\right)^3\right)}$$

The other currents and multipliers expressions are found in terms of $i_{sq}^{\ *}$ given (5.52) to (5.56).

$$i_{sd}^{\ *} = \frac{\left(-K_{em} + i_{sq}^{\ *}\sqrt{2\left(\frac{V_{smax}}{p\Omega}\right)^2 - L_{sq}^{\ 2} i_{sq}^{\ *2}}\right)}{L_{sq} i_{sq}^{\ *}} \tag{5.62}$$

$$i_f^{\ *} = \frac{\left(K_{em} - L_{sdq} i_{sd}^{\ *} i_{sq}^{\ *} - \Phi_M i_{sq}^{\ *}\right)}{M_{sf} i_{sq}^{\ *}} \tag{5.63}$$

$$\mu_{V1}^{\ *} = \frac{\left(2R_f L_{sdq} i_f^{\ *} - 3R_s M_{sf} i_{sd}^{\ *}\right) i_{sq}^{\ *}}{2L_{sq} M_{sf}\left(K_{em} + L_{sq} i_{sd}^{\ *} i_{sq}^{\ *}\right)} \tag{5.64}$$

$$\lambda^* = \frac{\left(3R_s M_{sf} i_{sd}^{\ *} - 2R_f L_{sd} i_f^{\ *}\right)}{L_{sq} M_{sf} i_{sq}^{\ *}} \tag{5.65}$$

The second order necessary and sufficient condition is verified as shown in (5.66).

$$\begin{aligned} \boldsymbol{y}^T \nabla^2 l\left(\boldsymbol{x}^*, \lambda^*, \mu_{V1}^{\ *}\right)\boldsymbol{y} \quad &= 3R_s y_1^{\ 2} + 2R_f y_3^{\ 2} + 2\mu_{V1}^{\ *}\left(y_1 L_{sd} + M_{sf} y_3\right)^2 \\ &+ 3y_2^{\ 2}\left(3R_s + 2\mu_{V1}^{\ *} L_{sq}^{\ 2}\right) > 0 \end{aligned} \quad \Big| \ \forall \boldsymbol{y} \neq 0 \tag{5.66}$$

5.3.1.e. <u>Optimal reference currents with no active constraint</u>

When both voltage and current constraints are inactive, μ_V *and* μ_I are set to zero. The problem formulation yields to equations (5.67) to (5.70). Its resolution gives (5.71).

$$3R_s i_{sd} + \lambda L_{sdq} i_{sq} = 0 \tag{5.67}$$

$$3R_s i_{sq} + \lambda\left(L_{sdq} i_{sd} + M_{sf} i_f + \Phi_M\right) = 0 \tag{5.68}$$

$$2R_f i_f + \lambda M_{sf} i_{sq} = 0 \tag{5.69}$$

$$\left(L_{sdq} i_{sd} + M_{sf} i_f + \Phi_M\right) i_{sq} - K_{em} = 0 \tag{5.70}$$

$$\left(L_{sdq}{}^2 + \frac{3R_s M_{sf}{}^2}{2R_f}\right) i_{sq}{}^4 + K_{em}\Phi_M i_{sq} - K_{em}{}^2 = 0 \tag{5.71}$$

Let $a = \left(L_{sdq}{}^2 + \frac{3R_s M_{sf}{}^2}{2R_f}\right)$.

Equation (5.71) has two real roots and only one positive root given by (5.72).

$$i_{sq}{}^* = sign\left(K_{em}\right)\frac{1}{2}\left(-\sqrt{U} + \sqrt{-U + 4\sqrt{\frac{U^2}{4} + \frac{K_{em}{}^2}{a}}}\right) \tag{5.72}$$

With

$$U = \left(\frac{\Phi_M{}^2 K_{em}{}^2}{2a^2} + \sqrt{D}\right)^{1/3} - \frac{4K_{em}{}^2}{3a\left(\frac{\Phi_M{}^2 K_{em}{}^2}{2a^2} + \sqrt{D}\right)^{1/3}}$$

$$D = \frac{K_{em}{}^4}{a^3}\left(\frac{64K_{em}{}^2}{27} + \frac{\Phi_M{}^4}{4a}\right)$$

$i_{sd}{}^*$, $i_f{}^*$ and the Lagrange multiplier λ expressions are established in terms of $i_{sq}{}^*$.

$$i_{sd}{}^* = \frac{L_{sdq}}{K_{em}} i_{sq}{}^{*3} \tag{5.73}$$

$$i_f{}^* = \frac{3R_s M_{sf} i_{sq}{}^{*3}}{2R_f K_{em}} \tag{5.74}$$

$$\lambda^* = \frac{-3R_s i_{sq}{}^{*2}}{K_{em}} \tag{5.75}$$

The second order necessary and sufficient condition is verified in (5.76).

$$\boldsymbol{y}^T \nabla^2 l\left(\boldsymbol{x}^*, \lambda^*\right)\boldsymbol{y} = 3R_s\left(y_1{}^2 + y_2{}^2\right) + 2R_f y_3{}^2 + \frac{6R_s i_{sq}{}^{*4}}{K_{em}{}^2}\left(y_1 L_{sdq} + M_{sf} y_3\right)^2 > 0 \;\middle|\; \forall \boldsymbol{y} \neq 0 \tag{5.76}$$

5.3.1.f. Algorithm flowchart

The procedure of the optimal reference currents computation is summarized in the flowchart in Figure 5.8. The optimization problem leads mathematically to the commonly known solution $i_{sd}^{*}=0$ when the machine presents no saliency.

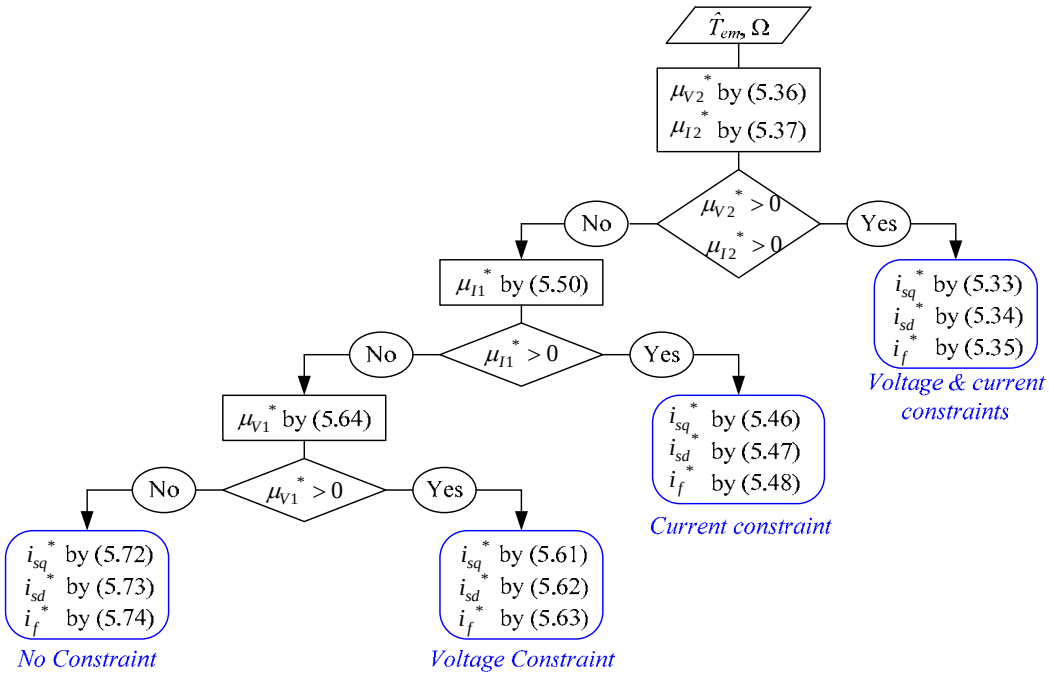

Figure 5.8. Optimal reference current computation with minimum copper losses

5.3.2. Algorithm validation

In order to validate the proposed optimization algorithm, it shall be proven that it leads to the solution presenting minimal copper losses with no current or voltage constraints violation.

The relation between torque and currents is nonlinear. Thus, at a given speed, the same torque can be produced by a set of distinct (i_{sd}, i_{sq}, i_f) combinations that satisfy the current and voltage constraints. These solutions are represented in dots in Figure 5.9. Figure 5.9 proves that the surface generated by the proposed optimization algorithm is indeed the lower limit of the copper losses produced by all possible solutions. No other combination can give smaller copper losses. In addition, the time taken by Matlab software to compute the optimal solution based on the analytical expression is four times smaller than the time needed by the program to find the solution when using recursive search algorithm over a limited current range with a step of 0.1 A.

The copper losses generated by the optimal reference currents are then compared to those obtained by two other control strategies (Figure 5.10). The first method is based on the MTPA approach; it optimizes the references i_{sd} and i_{sq} while the field current i_f is kept equal to a constant value. Three field current values are considered: $i_f = 2$ A, $i_f = 0$ A and $i_f = -2$ A. The second control method optimizes the i_{sq} and i_f while i_{sd} is set to zero [116]. Both control strategies aims to minimize the copper losses by regulating two currents out of three for a given torque. The current or the voltage constraints are not taken into account. Calculations are done over a normalized

NEDC: this driving cycle consists of four repeated urban driving cycles and an extra-urban driving cycle (Figure 5.10).

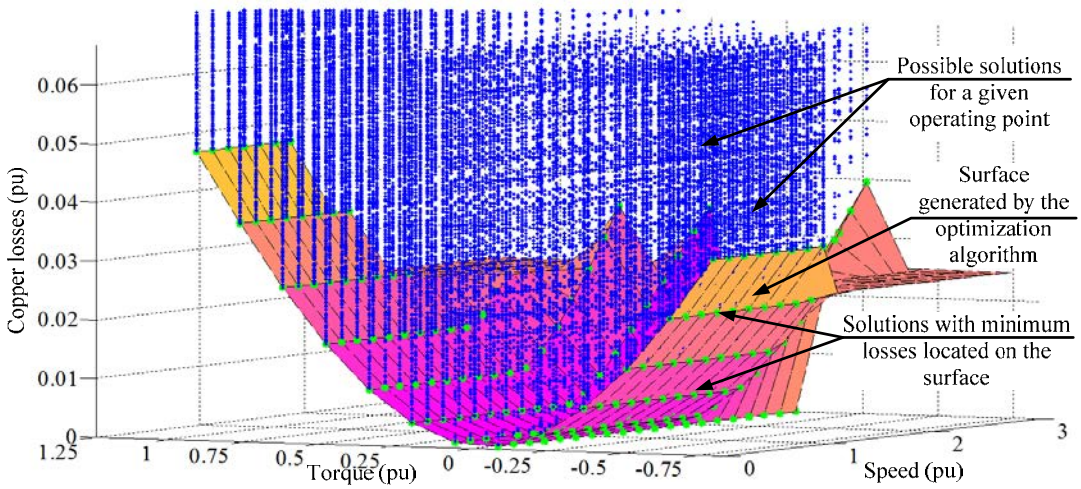

Figure 5.9. Optimization algorithm validation when only copper losses are considered and minimized

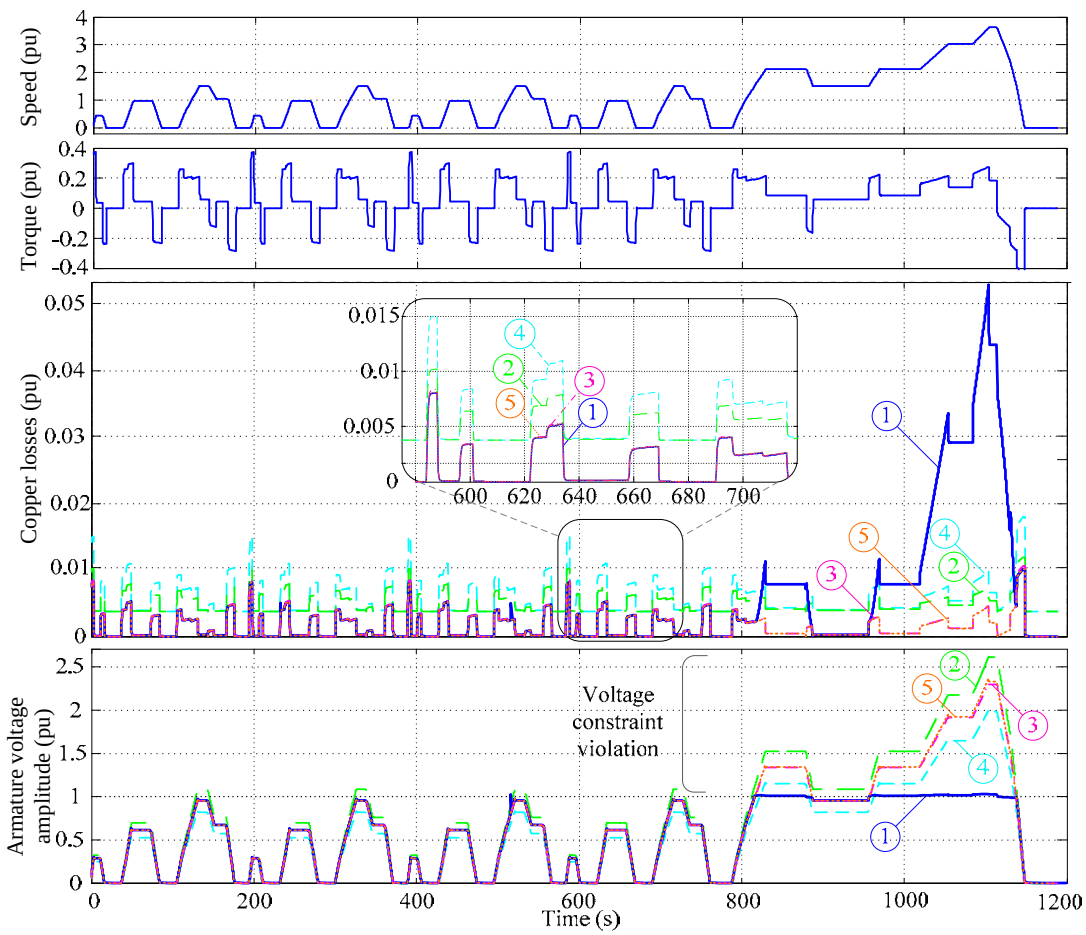

Figure 5.10. Copper losses and armature voltage magnitude with different control strategies over the NEDC: 1. ELMM, 2. MTPA with i_f = 2 A, 3. MTPA with i_f =0 A, 4. MTPA with i_f =−2 A, 5. Optimized i_{sq} and i_f with i_{sd} =0 A

Results prove that the proposed optimal control generated the reference currents that lead to the lowest copper losses with respect to current and voltage constraints over the whole cycle. The control strategies with negative field current ($i_f = -2$ A) presents the highest copper losses. The method that optimizes i_{sq} and i_f with $i_{sd} = 0$ A offers satisfactory results. This is expected since the machine saliency is not significant; the direct armature optimal current component is close to zero when the voltage constraint is not active. On other hand, the results obtained with $i_f = 2$ A are practically the same as those obtained with the optimization algorithm when the motor speed is below the base speed. In fact, $i_f = 2$ A is the nominal field current for the imposed speed. At high speed, when the flux weakening occurs, the other control strategies violate the voltage constraint.

5.4. Hybrid excitation synchronous motor control with minimum copper and iron losses

Few attempts to minimize both copper and iron losses have been presented in the literature [18] [75]. The loss minimization conditions are usually complex and often implemented using offline-made lookup tables. It is pointed that the core losses form a significant fraction of the losses in a machine . For the laboratory scale machine used for simulation and experiments, the iron losses are equal to half of the copper losses at nominal conditions. Therefore, an optimal control must minimize the iron losses as well as the copper losses. Figure 5.11 shows that the solution obtained by the algorithm developed in section 5.3 does not lead to the minimal copper and iron losses.

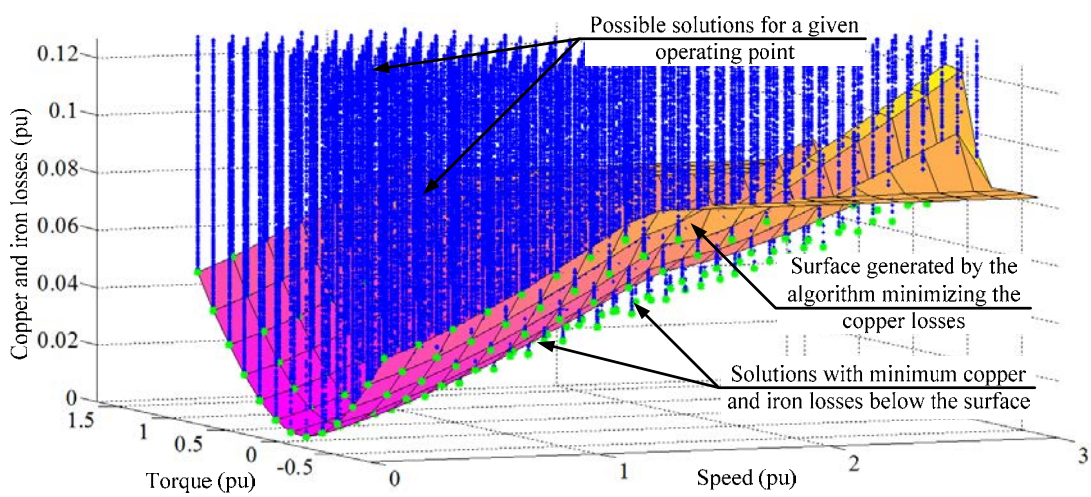

Figure 5.11. Results obtained by the optimization algorithm minimizing the copper losses only when copper and iron are considered

5.4.1. Optimal reference currents with minimum copper and iron losses

5.4.1.a. Problem Formulation

It was shown in paragraph 1.3.1 that the iron losses can be estimated using (1.22). This equation is recalled in (5.77).

$$P_{ir} = 2q \frac{1}{\left(2\pi f_{ref}\right)^{1.3} \left(pn_s B_{ref} l_a\right)^2} \left(\frac{9M_y}{\left(2e_y\right)^2} + \frac{M_{st}}{\left(l_{st}\right)^2} \right) \omega_s^{1.3} \left(M_{sf} i_f + \Phi_M\right)^2 \tag{5.77}$$

Once the machine is designed, the iron losses will depend on two quantities: the rotor speed and the excitation flux. Thus, (5.77) is reformulated.

$$P_{ir} = k_{ir}\left(M_{sf} i_f + \Phi_M\right)^2 \tag{5.78}$$

k_{ir} includes $\omega_s = p\Omega$ that is an image of the rotor speed.

The function to minimize is the sum of the copper and iron losses in terms of the machine currents as given in (5.79). i_{sd1}, i_{sq1} are the currents that govern the electromagnetic torque as shown in Figure 1.12.

$$f(\boldsymbol{x}) = \frac{3}{2} R_s \left(i_{sd1}{}^2 + i_{sq1}{}^2\right) + \left(R_f + M_{sf}{}^2 k_{ir}\right) i_f{}^2 + 2 k_{ir} \Phi_M M_{sf} i_f \tag{5.79}$$

When considering the objective function $f(\boldsymbol{x})$, two assumptions are raised.

- The iron losses are supposed to remain unchanged at no load and when the motor is loaded for the same speed and excitation flux. This is equivalent to neglect the armature reaction effect on the iron losses.
- The copper losses generated by the eddy currents do not occur explicitly in (5.79). However, it shall be noted that these losses are indirectly integrated in the optimization problem since the minimization of the iron losses implies the minimization of the eddy currents.

The equality and inequality constraints are given by (5.80), (5.81) and (5.82) respectively.

$$h(\boldsymbol{x}) = \frac{3}{2} p\left(\left(L_{sd} - L_{sq}\right) i_{sd1} + M_{sf} i_f + \Phi_M\right) i_{sq1} - T_{em} = 0 \tag{5.80}$$

$$g_I(\boldsymbol{x}) = \left(i_{sd1}{}^2 + i_{sq1}{}^2\right) - 2\alpha I_{s\max}{}^2 \le 0 \tag{5.81}$$

$$g_V(\boldsymbol{x}) = \left(\left(L_{sq} i_{sq1}\right)^2 + \left(L_{sd} i_{sd1} + M_{sf} i_f + \Phi_M\right)^2\right) - 2\left(\frac{V_{s\max}}{p\Omega}\right)^2 \le 0 \tag{5.82}$$

In (5.81), a coefficient $0 < \alpha \le 1$ is added. This factor defines the ratio i_{sd1}/i_{sd} or i_{sq1}/i_{sq}. In fact, $\sqrt{2} I_{s\max}$ is the line current upper limit. However, at full load when the current constraint might be active, $\left(i_{sd2}{}^2 + i_{sq2}{}^2\right) << \left(i_{sd1}{}^2 + i_{sq1}{}^2\right)$ and α tends to one. i_{sd2}, i_{sq2} are the d-q axis currents that flow through the shunting resistor R_{ir}.

For the HESM current control with minimum copper and iron losses, the optimal current vector is noted $\boldsymbol{x}^* = \left[i_{sd1}{}^* \quad i_{sq1}{}^* \quad i_f{}^*\right]$

The gradient of Lagrange function is given by (5.83). This function differs by one term from the gradient obtained when only copper losses were considered (5.23).

$$\nabla l(\boldsymbol{x},\lambda,\boldsymbol{\mu}) = \begin{bmatrix} 3R_s i_{sd1} \\ 3R_s i_{sq1} \\ 2k_{f2} i_f + k_{f1} \end{bmatrix} + \lambda \begin{bmatrix} L_{sdq} i_{sq1} \\ L_{sdq} i_{sd1} + M_{sf} i_f + \Phi_M \\ M_{sf} i_{sq1} \end{bmatrix} + \mu_{I2} \begin{bmatrix} 2i_{sd1} \\ 2i_{sq1} \\ 0 \end{bmatrix} + \mu_{V2} \begin{bmatrix} 2L_{sd}\left(L_{sd} i_{sd1} + M_{sf} i_f + \Phi_M\right) \\ 2L_{sq}{}^2 i_{sq1} \\ 2M_{sf}\left(L_{sd} i_{sd1} + M_{sf} i_f + \Phi_M\right) \end{bmatrix} \tag{5.83}$$

With $k_{f2} = R_f + k_{ir} M_{sf}{}^2$ and $k_{f1} = 2k_{ir} M_{sf} \Phi_M$.

Thus, the same procedure adopted in paragraph 5.3.1 is implemented. Four cases are studied depending on the active constraints.

5.4.1.b. <u>Optimal reference currents with active voltage and current constraints</u>

Setting $\nabla l(\boldsymbol{x},\lambda,\boldsymbol{\mu}) = 0$ and given $h(\boldsymbol{x}) = 0$, $g_V(\boldsymbol{x}) = 0$, $g_I(\boldsymbol{x}) = 0$ yields to equations (5.84) to (5.89).

$$3R_s i_{sd1} + \lambda L_{sdq} i_{sq1} + 2\mu_{V2} L_{sd}\left(L_{sd} i_{sd1} + M_{sf} i_f + \Phi_M\right) + 2\mu_{I2} i_{sd1} = 0 \tag{5.84}$$

$$3R_s i_{sq1} + \lambda\left(L_{sdq} i_{sd1} + M_{sf} i_f + \Phi_M\right) + 2\mu_{V2} L_{sq}{}^2 i_{sq1} + 2\mu_{I2} i_{sq1} = 0 \tag{5.85}$$

$$2k_{f2} i_f + k_{f1} + \lambda M_{sf} i_{sq1} + 2\mu_{V2} M_{sf}\left(L_{sd} i_{sd1} + M_{sf} i_f + \Phi_M\right) = 0 \tag{5.86}$$

$$\frac{3}{2} p\left(L_{sdq} i_{sd1} + M_{sf} i_f + \Phi_M\right) i_{sq1} - T_{em} = 0 \tag{5.87}$$

$$\left(\left(L_{sq} i_{sq1}\right)^2 + \left(L_{sd} i_{sd1} + M_{sf} i_f + \Phi_M\right)^2\right) - 2\left(\frac{V_{s\max}}{p\Omega}\right)^2 = 0 \tag{5.88}$$

$$\left(i_{sd1}{}^2 + i_{sq1}{}^2\right) - 2I_{s\max}{}^2 = 0 \tag{5.89}$$

The optimal reference currents and multipliers are computed by going through the same process detailed in paragraph 5.3.1.b.

$$i_{sq1}{}^* = \frac{K_{em}}{\sqrt{2}} \frac{\left(\left(\frac{V_{s\max}}{p\Omega}\right)^2 + L_{sq}{}^2 I_{s\max}{}^2 - L_{sq}\sqrt{4I_{s\max}{}^2\left(\frac{V_{s\max}}{p\Omega}\right)^2 - K_{em}{}^2}\right)^{1/2}}{\left(L_{sq}{}^2 K_{em}{}^2 + \left(L_{sq}{}^2 I_{s\max}{}^2 - \left(\frac{V_{s\max}}{p\Omega}\right)^2\right)^2\right)^{1/2}} \tag{5.90}$$

$$i_{sd1}{}^* = -\sqrt{2I_{s\max}{}^2 - i_{sq1}{}^{*2}} \tag{5.91}$$

$$i_f{}^* = \frac{\left(K_{em} - L_{sdq} i_{sd1}{}^* i_{sq1}{}^* - \Phi_M i_{sq1}{}^*\right)}{M_{sf} i_{sq1}{}^*} \tag{5.92}$$

$$\mu_{V2}{}^{*}=\frac{\left(\frac{k_{f2}}{M_{sf}}\left(K_{em}-L_{sdq}i_{sd1}{}^{*}i_{sq1}{}^{*}-\Phi_{M}i_{sq1}{}^{*}\right)+0.5k_{f1}i_{sq1}{}^{*}\right)\left(L_{sdq}i_{sq}{}^{*3}-K_{em}i_{sd}{}^{*}\right)}{M_{sf}K_{em}\left(L_{sq}i_{sq1}{}^{*3}+L_{sq}i_{sd1}{}^{*2}i_{sq1}{}^{*}+K_{em}i_{sd1}{}^{*}\right)} \tag{5.93}$$

$$\lambda^{*}=\frac{-2\mu_{V2}{}^{*}i_{sq1}{}^{*}\left(L_{sd}K_{em}+L_{sq}L_{sdq}i_{sd1}{}^{*}i_{sq1}{}^{*}\right)}{\left(L_{sdq}i_{sq1}{}^{*3}-K_{em}i_{sd1}{}^{*}\right)} \tag{5.94}$$

$$\mu_{I2}{}^{*}=\frac{\left(-3R_{s}+2\mu_{V2}{}^{*}L_{sq}{}^{2}\right)i_{sq1}{}^{*2}-\lambda^{*}K_{em}}{2i_{sq1}{}^{*2}} \tag{5.95}$$

With $K_{em}=\frac{2}{3p}T_{em}$.

The second order necessary and sufficient condition of Theorem A.3 is verified in (5.96).

$$\begin{aligned}\boldsymbol{y}^{T}\nabla^{2}l\left(\boldsymbol{x}^{*},\lambda^{*},\boldsymbol{\mu}^{*}\right)\boldsymbol{y} \quad &=\left(3R_{s}+2\mu_{I2}{}^{*}\right)y_{1}{}^{2}+2k_{f2}y_{3}{}^{2}+2\mu_{V2}{}^{*}\left(y_{1}L_{sd}+M_{sf}y_{3}\right)^{2} \\ &+3y_{2}{}^{2}\left(3R_{s}+2\mu_{I2}{}^{*}+2\mu_{V2}{}^{*}L_{sq}{}^{2}\right)>0\end{aligned} \quad \Big|\ \forall\boldsymbol{y}\neq 0 \tag{5.96}$$

5.4.1.c. <u>Optimal reference currents with active current constraint</u>

The multiplier μ_V is set to zero. $\nabla l\left(\boldsymbol{x},\lambda,\boldsymbol{\mu}\right)=0$, $h(\boldsymbol{x})=0$ and $g_I(\boldsymbol{x})=0$ form a system of five equations (5.97) to (5.101).

$$3R_{s}i_{sd1}+\lambda L_{sdq}i_{sq1}+2\mu_{I1}i_{sd1}=0 \tag{5.97}$$

$$3R_{s}i_{sq1}+\lambda\left(L_{sdq}i_{sd1}+M_{sf}i_{f}+\Phi_{M}\right)+2\mu_{I1}i_{sq1}=0 \tag{5.98}$$

$$2k_{f2}i_{f}+k_{f1}+\lambda M_{sf}i_{sq1}=0 \tag{5.99}$$

$$\left(L_{sdq}i_{sd1}+M_{sf}i_{f}+\Phi_{M}\right)i_{sq1}-K_{em}=0 \tag{5.100}$$

$$\left(i_{sd1}{}^{2}+i_{sq1}{}^{2}\right)-2I_{s\max}{}^{2}=0 \tag{5.101}$$

Calculations yield to (5.102) that is the same as (5.45).

$$\frac{L_{sdq}{}^{2}}{K_{em}{}^{2}}i_{sq1}{}^{6}+i_{sq1}{}^{2}-2I_{s\,max}{}^{2}=0 \tag{5.102}$$

The reference currents and multipliers are given by (5.103) to (5.107).

$$i_{sq1}{}^{*}=\left(\frac{K_{em}I_{s\,max}}{L_{sdq}}\right)^{1/3}\sqrt{\left(1+\sqrt{1+\frac{K_{em}{}^{2}}{27L_{sdq}{}^{2}I_{s\,max}{}^{4}}}\right)^{1/3}+\left(1-\sqrt{1+\frac{K_{em}{}^{2}}{27L_{sdq}{}^{2}I_{s\,max}{}^{4}}}\right)^{1/3}} \tag{5.103}$$

$$i_{sd1}{}^{*} = \frac{L_{sdq}}{K_{em}} i_{sq1}{}^{*3} \tag{5.104}$$

$$i_{f}{}^{*} = \frac{\left(K_{em} - L_{sdq} i_{sd1}{}^{*} i_{sq1}{}^{*} - \Phi_M i_{sq1}{}^{*}\right)}{M_{sf} i_{sq1}{}^{*}} \tag{5.105}$$

$$\lambda^{*} = \frac{-\left(2k_{f2} i_{f}{}^{*} + k_{f1}\right)}{M_{sf} i_{sq1}{}^{*}} \tag{5.106}$$

$$\mu_{I1}{}^{*} = -\frac{\lambda^{*} L_{sdq}}{2 i_{sq1}{}^{*2}} - \frac{3R_s}{2} \tag{5.107}$$

Equation (5.108) proves that the second order necessary and sufficient condition is verified.

$$\boldsymbol{y}^T \nabla^2 l\left(\boldsymbol{x}^{*}, \lambda^{*}, \mu_{I1}{}^{*}\right) \boldsymbol{y} = \left(3R_s + 2\mu_{I1}{}^{*}\right) y_1{}^2 + 2k_{f2} y_3{}^2 + y_2{}^2 \left(9R_s + 6\mu_{I1}{}^{*}\right) > 0 \;\middle|\; \forall \boldsymbol{y} \neq 0 \tag{5.108}$$

5.4.1.d. <u>Optimal reference currents with active voltage constraint</u>

When the current constraint is inactive, μ_I is set to zero. $\nabla l\left(\boldsymbol{x}, \lambda, \boldsymbol{\mu}\right) = 0$, $h(\boldsymbol{x}) = 0$ and $g_V(\boldsymbol{x}) = 0$ are five equations with five variables (5.109) to (5.113).

$$3R_s i_{sd1} + \lambda L_{sdq} i_{sq1} + 2\mu_{V1} L_{sd}\left(L_{sd} i_{sd1} + M_{sf} i_f + \Phi_M\right) = 0 \tag{5.109}$$

$$3R_s i_{sq1} + \lambda\left(L_{sdq} i_{sd1} + M_{sf} i_f + \Phi_M\right) + 2\mu_{V1} L_{sq}{}^2 i_{sq1} = 0 \tag{5.110}$$

$$2k_{f2} i_f + k_{f1} + \lambda M_{sf} i_{sq1} + 2\mu_{V1} M_{sf}\left(L_{sd} i_{sd1} + M_{sf} i_f + \Phi_M\right) = 0 \tag{5.111}$$

$$\left(L_{sdq} i_{sd1} + M_{sf} i_f + \Phi_M\right) i_{sq1} - K_{em} = 0 \tag{5.112}$$

$$\left(\left(L_{sq} i_{sq1}\right)^2 + \left(L_{sd} i_{sd1} + M_{sf} i_f + \Phi_M\right)^2\right) - 2\left(\frac{V_{s\max}}{p\Omega}\right)^2 = 0 \tag{5.113}$$

The same calculations developed in paragraph 5.3.1.d are carried out. $i_{sq1}{}^{*}$ is given by (5.114) which is the same as (5.61). The only difference is that R_f is replaced by k_{f2} and Φ_M by $\left(\Phi_M - \frac{k_{f1}}{2k_{f2}} M_{sf}\right)$ in all intermediate variables.

$$i_{sq1}{}^{*} = 0.5\left(sin\,g\left(K_{em}\right)\left(-\sqrt{U - \frac{2A}{3}} + \sqrt{-U - \frac{4A}{3} + 4S}\right) - \frac{b}{2c}\right) \tag{5.114}$$

The other currents and multipliers expressions are found in terms of $i_{sq1}{}^{*}$.

$$i_{sd1}{}^{*}=\frac{\left(-K_{em}+i_{sq1}{}^{*}\sqrt{2\left(\frac{V_{s\,max}}{p\Omega}\right)^{2}-L_{sq}{}^{2}i_{sq1}{}^{*2}}\right)}{L_{sq}i_{sq1}{}^{*}} \tag{5.115}$$

$$i_{f}{}^{*}=\frac{\left(K_{em}-L_{sdq}i_{sd1}{}^{*}i_{sq1}{}^{*}-\Phi_{M}i_{sq1}{}^{*}\right)}{M_{sf}i_{sq1}{}^{*}} \tag{5.116}$$

$$\mu_{V1}{}^{*}=\frac{\left(\left(2k_{f2}i_{f}{}^{*}+k_{f1}\right)L_{sdq}-3R_{s}M_{sf}i_{sd1}{}^{*}\right)i_{sq1}{}^{*}}{2L_{sq}M_{sf}\left(K_{em}+L_{sq}i_{sd1}{}^{*}i_{sq1}{}^{*}\right)} \tag{5.117}$$

$$\lambda^{*}=\frac{\left(3R_{s}M_{sf}i_{sd1}{}^{*}-L_{sd}\left(2k_{f2}i_{f}{}^{*}+k_{f1}\right)\right)}{L_{sq}M_{sf}i_{sq1}{}^{*}} \tag{5.118}$$

The second order necessary and sufficient condition is verified as shown in (5.119).

$$\begin{aligned}\boldsymbol{y}^{T}\nabla^{2}l\left(\boldsymbol{x}^{*},\lambda^{*},\mu_{V1}{}^{*}\right)\boldsymbol{y} &= 3R_{s}y_{1}{}^{2}+2k_{f2}y_{3}{}^{2}+2\mu_{V1}{}^{*}\left(y_{1}L_{sd}+M_{sf}y_{3}\right)^{2} \\ &\quad +3y_{2}{}^{2}\left(3R_{s}+2\mu_{V1}{}^{*}L_{sq}{}^{2}\right)>0\end{aligned} \quad \Big|\ \forall\boldsymbol{y}\neq 0 \tag{5.119}$$

5.4.1.e. <u>Optimal reference currents with no active constraint</u>

When both voltage and current constraints are inactive, μ_V *and* μ_I are set to zero. The problem formulation is reduced to (5.120) to (5.123). Its resolution yields to (5.124).

$$3R_{s}i_{sd1}+\lambda L_{sdq}i_{sq1}=0 \tag{5.120}$$

$$3R_{s}i_{sq1}+\lambda\left(L_{sdq}i_{sd1}+M_{sf}i_{f}+\Phi_{M}\right)=0 \tag{5.121}$$

$$2k_{f2}i_{f}+k_{f1}+\lambda M_{sf}i_{sq1}=0 \tag{5.122}$$

$$\left(L_{sdq}i_{sd1}+M_{sf}i_{f}+\Phi_{M}\right)i_{sq1}-K_{em}=0 \tag{5.123}$$

$$\left(L_{sdq}{}^{2}+\frac{3R_{s}M_{sf}{}^{2}}{2k_{f2}}\right)i_{sq1}{}^{4}+K_{em}\left(\Phi_{M}-\frac{k_{f1}}{2k_{f2}}M_{sf}\right)i_{sq1}-K_{em}{}^{2}=0 \tag{5.124}$$

$i_{sq1}{}^{*}$ has the same expression as $i_{sq}{}^{*}$ given by (5.72)under the condition of replacing R_f with k_{f2} and Φ_M with $\left(\Phi_M-\frac{k_{f1}}{2k_{f2}}M_{sf}\right)$ in all intermediate variables.

$$i_{sq1}{}^{*}=sign\left(K_{em}\right)\frac{1}{2}\left(-\sqrt{U}+\sqrt{-U+4\sqrt{\frac{U^{2}}{4}+\frac{K_{em}{}^{2}}{a}}}\right) \tag{5.125}$$

$i_{sd1}{}^{*}$, $i_{f}{}^{*}$ and the Lagrange multiplier λ expressions are established in terms of $i_{sq1}{}^{*}$.

$$i_{sd1}{}^{*} = \frac{L_{sdq}}{K_{em}} i_{sq1}{}^{*3} \tag{5.126}$$

$$i_{f}{}^{*} = \frac{3R_s M_{sf} i_{sq1}{}^{*3}}{2k_{f2}K_{em}} - \frac{k_{f1}}{2k_{f2}} \tag{5.127}$$

$$\lambda^{*} = \frac{-3R_s i_{sq1}{}^{*2}}{K_{em}} \tag{5.128}$$

The second order necessary and sufficient condition is verified in (5.129).

$$\boldsymbol{y}^T \nabla^2 l\left(\boldsymbol{x}^*, \lambda^*\right) \boldsymbol{y} = 3R_s\left(y_1{}^2 + y_2{}^2\right) + 2k_{f2} y_3{}^2 + \frac{6R_s i_{sq1}{}^{*4}}{K_{em}{}^2}\left(y_1 L_{sdq} + M_{sf} y_3\right)^2 > 0 \;\middle|\; \forall \boldsymbol{y} \neq 0 \tag{5.129}$$

5.4.2. Algorithm validation

Figure 5.12 proves that the surface generated by the optimal reference current expressions is the solution with minimal copper and iron losses. No other (i_{sd}, i_{sq}, i_f) combination can produce smaller losses with respect to voltage and current constraints.

The copper and iron losses obtained by this optimization algorithm are compared to those obtained with the algorithm developed in section 5.3 when only the copper loss minimization is considered. Calculations are done over a normalized NEDC. A comparison between plots 1 and plot 6 prove that a reduction of 15% of the electric losses in the machine is gained when the optimization algorithm considers the minimization of iron losses as well as copper losses. In addition, it is pointed that over the NEDC the proposed optimal control offers the lowest armature voltage, which can be reflected by a reduction of the inverter size.

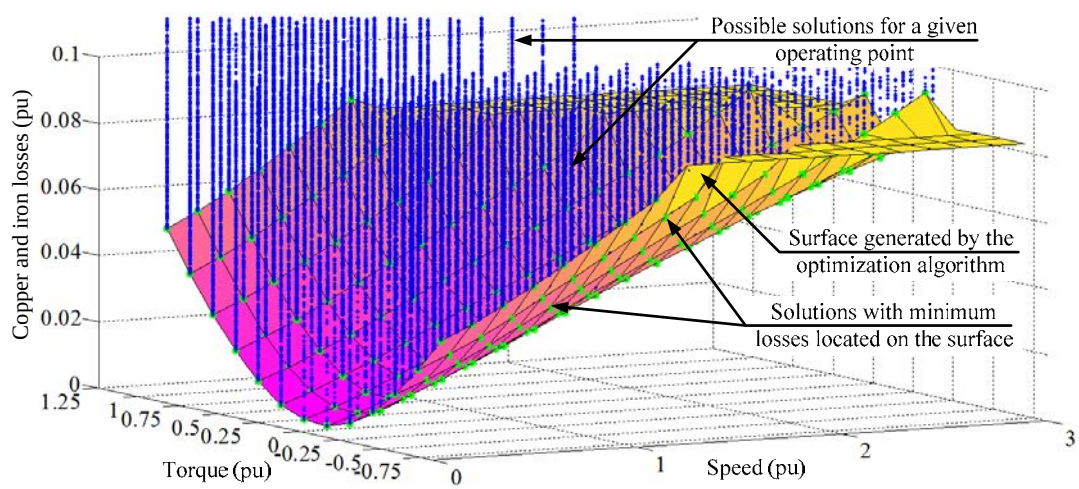

Figure 5.12. Optimization algorithm validation when iron and copper losses are considered and minimized

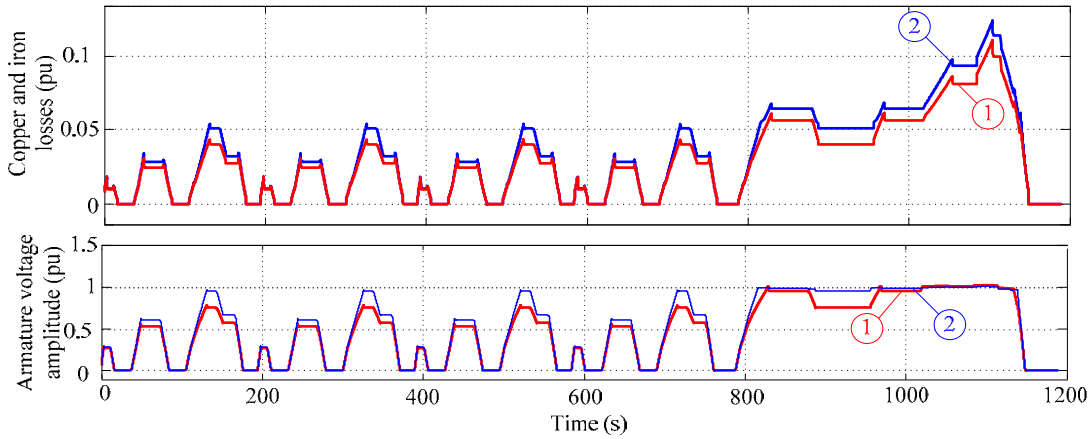

Figure 5.13. Losses and armature voltage magnitude using ELMM with 1. copper and iron losses minimization, 2. copper loss minimization.

5.5. Additional losses

5.5.1. Harmonic losses

The proposed minimization problem includes the copper and iron losses produced by the voltage and current first harmonics only. However, the inverter supply on one hand and the machine structure on the other hand induce non-sinusoidal voltage and current waveforms. The harmonic voltages increase the iron losses and the harmonic currents increase the armature copper losses. The harmonic loss reduction is an attractive objective during the machine design phase. Once the machine is designed, special attention is paid to the PWM modulation in an attempt to reduce these losses. In fact, the harmonic losses cannot be directly reduced by the field-oriented control technique, regardless the reference currents (optimal or not). Thus, the harmonic loss reduction is not considered in this document.

5.5.2. Mechanical losses

The mechanical losses include the friction losses and the windage losses that are proportional to the rotor speed and to the square of the rotor speed respectively. These losses are independent from electric currents and are not part of the proposed optimization problem.

5.6. Simulation results

The proposed optimal control is validated by simulation under Matlab/Simulink software. Simulations are carried out over one urban driving cycle and the extra-urban driving cycle as defined in the normalized NEDC. The optimal reference currents are generated while the simulation is running. The machine model takes into account the magnetic circuit saturation.

5.6.1. Comparison between the MTPA method and the proposed optimal control

The proposed optimal motor control methods minimizing the copper losses and the iron and copper losses are both tested by simulation. The machine model takes into account the iron losses and the magnetic circuit saturation. The simulation results are compared to those obtained with the MTPA control strategy, based on (5.11), for three excitation currents: $i_f = -2$ A, $i_f = 0$ A and $i_f = 2$ A. Figure 5.14 proves that the speed and torque requirements are met for all the control

methods. The electromagnetic torque counters the torque on the shaft and the torque due to the mechanical friction losses.

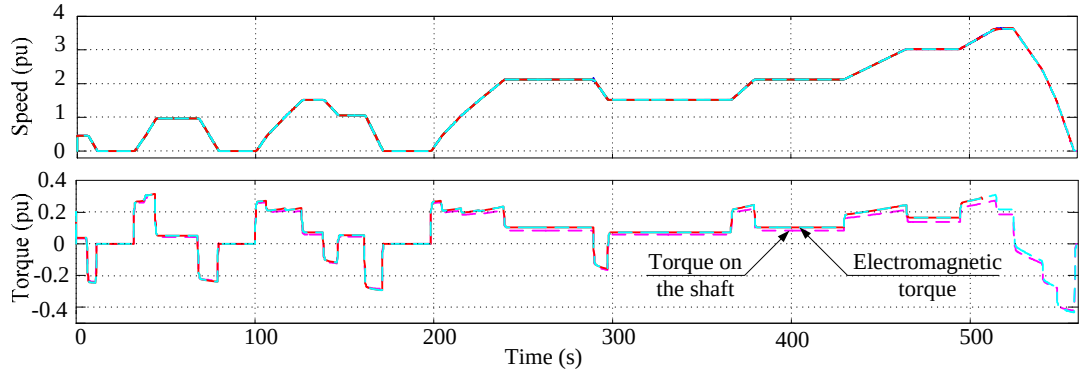

Figure 5.14. Speed and torque responses for the different control strategies

The optimization method minimizing the iron and copper losses presents the minimal losses compared to the other methods as shown in Figure 5.15. In addition, Figure 5.15 proves that the armature voltage magnitude obtained when applying ELMM (plots 1 and 2) remains below the voltage limit, equal to one in the per unit scale. It is noted that over almost 80% of the considered driving cycle, the iron losses are greater than the copper losses. This is to be interpreted in conjunction with the fact that the required torque remains below 40% of the machine rated torque. When the speed reaches four times the base speed, the copper losses increase due to the excessive d-axis and field currents needed to perform the flux weakening. As for the iron losses, the expression used to evaluate these losses (5.78) includes, in addition to the motor speed, the excitation flux in the air gap. At high speed, the flux weakening occurs and the air gap flux is reduced. This explains why the iron losses, evaluated by (5.78), do not necessarily increase at the end of the extra-urban driving cycle.

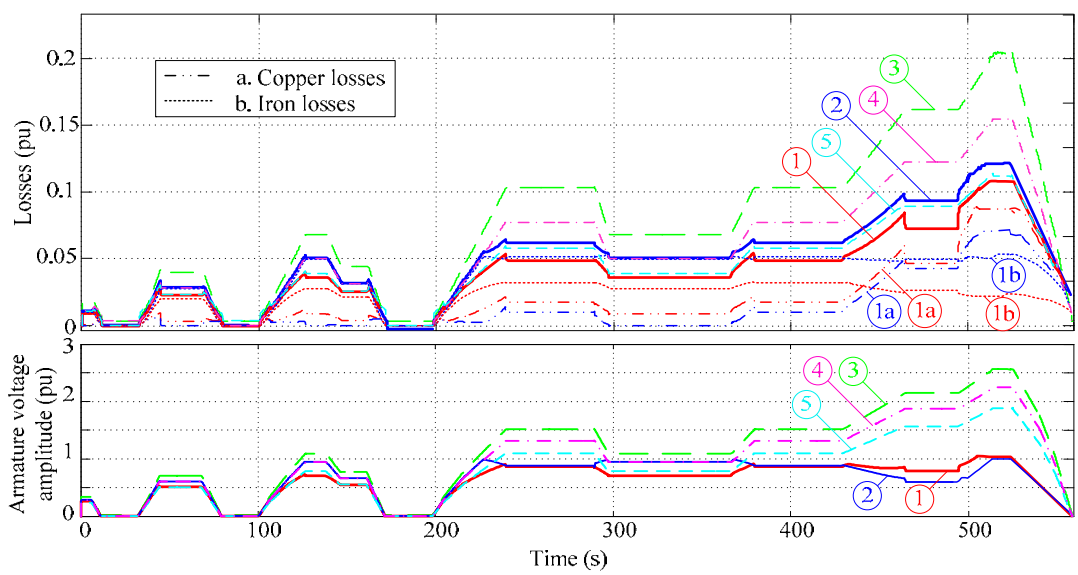

Figure 5.15. Losses and armature voltage magnitude obtained by simulation with different control strategies: 1. ELMM with iron and copper loss minimization, 2. ELMM with copper loss minimization, 3. MTPA with i_f =2 A, 4. MTPA with i_f =0 A, 5. MTPA with i_f =−2 A

The losses generated by simulation are greater than the losses obtained in paragraph 5.4.2. The maximum deviation is 25% at the end of the extra-urban cycle. In order to explain this difference, a closer look to the machine current is needed. It is clearly shown in Figure 5.16 that the armature current components are greater than the reference currents. In fact, due to the magnetic circuit saturation and the mechanical friction losses, the torque control reference is greater than the reference of the armature current magnitude.

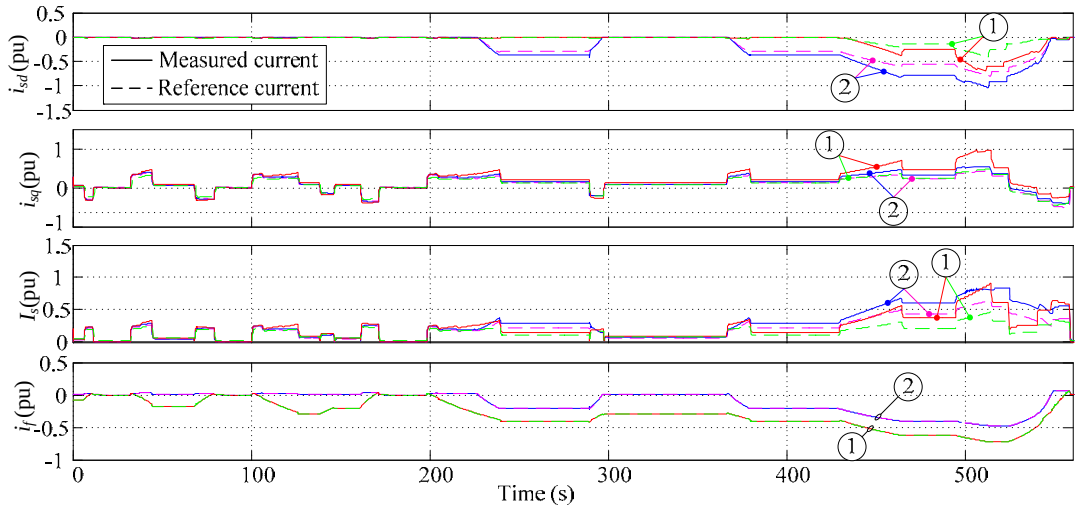

Figure 5.16. Generated currents with ELMM: 1. with iron and copper loss minimization, 2. with copper loss minimization

A particular attention is paid to the magnetic circuit saturation effect [74]. In fact, the optimal reference current expressions are found in terms of the nominal machine parameters. However, these parameters vary when the currents increase due to the magnetic circuit saturation.

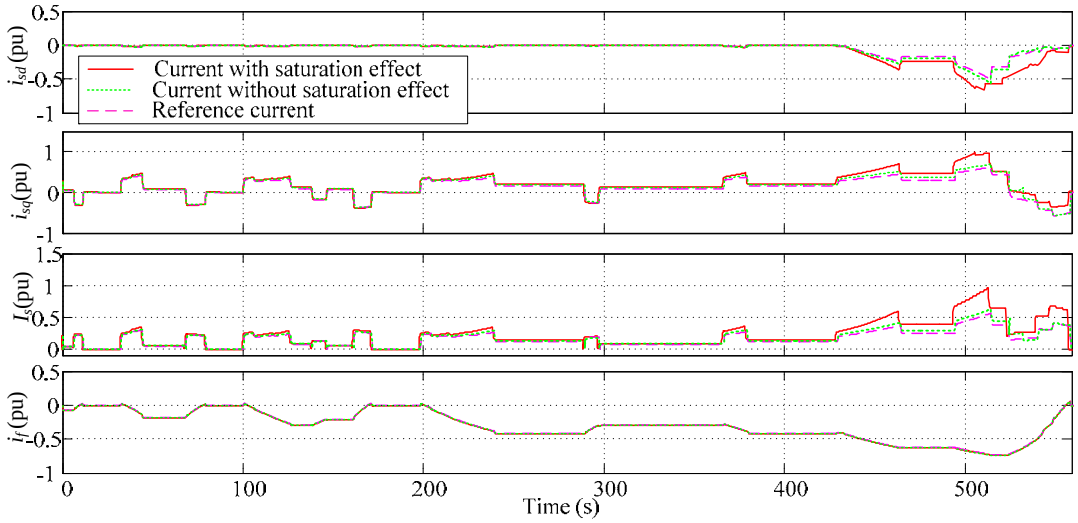

Figure 5.17. Currents obtained with ELMM with iron and copper loss minimization when the machine model takes or does not take into account the magnetic circuit saturation effect

Figure 5.17 proves that the torque control reference generated by the speed compensator and consequently the armature current components are greater than the optimal reference currents when

the machine model takes into account the saturation effect. When the saturation effect is neglected, the armature current components are closer to their optimal references. The small difference noted mainly at high speed in this case is due to the mechanical friction losses. It is recalled that these losses are proportional to the rotor speed. The optimization algorithm minimizing the copper and iron losses is used for this comparison. However, the same conclusion comes out when minimizing the copper losses only.

5.6.2. Vector control with decoupling terms

The iron losses introduce an additional coupling mechanism to the d-q axis circuits. To overcome this problem, a vector control with decoupling terms is proposed (Figure 5.7). This control requires the accurate estimation of the iron losses equivalent resistance R_{ir}, which is not easy. In this simulation, ideal estimation of R_{ir}, i_{sd} and i_{sq} is considered which represents the best scenario for the control. The results obtained with and without decoupling terms over the urban driving cycle are compared in Figure 5.18. The same is applicable for the extra-urban driving cycle. It is clearly shown that the shifting angle introduced by the iron losses does not really affect the control. The currents that govern the electromagnetic torque and the actual currents in the armature windings are practically the same, as noted in Figure 5.19. In fact, the ratio R_s-to-R_{ir} tends to zero. Referring to (1.27) and (1.28), since $R_{ir} >> R_s$, the induced currents are practically driven directly by the armature voltage with no need to any decoupling term. Therefore, the classic field-oriented control can be used even when iron losses are considered.

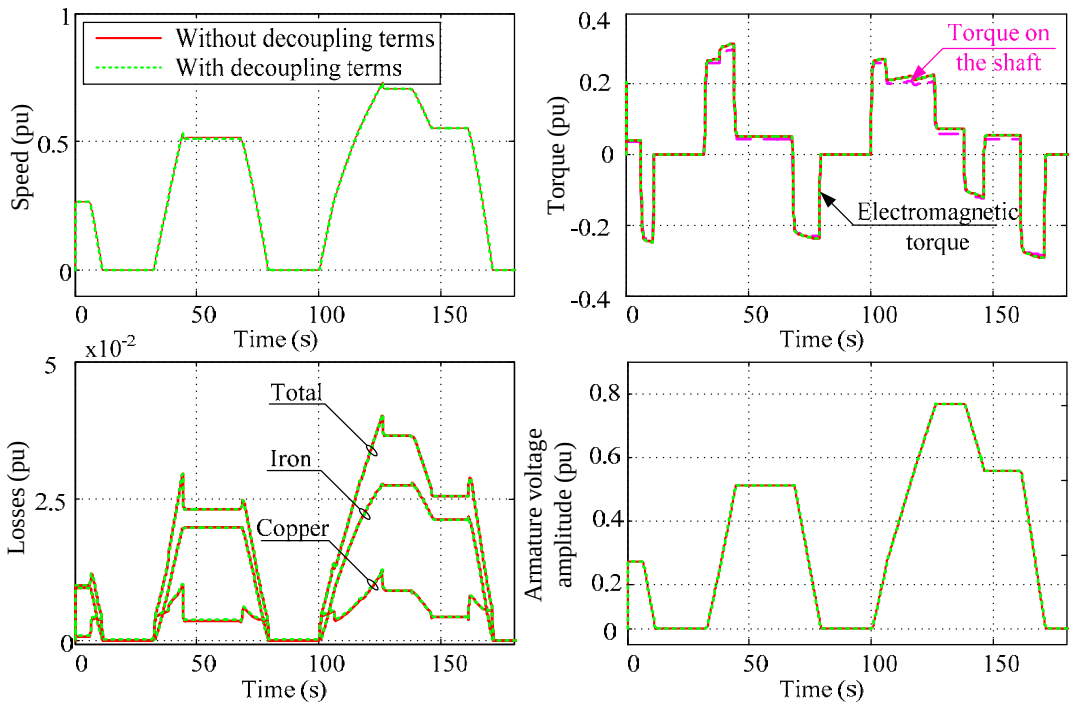

Figure 5.18. Simulation results obtained with iron and copper loss minimization by ELMM with and without decoupling terms

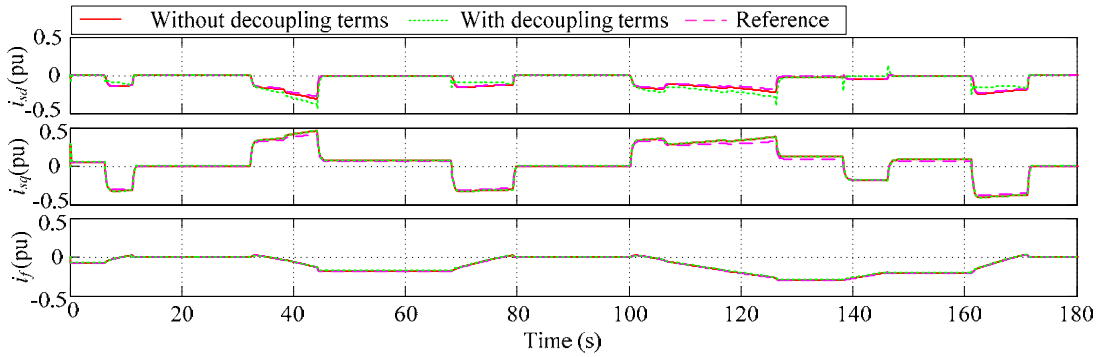

Figure 5.19. Comparison between the currents obtained with iron and copper losses minimization by ELMM with and without decoupling terms

5.6.3. Simulation with electric parameter variation

It is interesting to test the sensitivity of the proposed optimal control to the variation of the machine electrical parameters. In fact, the optimal reference currents are found in terms of the nominal parameter values. Nevertheless, these parameters are easy to vary with the motor state especially when the machine runs in saturation [74]. In addition, the identification of the machine parameters might be not accurate enough. Therefore, the motor parameter uncertainty might affect the control performance and the analytical equations have more limits in practice. In order to evaluate the robustness of the proposed approach, the control based on ELMM with iron and copper loss minimization is tested by simulation when the machine parameters vary over the urban driving cycle. The resistances, R_s and R_f, vary simultaneously by ±50%. The inductances, L_{sd}, L_{sq}, M_{sf}, and L_f are varied by ±25%.

Figure 5.20 attests that in spite of the parameters variation the speed and torque requirements are met. In addition, the proposed optimal control ensures the minimal losses when comparing to the other MTPA strategies under the same conditions as shown in Figure 5.21.

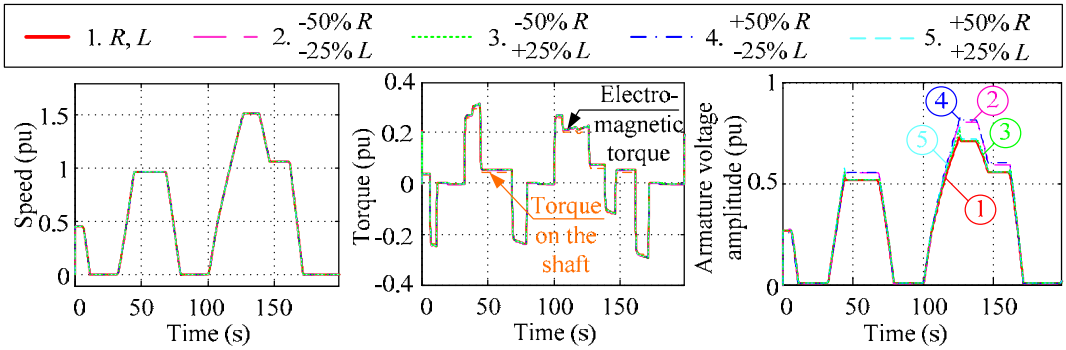

Figure 5.20. Simulation results obtained with the motor optimal control when the electrical parameters vary

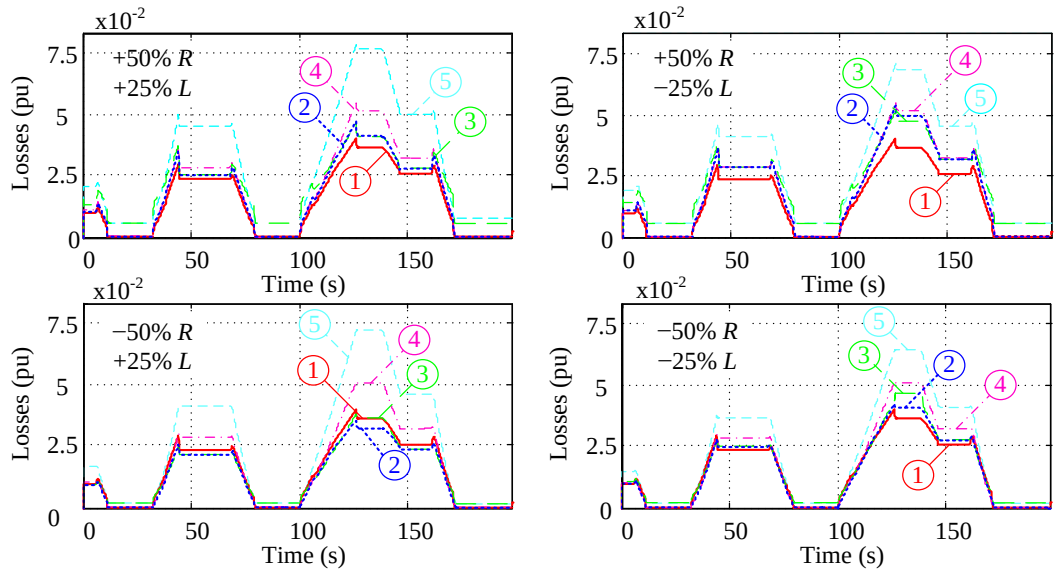

Figure 5.21. Iron and copper losses obtained with different control strategies when the electrical parameters vary: 1. Nominal parameters with ELMM minimizing iron and copper losses, 2. ELMM minimizing iron and copper losses, 3. MTPA ith $i_f = -2$ A, 4. MTPA with $i_f = 0$ A, 5. MTPA with $i_f = 2$ A

Conclusion

This chapter presents the HESM as a candidate machine to be used for electric propulsion, in EV application particularly. An optimal current control for the HESM operating in motor mode is studied. The aim of the control is to meet speed and torque imposed by the NEDC while insuring minimal losses. The approach consists of using classic PI controllers with optimal reference currents (armature current components and field current). Analytical expression of these references are found using ELMM. The copper losses are minimized at first. The optimization problem is extended next to include the iron losses too.

Compared with common motor control strategies, the proposed approach leads to the optimal solution with respect to voltage and current constraints. This is proven by calculation with Matlab software and by simulation with Matlab/Simulink.

Chapter 5 considers the minimization of the losses in the HESM itself. In Chapter 6, the attention will be paid to the entire electric propulsion system. The battery and the converters will be added to the simulation model. The minimization problem will be extended in order to include the losses due to the inverter and the chopper.

Chapter 6. Optimal Control of the HESM in an Electric Vehicle

Introduction

EV can be very useful to improve fuel economy and reduce the level of pollution especially in the urban area. With its compact size and its DC field winding, the HESM is a potential candidate machine to be used in EV. This chapter develops an optimal control of the HESM for such application.

Prior to the control design, the elements of the powertrain are to be modeled. Figure 6.1 represents the different components of the electric propulsion system in an EV. Each unit is modeled as an object and connected to the others by means of input signals and output state variables as shown in the figure.

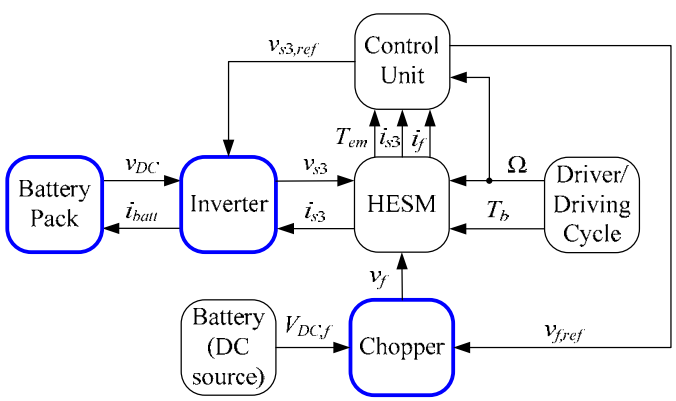

Figure 6.1. Functional diagram of the electric power set in an EV

The main battery pack is modeled in a first place (section 6.1). The proposed model takes into account the State Of Charge (SOC) variation. Since the excitation voltage is at least ten times smaller than the voltage across the main battery stack, a separate DC source is used to supply the

excitation coil. This independent battery is not a key component in the powertrain and will not be modeled. Concerning the power converters, the inverter feeding the motor is based on Insulated Gate Bipolar Transistors (IGBT) with Pulse Width Modulation (PWM) control. It is modeled in section 6.2. The excitation coil is supplied via a step down class E chopper that is modeled in section 6.3. The modeling of the converters includes the computation of their respective losses.

Concerning the motor control, the current and speed compensators designed in Chapter 5 are retained. ELMM is used to compute new optimal reference currents. The difference in this case is that, in order to improve the efficiency of the electric propulsion set and to assure a good autonomy and distance range, the HESM control is not limited to the minimization of the motor copper and iron losses. The control aims to minimize the electric losses in the entire electric propulsion set. Thus, the inverter losses and the chopper losses are part of the function to minimize [109]. The optimization problem solution is validated with Matlab software over the NEDC. The control is tested by simulation as well with Matlab/Simulink.

6.1. Battery modeling

6.1.1. State of art

For EVs, knowing the dynamic electric storage components is necessary for the optimization of the system. However, batteries remain the most difficult elements to model. The battery models shall be capable of predicting the SOC, the *I-V* characteristic, the dynamic behavior and the battery run-time of different battery types. The model must be simple enough to be easily implemented in the real time application but must be accurate enough to represent the main phenomena. Researchers have developed a wide variety of battery models with varying degree of complexity. There are basically three types of battery model reported in the literature: electrochemical, mathematical and electrical circuit-based. The electrochemical models characterize the physical aspect of the battery but they are complex and time consuming. The mathematical models adopt empirical equations and stochastic approaches to predict system level behavior. These models cannot offer any *I-V* information that is important to circuit simulation and optimization. In addition, they suffer from high prediction error [23]. Electric models are electric equivalent circuits using a combination of voltage sources, resistors and/or capacitors for co-design and co-simulation with other electrical systems.

The simplest electric model consists of an ideal voltage source in series with an internal resistance. However, this model does not take into account the battery SOC. The classic model is improved by considering an open circuit voltage source in series with a resistor and in parallel with a RC circuit, in order to represent the dynamic behavior of the battery [29]. The model is then enhanced and the parallel RC circuit turns to RC parallel network to track the battery response to transient loads (Thevenin models and impedance-based models) [23] [62]. These models are accurate only for a fixed SOC. The identification of all these models parameters is based in most of the cases on a complicated technique called the impedance spectroscopy or involves long test process [23] [63]. Since the SOC is an internal chemical state of battery and cannot be measured, many papers proposed to estimate it by online estimators [61] [139].

The model used in this document is based on the one exposed in [126]. It takes into account the charge and discharge dynamics of the battery. Its validity is extended for variable charging and discharging current. An interesting feature of the model is the simplicity to extract the dynamic model parameters from the battery datasheet [127]. The model used is a modified version of the Shepherd model. Shepherd developed an equation to describe the electrochemical behavior of a

battery directly in terms of terminal voltage, open circuit voltage, internal resistance, discharge current and SOC.

The model can be used for several battery types: Lead-Acid, Lithium-Ion (Li-Ion), Nickel-Cadmium (NiCd) and Nickel Metal Hydride (NiMH). In this document, the NiMH is considered since NiMH chemistry is the technology of choice of powering the hybrid electric cars until 2010 in hybrid electric cars. The study can be extended to other battery types in a later phase.

6.1.2. Mathematical model

In discharge mode, the battery voltage is given by (6.1) [126]. This equation is valid for any battery type.

$$v_{batt}(t) = E_{batt} - R_{batt} i_{batt} - \underbrace{K \frac{Q_{batt}}{Q_{batt} - i_{batt} t} i_{batt} t}_{\substack{polarization \\ voltage}} - \underbrace{K \frac{Q_{batt}}{Q_{batt} - i_{batt} t} i_{batt,fil}}_{\substack{polarization \\ resistance}} + \underbrace{v_{exp}(t)}_{\substack{exponentiel \\ voltage}} \tag{6.1}$$

For the Lead-Acid, NiMH and NiCd, a hysteresis phenomenon between the charge and discharge occurs in the exponential area and it should be taken into consideration [140]. Therefore, the exponential voltage is given by (6.2).

$$\dot{v}_{exp}(t) = B_{exp} \left| i_{batt}(t) \right| \left(A_{exp} u(t) - v_{exp}(t) \right) \tag{6.2}$$

$u(t) = 1$ in charge mode and $u(t) = 0$ in discharge mode.

The variables and parameters introduced in (6.1) and (6.2) are defined below.

v_{batt} is the battery voltage (V);

E_{batt} is the battery constant voltage (open circuit voltage) (V);

K is a polarization constant (V/Ah) or polarization resistance (Ω);

Q_{batt} is the battery capacity (Ah), given by the manufacturer datasheet;

$i_{batt} t = \int_0^t i_{batt} dt$ is the extracted battery charge (Ah);

A_{exp} is the exponential zone amplitude (V);

B_{exp} is the exponential zone time constant inverse $(\text{Ah})^{-1}$;

R_{batt} is the internal resistance given by the manufacturer datasheet (Ω);

i_{batt} is the battery current (A);

$i_{batt,fil}$ is the battery filtered current (A).

The model developed is based on the following assumptions [126]:

- The internal resistance is constant and does not vary with the current amplitude.

- The model parameters, extracted from the discharge curve, are the same for the charge phase.
- The temperature does not affect the model behavior.
- The self-discharge of the battery is neglected. This is justified since the recent technologies tend to minimize its effect.
- The battery has no memory effect. Actually, the NiMH batteries have low sensitivity to this effect.
- The maximum SOC cannot be greater than 100% if the battery is overcharged because the maximum capacity is Q_{batt}.

6.1.3. Model parameter extraction

As it is explained in [127], only three points on the manufacturer discharge curve, in steady state at constant current, are needed to identify the unknown parameters of (6.1) and (6.2). These points are the fully charged point, the end of the exponential zone and the end of the nominal zone, noted P_1, P_2 and P_3 in Figure 6.2 respectively. The nominal current discharge curve is considered.

A_{exp} is the voltage drop within the exponential zone.

$$A_{exp} = V_{P1} - V_{P2} \tag{6.3}$$

At the fully charged voltage, the extracted charge is nil, as well as the filtered current. Therefore, E_{batt} is found by (6.4).

$$V_{P1} = E_{batt} - R_{bqtt} i_{discharge} + A_{exp} \tag{6.4}$$

Assuming that the energy of the exponential term is almost zero after three time constants, B_{exp} is calculated given the charge at the end of the exponential zone.

$$Q_{batt,P2} = \frac{3}{B_{exp}} = i_{discharge}\left(t_{P2} - t_{P1}\right) \tag{6.5}$$

Finally, K is computed by subtracting V_{P3} from V_{P2}.

The battery used is the NiMH 1.2 V, 6.5 Ah (HHR650D from Panasonic). Its characteristics are listed in Appendix B. Its corresponding parameters are extracted from its datasheet and nominal discharge curve (Figure 6.2). The battery pack contains 250 battery cells in order to reach 300 V, voltage level required for the prototype machine supply. Figure 6.2 shows the simulation results superimposed to the datasheet curve for different discharge currents. It is noted that the simulated curves match the real curves during almost 80% of the discharge phase regardless the discharge current value.

6.2. Inverter modeling

As illustrated in Figure 6.1, the inverter model receives as inputs the available battery pack voltage, along with the three-phase currents in the machine armature windings. It calculates the current drawn from the battery pack and the three-phase voltages across the motor terminals given the three-phase reference voltages generated by the control unit. In a first place, the inverter modeling is carried out under the assumptions of ideal switching and no losses. The impact of the losses is then taken into account. A typical three-leg voltage source inverter consisting of six IGBTs and six anti-parallel diodes is considered.

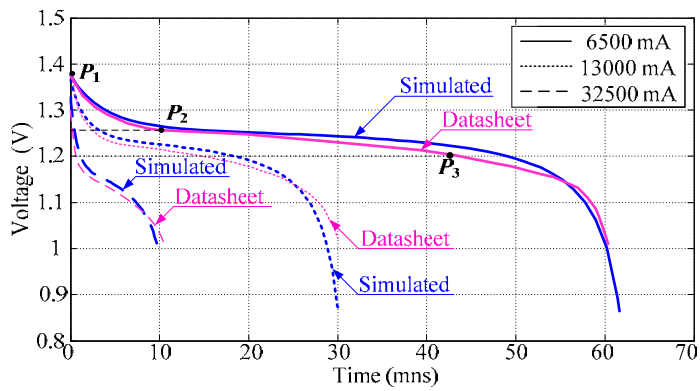

Figure 6.2. Discharge curves for three discharge currents: datasheet and simulation results

6.2.1. Mathematical model

6.2.1.a. Ideal inverter model

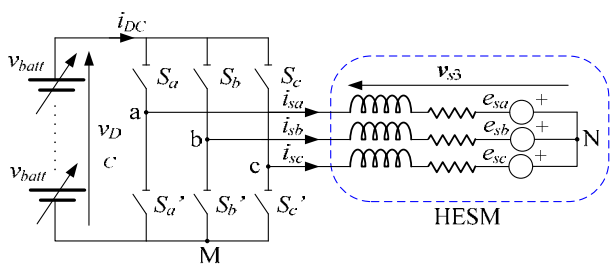

Figure 6.3. Inverter generic model

Figure 6.3 represents a generic model of the inverter. This model is the dual form of the diode bridge rectifier modeled in paragraph 4.1.1 under the continuous conduction mode assumption (Figure 4.1). Thus, the voltage relationship (4.3) and the current relationship (4.5) remain valid. The only difference is that the switching functions associated with the converter legs are not Heaviside functions anymore. For the PWM inverter, these functions are generated by comparing the reference voltage to the sawtooth carrier. f_j is the switching function associated with the leg j ($j = a, b, c$).

- $f_j = 1$ if $v_j(t) > v_{carrier}(t)$.
- $f_j = 0$ if $v_j(t) < v_{carrier}(t)$.

Equation (6.6) computes the three-phase alternating voltages in terms of the battery voltage. Equation (6.7) gives the DC current in terms of the three-phase currents.

$$\boldsymbol{v}_{s3} = \frac{1}{3}\begin{bmatrix} 2 & -1 & -1 \\ -1 & 2 & -1 \\ -1 & -1 & 2 \end{bmatrix} \boldsymbol{f}_3 v_{DC} = \boldsymbol{Q}\boldsymbol{f}_3 v_{DC} = 250\boldsymbol{Q}\boldsymbol{f}_3 v_{batt}(t) \tag{6.6}$$

$$i_{DC} = \boldsymbol{i}_{s3}{}^t \boldsymbol{f}_3 \tag{6.7}$$

With $\boldsymbol{f}_3 = \begin{pmatrix} f_a & f_b & f_c \end{pmatrix}^t$.

6.2.1.b. Inverter model taking into account the inverter losses

Due to the inverter losses, the real current drawn from the battery in discharge mode is greater than the one computed by (6.7). Let $P_{inv}(t)$ be the inverter losses for a given operating point. The battery current is then obtained by (6.8).

$$i_{batt}(t) = i_{DC}(t) + \frac{P_{inv}(t)}{v_{DC}(t)} \tag{6.8}$$

For $i_{DC}(t) > 0$, i.e. the HESM operates in motor mode, the battery is in discharge mode and $i_{batt}(t) > i_{DC}(t)$. For the regenerative braking case, $i_{DC}(t) < 0$, the battery is in charge mode and $i_{batt}(t) < i_{DC}(t)$. This proves that the model established hereby describes a bidirectional inverter with loss consideration.

6.2.2. Inverter losses

Regardless of the converter type, the main losses of a power electronic switch are the static losses that include conduction and blocking losses and the switching losses that include turn-on and turn-off losses of the semiconductor devices (IGBTs and diodes). Compared to the total losses, blocking losses as well as diode turn-on losses are too small and can be neglected. In addition, it shall be pointed that the switching loss contribution is greater than the conduction losses.

The inverter losses are computed considering the basic inverter cell composed of the IGBT and the anti-parallel diode. The switching and conduction losses for both devices are extracted and modeled separately in a first place. The average inverter losses are the sum of all terms.

6.2.2.a. Switching losses

The instantaneous losses of a basic cell P_{sw} are evaluated using (6.9). P_{swT} are the transistor switching losses, E_{onT} and E_{offT} are the transistor turn-on and turn-off energies. P_{swD} and E_{offD} are the reverse recovery diode power and energy respectively. f_{sw} is the inverter switching frequency, it is arranged at 8 kHz.

$$P_{sw} = P_{swT} + P_{swD} = \left(E_{onT} + E_{offT} + E_{offD}\right) f_{sw} \tag{6.9}$$

For the IGBT and diode, the switching energies versus the device current are usually given by the manufacturer. Hence, E_{onT}, E_{offT} and E_{offD} can be expressed in terms of the IGBT and diode direct currents, noted i_T and i_D respectively, as shown in (6.10) [77] [78]. The A coefficients tend to zero.

$$\begin{aligned} E_{onT}(i_T) &= A_{onT} + B_{onT} i_T + C_{onT} i_T^2 \\ E_{offT}(i_T) &= A_{offT} + B_{offT} i_T + C_{offT} i_T^2 \\ E_{offD}(i_D) &= A_{offD} + B_{offD} i_D + C_{offD} i_D^2 \end{aligned} \tag{6.10}$$

The coefficients introduced in (6.10) are found by fitting the datasheet curves [78]. The three-phase inverter model used in simulation is based on the SK30GB128 module manufactured by SEMIKRON. Its main characteristics are listed in Appendix B. The generated energy curves and those given by the manufacturer are superimposed in Figure 6.4.

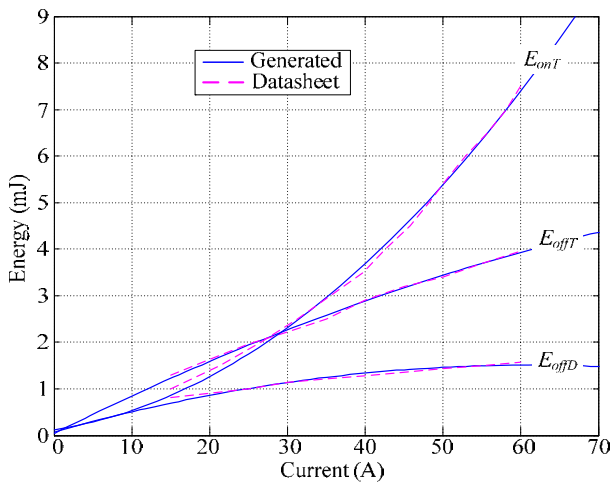

Figure 6.4. Typical turn-on/off energy for the SK30GB128 module (by SEMIKRON)

Assuming sinusoidal time dependence for the motor current [125], $i_{sa}(t) = \sqrt{2} I_s \cos(\omega t - \varphi)$, the basic cell switching losses can be evaluated by averaging the instantaneous losses in a modulation period [34] [47][78] [92].

$$P_{sw} = \left(\left(\frac{B_{onT} + B_{offT} + B_{offD}}{\pi} + \frac{C_{onT} + C_{offT} + C_{offD}}{4} \sqrt{2} I_s \right) \sqrt{2} I_s + A_{onT} + A_{offT} + A_{offD} \right) f_{sw} \tag{6.11}$$

6.2.2.b. Conduction losses

The IGBT and diode conduction losses are computed by (6.12) and (6.13).

$$P_{condT}(i_T) = V_{CE} i_T + r_{CE} i_T^{\,2} \tag{6.12}$$

$$P_{condD}(i_D) = V_D i_D + r_D i_D^{\,2} \tag{6.13}$$

V_{CE} and V_D are respectively the transistor and diode forward voltage drops. r_{CE} is the collector-emitter resistance. r_D is the diode resistance in forward bias. These parameters are extracted from the manufacturer datasheet [91]. They are assumed constant, which is true over the valid current range. Equations (6.12) and (6.13) are reformulated [92].

$$P_{condT} = V_{CE} I_{T,AVE} + r_{CE} I_{T,RMS}^{\,2} \tag{6.14}$$

$$P_{condD} = V_D I_{D,AVE} + r_D I_{D,RMS}^{\,2} \tag{6.15}$$

$I_{T,AVE}$ and $I_{T,RMS}$ ($I_{D,AVE}$ and $I_{D,RMS}$) are the IGBT (diode) average and RMS currents respectively. By integrating their instantaneous formulations over one period [34] [92], these currents are expressed in terms of the line current amplitude I_s, the PWM index m and the power factor $\cos\varphi$ as shown in (6.16) to (6.19) [47]. m is defined as the ratio of the reference voltage to the peak of the carrier.

$$I_{T,AVE} = \sqrt{\ } I_s \sqrt{2} \left(\frac{1}{2\pi} + \frac{m \cos\varphi}{8} \right) \tag{6.16}$$

$$I_{T,RMS} = I_s\sqrt{2}\sqrt{\frac{1}{8}+\frac{m\cos\varphi}{3\pi}} \tag{6.17}$$

$$I_{D,AVE} = I_s\sqrt{2}\left(\frac{1}{2\pi}-\frac{m\cos\varphi}{8}\right) \tag{6.18}$$

$$I_{D,RMS} = I_s\sqrt{2}\sqrt{\frac{1}{8}-\frac{m\cos\varphi}{3\pi}} \tag{6.19}$$

6.2.2.c. Total inverter losses

By adding the switching and conduction losses, the total basic cell losses are computed. Thereafter, the sum is multiplied by the number of devices, six, in order to obtain the total inverter losses.

$$\begin{aligned} P_{inv} &= 6\left(P_{swT}+P_{swD}+P_{condT}+P_{condD}\right) \\ &= 6\left(f_{sw}\left(\frac{B_{onT}+B_{offT}+B_{offD}}{\pi}\right)+V_{CE}\left(\frac{1}{2\pi}+\frac{m\cos\varphi}{8}\right)+V_D\left(\frac{1}{2\pi}-\frac{m\cos\varphi}{8}\right)\right)\sqrt{2}I_s \\ &\quad +6\left(f_{sw}\left(\frac{C_{onT}+C_{offT}+C_{offD}}{4}\right)+r_{CE}\left(\frac{1}{8}+\frac{m\cos\varphi}{3\pi}\right)+r_D\left(\frac{1}{8}-\frac{m\cos\varphi}{3\pi}\right)\right)2I_s^{\,2} \\ &\quad +6\left(A_{onT}+A_{offT}+A_{offD}\right) \end{aligned} \tag{6.20}$$

Practically, V_{CE} and V_D are almost equal. The same is true for the resistances r_{CE} and r_D. Thus, the cosine terms in (6.20) can be cancelled. Thus, for a given PWM switching frequency, the inverter losses depend on the armature current magnitude that can be expressed in terms of the direct and quadrature axes current components as shown in (6.21).

$$\begin{aligned} P_{inv}\left(I_s\right) &= \underbrace{\frac{6}{\pi}\left(f_{sw}\left(B_{onT}+B_{offT}+B_{offD}\right)+V_{CE}\right)}_{A}\sqrt{2}I_s+\underbrace{\frac{3}{2}\left(f_{sw}\left(C_{onT}+C_{offT}+C_{offD}\right)+r_{CE}\right)}_{B}2I_s^{\,2} \\ &\quad +6f_{sw}\left(A_{onT}+A_{offT}+A_{offD}\right) \\ &= A\sqrt{i_{sd}^{\,2}+i_{sq}^{\,2}}+B\left(i_{sd}^{\,2}+i_{sq}^{\,2}\right)+6f_{sw}\left(A_{onT}+A_{offT}+A_{offD}\right) \end{aligned} \tag{6.21}$$

6.3. Chopper modeling

During the flux weakening phase, the excitation current and voltage are negative. Thus, a four-quadrant chopper is needed to supply the excitation winding. The chopping frequency is set to 8 kHz.

6.3.1. Mathematical model

Figure 6.5 represents a step down class E chopper circuit. Each switch cell consists of one IGBT with an anti-parallel diode. There is no objection on using the same module as for the inverter model: SK30GB128 manufactured by SEMIKRON.

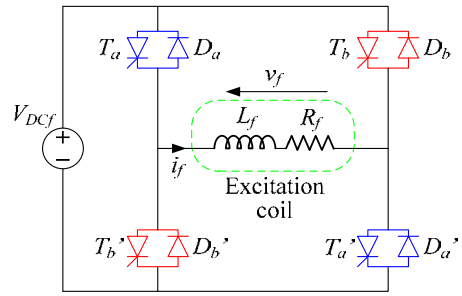

Figure 6.5. Class E chopper circuit

When the reference voltage is positive, T_a and T_a' are triggered and conduct for $t = d \times T_{chop}$. T_{chop} is the chopping period. d is the duty cycle. It is generated by comparing the carrier voltage and the reference voltage. When the reference voltage is negative, T_b and T_b' are triggered and conduct for $t = (1-d) \times T_{chop}$ (complementary control). Based on these conduction conditions, the chopper is modeled under the hypothesis of ideal switches. Figure 6.6 depicts the output voltage waveform. The mean value of the excitation voltage is computed as given by (6.22).

$$v_{f,mean} = (2d-1)V_{DCf} \tag{6.22}$$

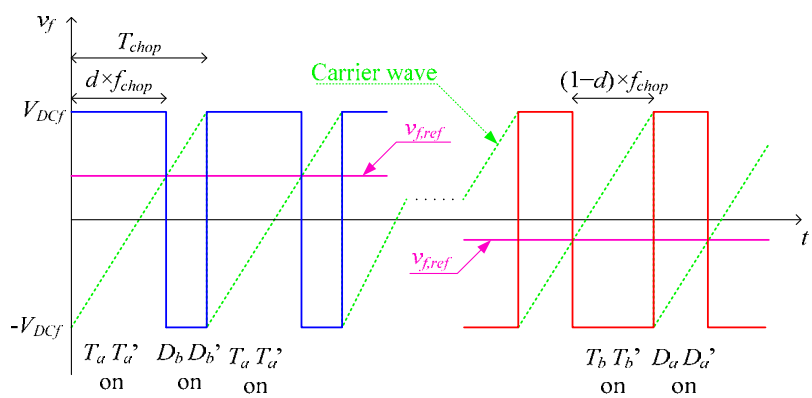

Figure 6.6. Output voltage waveform

6.3.2. Chopper losses

As it was the case for the inverter, the losses in the chopper are due to two phenomena: the switching and the conduction of the semiconductors.

6.3.2.a. <u>Switching losses</u>

During a switching period, the chopper operates in two different quadrants invoking a switching between two transistors and two diodes as shown in the waveform of Figure 6.6. The chopper switching losses are given by (6.23). Compared to the other converter losses, the diode turn-on losses are neglected.

$$P_{chop,sw} = 2\left(P_{chop,swT} + P_{chop,swD}\right) = 2 f_{chop}\left(E_{onT}(i_T) + E_{offT}(i_T) + E_{offD}(i_D)\right) \tag{6.23}$$

The switching energies are expressed in terms of the IGBT and diode direct currents based on the loss curves provided by the manufacturer. However, since the excitation circuit is highly

inductive, continuous conduction mode is assumed. Thus, the excitation current flows in the conducting devices. Hence, E_{onT}, E_{offT} and E_{offD} are computed in terms of the field current.

$$E_{onT}\left(i_T\right)+E_{offT}\left(i_T\right)+E_{offD}\left(i_D\right)=\left(A_{onT}+A_{offT}+A_{offD}\right)+\left(B_{onT}+B_{offT}+B_{offD}\right)\left|i_f\right| +\left(C_{onT}+C_{offT}+C_{offD}\right)i_f^{\,2} \tag{6.24}$$

6.3.2.b. Conduction losses

Figure 6.6 shows the conducting devices for each portion of the cycle. When $v_{f,ref} > 0$, the field current flows through two transistors for $t = d\times T_{chop}$ then it runs through two diodes for $(1-d)\times T_{chop}$. Hence, the IGBT and diode conduction losses are computed by (6.25) and (6.26) respectively.

$$P_{chop,condT}=\left(V_{CE}\left|i_f\right|+r_{CE}i_f^{\,2}\right)d \tag{6.25}$$

$$P_{chop,condD}=\left(V_D\left|i_f\right|+r_D i_f^{\,2}\right)(1-d) \tag{6.26}$$

The chopper conduction losses are then given by (6.27).

$$P_{chop,cond}=2\left(V_D\left|i_f\right|+r_D i_f^{\,2}\right)+\left(V_{CE}\left|i_f\right|+r_{CE}i_f^{\,2}-V_D\left|i_f\right|-r_D i_f^{\,2}\right)d \tag{6.27}$$

Practically, V_{CE} and V_D on one hand and r_{CE} and r_D on the other hand are almost equal. Equation (6.27) is simplified as shown in (6.28). Under this hypothesis, (6.28) is valid for $v_{f,ref} < 0$ too.

$$P_{chop,cond}=2\left(V_D\left|i_f\right|+r_D i_f^{\,2}\right) \tag{6.28}$$

6.3.2.c. Total chopper losses

The chopper losses are the sum of the switching losses and the conduction losses, both expressed in terms of the field current.

$$P_{chop}\left(i_f\right)=\underbrace{2\left(f_{chop}\left(B_{onT}+B_{offT}+B_{offD}\right)+V_D\right)}_{C}\left|i_f\right|+\underbrace{2\left(f_{chop}\left(C_{onT}+C_{offT}+C_{offD}\right)+r_D\right)}_{D}i_f^{\,2} +2f_{chop}\left(A_{onT}+A_{offT}+A_{offD}\right) \tag{6.29}$$

The power drawn from the source supplying the DC chopper equals (6.30).

$$P_{exc}=v_f i_f+P_{chop}\left(i_f\right) \tag{6.30}$$

6.4. Control of the electric propulsion set in an EV

6.4.1. Optimal reference currents

The ELMM, explained in Appendix A, is used to compute the optimal reference currents.

6.4.1.a. Problem formulation

The function to minimize is the sum of the machine copper losses (5.15), the machine iron losses (5.78), the inverter losses (6.21) and the chopper losses (6.29) [109].

$$\begin{aligned} f(\boldsymbol{x}) &= \left(\frac{3}{2}R_s + B\right)\left(i_{sd1}{}^2 + i_{sq1}{}^2\right) + \left(R_f + M_{sf}{}^2 k_{ir} + D\right) i_f{}^2 + \left(2k_{ir}\Phi_M M_{sf} + Csign\left(i_f\right)\right) i_f \\ &\quad + A\sqrt{i_{sd1}{}^2 + i_{sq1}{}^2} \\ &= k_s\left(i_{sd1}{}^2 + i_{sq1}{}^2\right) + k_{f2} i_f{}^2 + k_{f1} i_f + A\sqrt{i_{sd1}{}^2 + i_{sq1}{}^2} \end{aligned} \tag{6.31}$$

The equality and inequality constraints are given by (6.32), (6.33) and (6.34) respectively.

$$h(\boldsymbol{x}) = \frac{3}{2}p\left(\left(L_{sd} - L_{sq}\right) i_{sd1} + M_{sf} i_f + \Phi_M\right) i_{sq1} - T_{em} = 0 \tag{6.32}$$

$$g_I(\boldsymbol{x}) = \left(i_{sd1}{}^2 + i_{sq1}{}^2\right) - 2I_{s\max}{}^2 \le 0 \tag{6.33}$$

$$g_V(\boldsymbol{x}) = \left(\left(L_{sq} i_{sq1}\right)^2 + \left(L_{sd} i_{sd1} + M_{sf} i_f + \Phi_M\right)^2\right) - 2\left(\frac{\sqrt{2}V_{DC}}{3p\Omega}\right)^2 \le 0 \tag{6.34}$$

$V_{DC}(t)$ is the input voltage across the inverter terminals. It is equal to the voltage delivered by the battery pack as given by (6.1).

The optimal current vector is noted $\boldsymbol{x}^* = \begin{bmatrix} i_{sd1}{}^* & i_{sq1}{}^* & i_f{}^* \end{bmatrix}$. i_{sd1}, i_{sq1} are the currents that produce the electromagnetic torque in the machine.

The gradient of Lagrange function is given by (6.35).

$$\begin{aligned} \nabla l(\boldsymbol{x},\lambda,\boldsymbol{\mu}) &= \begin{bmatrix} 2k_s i_{sd1} + \dfrac{A i_{sd1}}{\sqrt{i_{sd1}{}^2 + i_{sq1}{}^2}} \\ 2k_s i_{sq1} + \dfrac{A i_{sq1}}{\sqrt{i_{sd1}{}^2 + i_{sq1}{}^2}} \\ 2k_{f2} i_f + k_{f1} \end{bmatrix} + \lambda \begin{bmatrix} L_{sdq} i_{sq1} \\ L_{sdq} i_{sd1} + M_{sf} i_f + \Phi_M \\ M_{sf} i_{sq1} \end{bmatrix} + \mu_{I2} \begin{bmatrix} 2i_{sd1} \\ 2i_{sq1} \\ 0 \end{bmatrix} \\ &\quad + \mu_{V2} \begin{bmatrix} 2L_{sd}\left(L_{sd} i_{sd1} + M_{sf} i_f + \Phi_M\right) \\ 2L_{sq}{}^2 i_{sq1} \\ 2M_{sf}\left(L_{sd} i_{sd1} + M_{sf} i_f + \Phi_M\right) \end{bmatrix} \end{aligned} \tag{6.35}$$

With two inequality constraints, four cases are to be considered depending on the active constraints. In addition, the term k_{f1} in (6.35) varies with the field current direction. Theoretically, this leads to two optimization problems with a new inequality constraint defined by (6.36) or (6.37), i.e. sixteen cases are to be studied. However, as it will be shown in the following paragraphs, the use of the equation containing the term k_{f1} prior to the optimal field current computation can be avoided in three of the four cases. Only when no constraint is active, two systems are defined depending on the field current direction. The retained solution in this case is the one that gives the lowest losses. Thus, instead of dealing with sixteen cases, only seven cases are to be studied. The algorithm is clearly explained in the flowchart in Figure 6.7.

$$g_{fp}\left(i_f\right)=-i_f\le 0 \text{ and } k_{f1}=2k_{ir}M_{sf}\Phi_M+C \tag{6.36}$$

$$g_{fn}\left(i_f\right)=i_f\le 0 \text{ and } k_{f1}=2k_{ir}M_{sf}\Phi_M-C \tag{6.37}$$

6.4.1.b. <u>Optimal reference currents with active voltage and current constraints</u>

Setting $\nabla l\left(\boldsymbol{x},\lambda,\boldsymbol{\mu}\right)=0$ with $h\left(\boldsymbol{x}\right)=0$, $g_V\left(\boldsymbol{x}\right)=0$, $g_I\left(\boldsymbol{x}\right)=0$ yields to equations (6.38) to (6.43).

$$2k_s i_{sd1}+\frac{Ai_{sd1}}{\sqrt{i_{sd1}^{\ 2}+i_{sq1}^{\ 2}}}+\lambda L_{sdq}i_{sq1}+2\mu_{V2}L_{sd}\left(L_{sd}i_{sd1}+M_{sf}i_f+\Phi_M\right)+2\mu_{I2}i_{sd1}=0 \tag{6.38}$$

$$2k_s i_{sq1}+\frac{Ai_{sq1}}{\sqrt{i_{sd1}^{\ 2}+i_{sq1}^{\ 2}}}+\lambda\left(L_{sdq}i_{sd1}+M_{sf}i_f+\Phi_M\right)+2\mu_{V2}L_{sq}^{\ 2}i_{sq1}+2\mu_{I2}i_{sq1}=0 \tag{6.39}$$

$$2k_{f2}i_f+k_{f1}+\lambda M_{sf}i_{sq1}+2\mu_{V2}M_{sf}\left(L_{sd}i_{sd1}+M_{sf}i_f+\Phi_M\right)=0 \tag{6.40}$$

$$\frac{3}{2}p\left(L_{sdq}i_{sd1}+M_{sf}i_f+\Phi_M\right)i_{sq1}-T_{em}=0 \tag{6.41}$$

$$\left(\left(L_{sq}i_{sq1}\right)^2+\left(L_{sd}i_{sd1}+M_{sf}i_f+\Phi_M\right)^2\right)-\left(\frac{2V_{DC}}{3p\Omega}\right)^2=0 \tag{6.42}$$

$$\left(i_{sd1}^{\ 2}+i_{sq1}^{\ 2}\right)-2I_{s\max}^{\ 2}=0 \tag{6.43}$$

Equations (6.41), (6.42) and (6.43) yield to (6.44) that is analogous to (5.30).

$$\left(2L_{sq}^{\ 2}I_{s\,max}^{\ 2}-\left(\frac{2V_{DC}}{3p\Omega}\right)^2\right)i_{sq1}^{\ 2}-2K_{em}L_{sq}i_{sq1}\sqrt{2I_{s\,max}^{\ 2}-i_{sq1}^{\ 2}}+K_{em}^{\ 2}=0 \tag{6.44}$$

With $K_{em}=\frac{2}{3p}T_{em}$.

Based on (5.33), the optimal q-axis current is given by (6.45). The computation of the two other optimal currents follows. The Lagrange and Kuhn-Tucker multipliers are computed next. As previously stated, (6.45), (6.46) and (6.47) are independent of k_{f1}. k_{f1} appears only in (6.48) when computing $\mu_{V2}^{\ *}$ once $i_f^{\ *}$ is known.

$$i_{sq1}^{\ *}=\frac{K_{em}}{\sqrt{2}}\frac{\left(0.5\left(\frac{2V_{DC}}{3p\Omega}\right)^2+L_{sq}^{\ 2}I_{s\,max}^{\ 2}-L_{sq}\sqrt{2I_{s\,max}^{\ 2}\left(\frac{2V_{DC}}{3p\Omega}\right)^2-K_{em}^{\ 2}}\right)^{1/2}}{\left(L_{sq}^{\ 2}K_{em}^{\ 2}+\left(L_{sq}^{\ 2}I_{s\,max}^{\ 2}-0.5\left(\frac{2V_{DC}}{3p\Omega}\right)^2\right)^2\right)^{1/2}} \tag{6.45}$$

$$i_{sd1}^{\ *}=-\sqrt{2I_{s\,max}^{\ 2}-i_{sq1}^{\ *2}} \tag{6.46}$$

$$i_f^* = \frac{\left(K_{em} - L_{sdq} i_{sd1}^* i_{sq1}^* - \Phi_M i_{sq1}^*\right)}{M_{sf} i_{sq1}^*} \tag{6.47}$$

$$\mu_{V2}^* = \frac{\left(\frac{k_{f2}}{M_{sf}}\left(K_{em} - L_{sdq} i_{sd1}^* i_{sq1}^* - \Phi_M i_{sq1}^*\right) + 0.5 k_{f1} i_{sq1}^*\right)\left(L_{sdq} i_{sq}^{*3} - K_{em} i_{sd}^*\right)}{M_{sf} K_{em}\left(L_{sq} i_{sq1}^{*3} + L_{sq} i_{sd1}^{*2} i_{sq1}^* + K_{em} i_{sd1}^*\right)} \tag{6.48}$$

$$\lambda^* = \frac{-2\mu_{V2}^* i_{sq1}^*\left(L_{sd} K_{em} + L_{sq} L_{sdq} i_{sd1}^* i_{sq1}^*\right)}{\left(L_{sdq} i_{sq1}^{*3} - K_{em} i_{sd1}^*\right)} \tag{6.49}$$

$$\mu_{I2}^* = \frac{\left(-2k_s + \frac{A}{\sqrt{2} I_{s\,max}} + 2\mu_{V2}^* L_{sq}^2\right) i_{sq1}^{*2} - \lambda^* K_{em}}{2 i_{sq1}^{*2}} \tag{6.50}$$

The second order necessary and sufficient condition of Theorem A.3 is verified in (6.51).

$$\begin{aligned} \boldsymbol{y}^T \nabla^2 l\left(\boldsymbol{x}^*, \lambda^*, \boldsymbol{\mu}^*\right) \boldsymbol{y} = {} & \left(2k_s + 2\mu_{I2}^*\right) y_1^2 + 2k_{f2} y_3^2 + 2\mu_{V2}^*\left(y_1 L_{sd} + M_{sf} y_3\right)^2 \\ & + y_2^2\left(6k_s + 6\mu_{I2}^* + 6\mu_{V2}^* L_{sq}^2 + \frac{A}{\sqrt{2} I_{s\,max}}\left(\frac{1}{i_{sd1}^{*2}} + 2\right)\right) > 0 \,\middle|\, \forall \boldsymbol{y} \neq 0 \end{aligned} \tag{6.51}$$

6.4.1.c. <u>Optimal reference currents with active current constraint</u>

When the voltage constraint is inactive, μ_V is set to zero. The optimization problem is reduced to (6.52) to (6.56).

$$2k_s i_{sd1} + \frac{A i_{sd1}}{\sqrt{i_{sd1}^2 + i_{sq1}^2}} + \lambda L_{sdq} i_{sq1} + 2\mu_{I1} i_{sd1} = 0 \tag{6.52}$$

$$2k_s i_{sq1} + \frac{A i_{sq1}}{\sqrt{i_{sd1}^2 + i_{sq1}^2}} + \lambda\left(L_{sdq} i_{sd1} + M_{sf} i_f + \Phi_M\right) + 2\mu_{I1} i_{sq1} = 0 \tag{6.53}$$

$$2k_{f2} i_f + k_{f1} + \lambda M_{sf} i_{sq1} = 0 \tag{6.54}$$

$$\left(L_{sdq} i_{sd1} + M_{sf} i_f + \Phi_M\right) i_{sq1} - K_{em} = 0 \tag{6.55}$$

$$\left(i_{sd1}^2 + i_{sq1}^2\right) - 2 I_{s\max}^2 = 0 \tag{6.56}$$

Equations (6.52), (6.53) and (6.55) yields to (6.57) and (6.58) that are the same as (5.47) and (5.45) respectively obtained when only the minimization of the copper losses in the machine is considered.

$$i_{sd1}^* = \frac{L_{sdq}}{K_{em}} i_{sq1}^{*3} \tag{6.57}$$

$$\frac{L_{sdq}^{\ 2}}{K_{em}^{\ 2}} i_{sq1}^{\ 6} + i_{sq1}^{\ 2} - 2I_{s\,max}^{\ 2} = 0 \tag{6.58}$$

The optimal q-axis armature current component is given by (5.46) and is recalled in (6.59).

$$i_{sq}^{\ *} = \left(\frac{K_{em} I_{s\,max}}{L_{sdq}} \right)^{1/3} \sqrt{\left(1 + \sqrt{1 + \frac{K_{em}^{\ 2}}{27 L_{sdq}^{\ 2} I_{s\,max}^{\ 4}}} \right)^{1/3} + \left(1 - \sqrt{1 + \frac{K_{em}^{\ 2}}{27 L_{sdq}^{\ 2} I_{s\,max}^{\ 4}}} \right)^{1/3}} \tag{6.59}$$

Given (6.55), the optimal field current is found subsequently.

$$i_f^{\ *} = \frac{\left(K_{em} - L_{sdq} i_{sd1}^{\ *} i_{sq1}^{\ *} - \Phi_M i_{sq1}^{\ *} \right)}{M_{sf} i_{sq1}^{\ *}} \tag{6.60}$$

Based on $i_f^{\ *}$ direction, the multipliers are computed next.

$$\lambda^* = \frac{-\left(2k_{f2} i_f^{\ *} + k_{f1} \right)}{M_{sf} i_{sq1}^{\ *}} \tag{6.61}$$

$$\mu_{I1}^{\ *} = -k_s - \frac{A}{2\sqrt{2} I_{s\,max}} + \frac{\left(2k_{f2} i_f^{\ *} + k_{f1} \right) K_{em}}{2 M_{sf} i_{sq1}^{\ *3}} \tag{6.62}$$

Finally, the second order necessary and sufficient condition is verified in (6.63).

$$\begin{aligned} \boldsymbol{y}^T \nabla^2 l\left(\boldsymbol{x}^*, \lambda^*, \mu_{I1}^{\ *} \right) \boldsymbol{y} = & \left(2k_s + 2\mu_{I1}^{\ *} \right) y_1^{\ 2} + 2k_{f2} y_3^{\ 2} \\ & + \left(6k_s + 6\mu_{I1}^{\ *} + \frac{A}{\sqrt{2} I_{s\,max}} \left(\frac{1}{i_{sd1}^{\ *2}} + 2 \right) \right) y_2^{\ 2} \quad > 0 \ \Big| \ \forall \boldsymbol{y} \neq 0 \end{aligned} \tag{6.63}$$

6.4.1.d. <u>Optimal reference currents with active voltage constraint</u>

The current constraint is inactive, thus μ_I is set to zero. The remaining equations are $\nabla l(\boldsymbol{x}, \lambda, \boldsymbol{\mu}) = 0$, $h(\boldsymbol{x}) = 0$ and $g_V(\boldsymbol{x}) = 0$, they lead to (6.64) to (6.68).

$$2k_s i_{sd1} + \frac{A i_{sd1}}{\sqrt{i_{sd1}^{\ 2} + i_{sq1}^{\ 2}}} + \lambda L_{sdq} i_{sq1} + 2\mu_{V1} L_{sd} \left(L_{sd} i_{sd1} + M_{sf} i_f + \Phi_M \right) = 0 \tag{6.64}$$

$$2k_s i_{sq1} + \frac{A i_{sq1}}{\sqrt{i_{sd1}^{\ 2} + i_{sq1}^{\ 2}}} + \lambda \left(L_{sdq} i_{sd1} + M_{sf} i_f + \Phi_M \right) + 2\mu_{V1} L_{sq}^{\ 2} i_{sq1} = 0 \tag{6.65}$$

$$2k_{f2} i_f + k_{f1} + \lambda M_{sf} i_{sq1} + 2\mu_{V1} M_{sf} \left(L_{sd} i_{sd1} + M_{sf} i_f + \Phi_M \right) = 0 \tag{6.66}$$

$$\left(L_{sdq} i_{sd1} + M_{sf} i_f + \Phi_M \right) i_{sq1} - K_{em} = 0 \tag{6.67}$$

$$\left(\left(L_{sq}i_{sq1}\right)^2+\left(L_{sd}i_{sd1}+M_{sf}i_f+\Phi_M\right)^2\right)-\left(\frac{2V_{DC}}{3p\Omega}\right)^2=0 \tag{6.68}$$

The system resolution yields to (6.69). The solution of (6.69) contains k_{f1} that depends on the field current direction. The problem is that the optimal field current is not known yet. In this case, theoretically two new problems are to be defined with an additional constraint related to the sign of i_f*.

$$\begin{aligned}
&\frac{L_{sdq}}{M_{sf}}\left(k_{f1}L_{sq}-\frac{2k_{f2}}{M_{sf}}\left(L_{sq}\Phi_M+L_{sdq}\sqrt{\left(\frac{2V_{DC}}{3p\Omega}\right)^2-L_{sq}{}^2 i_{sq1}{}^2}\right)\right)i_{sq1}{}^4\\
&+\left(2k_s+\frac{2k_{f2}L_{sd}L_{sdq}}{M_{sf}{}^2}\right)\frac{K_{em}}{L_{sq}{}^2}\left(\frac{2V_{DC}}{3p\Omega}\right)^2 i_{sq1}\\
&-\left(2k_s+\frac{2k_{f2}L_{sd}{}^2}{M_{sf}{}^2}\right)\frac{K_{em}{}^2}{L_{sq}{}^2}\sqrt{\left(\frac{2V_{DC}}{3p\Omega}\right)^2-L_{sq}{}^2 i_{sq1}{}^2}\\
&+\left(\frac{2k_{f2}\Phi_M}{M_{sf}}-k_{f1}\right)\frac{L_{sd}K_{em}}{L_{sq}M_{sf}}i_{sq1}\sqrt{\left(\frac{2V_{DC}}{3p\Omega}\right)^2-L_{sq}{}^2 i_{sq1}{}^2}\\
&+\frac{AK_{em}}{L_{sq}}\left(\frac{-K_{em}\sqrt{\left(\frac{2V_{DC}}{3p\Omega}\right)^2-L_{sq}{}^2 i_{sq1}{}^2}+i_{sq1}\left(\frac{2V_{DC}}{3p\Omega}\right)^2}{\sqrt{K_{em}{}^2+i_{sq1}{}^2\left(\frac{2V_{DC}}{3p\Omega}\right)^2-2K_{em}i_{sq1}\sqrt{\left(\frac{2V_{DC}}{3p\Omega}\right)^2-L_{sq}{}^2 i_{sq1}{}^2}}}\right)=0
\end{aligned} \tag{6.69}$$

On the other hand, no analytical solution for (6.69) can be found. Only recursive numeric algorithm can help to compute i_{sq1}*. To overcome these problems, an approached analytical solution is adopted. It is found that when the q-axis current is equal to (6.70), (6.69) tends to zero regardless the value of k_{f1}. The error brought by this approximation is less than 2% when comparing the losses obtained when using (6.70) to those found by recursive algorithm over the entire driving cycle. This error is negligible especially when considering the gain in computation time. Thus (6.70) is retained as the optimal analytical q-axis current expression.

$$i_{sq1}=\frac{K_{em}\left(\frac{2V_{DC}}{3p\Omega}\right)}{\sqrt{\left(\frac{2V_{DC}}{3p\Omega}\right)^4+K_{em}{}^2L_{sq}{}^2}} \tag{6.70}$$

The other currents and multipliers expression can be easily computed in terms of i_{sq1}*.

$$i_{sd1}{}^*=\frac{\left(-K_{em}+i_{sq1}{}^*\sqrt{\left(\frac{2V_{DC}}{3p\Omega}\right)^2-L_{sq}{}^2 i_{sq1}{}^{*2}}\right)}{L_{sq}i_{sq1}{}^*} \tag{6.71}$$

$$i_f^* = \frac{\left(K_{em} - L_{sdq} i_{sd1}^* i_{sq1}^* - \Phi_M i_{sq1}^*\right)}{M_{sf} i_{sq1}^*} \tag{6.72}$$

$$\mu_{V1}^* = \frac{\left(\left(2k_{f2} i_f^* + 2k_{ir} M_{sf} \Phi_M + C\, sign\left(i_f^*\right)\right) L_{sdq} - 3R_s M_{sf} i_{sd1}^*\right) i_{sq1}^*}{2L_{sq} M_{sf} \left(K_{em} + L_{sq} i_{sd}^* i_{sq1}^*\right)} \tag{6.73}$$

$$\lambda^* = \frac{\left(3R_s M_{sf} i_{sd1}^* - L_{sd}\left(2k_{f2} i_f^* + 2k_{ir} M_{sf} \Phi_M + C\, sign\left(i_f^*\right)\right)\right)}{L_{sq} M_{sf} i_{sq1}^*} \tag{6.74}$$

Finally, the second order necessary and sufficient condition is verified as shown in (6.75).

$$\begin{aligned} \boldsymbol{y}^T \nabla^2 l\left(\boldsymbol{x}^*, \lambda^*, \mu_{V1}^*\right) \boldsymbol{y} \quad &= 2k_s y_1^2 + 2k_{f2} y_3^2 + 2\mu_{V1}^* \left(y_1 L_{sd} + M_{sf} y_3\right)^2 \\ &+ 2y_2^2 \left(4k_s + 4\mu_{V1}^* L_{sq}^2 + \frac{A}{\sqrt{i_{sd1}^2 + i_{sq1}^2}}\right) \qquad \Big| \ \forall \boldsymbol{y} \neq 0 \\ &+ \frac{A}{\left(i_{sd1}^2 + i_{sq1}^2\right)^{3/2}} \left(y_1 i_{sq1} - y_2 i_{sd1}\right)^2 \quad > 0 \end{aligned} \tag{6.75}$$

6.4.1.e. <u>Optimal reference currents with inactive voltage and current constraints</u>

When the voltage and the armature current constraints are not active, both μ_V *and* μ_I are set to zero. The problem formulation is limited to a set of four equations (6.76) to (6.79).

$$2k_s i_{sd1} + \frac{A i_{sd1}}{\sqrt{i_{sd1}^2 + i_{sq1}^2}} + \lambda L_{sdq} i_{sq1} = 0 \tag{6.76}$$

$$2k_s i_{sq1} + \frac{A i_{sq1}}{\sqrt{i_{sd1}^2 + i_{sq1}^2}} + \lambda \left(L_{sdq} i_{sd1} + M_{sf} i_f + \Phi_M\right) = 0 \tag{6.77}$$

$$2k_{f2} i_f + k_{f1} + \lambda M_{sf} i_{sq1} = 0 \tag{6.78}$$

$$\left(L_{sdq} i_{sd1} + M_{sf} i_f + \Phi_M\right) i_{sq1} - K_{em} = 0 \tag{6.79}$$

The use of (6.78) that requires the knowledge of the field current direction cannot be avoided prior to i_f* computation. Thus, two cases are to be considered: $i_f \geq 0$ and $i_f \leq 0$. In each case, a new inequality constraint is introduced.

6.4.1.f. <u>Optimal reference currents with inactive voltage and current constraints with $i_f \geq 0$</u>

When the field current constraint is active, $i_f = 0$ A. The problem is formulated by (6.76), (6.77), (6.79) and (6.80). μ_{fp} is the Kuhn-Tucker multiplier associated to the inequality $i_f \geq 0$.

$$2k_{f2} i_f + k_{f1} + \lambda M_{sf} i_{sq1} - \mu_{fp} = 0 \tag{6.80}$$

The system resolution yields to the forth order polynomial (6.81). It has only two real roots of opposite signs given in (6.82). The index p means that the solution is obtained under positive field current condition.

$$\frac{L_{sdq}{}^2}{K_{em}} i_{sq1}{}^4 + \Phi_M i_{sq1} - K_{em} = 0 \tag{6.81}$$

$$i_{sq1p}{}^* = sign\left(K_{em}\right)\frac{1}{2}\left(-\sqrt{U} + \sqrt{-U + 4\sqrt{\frac{U^2}{4} + \frac{K_{em}{}^2}{L_{sdq}{}^2}}}\right) \tag{6.82}$$

With

$$U = \left(\frac{\Phi_M{}^2 K_{em}{}^2}{2L_{sdq}{}^2} + \sqrt{D}\right)^{1/3} - \frac{4K_{em}{}^2}{3L_{sdq}\left(\frac{\Phi_M{}^2 K_{em}{}^2}{2L_{sdq}{}^2} + \sqrt{D}\right)^{1/3}}$$

$$D = \frac{K_{em}{}^4}{L_{sdq}{}^6}\left(\frac{64K_{em}{}^2}{27} + \frac{\Phi_M{}^4}{4L_{sdq}{}^2}\right)$$

$i_{sd1p}{}^*$ and the multipliers are given by (6.83), (6.84) and (6.85).

$$i_{sd1p}{}^* = \frac{L_{sdq}}{K_{em}} i_{sq1p}{}^{*3} \tag{6.83}$$

$$\lambda_p^* = \frac{-i_{sd1p}{}^*}{L_{sdq} i_{sq1p}{}^*}\left(2k_s + \frac{A}{\sqrt{i_{sd1p}{}^{*2} + i_{sq1p}{}^{*2}}}\right) \tag{6.84}$$

$$\mu_{fp}{}^* = 2k_{ir} M_{sf}\Phi_M + C - \frac{M_{sf} i_{sq1p}{}^{*3}}{K_{em}}\left(2k_s + \frac{A}{\sqrt{i_{sd1p}{}^{*2} + i_{sq1p}{}^{*2}}}\right) \tag{6.85}$$

The necessary and sufficient condition is verified as proven in (6.86).

$$\begin{aligned} \boldsymbol{y}^T \nabla^2 l\left(\boldsymbol{x}^*, \lambda^*, \mu_{V1}{}^*\right)\boldsymbol{y} \quad &= 2k_s\left(y_1{}^2 + y_2{}^2\right) + 2k_{f2} y_3{}^2 + \frac{A\left(y_1 i_{sq1p}{}^* - y_2 i_{sd1p}{}^*\right)^2}{\left(i_{sd1p}{}^2 + i_{sq1p}{}^2\right)^{3/2}} \\ &+ 2\frac{i_{sq1p}{}^{*4}}{K_{em}{}^2}\left(2k_s + \frac{A}{\sqrt{i_{sd1p}{}^{*2} + i_{sq1p}{}^{*2}}}\right) \quad > 0 \end{aligned} \quad \Big| \ \forall \boldsymbol{y} \neq 0 \tag{6.86}$$

When the field current constraint is not active, i.e. $i_f > 0$, $\mu_{fp} = 0$. The problem is formulated by (6.76) to (6.79) with $k_{f1} = 2k_{ir} M_{sf}\Phi_M + C$. Its resolution leads to (6.87).

$$\left(\frac{L_{sdq}{}^2}{K_{em}} + \frac{k_s M_{sf}{}^2}{K_{em} k_{f2}}\right) i_{sq1}{}^4 + \left(\Phi_M - \frac{k_{f1}}{2k_{f2}} M_{sf}\right) i_{sq1} - K_{em} + \frac{M_{sf}{}^2 A}{2k_{f2}} \frac{i_{sq1}{}^3}{\sqrt{L_{sdq}{}^2 i_{sq1}{}^4 + K_{em}{}^2}} = 0 \tag{6.87}$$

The roots of (6.87) cannot be found by an analytical expression. Nevertheless, the approximation given by (6.88) is justified when the voltage constraint is not active.

$$I_s = \sqrt{i_{sd1}{}^2 + i_{sq1}{}^2} = \left|i_{sq1}\right| \tag{6.88}$$

Equation (6.88) turns to a fourth order polynomial (6.89) that has only one positive root given by (6.90).

$$\left(\frac{L_{sdq}{}^2}{K_{em}} + \frac{k_s M_{sf}{}^2}{K_{em} k_{f2}}\right) i_{sq1}{}^4 + \frac{M_{sf}{}^2 A}{2\left|K_{em}\right| k_{f2}} i_{sq1}{}^3 + \left(\Phi_M - \frac{k_{f1}}{2k_{f2}} M_{sf}\right) i_{sq1} - K_{em} = 0 \tag{6.89}$$

$$i_{sq1p}{}^* = sign\left(K_{em}\right)\frac{1}{2}\left(-\sqrt{D} - \sqrt{\frac{M_{sf}{}^4 A^2}{16a} + U} - \frac{M_{sf}{}^2 A}{4a}\right) \tag{6.90}$$

With

$$U = W - \frac{1}{3W}\left(\frac{4k_{f2} Kem}{a} + \frac{bK_{em} M_{sf}{}^2 A}{4a^2}\right)$$

$$W = \left(\frac{K_{em}{}^2}{8a^2}\left(b^2 - \frac{k_{f2} M_{sf}{}^4 A^2}{a} + \sqrt{\left(\frac{4k_{f2} K_{em}{}^2}{3a} + \frac{b\left|K_{em}\right| M_{sf}{}^2 A}{12a^2}\right)^3 + \left(\frac{-b^2 K_{em}{}^2}{8a^2} + \frac{k_{f2} K_{em}{}^2 M_{sf}{}^4 A^2}{8a^3}\right)^2}\right)\right)^{1/3}$$

$$a = L_{sdq}{}^2 k_{f2} + k_s M_{sf}{}^2$$

$$b = 2\Phi_M k_{f2} - k_{f1} M_{sf}$$

$$D = -U + \frac{M_{sf}{}^4 A^2}{8a^2} + 4\sqrt{\left(\frac{U}{2} + \frac{M_{sf}{}^4 A^2}{32a^2}\right)^2 + \frac{k_{f2} K_{em}{}^2}{a} + \frac{b\left|K_{em}\right| M_{sf}{}^2 A}{16a^2}}$$

$i_{sd1p}{}^*$ and λ_p^* have the same expressions in terms of $i_{sq1p}{}^*$ as in (6.83) and (6.84) respectively. The field current is derived from (6.79) and is given by (6.91). $i_{fp}{}^*$ is necessarily positive.

$$i_{fp}{}^* = \frac{-1}{M_{sf}}\left(L_{sdq} i_{sd1p}{}^* + \Phi_M + \frac{K_{em}}{i_{sd1n}{}^*}\right) \tag{6.91}$$

The Lagrange function Hessian $\nabla^2 l\left(\boldsymbol{x}, \lambda, \boldsymbol{\mu}\right)$ is not affected by the constraint on the field current. Thus, the second order sufficient and necessary condition remains the same as in (6.86).

6.4.1.g. <u>Optimal reference currents with inactive voltage and current constraints with $i_f \leq 0$</u>

The current expressions found for $i_f \geq 0$ remain valid. The only difference is that $k_{f1} = 2k_{ir} M_{sf} \Phi_M - C$ in this case. The Kuhn-Tucker multiplier is given by (6.92).

$$\mu_{fn}^{*} = 2k_{ir}M_{sf}\Phi_M - C - \frac{M_{sf}i_{sq1n}^{*3}}{K_{em}}\left(2k_s + \frac{A}{\sqrt{i_{sd1n}^{*2} + i_{sq1n}^{*2}}}\right) \tag{6.92}$$

6.4.1.h. Algorithm flowchart

The optimization algorithm is summarized in Figure 6.7.

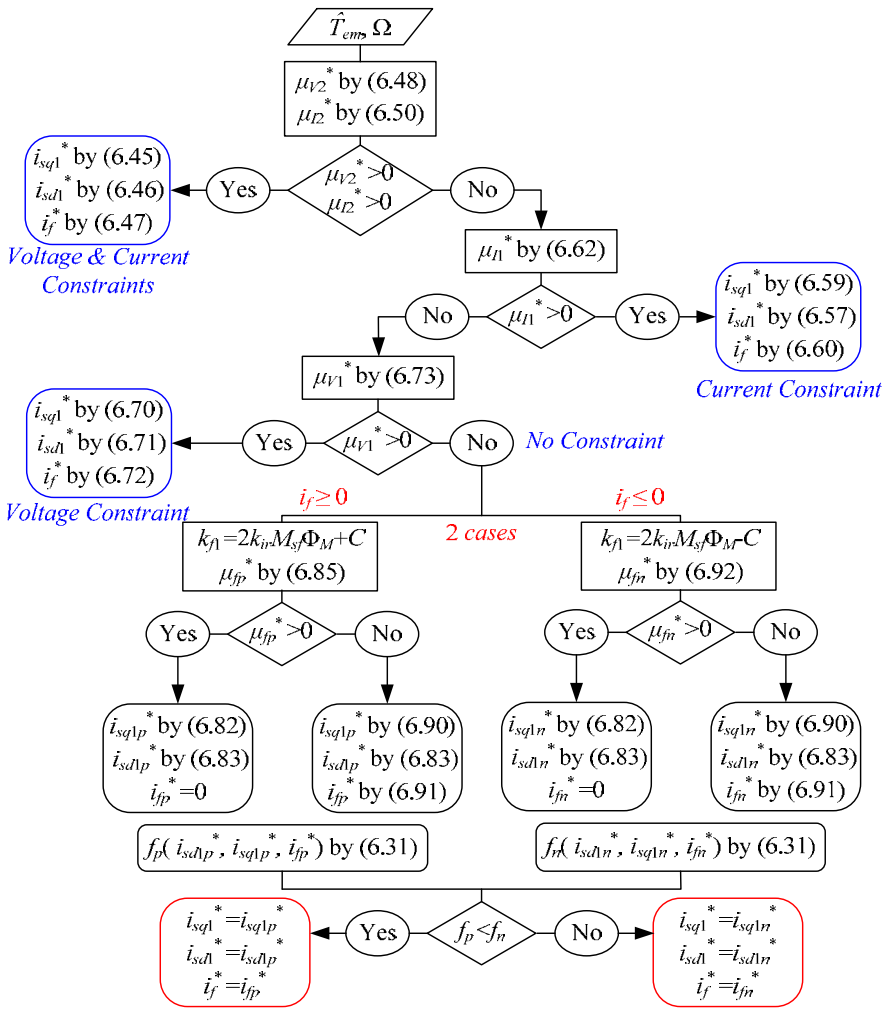

Figure 6.7. Optimization algorithm flowchart

6.4.2. Algorithm validation

At a given speed, the same torque can be produced by a large set of distinct (i_{sd}, i_{sq}, i_f) combinations that satisfy current and voltage constraints. Figure 6.8 proves that all the possible solutions are bounded by the surface generated by the proposed optimization algorithm. No other (i_{sd}, i_{sq}, i_f) combination can produce smaller losses.

In Figure 6.9, the total losses obtained by the proposed optimization algorithm over the NEDC are superimposed to those obtained in section 5.4 with Lagrange method minimizing copper and iron losses. The losses produced when using the exact numeric solution of (6.69) instead of the

(6.70) are plotted too. Over the urban driving cycle, the losses produced by the optimal currents are slightly smaller than those obtained when minimizing the copper and iron losses only. During the extra urban driving cycle, the voltage constraint is active. As shown in the detail, the losses generated by the approached solution given by (6.70) are greater than those obtained with the exact numeric solution of (6.69). Nevertheless, the difference does not exceed 2%. However, it is noted in this case that the algorithm minimizing the copper and iron losses only yields to a better result than the approached solution. In addition, it presents the smallest reference armature voltage.

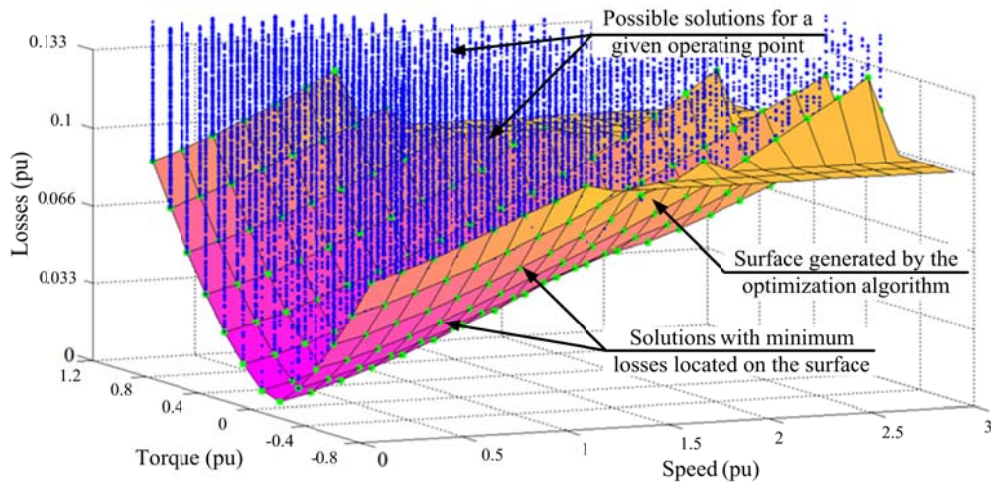

Figure 6.8. Optimization algorithm validation when motor losses and losses in the converters are minimized

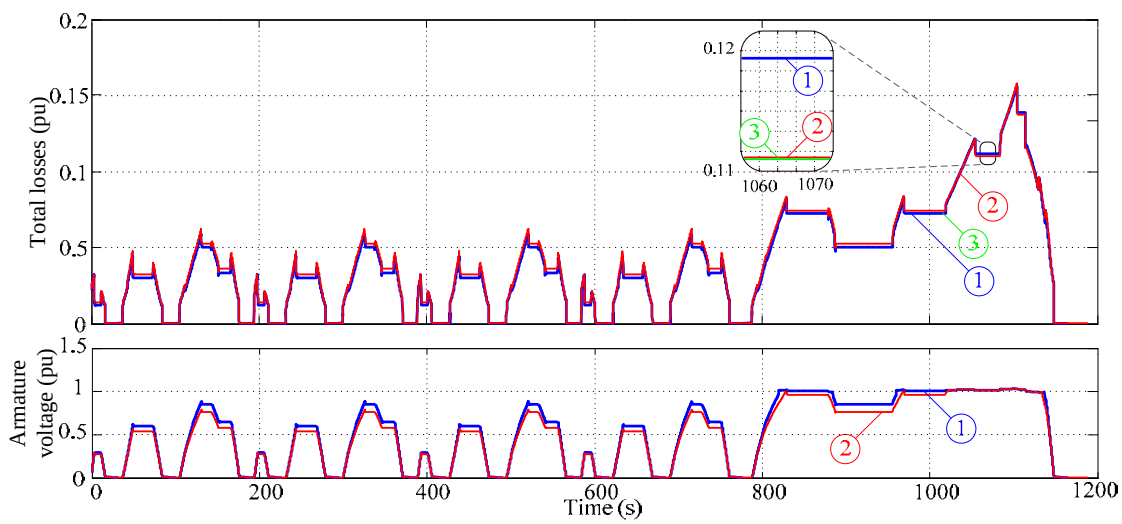

Figure 6.9. Losses and armature voltage magnitude over the NEDC with: 1. ELMM minimizing copper, iron and converter losses, 2. ELMM minimizing copper and iron losses, 3. ELMM with exact numeric solution of (6.69)

6.5. Simulation results

Simulation is carried out over one urban driving cycle. The results obtained with the considered algorithm are compared to those obtained in section 5.6 when only the copper losses and the copper and iron losses in the machine have been optimized. In this section, the simulation model includes

battery, inverter and chopper models. This was not the case of the simulations performed in Chapter 5.

Figure 6.10 verifies that the simulation system meets the required speed and torque imposed by the driving cycle for the four control strategies. Figure 6.11 proves that the proposed optimization algorithm leads to the solution that presents the minimum losses. However, as noted on the figure, the converter losses reduction goes along with iron losses increase. The gain in the overall loss reduction is less than 2% compared to the results obtained when minimizing only the iron and copper losses. The price to pay is a more complex algorithm. Therefore, a compromise can be proposed depending on the application requirements.

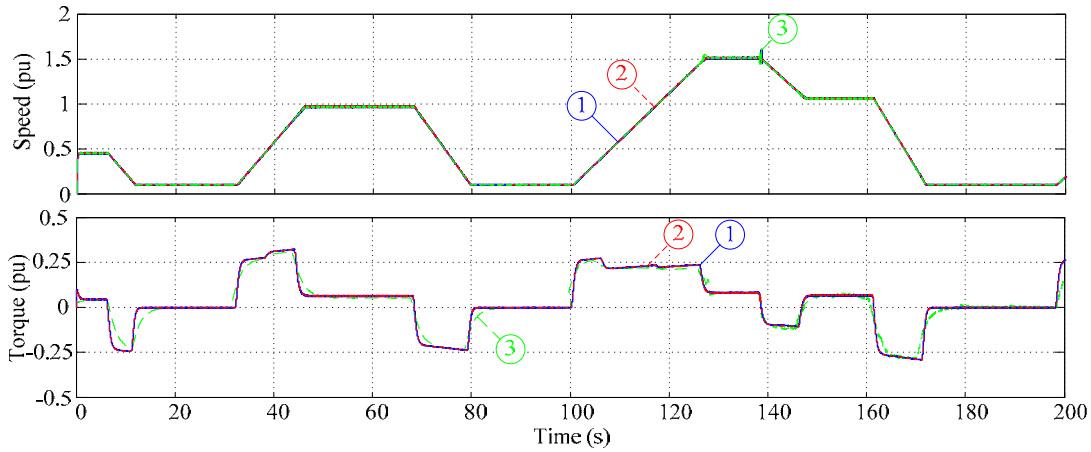

Figure 6.10. Speed and torque responses with different optimization algorithms over one urban driving cycle: 1. ELMM minimizing copper, iron and converter losses, 2. ELMM minimizing copper and iron losses, 3. ELMM minimizing copper losses

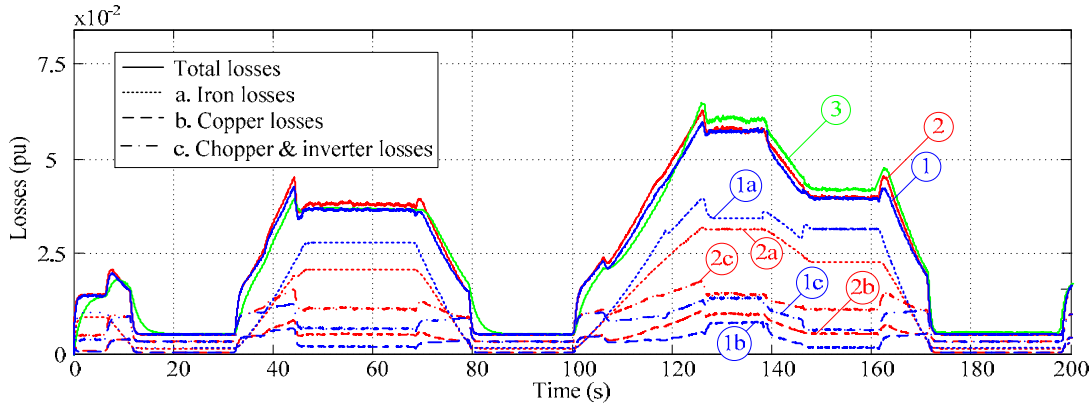

Figure 6.11. Losses obtained by simulation with different optimization algorithms over one urban driving cycle: 1. ELMM minimizing copper, iron and converter losses, 2. ELMM minimizing copper and iron losses, 3. ELMM minimizing copper losses

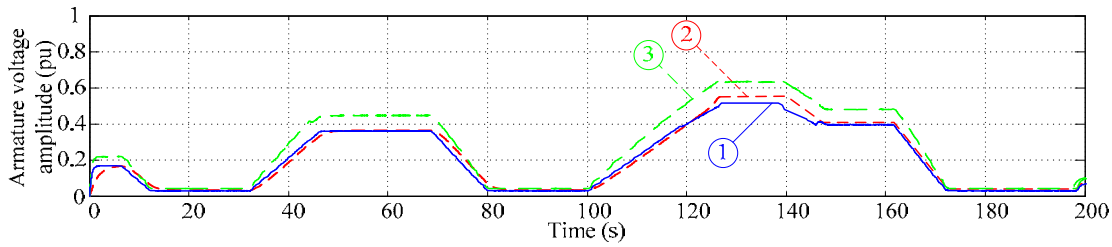

Figure 6.12. Armature voltage magnitude generated by simulation with optimization algorithms over one urban driving cycle: 1. ELMM minimizing copper, iron and converter losses, 2. ELMM minimizing copper and iron losses, 3. ELMM minimizing copper losses

Figure 6.12 proved that the proposed algorithm generated the smallest armature voltage magnitude. This translates into a smaller battery discharge as depicted in the detail of Figure 6.13. Finally, Figure 6.14 compares the evolution of the currents over the considered driving cycle.

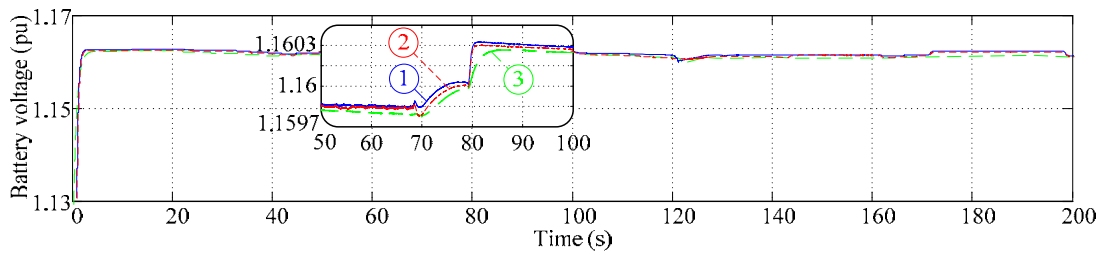

Figure 6.13. Battery voltage evolution with different optimization algorithms over one urban driving cycle: 1. ELMM minimizing copper, iron and converter losses, 2. ELMM minimizing copper and iron losses, 3. ELMM minimizing copper losses

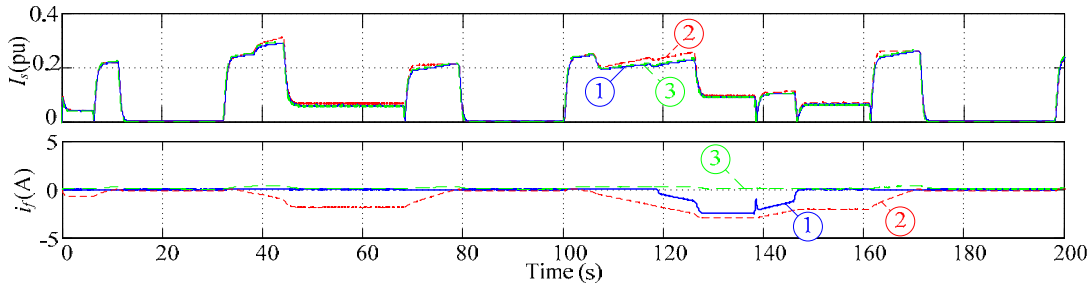

Figure 6.14. Currents generated by simulation with different optimization algorithms over one urban driving cycle: 1. ELMM minimizing copper, iron and converter losses, 2. ELMM minimizing copper and iron losses, 3. ELMM minimizing copper losses

Conclusion

In Chapter 5, the control focuses on the HESM alone. In this chapter, the inverter and chopper losses are added to the function to minimize. The optimal current references are computed based on ELMM. Simulation proves that the proposed control leads to the solution with minimum losses and, consequently, improves the vehicle autonomy. It is noted that a reduction of 2% of the propulsion set overall losses is gained when compared to losses obtained by the algorithm minimizing only the machine iron and copper losses developed in section 5.4.

It is pointed that only small part of the converter losses varies along with the current values for the given current operation range. An efficient loss reduction in the converters relies mainly on the proper selection of the switching frequency.

Summary and prospects

This thesis is a contribution to the control of the HESM. With its compact size, brushless structure, high power density and excitation flux control capability, this machine is a potential candidate for embedded applications in generator mode or motor mode operation.

The HESM modeling is based on Park first harmonic model of the synchronous machine. The model is then improved by including the iron losses and taking into account the magnetic circuit saturation effect. The electric parameters of the laboratory prototype are identified. The machine mathematical model is used in simulation and it helps to the control design in generator mode and in motor mode.

In power generation system, the study treats in particular the aircraft power supply. For motor mode operation, the attention is paid to the electric propulsion in an EV application.

For the aircraft power supply, the HESM is presented, in Part II, as a contender machine to replace the three-stage synchronous machine presently in use in most commercial and military aircraft power systems. Compared to the three-stage machine, the HESM offers higher power density, simpler structure and more compact size. Two distribution networks are studied: HVAC variable frequency network and HVDC network. For the HVDC, the HESM is coupled to a diode bridge rectifier. In both cases, the control aims to maintain the output voltage magnitude equal to its reference when the load and/or the rotor speed vary. The main contribution of the proposed control strategy is that the output voltage magnitude is driven by the field current only. The armature currents are monitored but not compensated. Thus, the control is scalar. Simulation with Matlab/Simulink software attests of the feasibility of the approach. The control is validated by experiments too with a laboratory scale HESM. The experimental results are satisfactory and comply with the simulation results.

Different machines can be proposed for EV application. With its compact size, brushless structure and flux weakening capability, the hybrid excitation synchronous motor is an attractive competitor. Part III studies the HESM control when operating in motor mode. An optimal control of the machine with minimal losses is elaborated. The copper losses are considered in a first place. Iron losses are added next. Finally, the optimization problem is extended and it includes the losses due to the inverter supplying the armature windings and to the chopper supplying the exciter. The battery source and the converters are modeled too. The motor speed is compensated in an outer control loop. The d-q axis armature currents and the field current are regulated in internal loops. The control consists of using PI controllers with optimal reference currents with respect to armature current and voltage constraints. The main contribution of the work is that analytical expressions of the reference currents are computed using ELMM (Kuhn-Tucker conditions). The reference currents are not found by recursive algorithm or lookup tables. Simulation with Matlab and Matlab/Simulink software proves that the analytical solution yields indeed to the current combination that guarantees the minimal losses over the NEDC. It is pointed that analytical expressions are useful since they generate the optimal reference currents for any operating point taking into consideration the battery voltage evolution. In addition, they are formulated in terms of the machine parameters. Thus, they are generic and can be used for different HESMs. Furthermore, these expressions are not limited to the HESM control. With minor modifications, they can be adopted to the interior PM motor control or wound rotor synchronous motor control.

In conclusion, the work done in this thesis proves that the HESM is an attractive machine to be used in embedded applications. The simulation and experimental results obtained in Part II in

addition to the simulation results obtained in Part III are promising. These results give way to new prospects.

Concerning the HESM modeling, experimental measurements show that the real phase voltage waveform is not the perfect sinusoid obtained by simulation. Hence, different points are raised.

- The mathematical model of the machine shall be improved in order to meet the imperfections generated by the machine structure. The model shall not be limited to the Park first harmonic model. It shall include higher order harmonics for more accurate simulation.
- The effect of the cross saturation shall be taken into account more explicitly.
- The expression estimating the iron losses shall be revised in order to include core losses due to high voltage harmonics.

In this thesis, the control of the HESM operating as a standalone generator is validated under normal conditions with resistive and inductive loads. In future work, advanced points can be considered.

- Simulation and/or experiments under more severe conditions can be performed.
- Different type of loads (motors, batteries, converters…) can be proposed for both networks (HVAC and HVDC).
- For the HVAC network, the generator control with an unbalanced load is an interesting point to study.
- It is important to test the control performance when a fault or a short circuit occurs. New control strategies can be elaborated accordingly.

It is pointed that the above-mentioned points are of a great importance when it comes to aircraft power system.

With regard to the HESM control in motor mode, several prospects come next.

- The design of speed and load torque estimators is an immediate obligation.
- Experimental validation of the proposed optimization algorithms follows. Experiments can be performed with DSpace card and/or with a more advanced component such as Field Programmable Gate Array (FPGA).
- For an easy implementation, the simplification of the analytical current expressions obtained by the optimization algorithms is to be considered.
- The control sensitivity to the variation of the machine parameters is to be quantified.
- Another interesting point is to take into account the magnetic circuit saturation effect in the optimization process.
- Given the optimal current values, the choice of the switching frequencies of the converters can be done based on other optimization criteria.
- Finally, the combination of the ELMM with an advanced control technique, such as predictive control, sliding mode control, neural network, is held as a gradual horizon.

Appendix A. Lagrange Method to Solve an Optimization Problem

A.1. Review

$f(\boldsymbol{x})$ is a continuous, second order differentiable function.

Let $\boldsymbol{x}^* \in R^n$.

Theorem A.1.

$\boldsymbol{x}^*$ is a minimum (maximum) of $f(\boldsymbol{x})$ if

- $\nabla f(\boldsymbol{x}^*) = 0$: First order condition
- $\boldsymbol{y}^t \nabla^2 f(\boldsymbol{x}^*) \boldsymbol{y} > 0$ ($\boldsymbol{y}^t \nabla^2 f(\boldsymbol{x}^*) \boldsymbol{y} < 0$) $\forall \boldsymbol{y} \neq 0$: Necessary and sufficient second order condition.

$\nabla f(\boldsymbol{x}^*)$ denotes the gradient of $f(\boldsymbol{x})$ at the point $\boldsymbol{x} = \boldsymbol{x}^*$

$\nabla^2 f(\boldsymbol{x}^*)$ denotes the Hessian of $f(\boldsymbol{x})$ at the point $\boldsymbol{x} = \boldsymbol{x}^*$.

A.2. Equality constrained minimization problem: Lagrange multipliers

The method of Lagrange multipliers gives a set of necessary conditions to identify optimal points of equality constrained optimization problems. This is done by converting a constrained problem to an equivalent unconstrained problem with the help of certain unspecified parameters known as Lagrange multipliers.

The classic problem formulation:

- Minimize $f(\boldsymbol{x})$
- Subject to $h_1(\boldsymbol{x}) = 0$, $h_2(\boldsymbol{x}) = 0$, $h_3(\boldsymbol{x}) = 0$, … $h_p(\boldsymbol{x}) = 0$

is converted to a new unconstrained problem:

- Minimize $l(\boldsymbol{x},\boldsymbol{\lambda}) = f(\boldsymbol{x}) + \sum_{i=1}^{p} h_i(\boldsymbol{x})\lambda_i$

$l(\boldsymbol{x},\boldsymbol{\lambda})$ is the Lagrange function.

λ_i is an unspecified positive or negative constant called the Lagrange multiplier.

Proof

If $\boldsymbol{\lambda} = \boldsymbol{\lambda}^*$ and the unconstrained minimum of $l(\boldsymbol{x},\boldsymbol{\lambda})$ occurs at $\boldsymbol{x} = \boldsymbol{x}^*$ and $\boldsymbol{x}^*$ satisfies $\boldsymbol{h}(\boldsymbol{x}^*) = 0$, then $\boldsymbol{x}^*$ minimizes $f(\boldsymbol{x})$ subject to $\boldsymbol{h}(\boldsymbol{x}) = 0$.

The problem is solved by treating $\boldsymbol{\lambda}$ as variables, finding the unconstrained minimum of $l(\boldsymbol{x},\boldsymbol{\lambda})$ and adjusting $\boldsymbol{\lambda}$ so that $\boldsymbol{h}(\boldsymbol{x}) = 0$ is satisfied.

The problem sufficient and necessary conditions are formulated as follows

Theorem A.2.

If

$$\exists \boldsymbol{x}^* \quad \exists \boldsymbol{\lambda}^* \quad \Big| \quad 1.\ \nabla l(\boldsymbol{x}^*,\boldsymbol{\lambda}^*) = \nabla f(\boldsymbol{x}^*) + \nabla \boldsymbol{h}^t(\boldsymbol{x}^*)\boldsymbol{\lambda}^* = 0 \quad \text{and} \quad \boldsymbol{h}(\boldsymbol{x}^*) = 0$$

$$2.\ \boldsymbol{y}^t \nabla^2 l(\boldsymbol{x}^*,\boldsymbol{\lambda}^*)\boldsymbol{y} > 0 \quad \forall \boldsymbol{y} \neq 0 \quad \Big| \quad \nabla h_i^t(\boldsymbol{x}^*)\boldsymbol{y} = 0$$

Then $\boldsymbol{x}^*$ is a local minimum of $f(\boldsymbol{x})$ subject to $\boldsymbol{h}(\boldsymbol{x}) = 0$.

A.3. Inequality Constrained Minimization Problem: Kuhn-Tucker Conditions

Kuhn and Tucker extended the Lagrange theory to include the general typical single-objective nonlinear problem with inequality constraints

- Minimize $f(\boldsymbol{x})$
- Subject to $\boldsymbol{h}(\boldsymbol{x}) = 0$ and $\boldsymbol{g}(\boldsymbol{x}) \leq 0$

An inequality constraint $g_j(\boldsymbol{x}) \leq 0$ is said to be active at a feasible point $\boldsymbol{x}^*$ if $g_j(\boldsymbol{x}^*) = 0$. It is inactive at $\boldsymbol{x}^*$ if $g_j(\boldsymbol{x}^*) < 0$.

Theorem A.3.

If

$$\exists \boldsymbol{x}^* \quad \exists \boldsymbol{\lambda}^*, \boldsymbol{\mu}^* \quad \Big| \quad \begin{array}{l} 1.\ \boldsymbol{\mu}^* \geq 0 \\ 2.\ \nabla l\left(\boldsymbol{x}^*, \boldsymbol{\lambda}^*, \boldsymbol{\mu}^*\right) = \nabla f\left(\boldsymbol{x}^*\right) + \nabla \boldsymbol{h}^t\left(\boldsymbol{x}^*\right)\boldsymbol{\lambda}^* + \nabla \boldsymbol{g}^t\left(\boldsymbol{x}^*\right)\boldsymbol{\mu}^* = 0 \\ \quad \text{and } \ \boldsymbol{h}\left(\boldsymbol{x}^*\right) = 0 \ \text{ and } \ \boldsymbol{g}\left(\boldsymbol{x}^*\right) \leq 0 \\ 3.\ \mu_j^* g_j\left(\boldsymbol{x}^*\right) = 0 \\ 4.\ \boldsymbol{y}^t \nabla^2 l\left(\boldsymbol{x}^*, \boldsymbol{\lambda}^*, \boldsymbol{\mu}^*\right)\boldsymbol{y} > 0 \quad \forall \boldsymbol{y} \neq 0 \quad \Big| \quad \begin{cases} \nabla h_i^{\,t}\left(\boldsymbol{x}^*\right)\boldsymbol{y} = 0 \\ \nabla g_j^{\,t}\left(\boldsymbol{x}^*\right)\boldsymbol{y} = 0 \end{cases} \end{array}$$

Then $\boldsymbol{x}^*$ is a local minimum of $f(\boldsymbol{x})$ subject to $\boldsymbol{h}(\boldsymbol{x}) = 0$ and $\boldsymbol{g}(\boldsymbol{x}) \leq 0$.

μ_j are the Kuhn-Tucker multipliers.

From condition 3, it can be noted that when the constraint $g_j(x^*)$ is inactive, the corresponding μ_j^* is nil and the term $g_j(x^*)$ will not appear in the Lagrange function anymore. On the other hand, the constraint $g_j(x^*)$, if active, is equivalent to an equality constraint. Thus, after determining the Kuhn-Tucker multipliers, the inequality constrained optimization problem can be converted to an equality constrained Lagrange optimization problem.

Appendix B. HESM Laboratory Prototype

Machine characteristics

P_n	Rated power (motor mode)	3000 kW
Ω_b	Rotor base speed	2000 rpm
p	Number of pair of poles	6
V_{DC}	DC bus supply (motor mode)	300 V
I_{sn}	Rated armature current	10 A

Machine electrical parameters

R_s	Stator winding resistance per phase	0.75 Ω
R_f	Field winding resistance	2.82 Ω
L_{sd}	Stator direct axis inductance (maximum value)	3.6 mH
ρ	Saliency ratio ($\rho = L_{sq} / L_{sd}$)	1.41
L_f	Field winding inductance (maximum value)	53.8 mH
M_{sf}	Armature-to-field mutual inductance (maximum value)	7 mH
Φ_M	Maximum magnetic flux produced by the PMs in an armature winding	100 mWb

Machine dimensions

l_a	Active length	40 mm
l_{st}	Width of one stator tooth	7.2 mm
e_c	Yoke thickness	7 mm
M_y	Yoke mass	1.22 kg
M_{st}	Stator teeth mass	1.33 kg
n_s	Number of turns in a stator winding per phase	33

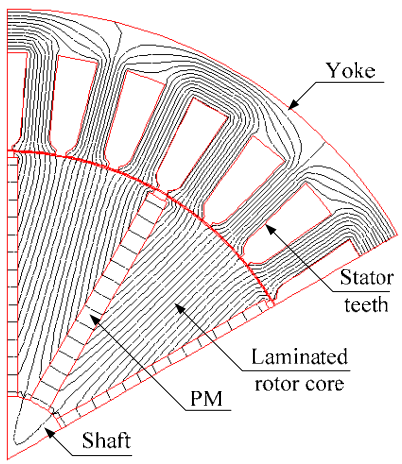

Figure B.1. Field lines computed by FEA of the machine [4]

Characteristic of the HHR650D NiMH battery manufactured by Panasonic

V_{batt}	Nominal voltage	1.2 V
Q_{batt}	Rated discharge capacity	6500 mAh (1 It)
R_{batt}	Battery internal resistance	2 mΩ

Characteristic of the SK30GB128 module manufactured by SEMIKRON

V_{CE}	Typical IGBT voltage drop	2 V
r_{CE}	IGBT collector-emitter resistance	36 mΩ
V_D	Typical inverse diode voltage	2 V
r_D	Diode resistance in forward bias	32 mΩ
E_{onT}	Typical IGBT turn-on energy	2.8 mJ
E_{offT}	Typical IGBT turn-off energy	2.19 mJ
E_{offD}	Typical inverse diode turn-off energy	1 mJ

References

[1] Adnanes, A. (Jun. 1991). Torque analysis of permanent magnet synchronous motors. *22nd Annual IEEE Power Electronics Specialists Conference (PESC '91) Record*, (pp. 695 - 701). Cambridge, MA, USA.

[2] Akemakou, A. (2000). Dual excitation electrical machine and especially motor vehicle alternator. *Patent No. 6 037 691*. US.

[3] Akemakou, A. D., & Phounsombat, S. K. (2000). Electrical machine with double excitation, especially a motor vehicle alternator. *Patent No. 6 147 429.* US.

[4] Amara, Y. (2001). *Contribution to the design and control of the hybrid excitation synchronous machines, electric vehicle application (in French).* PhD Thesis, Paris XI University, Paris, France.

[5] Amara, Y., Ben Ahmed, A. H., Hoang, E., Vido, L., Gabsi, M., & Lecrivain, M. (Feb. 2003). Hybrid excitation synchronous alternator debiting on a diode rectifier with a resistive load. *European Conference on Power Electronics and Application (EPE).* Toulouse, France.

[6] Amara, Y., Lucidarme, J., Gabsi, M., Lecrivain, M., Ben Ahmed, A. H., & Akemakou, A. (2001). A new topology of hybrid synchronous machine. *IEEE Transactions on Industrial Applications , 37* (5), 1273-1281.

[7] Amara, Y., Oujehani, K., Hoang, E., Gabsi, M., Lecrivain, M., Ben Ahmed, A. H., et al. (Jun. 2001). Flux weakening of hybrid synchronous machines. *IEEE Electric Machines and Drive Conference (IEMDC'01)*, (pp. 367-373). Cambridge, USA.

[8] Amara, Y., Vido, L., Gabsi, M., Hoang, E., Lecrivain, M., & Chabot, F. (2009). Hybrid excitation synchronous machines: Energy efficient solution for vehicle propulsion. *IEEE Transactions on Vehicular Technology , 58* (5), 2137-2149.

[9] Avery, C. R., Burrow, S. G., & Mellor, P. H. (Sept. 2007). Electrical generation and distribution for the more electric aircraft. *IEEE 42nd International Universities Power Engineering Conference (UPEC 2007)*, (pp. 1007 - 1012). Brighton, UK.

[10] Aydin, M., Huang, S., & Lipo, T. A. (Oct. 2002). A new axial flux surface mounted permanent magnet machine capable of field control. *Conference record of the IEEE Industry Applications Conference : 37th IAS Annual Meeting*, *2*, pp. 1250 - 1257. Pittsburgh, Pennsylvania, USA.

[11] Aydin, M., Huang, S., & Lipo, T. A. (Jun. 2003). Performance evaluation of an axial flux consequent pole PM motor using finite element analysis. *IEEE International Electric Machines and Drives Conference (IEMDC'03)*, *3*, pp. 1682 - 1687. Madison, USA.

[12] Aydin, M., Yao, J., Kayikci, E., Huang, S., & Lipo, T. A. (2004). *Design considerations and experimental results of an axial flux PM motor with field control.* University of Wisconsin-Madison College of Engineering. Wisconsin Electric Machines & Power Electronics Consortium.

[13] Baoquan, K., Chunyan, L., & Shukang, C. (Sept. 2005). A new flux weakening method of permanent magnet synchronous machine. *Proceedings of the IEEE 8th International Conference on Electrical Machines and Systems (ICEMS 2005)*, *1*, pp. 500 - 503. Nanjing, China.

[14] Baudart, F., Dehez , B., Matagne , E., Telteu-Nedelcu, D., Alexandre. , P., & Labrique, F. (2012). Torque control strategy of polyphase permanent-magnet synchronous machines with minimal controller reconfiguration under open-circuit fault of one phase. *IEEE Transactions on Industrial Electronics*, *59*(6), 2632-2644.

[15] Baumann, C., Piquet, H., & Roboam, X. (May 2007). A novel structure for aeronautic DC distribution: the Mixed function for Actuation & Power Flow Control (MAPFC). *IEEE International Electric Machines & Drives Conference (IEMDC '07)*, (pp. 1695 - 1700). Antalya, Turkey.

[16] Bekhaled, C., Hlioui, S., Vido, L., Gabsi, M., Lecrivain, M., & Amara, Y. (Sept. 2007). 3D magnetic equivalent circuit model for homopolar hybrid excitation synchronous machines. *IEEE International Aegean Conference on Electrical Machines and Power Electronics (ACEMP '07)*, (pp. 575 - 580). Bodrum, Turkey.

[17] Berman, B., & Gelb, G. (2006). Propulsion systems for electric cars. *IEEE Transactions on Vehicular Technology , 23* (3), 61 - 72.

[18] Bernal, F., Garefa-Cerrada, A., & Faure, R. (May 1998). Loss-minimization control of synchronous machines with constant excitation. *29th Annual IEEE Power Electronics Specialists Conference (PESC 98) Record, 1*, pp. 132 - 138. Fukuoka , Japan.

[19] Bodson, M., Chiasson, J., & Tolbert, L. (Jun. 2001). A complete characterization of torque maximization for permanent magnet non-salient synchronous motors. *Proceedings of the IEEE American Control Conference, 3*, pp. 2148 - 2149. Arlington, VA , USA.

[20] Boglietti, A., Cavagnino, A., Tenconi, A., & Vaschetto, S. (Nov. 2009). The safety critical electric machines and drives in the more electric aircraft: A survey. *35th Annual Conference of IEEE Industrial Electronics (IECON '09)*, (pp. 2587 - 2594). Porto, Portugal.

[21] Brown, N., & Haydock, L. (Nov. 2003). New brushless synchronous alternator. *IEE Proceedings of Electric Power Applications , 150* (6), 629 - 635.

[22] Chan, C. (Feb. 2002). The state of the art of electric and hybrid vehicles. *Proceedings of the IEEE , 90* (2), 247-275.

[23] Chen, M., & Rincon-Mora, G. (Jun. 2006). Accurate electrical battery model capable of predicting runtime and I-V performance. *IEEE Transactions on Energy Conversion , 21* (2), 504 - 511.

[24] Chen , Q., Jiang, Y., Zhao, L., Gao, G., & Kuang , G. (Oct. 2009). An optimization procedure of the Lagrange multiplier method for polarimetric power optimization. *IEEE Geoscience and Remote Sensing Letters, 6*, pp. 699-702.

[25] Coultes, M., & Watson, W. (1981). Synchronous machine models by standstill frequency response tests. *IEEE Transactions on Power Apparatus and Systems , PAS-100* (4), 1480 - 1489.

[26] Dan, J., Dongqi, Z., Xinjian, J., Seto, M., Kimata, M., Satake, A., et al. (Aug. 2000). Research of control system of permanent magnet brushless synchronous motor for EV. *IEEE 3rd International Power Electronics and Motion Control Conference (IPEMC 2000) Proceedings, 1*, pp. 353 - 358. Beijing , China.

[27] Del Bue , A., Xavier, J., Agapito, L., & Paladini, M. (2012). Bilinear modeling via Augmented Lagrange Multipliers (BALM). *IEEE Transactions on Pattern Analysis and Machine Intelligence, 34*(8), 1496-1508.

[28] Dorrell, D., Knight, A., Popescu, M., Evans, L., & Station, D. (Sept. 2010). Comparison of different motor design drives for hybrid electric vehicles. *IEEE Energy Conversion Congress and Exposition (ECCE)*, (pp. 3352-3359). Atlanta, GA, USA.

[29] Einhorn, M., Conte, V., Kral, C., Fleig, J., & Permann, R. (Sept. 2010). Parameterization of an electrical battery model for dynamic system simulation in electric vehicles. *2010 IEEE Vehicle Power and Propulsion Conference (VPPC)*, (pp. 1 - 7). Lille, France.

[30] Emadi, A., & Ehsani, M. (2002). More-Electric Vehicles. In T. Skvarenina (Ed.), *Power Electronics Handbook* (pp. 582-594 (Chapter 21)). USA: CRC PRESS.

[31] Emadi, K., & Ehsani, M. (2000). Aircraft power systems: technology, state of the art, and future trends. *IEEE Aerospace and Electronic Systems Magazine , 15* (1), 28 - 32.

[32] Evans, P. M., & Schultz, R. (1997). Rotating electrical machine with electromagnetic and permanent magnet excitation. *Patent No. 5 663 605.* US.

[33] Forouzan, A., & Moonen, M. (Jun. 2011). Lagrange multiplier optimization for optimal spectrum balancing of DSL with logarithmic complexity. *IEEE International Conference on Communications (ICC)*, (pp. 1-6). Kyoto, Japan.

[34] Fratta, A., & Scapino, F. (Jun. 2004). Modeling inverter losses for circuit simulation. *IEEE 35th Annual Power Electronics Specialists Conference (PESC 04), 6*, pp. 4479-4485. Anchen, Germany.

[35] Friedrich, G. (Oct. 1994). Comparative study of three control strategies for the synchronous salient poles and wound rotor machine in automotive applications with on board energy. *IET 5th International Conference on Power Electronics and Variable-Speed Drives*, (pp. 706 - 709). London , UK.

[36] Guo, Q., Jiang, L., Gao, J., Wang, X., & Xiao, X. (Oct. 2011). Research on reliability optimization of weapon system based on Generalized Lagrange multipliers. *International Conference on System Science, Engineering Design and Manufacturing Informatization (ICSEM), 2*, pp. 17-19. Guiyang, China.

[37] Henneberger, G., Hadji-Minaglou, J. R., & Ciorba, R. C. (Oct. 1994). Design and test of permanent magnet synchronous motor with auxiliary excitation winding for electric vehicle application. *European Power Electronics Chapter Symposium*, (pp. 645 - 649). Lausanne, Switzerland.

[38] Hlioui, S., Vido, L., Amara, Y., Gabsi, M., Lecrivain, M., & Miraoui, A. (Sept. 2008). PM and hybrid excitation synchronous machines: Performances comparison. *IEEE 18th International Conference on Electrical Machines (ICEM 2008)*, (pp. 1 - 6). Nanjing, China.

[39] Hoang, E., Gabsi, M., Lecrivain, M., & Multon, B. (Oct. 2000). Influence of magnetic losses on maximum power limits of synchronous permanent magnet drives in flux-weakening mode. *Conference Record of the 2000 IEEE Industry Applications Conference, 1*, pp. 299 - 303. Rome , Italy.

[40] Hoang, E., Lecrivain, M., & Gabsi, M. (Sept. 2007). A new structure of a switching flux synchronous polyphased machine with hybrid excitation. *European Conference on Power Electronics and Applications (EPE 2007)*, (pp. 1 - 8). Aalborg, Denmark.

[41] Hsu, J. S. (2000). Direct control of air gap flux in permanent magnet machines. *Patent No. 6 057 622*. US.

[42] Hsu, J. S. (2000). Direct control of air-gap flux in permanent magnet machines. *IEEE Transactions on Energy Conversion , 15* (4), 203-210.

[43] Hsu, J. S. (May 2007). Study on enhancement and weakening of permanent magnet air gap flux density. *IEEE International Electric Machines & Drives Conference (IEMDC '07)*, (pp. 1552 - 1556). Antalya, Turkey.

[44] Huang, P., Miao, C. Y., Li, H. Q., & Zhang, C. (Jul. 2011). Maximum-torque-per-ampere control of interior permanent magnet synchronous machine applied for hybrid electric vehicles. *IEEE International Conference on Control, Automation and Systems Engineering (CASE)*, (pp. 1 - 3). Singapore.

[45] Huang , Y. (Oct. 2006). Improved Lagrange nonlinear programming neural networks for inequality constraints. *6th International Conference on Intelligent Systems Design and Applications (ISDA '06), 1*, pp. 158-166. Jinan, China.

[46] IEEE Standard Procedures for obtaining synchronous machine parameters by standstill frequency response testing (Supplement to ANSI/IEEE Std 115-1983, IEEE Guide: Test procedures for synchronous machines). (1987).

[47] Ikeda, Y., Itsumi , J., & Funato, H. (Apr. 1988). The power loss of the PWM voltage-fed inverter. *19th Annual IEEE Power Electronics Specialists Conference (PESC '88), 1*, pp. 277-283. Kyoto, Japan.

[48] Izquierdo, D., Azcona, R., del Cerro, F., Fernandez, C., & Delicado, B. (Feb. 2010). Electrical power distribution system (HV270DC), for application in more electric aircraft. *25th Annual IEEE Applied Power Electronics Conference and Exposition (APEC)*, (pp. 1300 - 1305). Palm Springs, CA, USA.

[49] Jahns, T. (1987). Flux-weakening regime operation of an interior permanent-magnet synchronous motor drive. *IEEE Transactions on Industry Applications , IA-23* (4), 681 - 689.

[50] Jahns, T. M., Kliman, G., & Neumann, T. W. (1986). Interior permanent-magnet synchronous motors for adjustable-speed drives. *IEEE Transactions on Industry Applications , IA-22* (4), 738 - 747.

[51] Jeong , Y., Sul , S., Hiti, S., & Rahman, K. (Mar. 2005). On-line minimum-copper-loss control of an interior permanent-magnet synchronous machine for automotive applications. *20th Annual IEEE Applied Power Electronics Conference and Exposition (APEC), 2*, pp. 943-949. Austin, Texas, USA.

[52] Jeong , Y., Sul, S., Hiti, S., & Rahman, K. (2006). Online minimum-copper-loss control of an interior permanent-magnet synchronous machine for automotive applications. *IEEE Transactions on Industry Applications, 42*(5), 1222-1229.

[53] Jezernik, K., & Horvat, R. (Jul. 2010). High performance control of PMSM. *IEEE 1st Symposium on Sensorless Control for Electrical Drives (SLED)*, (pp. 72 - 77). Padova, Italy.

[54] Jones, R. I. (1999). The More Electric Aircraft: the past and the future? *IEE Colloquium on Electrical Machines and Systems for the More Electric Aircraft*, (pp. 1/1 - 1/4). London, UK.

[55] Joong, K. H., & Shigeta, U. (2003). Wind power generation system. *Patent No. 6 541 877.*

[56] Joong, K. H., Tahara, K., Ajima, K., Ueta, K., Innami, T., Hino, N., et al. (2003). Hybrid car and dynamo-electric machine. *Patent No. 6 577 022.* US.

[57] Joong, K., Tahara, K., Ajima, K., Ueta, K., & Innami, T. (2002). Hybrid car and dynamo-electric machine. *Patent No. 6 462 430.* US.

[58] Kajino, M., Hoshi, N., & Meifen, C. (Jun. 2011). Comparison of driving characteristics in two kind of control schemes for permanent magnet synchronous motor mounted on electric vehicle. *IEEE 8th International Conference on Power Electronics and ECCE Asia (ICPE & ECCE)*, (pp. 1969 - 1975). Jeju, Korea.

[59] Kennett, R. J. (1971). Integrated drive generators for aircraft. *Electronics and Power , 17* (2), 73 - 76.

[60] Keshtkar, A., Maleki, T., & Kalantarnia, A. (2009). Determination of optimum rails dimensions in railgun by Lagrange's equations. *IEEE Transactions on Magnetics, 45*(1), 594-597.

[61] Kim, S. (2008). Nonlinear state of charge estimator for hybrid electric vehicle battery. *IEEE Transactions on Power Electronics , 23* (4), 2027 - 2034.

[62] Kroeze, R., & Krein, P. (Jun. 2008). Electrical battery model for use in dynamic electric vehicle simulations. *IEEE Power Electronics Specialists Conference (PESC 2008)*, (pp. 1336 - 1342). Rhodes, Greece.

[63] Kuhn, E., Forgez, C., Lagonotte, P., & Friedrich, G. (2006). Modelling Ni-MH battery using Cauer and Foster structures. *ELSEVIER, Journal of Power Sources* , 1490-1497.

[64] Lai, J., Bailey, J., Young, R., Sohns, C., & Hawsey, R. (Oct. 1989). Optimum current control for a high speed axial gap permanent magnet synchronous motor. *Conference Record of the IEEE Industry Applications Society Annual Meeting, 1*, pp. 767 - 772. San Diego, CA , USA.

[65] Langlois, O., Foche, E., Roboam, X., & Piquet, H. (2005). From more electric aircraft to all electric aircraft: state of art and prospective on on-board network (in French). *J3eA, Journal sur l'enseignement des sciences et technologies de l'information et des systèmes , 4* (Hors Série 1).

[66] Li, Y., & Lipo, T. A. (Jun. 1995). A doubly salient permanent magnet motor capable of field weakening. *26th Annual IEEE Power Electronics Specialists Conference (PESC 95) Record, 1*, pp. 565 - 571. Atlanta, USA.

[67] Liang, F., & Miller, J. M. (Apr. 2002). Permanent magnet electric machine with flux control. *Patent No. 6 373 162.* US.

[68] Lipo, T. A., & Aydin, M. (Sept. 2004). Field weakening of permanent magnet machines: Design approaches. *EPE Power Electronics and Motion Control Conference (EPE-PEMC 04).* Riga, Latvia.

[69] Lipo, T. A., Liao, Y., & Liang, F. (1995). Field weakening for a doubly salient motor with stator permanent magnets. *Patent No. 5 455 473.* US.

[70] Lucidarme, J., Ben Ahmed, A. H., Gabsi, M., Multon, B., Santander, E., & Hoang, E. (1999). Rotating electrical machine with excitation coils, by magnets or with double excitation. *Patent No. 5 952 758.* US.

[71] Lucidarme, J., Ben Ahmed, A. H., Gabsi, M., Multon, B., Santander, E., Hoang, E., et al. (2001). Electrical machine with double excitation. *Patent No. 6 229 239.* US.

[72] Luo, X., & Lipo, T. A. (2000). A synchronous permanent magnet hybrid AC machine. *IEEE Transaction on Energy conversion , 15* (2), 203-210.

[73] Ma, L., Sanada, M., Morimoto, S., & Taketa, Y. (Apr. 2002). Advantages of IPMSM with adjustable PM armature flux linkage inefficiency improvement and operating range extension. *IEEE Proceedings of the Power Conversion Conference (PCC), 1*, pp. 136 - 141. Osaka, Japan.

[74] Mademlis, C., & Agelidis, V. (Jan. 2002). On considering magnetic saturation with maximum torque to current control in interior permanent magnet synchronous motor drives. *IEEE Power Engineering Society Winter Meeting, 2*, p. 1234.

[75] Mademlis, C., Kioskeridis, I., & Margaris, N. (2004). Optimal efficiency control strategy for interior permanent-magnet synchronous motor drives. *IEEE Transactions on Energy Conversion , 19* (4), 715 - 723.

[76] Malan, J., Kamper, M., & Williams, P. (Jul. 1998). Reluctance synchronous machine drive for hybrid electric vehicle. *IEEE International Symposium on Industrial Electronics (ISIE '98) Proceedings, 2*, pp. 367 - 372. Pretoria , South Africa.

[77] Manigrasso, R., Mapelli, F., Mauri, M., & Tarsitano, D. (Jun. 2008). Inverter loss minimization for a plug-in hybrid vehicle traction drive using DSC control. *IEEE International Symposium on Power Electronics, Electrical Drives, Automation and Motion (SPEEDAM 2008)*, (pp. 889 - 894). Ischia, Italy.

[78] Mapelli, F., Tarsitano, D., & Mauri, M. (2010). Plug-In hybrid electric vehicle: Modeling, prototype realization, and inverter losses reduction analysis. *IEEE Transactions on Industrial Electronics* , 598 - 607.

[79] Marques, G. D. (Sep. 1998). A simple and accurate system simulation of three-phase diode rectifier. *24th Annual Conference of the IEEE Industrial Electronics Society (IECON'98), 1*, pp. 416 - 421. Aachen, Germany.

[80] Masuzawa, M., Hirao, N., Sasaki, T., & Mita, M. (1998). Brushless motor having permanent magnets. *Patent No. 5 821 710.* US.

[81] Mellor, P. H., Burrow, S. G., Sawata, T., & Holme, M. (Jun. 2003). A wide speed range permanent magnet generator for future embedded aircraft generation systems. *IEEE International Electric Machines and Drives Conference (IEMDC'03), 2*, pp. 1308 - 1313. Madison, Wisconsin, USA.

[82] Meyer, M., Grote, T., & Bocker, J. (Sept. 2007). Direct torque control for interior permanent magnet synchronous motors with respect to optimal efficiency. *European Conference on Power Electronics and Applications (EPE)*, (pp. 1-9). Aalborg, Denmark.

[83] Mi, C., Selmon, G. R., & Bonert, R. (2005). Minimization of iron losses of permanent magnet synchronous machines. *IEEE Transactions on Energy Conversion , 20* (1), 121 - 127.

[84] Mi, C., Slemon, G. R., & Bonert, R. (2003). Modeling of iron losses of permanent-magnet synchronous motors. *IEEE Transactions on Industrial Applications, 39* (3), 734 - 742.

[85] Mitcham, A. J., & Cullen, J. A. (Jun. 2002). Permanent magnet generator options for the More Electric Aircraft. *IEEE International Conference on Power Electronics, Machines and Drives*, (pp. 241 - 245). Bath, UK.

[86] Mizuno, T. (1997). Hybrid excitation type permanent magnet synchronous motor. *Patent No. 5 682 073.* US.

[87] Moir, I. (1999). More-electric aircraft-system considerations. *IEE Colloquium on Electrical Machines and Systems for the More Electric Aircraft*, (pp. 10/1 - 10/9). London, UK.

[88] Morimoto, S., Hatanaka, K., Tong, Y., Takeda, Y., & Hirasa, T. (Oct. 1991). High performance servo drive system of salient pole permanent magnet synchronous motor. *Conference Record of the 1991 IEEE Industry Applications Society Annual Meeting*, *1*, pp. 463 - 468. Dearborn, MI, USA.

[89] Naouar, M. W., Monmasson, E., & Slama Belkhodja, I. (Nov. 2006). Identification of synchronous machine parameters using hysteresis based current controller. *IEEE Industrial Electronics Conference (IECON'06)*, (pp. 1357-1362). Paris, France.

[90] Navrapescu, V., Popescu, M., Kisck, D., Andronescu, G., & Kisck, M. (Oct. 2007). Modelling of iron losses in salient pole permanent magnet synchronous motors. *IEEE 7th International Conference on Power Electronics (ICPE '07)*, (pp. 352 - 357). Daegu, South Korea.

[91] Nikzad, M., & Radan, A. (Feb. 2010). Accurate loss modelling of fuel cell boost converter and traction inverter for efficiency calculation in fuel cell-battery hybrid vehicles. *IEEE 1st Power Electronic & Drive Systems & Technologies Conference (PEDSTC)*, (pp. 218 - 223). Tehran, Iran.

[92] Nikzad, M., & Radan, A. (Sept. 2009). Accurate modelling of traction inverter losses for efficiency calculation in parallel hybrid electric vehicles. *13th European Conference on Power Electronics and Applications (EPE '09)*, (pp. 1 - 7). Barcelona, Spain.

[93] Nino, C., Tariq, A., Jurkovic, S., & Strangas, E. (May 2009). Optimal speed control of an Interior Permanent Magnet Synchronous Motor including cross saturation. *IEEE International Electric Machines and Drives Conference (IEMDC '09)*, (pp. 292 - 298). Miami, FL, USA.

[94] Pan, C., & Sue, S. (2005). A linear maximum torque per ampere control for IPMSM drives over full-speed range. *IEEE Transactions on Energy Conversion , 20* (2), 359 - 366.

[95] Patin, N., Vido, L., Monmasson, E., & Louis, J. P. (2006). Control of a DC generator based on a hybrid excitation synchronous machine connected to a PWM rectifier. *IEEE Industrial Symposium on Industrial Electronics (ISIE 2006)*, (pp. 2229-2234). Montreal, Canada.

[96] Patin, N., Vido, L., Monmasson, E., Louis, J. P., Gabsi, M., & Lecrivain, M. (2008). Control of a hybrid excitation synchronous generator for aircraft applications. *IEEE Transactions on Industrial Electronics , 55* (10), 3772-3783.

[97] Pearson, W. (Jun. 1998). The more electric/all electric aircraft-a military fast jet perspective. *IEE Colloquium on All Electric Aircraft*, (pp. 5/1 - 5/7). London, UK.

[98] Polprasert, J., & Ongsaku , W. (Dec. 2007). Augmented Lagrange Hopfield Network for economic dispatch. *Australasian Universities Power Engineering Conference (AUPEC)*, (pp. 1-5). Perth, Australia.

[99] Profumou, F., Tenconiu, A., Zhang, Z., & Cavagnino, A. (Oct. 1998). Novel axial flux interior PM synchronous motor realized with powdered soft magnetic materials. *IEEE Industry Applications Conference, 33rd IAS Annual Meeting*, *1*, pp. 152 - 158. St. Louis, MO, USA.

[100] Qinghua, L., Khambadkone, A., & Jabbar, M. (Nov. 2003). Direct flux control of interior permanent magnet synchronous motor drives for wide-speed operation. *IEEE 5th International Conference on Power Electronics and Drive Systems (PEDS 2003)*, *2*, pp. 1680 - 1685. Singapore.

[101] Quigley, R. J. (Mar. 1993). More Electric Aircraft. *IEEE 8th Annual Applied Power Electronics Conference and Exposition (APEC '93)*, (pp. 906 - 911). San Diego, CA, USA.

[102] Radomski, T. A. (1990). Alternating current generator. *Patent No. 4 959 577.* US.

[103] Raimondi, G. M., Sawata, T., Holme, M., Barton, A., White, G., Coles, J., et al. (Jun. 2002). Aircraft embedded generation systems. *IEEE International Conference on Power Electronics, Machines and Drives*, (pp. 217 - 222).

[104] Roboam, X. (Jun. 2011). New trends and challenges of electrical networks embedded in “more electrical aircraft”. *IEEE International Symposium on Industrial Electronics (ISIE)*, (pp. 26 - 31). Gdansk, Poland.

[105] Rosero, J. A., Ortega, J. A., Aldabas, E., & Romeral, L. (2007). Moving towards a more electric aircraft. *IEEE Aerospace and Electronic Systems Magazine , 22* (3), 3 - 9.

[106] Roshen, W. (2007). Iron loss model for permanent-magnet synchronous motors. *IEEE Transactions on Magnetics , 43* (8), 3428 - 3434.

[107] Russenschuck, S. (1990). Mathematical optimization techniques for the design of permanent magnet synchronous machines based on numerical field calculation. *IEEE Transactions on Magnetics, 26*(2), 638-641.

[108] Russenschuck, S. (1992). Application of Lagrange multiplier estimation to the design optimization of permanent magnet synchronous machines. *IEEE Transactions on Magnetics, 28*(2), 1525-1528.

[109] Schramm, A., & Lanfer, H. (Jul. 2011). An offline optimization method for efficiency optimized operation of interior permanent magnet synchronous machines. *IEEE/ASME International Conference on Advanced Intelligent Mechatronics (AIM)*, (pp. 86 - 91). Budapest, Hungary.

[110] Senjyu, T., Shimabukuro, T., & Uezato, K. (Feb. 1995). Vector control of synchronous permanent magnet motors including stator iron loss. *IEEE International Conference on Power Electronics and Drive Systems, 1*, pp. 309 - 314. Singapore.

[111] Shafranek, R. J. (1967). Self-excited brushless alternator. *Patent No. 3 346 749.* US.

[112] Shakal, A., Liao, Y., & Lipo, T. A. (Jun. 1993). A permanent magnet AC machine structure with true field weakening capability. *Conference Proceedings of IEEE International Symposium on Industrial Electronics (ISIE 93)*, (pp. 19 - 24). Budapest, Hungary.

[113] Shang , Y., & Wah, B. (Nov. 1998). Improving the performance of discrete Lagrange-multiplier search for solving hard SAT problems. *10th IEEE International Conference on Tools with Artificial Intelligence*, (pp. 176-183). Taipei, Taiwan.

[114] Sheng, Y., Zhou, W., Hong, Z., & Yu, S. (Jul. 2010). Field weakening operation control of permanent magnet synchronous motor for railway vehicles based on maximum electromagnetic torque at full speed. *IEEE 29th Chinese Control Conference (CCC)*, (pp. 1608 - 1613). Beijing, China.

[115] Shinnaka, S. (Sep. 1998). Proposition of new mathematical models with core loss factor for controlling AC motors. *Proceedings of the 24th Annual Conference of the IEEE Industrial Electronics Society (IECON '98), 1*, pp. 297 - 302. Aachen , Germany.

[116] Shinnaka, S., & Sagawa, T. (2007). New optimal current control methods for energy-efficient and wide speed-range operation of hybrid-field synchronous motor. *IEEE Transactions on Industrial Electronics , 54* (5), 2443 - 2450.

[117] Shinnaka, S., & Sagawa, T. (May 2005). New optimal current control methods for energy-efficient and wide speed-range operation of hybrid-field synchronous motor. *IEEE International Conference on Electric Machines and Drives (IEMDC)*, (pp. 535-542). San Antonio, TX, USA.

[118] Son, Y., Hwang, K., & Kwon, B. (Sept. 2010). Maximum torque control for optimal design to reduce cogging torque in spoke type interior permanent magnet synchronous motor. *IEEE Energy Conversion Congress and Exposition (ECCE)*, (pp. 3654 - 3658). Atlanta, GA, USA.

[119] Song, J., Zhou, M., & Su, Y. (Nov. 2003). Study of optimal efficient control of permanent magnet synchronous motor. *IEEE 6th International Conference on Electrical Machines and Systems (ICEMS 2003), 1*, pp. 41 - 44. Beijing, China.

[120] Spitzer, C. R. (1984). The All-Electric Aircraft: A systems view and proposed NASA research programs. *IEEE Transactions on Aerospace and Electronic Systems , AES-20* (3).

[121] Sriyanyong, P., & Song, Y. (Jun. 2005). Unit commitment using particle swarm optimization combined with Lagrange relaxation. *IEEE Power Engineering Society General Meeting, 3*, pp. 2752-2759. Tampa, Forida, USA.

[122] Syverson, C. D. (1995). Hybrid alternator. *Patent No. 5 397 975.* US.

[123] Syverson, C. D., & Curtiss, W. (1997). Hybrid alternator with voltage regulator. *Patent No. 5 631 544.* US.

[124] Tapia, J., Leonardi, F., & Lipo, T. A. (2003). Consequent-pole permanent magnet machine with extended field-weakening capability. *IEEE Transactions on Industry Applications , 39* (6), 1704-1709.

[125] Thurston , R., & Legowski, S. (1993, Apr.). A simple and accurate method of computing average and RMS currents in a three-phase PWM inverter. *IEEE Transactions on Power Electronics, 8*(2), 192-199.

[126] Tremblay, O., & Dessaint, L. (2009). Experimental validation of a battery dynamic model for EV. *World Electric Vehicle Journal , 3*.

[127] Tremblay, O., Dessaint, L., & Dekkiche, A. (Sept. 2007). A generic battery model for the dynamic simulation of hybrid electric vehicles. *IEEE Vehicle Power and Propulsion Conference (VPPC),* (pp. 284 - 289). Arlington, TX, USA.

[128] Tsiaflakis, P., Vangorp, J., Moonen, M., Verlinden, J., & Van Acker , K. (May 2006). An efficient search algorithm for the Lagrange multipliers of optimal spectrum balancing in multi-user XDSL systems. *IEEE International Conference on Acoustics, Speech and Signal Processing (ICASSP), 4*, p. IV. Toulouse, France.

[129] Ugalde, G., Almandoz, G., Poza, J., & Gonzalez, A. (Sept. 2009). Computation of iron losses in permanent magnet machines by multi-domain simulations. *13th European Conference on Power Electronics and Applications (EPE '09),* (pp. 1 - 10). Barcelona, Spain.

[130] Verbeeck, J., Pintelon, R., & Lataire, P. (1999). Identification of synchronous machine parameters using a multiple input multiple output approach. *IEEE Transactions on Energy Conversion , 14* (4), 909 - 917.

[131] Vido, L., Amara, Y., Gabsi, M., Lecrivain, M., & Chabot, F. (Oct. 2005). Compared performances of homopolar and bipolar hybrid excitation synchronous machines. *IEEE Industry Applications Conference, 40th IAS Annual Meeting, 3*, pp. 1555 - 1560.

[132] Vido, L., Gabsi, M., Lecrivain, M., Amara, Y., & Chabot, F. (May 2005). Homopolar and bipolar hybrid excitation synchronous machines. *IEEE International Conference on Electric Machines and Drives,* (pp. 1212 - 1218). San Antonio, TX, USA.

[133] Wang, F. (Oct. 2003). A nonlinear saturation model for salient-pole synchronous machines in high performance drive applications. *IEEE Conference Record of the Industry Applications Conference, 38th IAS Annual Meeting, 2*, pp. 906 - 910. Salt Lake City, USA.

[134] Weeber, K., & Hoole, S. (1992). Geometric parametrization and constrained optimization techniques in the design of salient pole synchronous machines. *IEEE Transactions on Magnetics, 28*(4), 1948-1960.

[135] Weimer, J. A. (Oct. 1993). Electrical power technology for the more electric aircraft. *12th AIAA/IEEE Digital Avionics Systems Conference (DASC),* (pp. 445 - 450). Fort Worth, TX, USA.

[136] Weimer, J. A. (Jun. 2003). The role of electric machines and drives in the more electric aircraft. *IEEE International Electric Machines and Drives Conference (IEMDC'03), 1*, pp. 11 - 15. Madison, Wisconsin, USA.

[137] Xu, D., Wang, T., Liu, J., & Wei, H. (Jun. 2008). Research on optimal-torque control method of permanent magnet synchronous motor. *3rd IEEE Conference on Industrial Electronics and Applications (ICIEA 2008),* (pp. 1229 - 1233). Singapore.

[138] Xu, L., & Yao, J. (Oct. 1991). A compensated vector control scheme of a synchronous reluctance motor including saturation and iron losses. *Conference Record of the 1991 IEEE Industry Applications Society Annual Meeting, 1*, pp. 298 - 304. Dearborn, MI, USA.

[139] Xu, L., Xu, X., Lipo, T. A., & Novotny, D. W. (1991). Vector control of a synchronous reluctance motor including saturation and iron loss. *IEEE Transactions on Industry Applications , 27* (5), 977 - 985.

[140] Xuyun, F., & Zechang, S. (Sept. 2008). A battery model including hysteresis for State-of-Charge estimation in Ni-MH battery. *IEEE Vehicle Power and Propulsion Conference (VPPC '08)*, (pp. 1 - 5). Harbin, China.

[141] Zhang, H., Saudemont, C., Robyns, B., & Petit, M. (Sept. 2008). Comparison of technical features between a More Electric Aircraft and a Hybrid Electric Vehicle. *IEEE Vehicle Power and Propulsion Conference (VPPC '08)*, (pp. 1 - 6). Harbin, China.

[142] Zhang, H., Saudemont, C., Robyns, B., Huttin, N., & Meuret, R. (Sept. 2008). Stability analysis on the DC power distribution system of More Electric Aircraft. *13th IEEE Power Electronics and Motion Control Conference (EPE-PEMC)* , (pp. 1523 - 1528). Poznan, Poland.

[143] Zhang, T., Liu, B., & Zhang, H. (Jul. 2010). Direct torque control of permanent magnet synchronous motor. *IEEE 29th Chinese Control Conference (CCC)*, (pp. 3358 - 3361). Beijing, China.

[144] Zhang, Z., Yan, Y., Yang, S., & Bo, Z. (2008, Sept.). Principle of operation and feature investigation of a new topology of hybrid excitation synchronous machine. *IEEE Transactions on Magnetics, 44*(9), 2174 - 2180.

[145] Zhao, X., & Liang, H. (May 2009). Flux-weakening control of permanent magnet synchronous motor using in electric vehicles. *IEEE 6th International Power Electronics and Motion Control Conference (IPEMC '09)*, (pp. 1050 - 1054). Wuhan, China.

Publications

Communications at international conferences with a lecturer committee

- Mbayed, R., Vido, L., Salloum, G., Monmasson, E., & Gabsi, M. (May 2011). Effect of iron losses on the model and control of a hybrid excitation synchronous generator. *2011 IEEE International Electric Machines & Drives Conference (IEMDC 2011)*, (pp. 971 - 976). Niagara Falls, ON, Canada.

- Mbayed, R., Salloum, G., Vido, L., Monmasson, E., & Gabsi, M. (Jun. 2011). Control of a hybrid excitation synchronous generator supplying an isolated load. *Electrimacs 2011*. Cergy - Pontoise, France.

- Mbayed, R., Salloum, G., Vido, L., Monmasson, E., & Gabsi, M. (Jun. 2011). Control of a Hybrid Excitation Synchronous Generator connected to a diode rectifier supplying a DC bus. *20th IEEE International Symposium on Industrial Electronics (ISIE 2011)*, (pp. 562 - 567). Gdansk, Poland.

- Mbayed, R., Salloum, G., Vido, L., Monmasson, E., & Gabsi, M. (Mar. 2012). Hybrid excitation synchronous machine control in electric vehicle application with copper losses minimisation. *6th IET International Conference on Power Electronics, Machines and Drives (PEMD)*, (p. B22). Bristol, UK.

- Mbayed, R., Salloum, G., Vido, L., Monmasson, E., & Gabsi, M. (Oct. 2012). Hybrid Excitation Synchronous Motor control in Electric Vehicle with copper and iron losses minimization. *38th Annual Conference of the IEEE Industrial Electronics Society (IECON).* Montreal, Canada.

Communications at international journals with a lecturer committee

- Mbayed, R., Salloum, G., Vido, L., Monmasson, E., & Gabsi, M. (2012). Hybrid excitation synchronous generator in embedded applications: Modeling and control. *Transactions on Mathematics and Computers in Simulation Elsevier*. Online early access, DOI: 10.1016/j.matcom.2012.07.018

- Mbayed, R., Salloum, G., Vido, L., Monmasson, E., & Gabsi, M. (2012). Control of a hybrid excitation synchronous generator connected to a diode bridge rectifier supplying a DC bus in embedded applications. *IET Electric Power Application*. *Accepted*